Isotopic tracing (Si, Ca, Sr, H and O) of biogeochemical processes in Indian groundwater along the land-to-ocean continuum

Sarath Pullyottum Kavil

Sorbonne Université

École doctorale des Sciences de l'Environnement d'Île-de-France (ED 129)

Laboratoire d'Océanographie et du Climat : Expérimentations et Approches Numériques (LOCEAN) - UMR 7159

Équipe de recherche CYBIOM

Isotopic tracing (Si, Ca, Sr, H and O) of biogeochemical processes in Indian groundwater along the land-to-ocean continuum

Par Sarath PULLYOTTUM KAVIL

Thèse de doctorat en Biogéochimie

Dirigée par Damien CARDINAL et Ramananda CHAKRABARTI

Présentée et soutenue publiquement le mardi 24 Janvier 2023

devant le jury composé de:

M. Karim BENZERARA	IMPMC, CNRS, Paris	Président du jury
Mme. Sophie OPFERGELT	ELIE, UCLouvain, Louvain-la-Neuve	Rapportrice
M. Gregory DE SOUZA	Earth Sciences, ETH, Zurich	Rapporteur
Mme. Sophie CORNU	CEREGE, INRAE, Aix-en-Provence	Examinatrice
M. Jean RIOTTE	GET, IRD, Toulouse	Co-encadrant de these, Invité
M. Ramananda CHAKRABARTI	CEaS, IISc, Bangalore	Co-directeur de thèse
M. Damien CARDINAL	LOCEAN, Sorbonne Université, Paris	Directeur de thèse

Dedication

To,

autumn rain and winter sun,

purple skies and crashing waves,

weeping willow and my dear ferns,

fluffy Zoro and warm memories,

and to all the loving, caring people in my life.

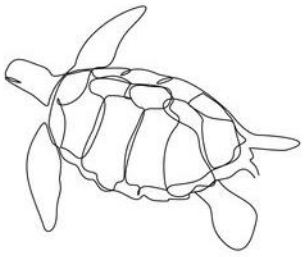

Acknowledgements

Undertaking this PhD was a profound experience and can only be described as a product of constant support, guidance, and care from a lot of people, some of whom I might have missed here. I would like to take this opportunity to express my heartfelt gratitude of all of them and mention a few here.

First and foremost, this endeavor would not have been possible without the guidance and encouragement of my research supervisor, Prof. Damien Cardinal. I was a complete novice to the field of biogeochemistry at the start, and he inspired me to take the journey into the world of silicon and guided me throughout the doctoral work. Thank you for trusting me from day one, I am sure your dedication and patience has rubbed off on me. Starting from the first time I met you during my undergraduate period and the internship that followed, I learned a lot from you these years and I hope I can keep learning and I am forever thankful to have got a mentor like you. I am grateful to have worked with and mentored by two research co-supervisors, Prof. Ramananda Chakrabarti and Dr. Jean Riotte. I have known Prof. Ramananda since my BS-MS in IISc, and he first introduced me to isotope geochemistry through course works in CEaS. I was excited to learn that my PhD project involved working half time at his lab in CEaS. Owing to the pandemic situation in India, we had a hard time accessing lab or even the university for that matter, and he was always there to support me throughout the difficult and tricky times. I learned a lot about efficiency and responsibility working with you and in your lab, and I greatly appreciate the confidence you had in me. The doctoral work involved diverse research areas and multiple isotopic proxies, and I was fortunate to have Jean as a supervisor to brainstorm and explore new ideas and inspired me look beyond conventional patterns. I highly appreciate that you always found time to discuss work and the patience in explaining me critical zone biogeochemistry.

Also take this opportunity to thank my PhD jury: Karim Benzerara, Sophie Opfergelt, Gregory De Souza and Sophie Cornu for the thoughtful comments and interesting discussions we had following the defense which greatly improved the thesis manuscript. I am grateful to Sophie Opfergelt for being part of my thesis committee and guiding me throughout the doctoral work, and Karim, Gregory and Sophie Cornu for the fruitful discussion we had during GES12 in Zurich and later as well, which was of immense help in forming and writing the final thesis discussion.

I was fortunate to have associated with Prof. V.V.V.S Sarma, chief scientist at NIO, India, and his expertise in estuarine and coastal biogeochemistry greatly helped forming some of the key ideas of the thesis. I thank him for his advice and suggestions during the field work and also making time to discuss, read and review final thesis chapters during his stay in Paris. I am grateful to Sandrine Caquineau for introducing me to SEM analysis and helping me take a closer look at the little things that really mattered. I also take this opportunity to thank all the IRD personnel for the support throughout the thesis work. I would like to express my heartfelt thanks to Arnaud Dapoigny, Irina Djouraev and Pierre Burckel for helping me with data acquisition and analysis using MCICPMS and ICMPS. I really appreciate the dedication and effort by Arnaud, which is one reason why we were able to produce a large dataset of Si isotopes in such a short time. A very special thanks goes to Mustapha Benrahmoune for his constant support and help with maintaining the clean lab which made all the analysis possible. I am also grateful to Jonathan Prunier for all his efforts and help with Germanium analysis and patiently teaching me the techniques and data analysis. In addition, I had the pleasure of meeting and discussing with so many inspiring people including Laurent Riuz, Haimanti Biswas, Sambuddha Misra, Mathieu Sébilo, Sridevi Bobbili, Véronique Vaury and B.S.K Kumar.

It has been a great privilege to be part of the NUNDERGROUND project team and I would like to express my sincere gratitude to the entire team. I would like to take this opportunity to convey a big thanks ARTS-IRD Scholarship team for the constant support and care throughout, I could not have done this without your genuine effort of the entire team. Given the pandemic situation I can't imagine how difficult it must have been to handle all the administrative work and I express my heartfelt thanks to the whole team for the effort. I want to extend a special thanks to Gaelle Brule, who handled my PhD scholarship for all her effort and care starting from my day one as a PhD student.

I would like to thank all my colleagues and PhD fellows, from both LOCEAN and RC lab, who probably best understood the ups and downs and supported me throughout the PhD journey. Thanks for all the lunchtime chitchats, coffee/tea breaks, evening drinks and holiday celebrations. I have no clue how to thank two very special people in my life, Carla Geisen and Coraline Lesseure, without a doubt the best part of the PhD life. Meeting them during my internship in Paris was one reason I confidently accepted the PhD position, and I owe it to them for all the cheers, smiles and plans that made me feel at home when I was so far from home. I am so looking forward to our future trips and plans and thank you so much for being there for me always. I am greatful to all the warm memories from 46-00 family, thank to Edwin, Céline, Jonathan, Fanny, Diego, Han, Valentin, Lloyd, Claude and Catherine and from RC lab group,

thanks to Sourav, Valens, Utpalendu, Gaurav, Walter and Biswajit. I like to especially thank Sourav Ganguly for helping with the TIMS analysis, chats over tea and for the exciting discussions.

I could not have undertaken this journey or any journey for that matter without my lovely friends and family. Last few years have been challenging at best and I owe it all to them for cheering me up every time I felt low, making plans with me, and including me in every plan, even though I was far away, and standing right next to me through all the difficult times. I can't begin to describe how much it meant, and as long as you are all with me, I am never going to run out of hopes, dreams and inspirations. Thanks to all my dear friends, Aadarsh, Amaya, Anju, Anandthan, Athul, Sayooj, Shehal, Rahul, Meenu, Amith, Bharath, Nrutyati, Bharath, Subeesh, Sandesh, Arshi and many more. I also like to thank Soundharya for all the warm memories and times together, I cherish them, and all the care and love meant so much to me. I want you all to know that every phone call, every meetup, every trip plan, every smile, and every words you said and did matter a lot to me. Wherever you all are, I love you all so much and I know we have so much more to plan and do. Finally, to my little bundle of joy, my family. I am forever indebted to my Achan and Amma for everything they have done for and with me throughout my life. Whatever I am and I become, is all because of your care and nurture. Ammu and Kannan, watching you both grow up alongside me was my biggest joy and I am so lucky to have such gem of siblings. I know you are going to be there with me always and I love you all so much. Whatever life has got for me in the future, I am happy to do it with you all by my side.

Scientific activities during thesis

Publications

Sarath P. K., Riotte J., Chakrabarti R., Dapoigny A., Vaury V., Ruiz L., Cardinal D.. Deep regolith weathering controls δ^{30}Si composition of groundwater under contrasting land use in tropical watersheds. *Submitted to Geochim. Cosmochim. Acta., November 2022*

Sarath P. K., Mangalaa K. R., Cardinal D., Gurumurthy G. P., Dapoigny A., Sarma V. V. S. S. and Riotte J. (2022). Seasonal, weathering and water use controls of silicon cycling along the river flow in two contrasting basins of South India. *Chem. Geol*. 604, 120883.

Sarath P. K., Bala P. R., Ghosh D., Kumar P. and Sukumar R. (2021) Climate change and the migration of a pastoralist people c. 3500 cal. years BP inferred from palaeofire and lipid biomarker records in the montane Western Ghats, India. *Environ. Archaeol,* 1-15.

Ramya Bala P., **Sarath P. K.**, Tayasu I., Yoshimizu C., Thirumalai K., Sajeev K. and Sukumar R. (2021) Paleovegetation dynamics in an alternative stable states landscape in the montane Western Ghats, India. *The Holocene* 32, 297–307.

Sarath P. K., Devanita Ghosh, Indira Pašić, Joyanto Routh. (2020). Temporal dynamics of arsenic uptake and distribution: food and water risks in the Bengal basin, *Toxicological Environmental Chemistry* 102, 62-77.

Conferences

12th International Symposium Geochemistry of the Earth's Surface (GES12) ETH, Zurich, July 2022: **'**Seasonal, weathering and biotic controls of Si cycling in coastal groundwater and estuary in Southern India; insights from a multi-isotope approach' (poster).

Goldschmidt conference, July 2021: **'**Tracing weathering and anthropogenic controls of groundwater geochemical cycling from tropical watershed' (virtual poster presentation).

52nd International Liege colloquium on Ocean Dynamics, July 2020: 'Seasonal variability of dissolved silicon and silicon isotopes in tropical estuary and coastal groundwater; implications in Si cycling and transport to coastal ocean' (virtual oral presentation).

EGU General Assembly 2020, European Geoscience Union, May 2020: 'Assessing seasonal controls in silicon cycle and isotopic signatures of groundwater under anthropogenic stress in tropical watershed' (virtual oral presentation).

Field work

NUNDERGROUND Project
Groundwater and surface water sampling in Karnataka and Godavari (August 2019)
Field survey, water sampling, filtration techniques.

Thesis coursework

Silica School, a virtual small private online course (SPOC) organized by Institut Universitaire Européen de la mer, University of Brest (60 hours).

French A1 level coursework organized by Sorbonne university (50 hours).

Advanced statistical inference and modelling using R course organized by University of Canterbury, Christchurch, New Zealand through edX (30 hours).

Laboratory techniques

Clean lab procedures for elemental and isotopic analysis, ICP-MS, Spectrophometer, MC-ICPMS (LOCEAN and LSCE, IPSL), TIMS (IISc, India).

PhD timeline

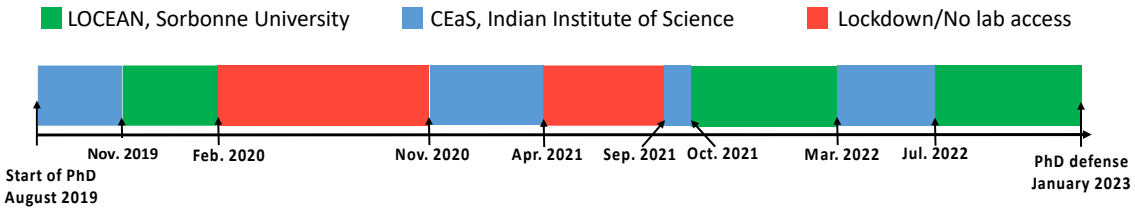

Résumé

Les eaux souterraines forment un système dynamique avec une grande hétérogénéité spatiale et temporelle, et agissent en tant qu'intermédiaire entre les processus de surface dans la zone critique et les fleuves qui apportent les solutés vers l'océan. Des études récentes révèlent que la décharge sous-marine d'eaux souterraines (SGD) est une voie dominante pour l'apport de nutriments aux côtes, dépassant souvent les flux de nutriments fluviaux, formant ainsi une composante importante des cycles biogéochimiques marins. Cependant, les SGD restent négligées dans les bilans de nutriments et sont difficiles à quantifier. Parmi ceux-ci, le silicium (Si) est un nutriment essentiel pour les diatomées, l'un des principaux producteurs primaires des écosystèmes aquatiques. Les bassins versants tropicaux humides avec précipitations saisonnières de mousson, généralement trouvés en Inde, favorisent une altération intense des silicates, ce qui entraîne des flux élevés de Si vers les eaux. Cependant, l'agriculture peut moduler le cycle de Si ce qui nécessite une évaluation plus poussée, notamment dans les eaux souterraines. Cette thèse étudie trois aspects majeurs du cycle de Si dans les eaux souterraines : i) l'impact des modifications de l'utilisation des terres et des précipitations de mousson sur Si dissous (DSi) et la signature isotopique de Si ($\delta^{30}Si$) des eaux souterraines en comparant un bassin versant agricole (Berambadi) et un bassin versant forestier (Mule Hole) à deux saisons, ii) élucider les interactions entre eaux souterraines et eaux de surface dans le plus grand système estuarien de mousson en Inde (Godavari) et, iii) quantifier les flux de Si apportés par la contribution en eaux douces des SGD vers l'Océan Indien grâce à une série d'échantillons d'eaux souterraines côtières. Pour cela, nous utilisons des traceurs isotopiques : isotopes de l'eau et $^{87}Sr/^{86}Sr$ pour identifier les sources et les mélanges, $\delta^{30}Si$ et rapports Ge/Si pour tracer le cycle du Si, et $\delta^{44/40}Ca$ pour déterminer l'altération des carbonates.

Ce travail a permis d'augmenter la moyenne des $\delta^{30}Si$ des eaux souterraines mondiales de 0,49±0,9‰ (1SD, n=66) à 0,81±0,9‰ (1SD, n=224), inférieure aux $\delta^{30}Si$ des eaux de rivière et de l'océan. Nous montrons que les signatures $\delta^{30}Si$ des eaux souterraines ne sont pas impactées par les modifications de l'utilisation des terres ni la saisonnalité, et sont principalement contrôlées par l'altération des silicates et la formation d'argiles secondaires. Les eaux souterraines présentent généralement un comportement stable avec un équilibre dynamique entre l'apport de Si et la formation de phases secondaires. Les $\delta^{30}Si$ issus de l'altération, de l'adsorption et de l'absorption par les plantes qui se produisent dans les horizons peu profonds du sol et du saprolite sont partiellement homogénéisés par l'altération du régolithe dans la zone profonde. Les $\delta^{30}Si$ de l'estuaire de Godavari présentent une variabilité saisonnière importante,

principalement due aux diatomées et parfois à un apport hétérogène issus des eaux souterraines pendant la saison sèche, alors que l'altération des silicates et la formation d'argiles secondaires dominent pendant la saison humide. L'estuaire est un filtre important pour l'apport en Si à l'océan, en retirant ~15% du DSi total apporté par le fleuve Godavari. Les $\delta^{44/40}$Ca dans l'estuaire (1,3±0,5‰, 1SD, n=16) et ses eaux souterraines (1,6±0,7‰, 1SD, n=15) sont très hétérogènes. Le fractionnement isotopique du Ca, tant dans l'estuaire que dans les eaux souterraines, est principalement dû à la précipitation des carbonates secondaires, un processus qui nécessiterait une étude plus approfondie. Enfin, DSi et δ^{30}Si des eaux souterraines côtières indiennes indiquent que les apports d'eaux douces par SGD contribuent à <1% du flux total de Si apporté par les fleuves ce qui est considéré comme ayant un impact insignifiant sur les budgets océaniques de Si et d'isotopes dans l'Océan Indien Nord.

Résumé de thèse vulgarisé pour le grand public

La décharge sous-marine d'eaux souterraines (GW), bien que très hétérogène, serait une voie dominante pour l'apport de nutriments aux côtes, formant une composante importante des cycles biogéochimiques marins. Parmi ces éléments, le silicium (Si) est un nutriment clé pour la productivité primaire, jouant également un rôle dans la limitation de l'eutrophisation. En utilisant les isotopes, nous étudions le cycle de Si dans les GW en Inde, et montrons que : i) les signatures isotopiques des GW sont dominées par l'altération des silicates, et ne sont pas affectées par les modifications de l'utilisation des terres ni par la mousson, ii) l'estuaire de Godavari est dominé par la croissance des algues diatomées et la décharge de GW pendant la saison sèche et, par l'altération des silicates pendant la mousson, iii) l'apport d'eau douce par GW le long de la côte indienne est <1% du Si délivré par les fleuves et est insignifiant pour le bilan du Si et des isotopes dans l'Océan Indien Nord.

Mots clés: Isotopes silicium, décharge sous-marine d'eaux souterraines, alteration, estuaires, usage des sols

Abstract

Groundwater forms a dynamic system exhibiting spatial and temporal heterogeneity, and acts as an intermediate between surface processes occurring in critical zone and the riverine systems, which ultimately delivers solutes from continents to ocean. Recent studies reveal that the submarine groundwater discharge (SGD) is a dominant pathway for nutrient delivery to the coastal ocean, often exceeding riverine nutrient fluxes, thus forming a significant component of oceanic biogeochemical cycling. However, SGD remains overlooked in coastal nutrient budgets and is difficult to quantify given large spatial and temporal variability. Among the elements delivered to the coast through SGD, silicon (Si) forms a key nutrient for diatoms, one of the dominant primary producers in freshwaters, estuary and coastal ecosystems. Tropical humid watersheds with seasonal monsoonal precipitation, commonly found in Indian subcontinent, favors intense silicate weathering resulting in high Si fluxes to surface and groundwaters. However, anthropogenic activities including agriculture and damming can significantly modulate Si cycling and requires further evaluation, particularly in groundwater. The present research investigates three major aspects of groundwater Si cycling: i) the impact of land use changes (such as agriculture) and monsoon precipitation in groundwater dissolved silicon (DSi) and silicon isotopic signature (δ^{30}Si) by comparing an agricultural (Berambadi) and forested (Mule Hole) watersheds across two seasons, ii) elucidating groundwater-surface water interactions in the largest monsoonal estuarine system in India (Godavari) and, iii) quantify the fresh submarine groundwater derived Si fluxes to Indian Ocean using a series of coastal groundwaters along Indian coastline. We employ multiple isotopic tracers to understand biogeochemical processes in groundwater including water isotopes and $^{87}Sr/^{86}Sr$ to understand sources and mixing, δ^{30}Si and Ge/Si ratios to trace Si cycling, and $\delta^{44/40}$Ca to decipher carbonate weathering in critical zone.

The present work increased the δ^{30}Si average of global groundwater from 0.49±0.9‰ (1SD, n=66) to 0.81±0.9‰ (1SD, n=224), lower than the river water and seawater δ^{30}Si. We show that the δ^{30}Si signatures of groundwater are not impacted by land use changes and seasonal monsoon, and are primarily driven by silicate weathering and secondary clay formation in soil and saprolite. Groundwater system generally exhibits a steady state behaviour with a dynamic equilibrium between Si supply and formation of secondary phases. We conclude that Si isotopic signatures of weathering, adsorption, and plant uptake occurring in the shallow soil and saprolite horizons are partly overprinted and homogenized by the regolith weathering in the deep critical zone. In the second part of the thesis, we study Godavari estuary and adjacent

groundwater to discern sources *vs.* mixing *vs.* processes along this land-to-ocean interface. The δ^{30}Si signatures of estuary exhibit significant temporal variability, primarily driven by diatom uptake and some heterogeneous groundwater discharge during dry season while silicate weathering and secondary clay formation in the basin dominate during wet season. We note that estuaries can act as significant filters for Si supply to ocean, removing ~15% of the total DSi supplied by the Godavari river. The $\delta^{44/40}$Ca composition in Godavari estuary (1.3±0.5‰, 1SD, n=16) and groundwaters (1.6±0.7‰, 1SD, n=15) are highly heterogenous. The Ca isotopic fractionation in both estuary and groundwater are primarily driven by precipitation of secondary carbonates, a process that would require further study. Finally, the dissolved silicon and δ^{30}Si of coastal groundwater all over India indicates that fresh SGD discharge contributes to <1% of the total Si flux of the rivers and is considered to have insignificant impact on oceanic Si and isotopic budgets in North Indian Ocean.

Popularized thesis summary for general public

Groundwater (GW) forms a dynamic system with high spatial heterogeneity. Recent studies reveal that submarine groundwater discharge (SGD) is a dominant pathway for nutrient delivery to the coastal ocean, thus forming a significant component of oceanic biogeochemical cycles. Among those elements, silicon (Si) is a key nutrient for riverine, estuarine and coastal primary productivity, also playing a role in limiting eutrophication. Using isotopic tools we investigate GW Si cycling in India, and we conclude: i) Si isotopic signatures of GW are heterogenous, primarily driven by silicate weathering, and are not impacted by anthropogenic land use changes nor seasonal monsoon, ii) estuarine systems are impacted by growth of diatom algae and groundwater discharge during dry season and silicate weathering during monsoon, iii) direct input of fresh groundwater along Indian coast is <1% of the total Si delivered by rivers and are insignificant for Si and isotopic budget in North Indian Ocean.

Keywords: Silicon isotopes, submarine groundwater discharge, weathering, estuary, land use.

Table of Contents

I. Introduction

1. Critical zone: The living skin of planet Earth

Critical zone (CZ) is an integral part of continental surfaces, from tree-top to lower limits of groundwater, where atmosphere, biosphere, lithosphere, and atmosphere actively interact (NRC, 2001). Processes occurring within the critical zone, such as mass and energy exchange, soil formation, generation of stream flow and therefore, landscape evolution is crucial for sustaining terrestrial life (Field et al., 2015). A wide array of biogeochemical reactions occurring in the CZ are responsible for the supply of nutrients and energy, that helps to sustain life on continents. In short, CZ can be considered as a weathering engine or a reactor where rocks containing minerals formed under high temperature encounter with the fluids in the surface and are weathered into transportable materials and dissolved load, ultimately shaping the composition of both the atmosphere and ocean at geological time scales (Fig. 1, Anderson et al., 2004; Brantley et al., 2007). Understanding the extend and functioning of the critical zone requires extensive information of the surface processes as well as subsurface processes. The challenges get complex as we look into the belowground processes, where ambiguity starts even in the very definition of critical zone: what do you define as the lower limit of groundwater? To start with, in National Research Council (NRC, 2001) definition of critical zone clearly states top of canopy as upper limit but proposing groundwater as a bottom limit is problematic. Groundwater is a dynamic system exhibiting heterogeneity spatially and temporally and can circulate within the critical zone depending on the existing climate (Riebe et al., 2016). To make it more transparent, Brantley et al. (2011) suggested to set the lower limit of CZ boundary to the subsurface layer where weathered material grades into rock and are no longer affected by meteoric fluids. Fan et al. (2015) considered base of active groundwater as the bottom of CZ, while Guo and Lin (2016) proposed a zone ranging from top of the vegetation canopy to the bottom of weathering zone. Recently a more refined definition considered base of the modern groundwater (<50 years old) as lower limit of critical zone (Xu and Liu, 2017). Such ambiguity exists due to the challenges in characterizing belowground processes and require further research to answer first order questions such as i) how thick is the critical zone? ii) how critical zone compartments interact, iii) Finally, to assess the impact of human activities in critical zone processes.

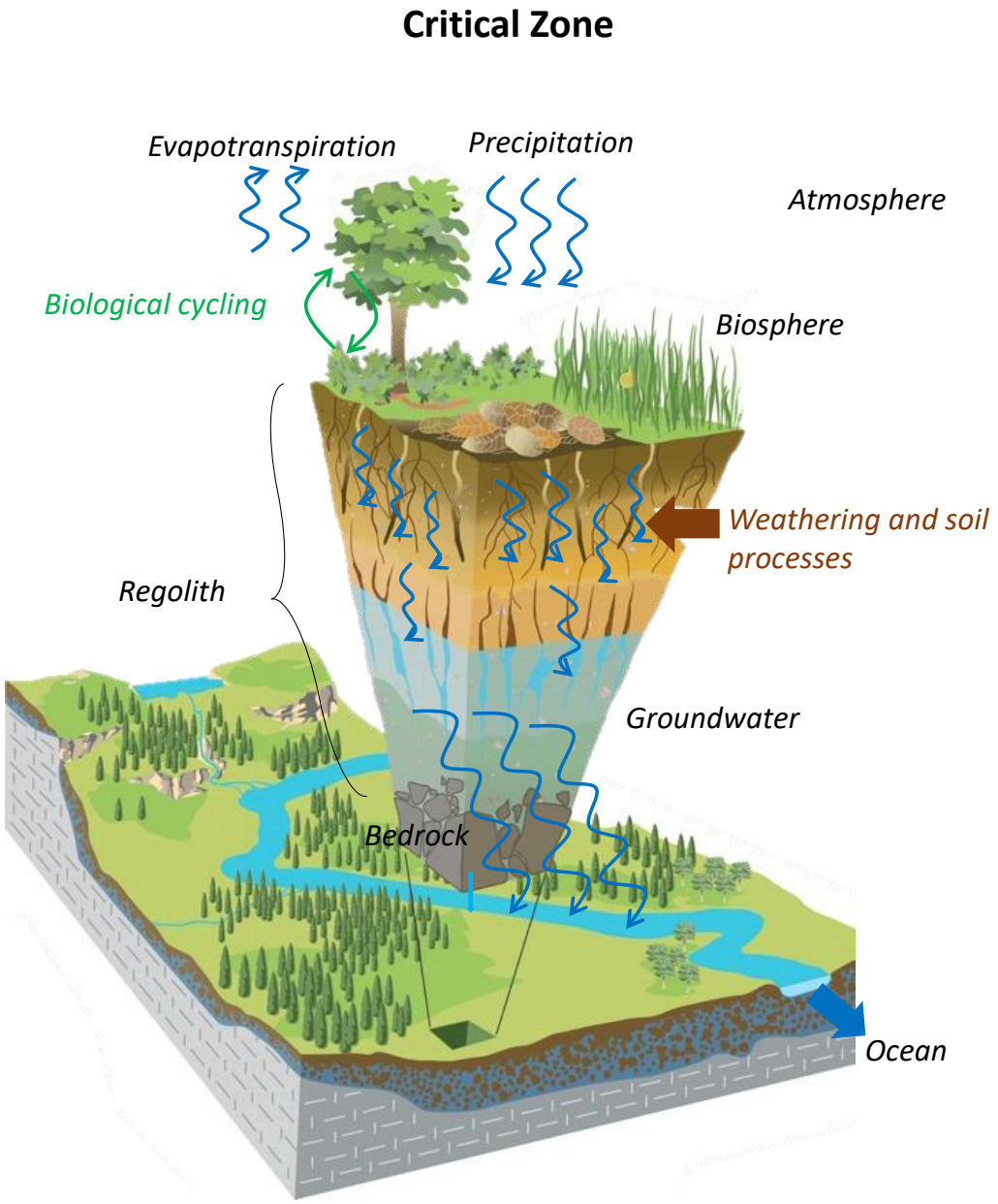

Figure 1. *A simple schematic of critical zone and the processes as the rainwater percolates through the unsaturated zone reaching groundwater, rivers and ultimately ocean. The figure modified from Chorover et al. (2007).*

Over geological timescales, CZ evolved in response to climatic and tectonic forcing, and more recently perturbed by human activities in Anthropocene (Steffen et al., 2007; White et al., 2015). To simplify, we can consider CZ as three co-evolving surfaces; the top of the vegetation canopy, the ground surface, and the deeper subsurface with weathered and unweathered materials (Brantley et al., 2017). Understanding the link between surface and subsurface processes is crucial to assess the sustainability of soil and water. Assessing the above ground and surface processes are increasingly efficient due to rapid development of remote sensing

techniques (Harpold, 2014). Evaluating deep critical zone processes are commonly shielded by meters of thick overlaying regolith and rock, limiting the access to sample, and thus received little attention in the past (Zanner and Graham, 2005; Riebe et al., 2016). However, the subsurface processes have profound implications in the overall functioning of critical zone and requires more attention. Water is considered as the thread that stiches the different components of critical zone, traveling from atmosphere to the lithosphere, interacting with both lithosphere and biosphere and entering soil water, groundwater, surface water and finally ocean (Brantley et al., 2007). Groundwater is by far the largest reservoir of water in critical zone and an active component of the hydrological cycle, but its role is often simplified or even ignored in studies related to climate change and land surface processes due to its inherent slow response time (Yang, 2004). Recent works have demonstrated that more than half of the global groundwater are sensitive to recharge variations related to climate change and can equilibrate within human time scales (Cuthbert et al., 2019).

2. Groundwater

2.1. Groundwater as a major hydrological compartment

Groundwater is fundamental part of hydrogeochemical system, a boundary in Earth's CZ and sustains stream flow, supports vegetation, dissolves solutes through water rock interactions in regolith and influence energy fluxes between land-atmosphere interface (Singha and Navarre-Sitchler, 2022). An estimated 1.4 billion km^3 of water is present on the Earth, but just 3% accounts for freshwater. Out of the 3% of the global freshwater volume, almost 69% is trapped as ice and snow, 30% as groundwater and remaining 1% in surface water systems including rivers, streams, lakes, and swamps (Gleick, 1993). Thus, almost 97% of the available freshwater for sustaining life on Earth is present in groundwater (Gleeson et al., 2016). Groundwater resources can be considered either in terms of water stocks or recharge (Döll, 2009). The first question to answer would be how deep is the groundwater and how much is accessible to surface ecosystems? A global compilation of the groundwater table depth by Fan et al. (2013) has shown that almost a third of the global land area is underlain by shallow groundwater, at an average depth of less than 5 meter. Groundwater table levels are often decoupled with the local rainfall and follow a delayed or even no response to precipitation events (Weider and Boutt, 2010; Fan et al., 2015). Even though the groundwater is ultimately sourced from precipitation, the patterns of recharge spatially and temporally depend on topography of the terrain (Fan et al., 2015). Shallow groundwaters sustain river base flow and other surface water components

such as springs, wetlands, riparian and estuarine ecosystems, act as source of water for deep rooted trees, and are shallow enough to contribute to land energy fluxes (Fan et al., 2015; Maxwell and Condon, 2016). Recent estimate by Gleeson et al. (2016) suggests that the volume of groundwater in the upper 2 km of the continental crust is approximately 23 million km^3, out of which between 0.1 to 5 million km^3 is modern (<50 years old). The age of groundwater is also important in terms of chemical weathering fluxes, ocean discharge, and climate change which are impacted by recharge-discharge balance and also in terms of vulnerability above surface changes (Gleeson et al., 2016). Even though the total groundwater storage dwarfs all other components of hydrological cycle, modern groundwater which can be replenished within human lifespan are limited in quantity and spatially heterogenous (Gleeson et al., 2016). When compared to surface waters, groundwaters are spatially more extensive, making it more available source of water supply and also less likely to be affected by surface pollutants. But the difficulty to access the groundwater, costs related to pumping and the inherent slowness (in terms of active flow) when compared to other CZ components makes groundwater understudied. There is growing evidence that the groundwater levels are depleting in many aquifers globally, especially in arid and semi-arid regions (Famiglietti et al., 2014). Depletion of groundwater table depth increases the cost of abstraction, reduces the groundwater discharge to small streams and can even lead to land subsidence (Amananbu et al., 2020). To achieve a sustainable groundwater use, withdrawal/pumping of groundwater should not exceed the long-term aquifer recharge, which requires extensive understanding of the climate, lithology, and aquifer characteristics of the region.

2.2. Groundwater system and climate change

Groundwater is one of the largest sources of freshwater in the world and 1.5 to 3 billion people all over the globe depends on groundwater for drinking purposes, along with other animals and plants (Taylor et al., 2013). Understanding the intricate relationship between climate and groundwater is critical, especially since the surface water resources are becoming unsustainable under the threat of climate change and anthropogenic activities. Groundwater systems exist in a delicate balance with the climate system, where the recharge, storage and discharge depend on the climatic feedback and acts as a coupled system. As climate varies the patterns of discharge, storage and discharge can change over different spatial and temporal scales depending on the sensitivity of the couple systems (Cuthbert et al., 2019). Projected changes in climate such as intensification of hydrological cycle, increased evaporation and evapotranspiration, extreme precipitation events, lesser snowfall and quick melting which

increases stream flow are all likely to impact the groundwater resources, but the complex interactions and feedbacks are difficult to characterize (Amananbu et al., 2020 and references therein). Groundwater resources are more difficult to identify, recover, assess and monitor, and the nature and characteristics of water below the Earth surface remains largely unknown. Interactions and responses of hydrological systems to climate change is subjected to complicated feedback networks. For example, even with intensification of hydrological processes, groundwater recharge is found to be decreasing in both temperate and tropical climate regions due to shift in precipitation patterns and increased evapotranspiration associated to climate change (Amananbu et al., 2020). Land use/land cover changes linked rapid urbanization can also modify the water balance by altering the runoff, evaporation-transpiration, and infiltration (Kundu et al., 2017). Due to projected increase in global air temperatures and subsurface temperatures, the discharging groundwater to the streams and rivers can have elevated temperatures which can lead to detrimental effects on temperature sensitive aquatic ecosystems (Kurylyk et al., 2014).

2.3. Groundwater in India

India is one of the most densely populated countries in the world, with just 4% of total world's land area supporting almost 24% of the global population (FAO, 2013). The country receives majority of the rainfall during southeast monsoon from June and September, and exhibit significant spatial variability in rainfall, from <150 mm/year in the northwestern regions and >2500 mm/year in certain places in northeast and southwest coast of India (Fig. 2, CGWB, 2012). Every year, India receives almost 4000 km^3 of fresh precipitation and half of it escapes the critical zone through overland flow, discharge into rivers, submarine groundwater discharge, and evapotranspiration (Fig. 2, Verma and Phansalkar, 2007). The aquifer systems in India are related to the river basins, comprising of highly productive alluvium aquifers in Indus-Ganges-Brahmaputra (IGB) systems to fractured aquifer systems in peninsular India with limited groundwater availability (Fig. 2, Mukherjee et al., 2015). The country is under regular water stress and the majority of the increasing demand is met from groundwater, which is considered as the backbone of India's agricultural as well as drinking water security (Vijay Shankar et al., 2011). Presently, groundwater contributes to 62% of agricultural irrigation, 85% rural and 62% urban domestic use water supply in India (Rodell et al., 2009; Saha and Ray, 2018). Annual groundwater withdrawal from aquifers in Indian subcontinent exceeds 340×10^9 m^3, one of the highest groundwater consumptions in the world (FAO, 2013). Rapid rise in population, water use and demand as well as intense pollution of surface water resources forces

people to switch to groundwater in order to meet the drinking water as well as agricultural water needs. Spatial and temporal variability of groundwater storage is related to uneven rainfall distribution and mismanagement of water resources (Mukherjee et al., 2015). India is one of the most intensively cultivated country in the world and occupies almost 30% of the total irrigated land area globally, which increased from 58.8% to 60.4% from early 1960s to 2016 (World Bank, 2017). At the same time India also contributed to 23% of the global increase in groundwater depletion from 2000 to 2010 (Dalin et al., 2017). Rapid groundwater depletion is one of the major sustainability challenges for India and many of the aquifers are under stress (Gleeson et al., 2012). For example, aquifers in Northwestern regions of India with a high abstraction rate led to declining groundwater levels at a rate of ~1m/year, with several aquifers with water levels decreased beyond 20 m (MacDonald et al., 2016). Groundwater abstraction considerably higher than annual rainfall in north and central India to support non-monsoon crops lead to rapid decline of groundwater storage and levels (Mishra et al., 2018). Rodell et al. (2018) estimated that the abstraction rate in North India is at 19.2±1.1 km^3/yr during 2000-2016, higher than the groundwater recharge during annual monsoon. Unsustainable abstraction of groundwater will negatively impact India's food production and threatening food security. Changes in monsoon intensity and also climatic extremes which are projected under the climate change scenario will exacerbate the problem and will put India under tremendous stress related to water availability. Groundwater depletion also leads to decreased discharge to streams and rivers to support base flow, which lead to decline in surface water, putting groundwater under further stress of pumping (Mukherjee et al., 2018). Irrigated agriculture and pumping with extensive use of fertilizers and manures can lead to salinization of the aquifers, alter the hydrogeochemistry of the groundwater and also pollutes the nearby streams, as documented in cultivated regions of Southern India (Buvaneshwari et al., 2017; Buvaneshwari et al., 2020). Increased pumping and decline in water table can also lead to seawater intrusion in coastal areas decreasing the availability of fresh drinking water and also can impact the submarine groundwater discharge patterns which supports coastal ecosystems (Moore et al., 2010).

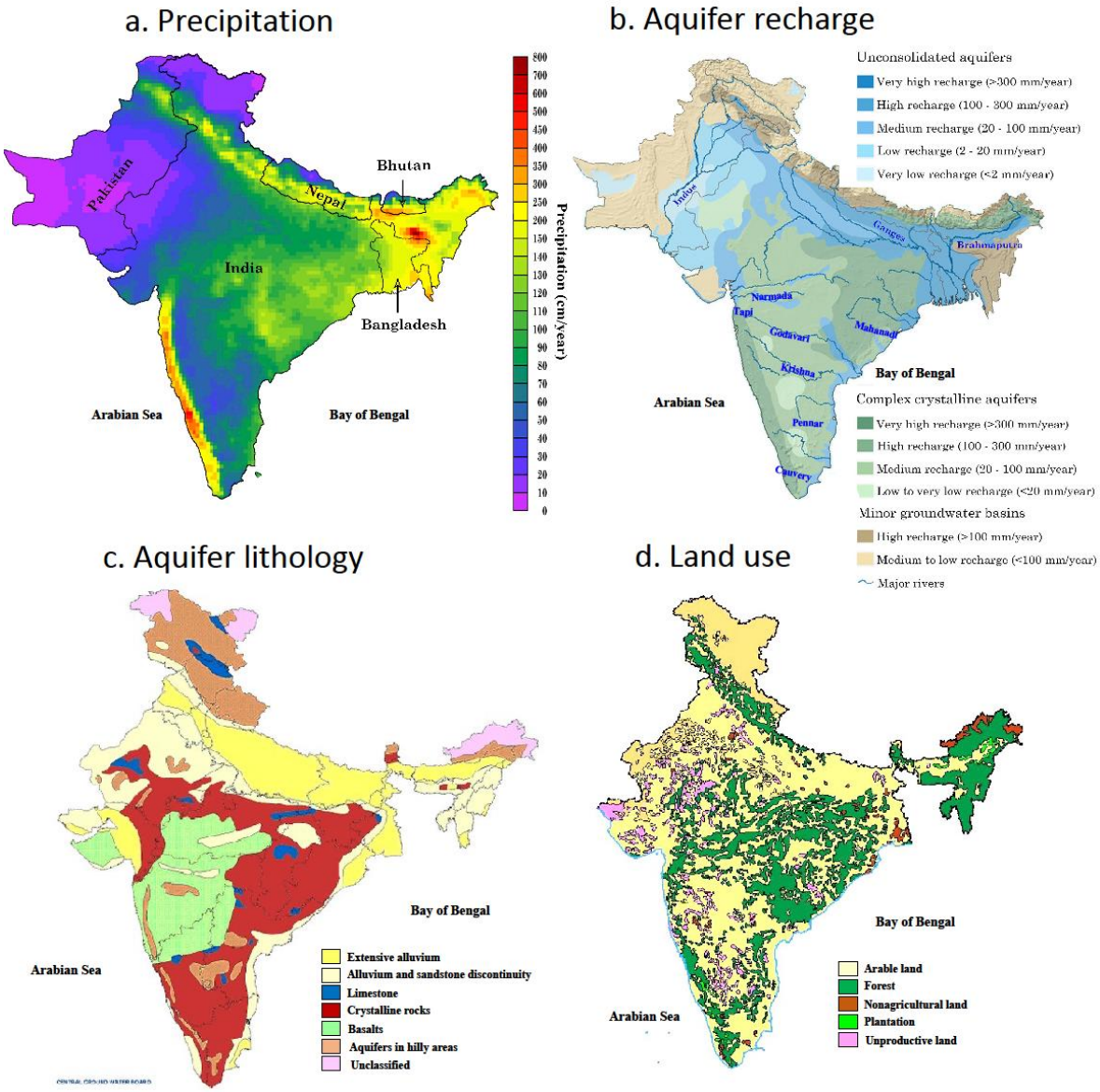

Figure 2. *Maps of Indian subcontinent distinguishing a) annual precipitation, b) aquifer recharge, c) aquifer lithology and, d) land use, with major rivers identified. The figure is modified from Mukherjee et al. (2015), India water portal, National Institute of Hydrology, India, and CGWB, (2012). Please note that the scale and borders are for illustrative purpose only.*

3. Coastal critical zone

Coastal zones are defined as the land are within 100 km of the shoreline, that are influenced by marine as well as terrestrial processes (Crossland, 2005; Lange, 2010). Coastal zones cover almost 2.3% of the total land area but supports almost 11% of the global population (Jiao and Post, 2019). Around 2 billion people living in coastal areas directly depends on groundwater as a fresh water source (Ferguson and Gleeson, 2012). The geology, geomorphology and climate vary considerably along the coastlines and lead to development of wide variety of coastal zones.

Coasts are the interface between continental freshwater and marine saline ecosystems, harboring high biological diversity. Rapid population growth along the coastlines followed by land use changes and urbanization can significantly alter the coastal ecosystems (Shi and Jiao, 2014). Increased water demand and food production lead to significant water withdrawal from coastal aquifers making them vulnerable to seawater intrusion (Poore and Nemecek, 2018). In addition to increased water use, freshwater resources are threatened by pollution caused by anthropogenic contaminants from agriculture, landfills, wastewater, and spills from industries (Michael et al., 2017).

3.1. Coastal aquifer processes

Coastal aquifers are generally defined as permeable geological units in the subsurface areas that can support significant water flow and are connected to the sea (Duque et al., 2020). They have unique characteristics compared to other aquifers and generally consist of unconsolidated surficial deposits (deriving from alluvial, lacustrine, deltaic, glacial or eolian processes), permeable rocks (e.g., limestones, shield, sandstone) or fractured systems such as karstified rocks. The waterflow is driven by variable density flow and mixing between freshwater and seawater with water table fluctuations induced by tidal actions (Jiao and Post, 2019). Deep in the subsurface, fresh groundwater meets seawater forming a freshwater-seawater interface. Because of the high salinity, seawater is denser than the freshwater by almost 2.5%, giving rise to a wedge-shaped body at the bottom of the freshwater. A dynamic equilibrium exists between the seawater and freshwater where the position of the wedge does not change, and seawater protrudes inland from coastline depending on the density differences between the two water bodies (Fig. 3). Such dynamic equilibrium indicates that the groundwater is not stagnant, freshwater flows towards the sea and a circulatory flow exists between fresh and saline groundwater. The boundary separating the freshwater and seawater is a gradual zone with varying salinity, which can be described as transition zone, mixing zone, zone of diffusion or subterranean estuary (STE) (Burnett et al., 2003; Moore et al., 2010).

3.2. Submarine groundwater discharge (SGD)

Long term chemical composition of global ocean is controlled by the balance between the input of solutes from continents and burial into deep ocean sediments (Broecker and Peng, 1982; Berner and Berner, 1987). Up until recently, riverine discharge and dust input from continents were thought to be the primary source of elemental flux to the ocean. Rivers, considered as the arteries of the continents, are known to supply 90-99% of the freshwater to the coasts and the

remaining 1-10% resulting from direct discharge of the coastal aquifers (Burnett et al., 2003). However, recent evidence suggests that submarine groundwater discharge (SGD), comprising of fresh and saline SGD discharge, accounts for 300-400% of the riverine discharge and can be a major driver of biogeochemical cycling in coastal ocean (Burnett et al., 2003; Taniguchi 2002; Moore et al., 2010). Submarine groundwater discharge is defined as the seaward flow of water across the land-sea interface, which includes both fresh terrestrial groundwater and recycled saline groundwater (Taniguchi et al., 2002; Burnett et al., 2003). The scale of SGD can be broadly described into three: nearshore scale, with a range of 1-10 m; the embayment scale ranging from 10m to 10 km offshore; and the continental shelf scale extending till the shelf region (Fig. 3, Bratton, 2010). Submarine groundwater discharge is the dominant pathway of the dissolved nutrient export to the coastal oceans and accounts for a total flux of $12\pm3*10^4$ km^3/yr in Atlantic and Indo-Pacific Oceans (Kwon et al., 2014). Integrated SGD fluxes to Atlantic and Indian Ocean is almost 3-4 times greater than the total riverine freshwater discharge (3 to $3.5*10^4$ km^3/yr, Milliman, 2001) and Indo-Pacific Oceans account for almost 70% of the total SGD (Kwon et al., 2014). Tropical coasts are known to export 56% of the fresh SGD to the ocean (Zhou et al., 2019). The mixture of fresh and saline SGD from coastal aquifers, significantly enriched in nutrients, and trace metals, can transport dissolved materials to coastal oceans and impact the biogeochemistry. Santos et al. (2021) observed in a recent compilation that SGD nutrient fluxes to coastal ocean exceeds riverine discharge in almost 60% of the studied regions, with median total SGD flux of 6 mmol $m^{-2}day^{-1}$ for dissolved inorganic nitrogen (DIN), 0.1 mmol $m^{-2}day^{-1}$ for dissolved inorganic phosphorus (DIP) and 6.5 mmol $m^{-2}day^{-1}$ for dissolved silicon (DSi). Estimated SGD derived fluxes DIN, DIP and DSi is approximately 1.4-, 1.6-, and 0.7-fold of the river fluxes to the global ocean (Atlantic+Indo-Pacific Oceans) (Cho et al., 2018). However, the fresh SGD component constrained by the global hydrological cycle typically accounts for only 0.01 to 10% of the riverine fluxes, consistent with the observation that salty groundwater is the dominant source of SGD flux into coastal ocean (Burnett et al., 2003; Taniguchi et al., 2002). Even though fresh SGD contribution to ocean is limited, they are critical as they have high concentration of land-derived nutrients (Rad et al., 2007; Rahman et al., 2019). Flow of fresh SGD to the ocean also buffers seawater intrusion in coastal aquifers, where a delicate balance is maintained between dense saline groundwater and fresh groundwater (Elango and Manivannan, 2019). Globally, climate, topography and soil properties exert first order control over the fresh SGD to the coasts (Zhou et al., 2019). However, intense groundwater extraction by coastal communities can lead to intrusion of the saline front and salinization of the aquifers, thereby reducing the fresh SGD

fluxes. Despite recognizing the potential importance of SGD in global biogeochemical cycles, highly heterogenous nature spatially and temporally along with difficultly in direct measurement make the estimate uncertain.

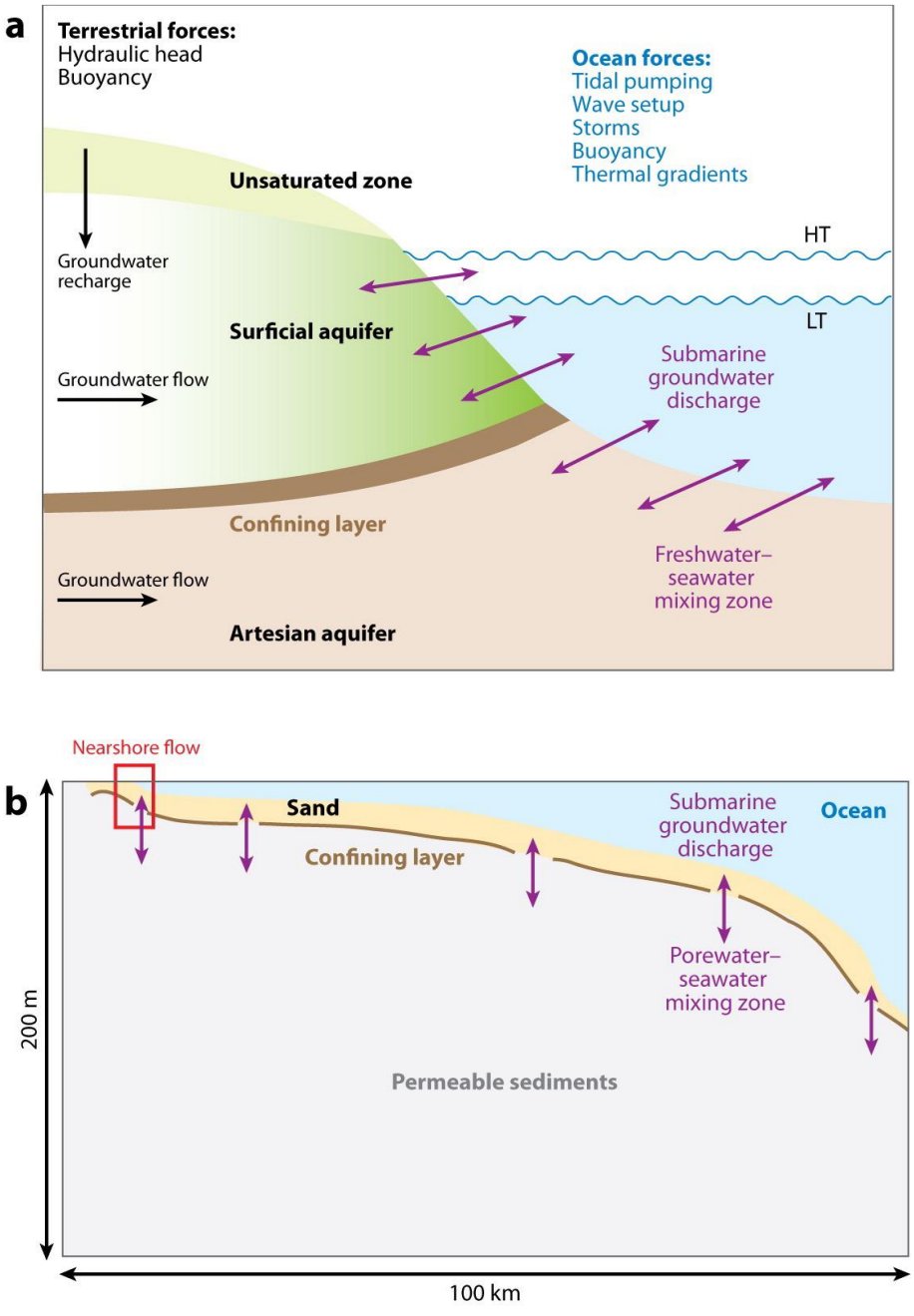

Figure. 3. *a) A Schematic diagram of near shore scale submarine groundwater flow and discharge in the transition zones, the width and thickness can vary depending on the basin, b) the submarine groundwater discharge can happen also in embayment and continental shelf scale (see text for details). The figure is taken from Moore et al. (2010).*

4. Tracing biogeochemical cycling in critical zone

Isotope geochemistry has applications in almost every field or geoscience and more, particularly as a tracer to understand biogeochemical cycling in atmosphere, lithosphere, biosphere, and hydrosphere. Advancement in the field of mass spectrometry techniques and new analytical methods have increased the number of elements and their isotope ratio that can be measured precisely which enable us to investigate more about the properties of isotope distributions (Eiler et al., 2014). In the subsequent sections we will look into various tracers used in the thesis to decipher biogeochemical processes.

4.1. Si and Si isotopes

Silicon (Si) is the second most abundant non-volatile element in the solar system, third most abundant element on the Earth, and the second most abundant element in the upper crust (Wedepohl 1995). Silicon has three naturally occurring stable isotopes; ^{28}Si (92.23%), ^{29}Si (4.67%), and ^{30}Si (3.10%) (Debievre and Taylor 1993). The combination of widespread abundance and large mass-dependent isotopic variation makes Si a very suitable element to understand fundamental processes occurring in Earth system (Reynolds and Verhoogen, 1953, Douthitt, 1982, Savage et al 2010, Opfergelt and Delmelle 2012). Silicon commonly occurs in tetravalent oxidation state, combining with oxygen forming silicate minerals or amorphous Si in solids and occurs as orthosilicic acid (H_4SiO_4) in aqueous systems.

4.1.1. Si isotope systematics

We can now define the nomenclature related to stable isotope systematic which we will be using throughout the thesis. Stable isotope geochemistry involves precise measurement of isotopic ratios which are very small and stable isotopic composition are commonly reported relative to a reference standard, known as δ-notation:

$$\delta^{30}Si = \left(\frac{(^{30}Si/^{28}Si)_{sample}}{(^{30}Si/^{28}Si)_{standard}} - 1 \right) * 1000 \qquad (1.1)$$

Similar definition can be applied to ^{29}Si isotope instead of ^{30}Si and can be reported as δ^{29}Si. In the case of Si, NIST RM-8546 (NBS28) was used as reference standard to report the isotope values. *δ*-value are expressed in per mill (‰). A positive *δ*-value indicates enrichment of heavy isotope relative to reference standard and a negative value indicates enrichment in lighter isotope. The partitioning of isotopes between two substances or phases is called “isotope

fractionation". Isotopic fractionation factor (α) denotes partitioning of stable isotopes of the same element between a compound A and a compound B, is defined as:

$$\alpha_{B-A} = \frac{(^{30}Si/^{28}Si)_B}{(^{30}Si/^{28}Si)_A} \quad (1.2)$$

Since α is very close to unity, we define enrichment factor (ε) as:

$$\epsilon = (\alpha_{B-A} - 1) * 1000 \quad (1.3)$$

We also define isotopic differences between 2 compounds or phases at isotopic equilibrium A and B as Δ value:

$$\Delta Si_{B-A} = \delta^{30}Si_B - \delta^{30}Si_A \quad (1.4)$$

The δ- and Δ- value indicates isotopic compositions, and α- and ε- and Δ- notation for two compounds A and B are related by:

$$\Delta_{B-A} \approx 1000 ln\alpha \approx 1000(\alpha - 1) \approx \epsilon \quad (1.5)$$

The physiochemical differences in the isotopes of the same element arises due to slight differences in the mass of the isotopes, and processes where the isotope abundances deviate according to masses of the isotopes are generally called mass-dependent fractionation. Mass dependent fractionation occurring during terrestrial processes can be described in δ^{30}Si vs. δ^{29}Si dual isotope plot, with slope depending on the fractionation types; kinetic fractionation and equilibrium fractionation (Young et al., 2002). Mass dependent fractionation in elements with more than two stable isotopes (like Si), can be related to fractionation factor by equation:

$$^{29}\alpha = (^{30}\alpha)^{\beta} \quad (1.6)$$

The β is defined as a function of atomic mass of Si, with a value of 0.517 for equilibrium fractionation and 0.509 for kinetic fractionation (Young et al., 2002). Equilibrium isotope fractionation occurs due to vibrational, rotational, and translational energy associated with different phases and depends on mass alone, whereas kinetic fractionation results from incomplete unidirectional processes, such as evaporation and biologically mediated reactions.

4.1.2. Continental Si cycle

Silicon cycle begins as weathering solubilizes Si from the primary minerals, following which a fraction of the solubilized Si is incorporated into secondary phases and the rest is mobilized as dissolved silicon (DSi). The chemical weathering of silicate minerals forms a major sink for atmospheric CO_2 and regulates long term climate of the Earth through a negative feedback loop (Walker ,1981; Berner et al., 1983). The long term weathering thermostat of the Earth is thought to be responsible for creating habitable conditions following ubiquitous geological perturbations in the Earth's history (Kasting and Catling, 2003). A simplified reaction for the weathering of crustal silicate minerals by reaction with carbonic acid (formed by dissolution of atmospheric CO_2 in water) and can be written as:

$$CaSiO_{3(s)} + 2CO_{2(g)} + H_2O \rightarrow H_4SiO_{4(aq)} + 2HCO^-_3 + Ca^{2+}$$

The precipitation of calcium carbonates by calcifiers in the ocean can lead to burial and subsequent preservation of carbonates. The reaction also delivers dissolved silicon (H_4SiO_4), dissolved inorganic carbon (HCO^-_3) and solubilized cations to the ocean through fluvial systems (Gaillardet et al., 1999). The $\delta^{30}Si$ of the solubilized Si in solution represent a weighted average of primary mineral phases in the bulk bedrock and soil (assuming there is no isotopic fractionation during dissolution, see below), which is further fractionated by subsequent processes. The silicon isotopic composition of bulk silicate earth (BSE) is estimated to be -0.29±0.07‰, and the weighted lithological average of upper continental crust at -0.25±0.16‰, which is also identical to the granitic average (Savage et al., 2013, 2014). The mineral specific variability of $\delta^{30}Si$ depends on the degree of polymerization, vibrational frequency of Si-O bond and the presence of cations (Méheut et al., 2009; Savage et al 2014). This explains why quartz grains are typically heavier in $\delta^{30}Si$ than the plagioclase and olivine, and biotite forms more fractionated lighter $\delta^{30}Si$ component in bulk rock (Savage et al., 2014; Frings et al., 2021a). Even though a kinetically controlled release of lighter ^{28}Si is documented during early stages of dissolution, the effects are transient as progressive dissolution will release the residual heavy surface layers (Demarest et al., 2009; Sun et al., 2014; Wetzel et al., 2015).

The dissolved silicon can further undergo biotic uptake, by vascular plants from soil water and siliceous organisms in lakes, rivers and finally in ocean. Both abiotic and biotic process of Si uptake is associated with significant fractionation, both favouring preferential incorporation of lighter ^{28}Si into the solid phase making the residual solution enriched in $\delta^{30}Si$ (Ziegler et al., 2005; Opfergelt and Delmelle, 2012; Frings et al., 2016). The $\delta^{30}Si$ of the remaining solution depends on the fractionation factor (ε) associated with the processes, ranging from -1.1 to -

3.3‰ for secondary mineral precipitation, +0.3 to -1.9‰ for plant uptake, and -1.1 to -3‰ for Fe-Al oxyhydroxides (Fig. 4, Delstanche et al., 2009; Oelze et al., 2014; Frings et al., 2021a). Globally, terrestrial plants can take up to 84±29 TmolSi/yr, and the accumulation of Si by plants can range from 0.1 to 10% of the biomass (Epstein, 2009; Carey and Fulweiler, 2012). The biogenic silica (BSi) formed by plants (mainly as phytoliths) can further undergo recycling through litterfall, which also adds a human dimension to Si cycling through landscape cultivation and Si export as food crops (Struyf et al., 2010; Carey and Fulweiler, 2012).

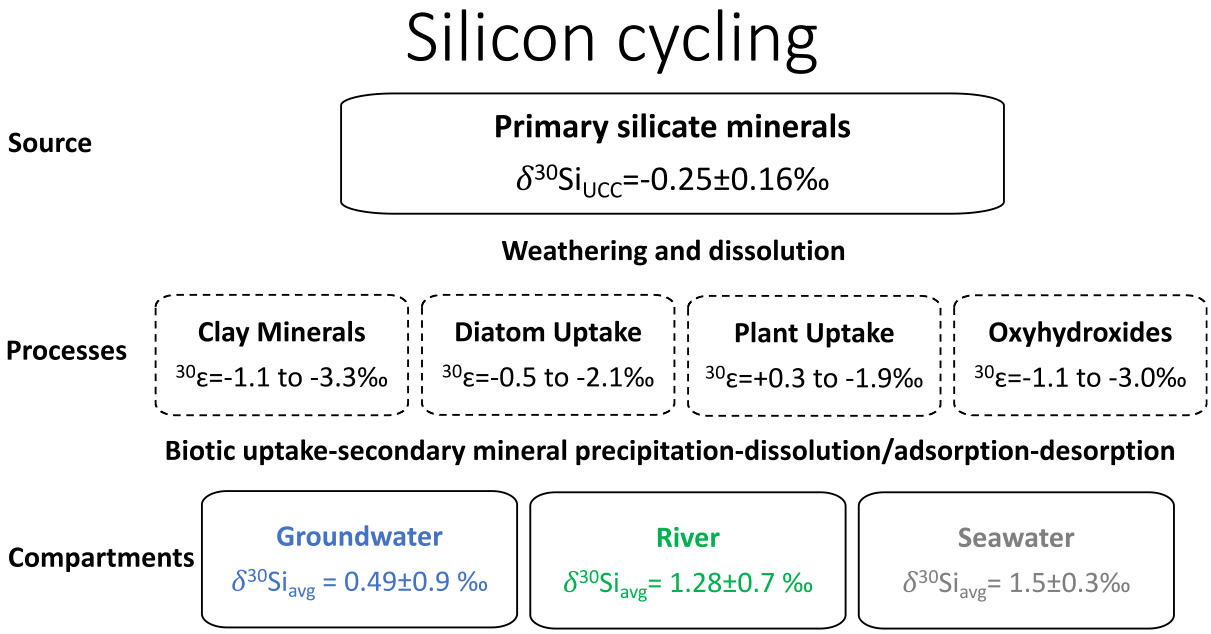

Figure 4. *A simplified schematic of silicon cycling with primary silicate rocks as the source, various abiotic and biotic processes affecting the Si biogeochemistry with fractionation factors and major hydrological compartments. The isotopic endmember compositions are taken from Savage et al. (2014), Frings et a. (2016), (2021a), Sutton et al. (2018).*

4.1.3. Modern ocean Si budget

The fluvial transport forms the largest source of DSi to the global ocean, supplying almost 14.8±2.6 TmolSi/yr (Tréguer et al., 2021). Riverine Si delivery contributes to 54% of the total Si supply to the ocean, and constitutes of 6.1±1.8 TmolSi/yr as dissolved silicon and 1.9±1.0 TmolSi/yr as soluble particulate Si in amorphous phases (Frings et al., 2016; Tréguer et al., 2021). The amorphous Si (ASi) phases includes BSi (phytoliths, silicates shells of diatoms, radiolarians, amoeba etc.) and also minerogenic Si phases such as pedogenic oxides (Saccone et al., 2007). Before entering the ocean system, Si passes through fluvial filters such as estuary, wetlands, and marshes, where biogeochemical alterations and sedimentation can modify the elemental fluxes and isotopic composition (Weiss et al., 2015; Zhang et al., 2020). Estuaries

and continental shelf regions are highly productive and can act as a permanent or atleast transient storage system for Si reaching the ocean. For example, diatom growth in the deltaic environment of Amazon river consumes significant amount of DSi and burial of the biogenic silica is followed by rapid conversion and preservation into authigenic silicates through a process known as reverse weathering (Michalopoulos and Aller, 1995, 2004; DeMaster, 2002). Reverse weathering fluxes of Si forms a significant sink of Si in continental margins, and recently was recalculated to be 4.7±2.3 TmolSi/yr (Tréguer et al., 2021). Recent estimates from Amazon river indicates that isotopic effects of diatoms growth in estuarine environments are known to increase the δ^{30}Si of the riverine supply to 0.2-0.3‰ (Zhang et al., 2020). Biotic uptake, diagenetic processes along with dissolution of labile amorphous phases in the estuary due to salinity gradient can alter the oceanic Si isotope budget (Jones et al., 2012). Submarine groundwater discharge (SGD) forms the second largest source of Si delivery to the global ocean, allegedly supplying almost 3.8±1.0 TmolSi/yr (Cho et al., 2018; Tréguer et al., 2021). Unlike river systems, fresh groundwater DSi and δ^{30}Si is mainly controlled by local weathering regime and can undergo biogeochemical modification as they mix with recycled saline groundwater in subterranean mixing zones (Ehlert et al., 2016). The fresh SGD typically contain high DSi, but contributes only 0.7±0.1 TmolSi/yr, which is almost 10% of the total riverine flux. (Rahman et al., 2019). However, the fresh SGD fluxes are poorly constrained with recent estimate using numerical modelling of density dependednt groundwater flow putting global fresh SGD Si flux at 0.08 Tmol/yr, almost an order of magnitude lower than proposed earlier (Luijendijk et al., 2020). Groundwater δ^{30}Si range from -1.5‰ to 2.6‰, with source of Si from primary silicate minerals to secondary clays and silcretes (Frings et al., 2016; Martin et al., 2021). As a result of additional sources from SGD, the geochemical residence time of Si in global ocean has been recently re-evaluated to be 8000 years (instead of 12-15 kyr previously), and perturbations that occur in the input fluxes over similar time scales, e.g. glacial-interglacial cycles can alter oceanic cycling (Tréguer et al., 2021).

Open ocean represents the largest reservoir of dissolved silicon (in the form of orthosilicic acid), with concentration ranging from <0.1 to 180 µM and δ^{30}Si from 0.5 to 4.4‰ (de Souza et al., 2014; Poitrasson et al., 2017; Sutton et al., 2018). The DSi is a critical macronutrient for silicifying organisms such as diatoms, radiolarians, siliceous sponges and silicoflagellates. The global oceanic biogenic silicon (BSi) production by silicifying organisms, predominantly diatoms, is estimated to be 255±52 TmolSi/yr (Tréguer et al., 2021). Diatoms are the key drivers of silicon cycle in ocean and are estimated to contribute about 20% and 40% of the global and oceanic primary production of organic carbon respectively (Field et al., 1998; Tréguer et al.,

2017). The diatom uptake and export from surface ocean thus links marine Si and C cycling through biologic carbon pump, where the efficiency of C export depends on the type of diatom and their traits (Tréguer et al., 2017). The diatoms preferentially take up lighter silicon isotopes during silicification of the frustules, resulting in a heavier $\delta^{30}Si$ of DSi from surface ocean euphotic zone (De La Rocha et al., 1997). The observed fractionation factor ($^{30}\varepsilon$) for diatom uptake range from -0.54 to -2.1‰ with an average of -1.1‰ for seawater (De La Rocha et al., 1997; Sutton et al., 2013) and -1.1±0.2 ‰ for freshwaters (Alleman et al., 2005). The distribution of $\delta^{30}Si$ in the global ocean is primarily controlled by surface fractionation by diatoms and other siliceous organism, and the oceanic circulation.

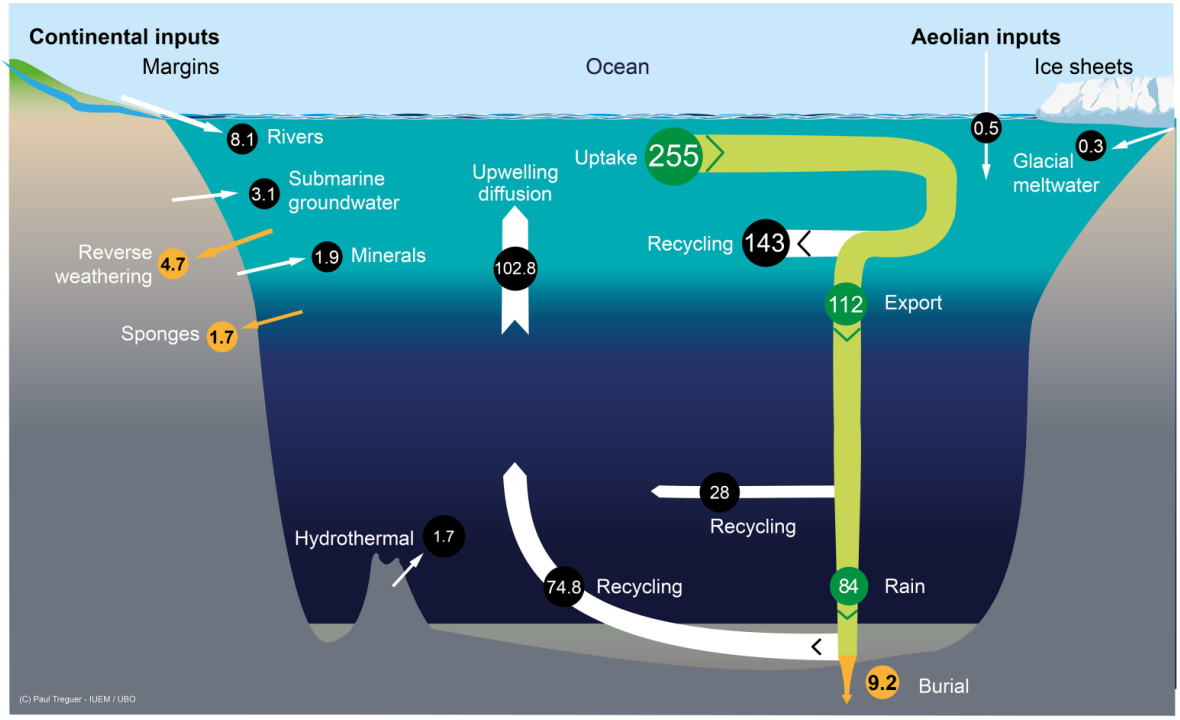

Figure 5*. A schematic of recently updated modern ocean Si cycle by Tréguer et al. (2021). The Si input and sink fluxes are given in TmolSi/yr and are represented as white and orange arrows respectively. The internal biological Si cycling and fluxes are given in green arrows. The figure taken from Tréguer et al. (2021).*

4.2. Germanium and Ge/Si ratio

Germanium (Ge) is trace metalloid whose chemical behavior in natural environment closely resembles that of silicon. Germanium and Si are both group IV elements and have the same outer electronic structure (ns^2 np^2, n=3 for Si and n=4 for Ge), atomic radii and lithophilic tendencies, allowing Ge substitution within silicate minerals (Goldschmidt, 1926). Given the coupled behavior, Ge is often considered as a pseudo isotope of Si, partitioning with respect to

silicon in natural processes which can be traced using Ge/Si ratio (Kurtz et al., 2002). However, Ge can also display octahedral valence state (six-fold coordination) and can exhibit distinct siderophilic, chalcophilic and organophilic tendencies in different environments (Bernstein, 1985). In aqueous system Ge mainly exists in two forms: inorganic $Ge(OH)_4$ similar to silicic acid ($Si(OH)_4$) and organometallic Ge species such as methyl-(MMGe) and dimethyl-(DMGe) forms (Rouxel et al., 2017). In crustal rocks, the average Ge concentration is 1.6 ppm with a Ge/Si ratio in silicate rocks varying between 1-3 µmol/mol (Bernstein, 1985, Lugolobi et al., 2010). During incongruent weathering, precipitation of secondary phases can lead to preferential removal of Ge relative to Si from dissolved phases, leading to a Ge/Si ratio varying between 0.1 to 3 µmol/mol in natural waters (Fig. 5, Mortlock and Froelich, 1987; Froelich et al., 1992; Kurtz et al., 2002; Lugolobi et al., 2010; Baronas et al., 2017, 2018). The Ge/Si ratio in streams and rivers are predominantly controlled by weathering intensity, where highly weathered terrains under transport limited conditions can lead to leaching of secondary phases such as clays and oxyhydroxides with high Ge/Si (>4 µmol/mol, Froelich et al., 1992, Kurtz et al., 2002, Lugolobi et al., 2010). Plants are generally thought to discriminate against Ge, with phytoliths exhibiting a low Ge/Si ratio (typically <1 µmol/mol) compared to soil solutions and bedrock (Derry et al., 2005; Cornelis et al., 2010; Lugolobi et al., 2010; White et al., 2012; Meek et al., 2016). However, some studies suggest that plant discrimination against Ge relative to Si is not widespread and some plants do indeed prefer Ge or not discriminate at all, and most of the Ge pool is associated with non-phytolith plant biomass, e.g., in roots, due to its high affinity with carbon contrary to Si (Delvigne et al., 2009; Frings et al., 2021b).

Rivers represent one of the main sources of Ge to the ocean and the Ge concentration in pristine rivers generally depends on the rock composition of the river basin, weathering intensity, atmospheric deposition, and biotic controls (Baronas et al., 2020). Due to preferential uptake of Ge relative to Si in secondary phases, global pristine river water Ge/Si is estimated to be 0.68±0.05 µmol/mol, significantly lower than the average continental crustal composition of 1.3 µmol/mol (Mortlock and Froelich, 1987; Baronas et al., 2020). Ge behavior in natural waters can be strongly modified by organic matter dynamics and pollution, causing significant shift in Ge/Si ratio (Mortlock and Froelich, 1987; Pokrovski et al., 2000). Ge uptake by diatoms can be viewed under two different mechanisms: i) at low Si concentration (<10 µM DSi) the uptake is mediated by active Si transporters which discriminate against Ge, ii) at high Si content the uptake is controlled by diffusion based on gradient between intra- and extracellular Ge concentration (Ellwood and Maher, 2003; Sutton et al., 2010). Riverine supply and hydrothermal fluid discharge together contribute to almost 70% of Ge in the ocean and the rest

is attributed to aeolian dust input, basalt weathering, biogenic silica, and groundwater input (Hammond et al., 2000; Wheat and McManus, 2008). The Ge fluxes from groundwater discharge remains poorly constrained and only known sink of Ge in ocean is biogenic opal snow which leaves a huge missing sink of $4.1x10^6$ mol/y to compensate for inputs (Hammond et al., 2000; King et al., 2000; McManus et al., 2003). Despite the high potential Ge biogeochemical cycling remains poorly constrained due to missing sinks and complex geochemical behavior.

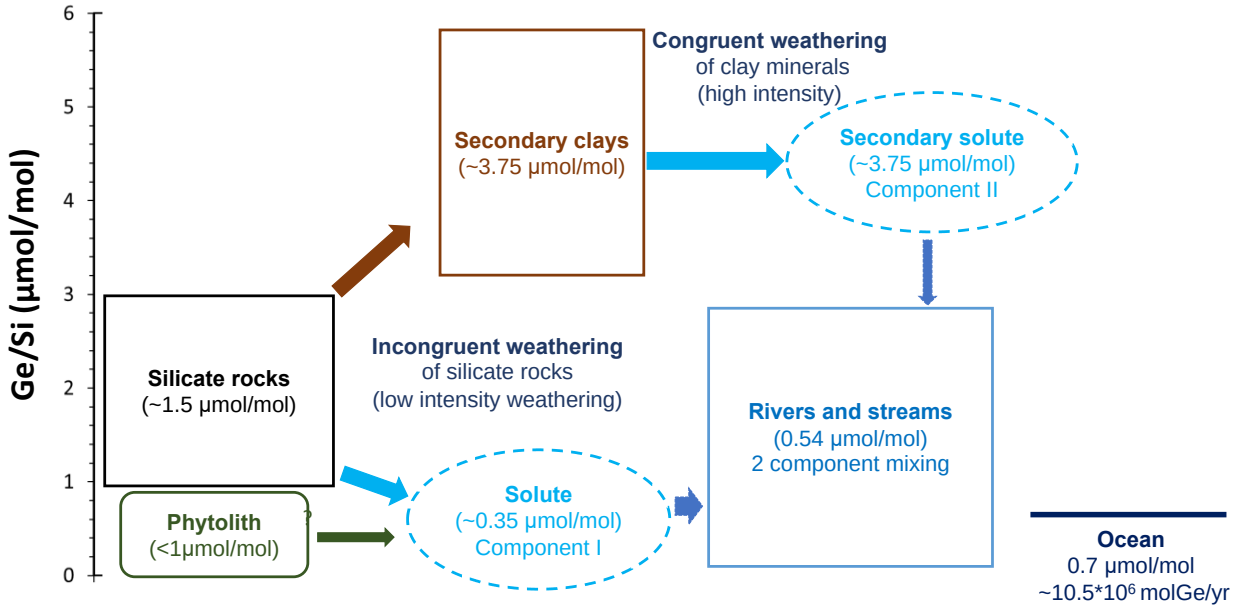

Figure 6. *A schematic of weathering control of Ge/Si fractionation in terrestrial systems. During low intensity weathering, Ge is preferentially taken up by secondary clays, which results in low Ge/Si ratio in residual soil solution. Intense weathering can leach the Ge from the secondary phases which can result in higher Ge/Si in streams and rivers. The figure adapted from Froelich et al (1992) and Kurtz et al (2002) and the scales are approximate with modifications based on recent measurements (Rouxel et al., 2017, Frings et al., 2021b).*

4.3. Ca and Ca isotopes

Calcium (Ca) is the fifth most abundant element and most abundant alkaline earth metal in the Earth's crust. Calcium occurs as a major element in igneous, metamorphic, and sedimentary rocks, and are major constituents of minerals including carbonates, silicates, sulfates, phosphates, halides as well as organo-minerals. Weathering mobilizes the Ca, which moves readily through hydrosphere and biosphere, taking part in variety of Earth surface processes. Ca is one of the most abundant dissolved cations in seawater (present abundance of ~400 ppm) and river water (~20 ppm) (Broecker, 1971; Gibbs, 1972; Drever, 1997). Rivers are the primary source of Ca in seawater. Ca reaching the ocean is removed from seawater and accumulated as

Ca rich carbonates ($CaCO_3$) in organisms, acting as the dominant sink for Ca which is orders of magnitude larger than atmosphere-ocean reservoir (Ridgwell and Edwards, 2007). Global biogeochemical cycling of carbon is also linked with Ca cycling as weathering of Ca rich primary minerals consumes CO_2, followed by formation of $CaCO_3$ in the ocean, providing negative feedback for climate over geological time (Berner et al., 1983). Weathering reactions mobilizing one mole of Ca into the hydrosphere sequesters one mole of CO_2 from the atmosphere, mediating CO_2 levels in the Earth's history (Walker, 1981).

$$Ca^{2+} + 2HCO^{-}_{3} + H_4SiO_4 \rightarrow CaCO_3 + SiO_2 + 3H_2O + CO_2$$

In total, Ca has 24 isotopes, out of which 6 are stable, naturally occurring isotopes. The abundant isotopes include, ^{40}Ca (96.94%), ^{42}Ca (0.65%), ^{43}Ca (0.13%), ^{44}Ca (2.09%) and ^{48}Ca (0.19%), spanning a mass range of 8 atomic mass unit (Amos et al., 2011). Previously, radiogenic Sr isotope ratio ($^{87}Sr/^{86}Sr$) was applied in combination with Ca concentration to understand Ca cycling and its behavior in the ecosystem. However, recent studies found that Sr and Ca are decoupled in many terrestrial ecosystems (Schmitt et al., 2003, 2017; Cenki-Tok et al., 2009; Holmden and Bélanger, 2010). Mass dependent isotopic variations in the Ca are driven by a variety of abiotic and biological processes. Variability in Ca isotopic composition arising from mass dependent fractionation is commonly expressed relative to a standard reference material in δ notation, similar to Si isotopes (Coplen, 2011).

$$\delta^{44/40}Ca = \left(\frac{(^{44}Ca/^{40}Ca)_{sample}}{(^{44}Ca/^{40}Ca)_{standard}} - 1 \right) \quad (1.6)$$

δ-values are typically expressed in per mill (‰), with positive values indicating enrichment in heavy isotopes relative to light isotopes and negative values vice versa. Due to the prevalence of multiple stable isotopes, Ca isotopic composition is commonly denoted with both numerator and denominator displayed, $\delta^{44/40}Ca$ rather than $\delta^{44}Ca$. Throughout the thesis we will be following $\delta^{44/40}Ca$ with reference standard SRM915a. The definition of fractionation factor and related notations remain the same as those of Si, described in detail section 1.4.1.

Ca isotopic composition in the Earth's surface is controlled by chemical weathering, secondary mineral formation, biological cycling, and adsorption/desorption on phyllosilicate/phyllo manganese minerals (Schmitt et al., 2016). High temperature processes such as igneous differentiation and crystallization are known to fractionate stable Ca isotopes and preferential weathering of such isotopically distinct mineral phases can alter the dissolved isotopic

composition compared to bedrock (Huang et al., 2010). The $\delta^{44/40}$Ca of continental silicate rocks is 0.94±0.5‰ and carbonate rocks exhibit a 3‰ range with an average of 0.60±0.7‰ (Fantle and Tipper, 2014). Weathering of both silicate and carbonate rocks mobilizes aqueous Ca^{2+} as well as particulate Ca, which is transferred to soil solution, groundwater, rivers and finally reach the ocean. Subsequently marine calcifiers form Ca-rich shells and skeletons made of calcium carbonates, which act as the dominant sink for Ca and C in seafloor. In critical zone, Ca cycles through pedogenic processes such as precipitation/dissolution of secondary clays and carbonates and also uptake by biosphere. Calcium is an essential nutrient for biological tissues of plants and animals, forming biomineralized products including calcite, aragonite, apatite, and several organic complexes (Weiner and Dove, 2004). They also take part in metabolic pathways including cell signaling, cell wall stability, and membrane functioning (Taiz and Zeiger, 2010). Among the continental reservoirs, vegetation exhibits the largest $\delta^{44/40}$Ca variability (~ 4‰), ranging from -2.2 to +1.76‰, with an average of 0.01‰ (Fantle and Tipper, 2014). Plants preferentially take up lighter Ca isotopes and dictates the Ca isotopic composition of the Ca soil pool reservoir under Ca limiting conditions (Cenki-Tok et al., 2009; Schmitt et al., 2013). The soil Ca pool exhibits the second highest variability, ranging from -0.74 to 2.77 ‰ (Schmitt, 2016). Precipitation of secondary minerals also takes up lighter ^{40}Ca in the solid phase, leaving the residual solution enriched in heavier isotopes. The magnitude of the fractionation depends on the precipitation rate, dissolved phase, and precipitated minerals (Gussone et al., 2005, 2011; Tang et al., 2012). Ion exchange reactions involving adsorption of Ca onto secondary clays and phyllosilicates, such as montmorillonites, fractionate against heavier Ca isotopes (Brazier et al., 2019). Thus, both secondary mineral precipitation and biotic uptake leave the residual solution enriched, which is reflected in enrichment of ^{44}Ca isotope in waters (0.96±0.6‰), groundwaters (0.86±0.8‰) and rivers (0.88±0.5‰) enriched in ^{44}Ca isotope (Fantle and Tipper 2014). Riverine Ca delivery is the major source of Ca flux to the ocean, and accounts for almost 50 TgCa/yr, with an average $\delta^{44/40}$Ca of 0.88±0.5‰ closer to silicate rock endmember composition (Berner and Berner, 1996; Griffith et al., 2020). However, silicates only contribute to 10-26 % of the global Ca flux generated by weathering, reflecting considerable fractionation associated with formation of secondary carbonates and clays, and biotic uptake in continental Ca cycling (Gaillardet et al., 1999; Hindshaw et al., 2011). Assuming steady state, oceanic Ca budgets lacks a significant source of Ca, between 210 to 530 TgCa/yr, potentially from submarine groundwater discharge and diffuse flux from the flanks of mid-ocean ridges (Berner and Berner 1996; Holmden et al 2012; Fantle and Tipper, 2014). Modern seawater is quite homogenous in $\delta^{44/40}$Ca composition with an average of 1.89±0.16‰

(2SD, n=62) (Holmden et al., 2012; Fantle and Tipper, 2014; Tipper et al., 2016). The residence time of Ca in seawater is ~1 Myr, owing to the small input and output fluxes and high Ca concentration in the ocean (Griffith et al., 2020).

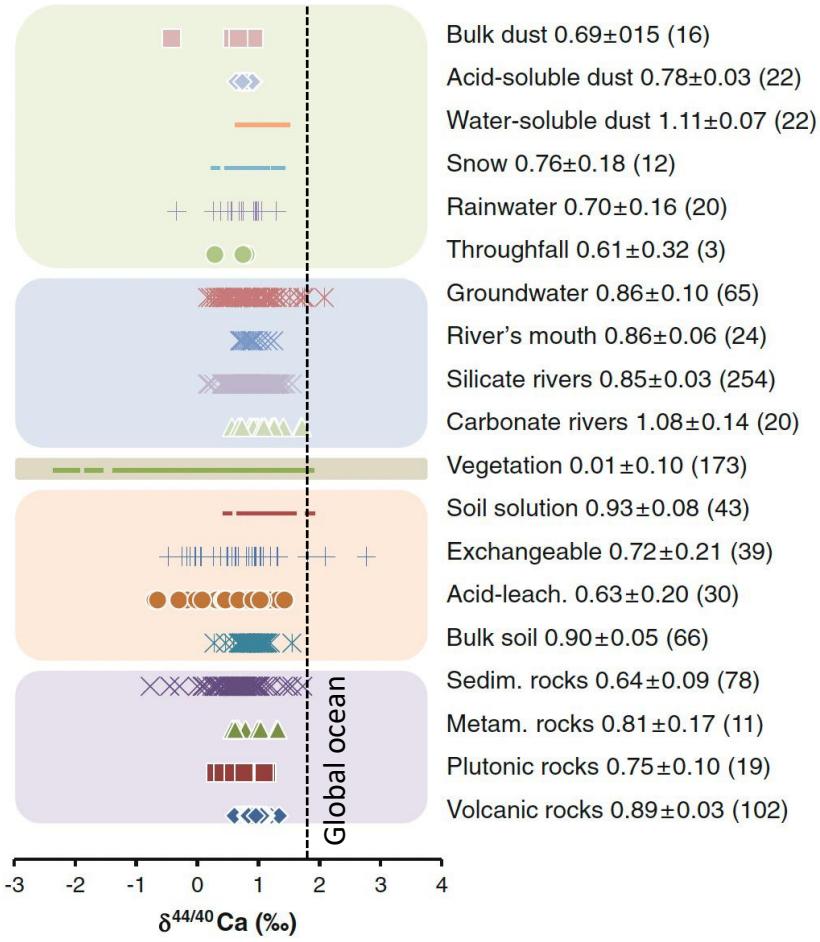

Figure 6. *The variability of Ca isotopes in continental reservoirs. The average* $\delta^{44/40}Ca_{SRM915a}$*, 2SE and number of samples are given for each reservoir. The figure modified from Tipper et al. (2016) (see section 4.3 for details and references).*

4.4. Sr and $^{87}Sr/^{86}Sr$ *ratio*

Strontium (Sr) is an alkaline earth element with similar chemical properties as those of Ca, substituting for Ca in carbonates, sulfates, feldspars, and other rock forming minerals. Strontium has four naturally occurring stable isotopes, ^{84}Sr (<1%), ^{86}Sr (10%), ^{87}Sr (7%) and ^{88}Sr (83%). Out of the four, ^{87}Sr is formed by the radioactive beta decay of ^{87}Rb with a half-life of 48.8 Ga (Faure, 1991). The $^{87}Sr/^{86}Sr$ ratio of the different mineral assemblages thus depends on the initial $^{87}Sr/^{86}Sr$ ratio, Rb/Sr ratio and the age (Faure, 1991). Rubidium substitutes for Potassium (K) in K bearing minerals, thus alkaline rocks with abundant K will be more radiogenic than basic rocks such as basalts. Mineral phases with more K and high Rb/Sr ratio

such as biotite and muscovite have higher $^{87}Sr/^{86}Sr$ ratio compared to low Rb/Sr minerals such as plagioclase, while Sr in Ca-rich minerals such as calcite or gypsum will have even lower $^{87}Sr/^{86}Sr$ that will remain stable over time (Faure, 1991; McNutt, 2000). Differences in parent rock mineralogy translates to variable $^{87}Sr/^{86}Sr$ ratio in fluvial systems. Unlike Si and Ca isotopes, mineral precipitation and dissolution reaction will not fractionate $^{87}Sr/^{86}Sr$ ratio in the mineral phases and aqueous systems, making this isotopic ratio a possible indicator of the sources and pathways of dissolved ions in hydrological cycling (Wadleigh et al., 1985; Palmer and Edmond, 1992; Pett-Ridge et al 2009; Meek et al 2016). Weathering reactions solubilize Sr as Sr^{2+} from silicates, carbonates and evaporites, and Sr closely follows Ca in critical zone (Goldstein and Jacobsen, 1987). At watershed or aquifer scales, $^{87}Sr/^{86}Sr$ compositions of natural waters reflect first order control of weathered rock type and age. For example, rivers draining Proterozoic and Archean crust in Greenland and Australia exhibits a high $^{87}Sr/^{86}Sr$ ratio as do metamorphic rocks from Himalayas, while the rivers draining the volcanic terrains of Japan and Philippines exhibits $^{87}Sr/^{86}Sr$ ratio of 0.704 to 0.708, consistent with young mantle-derived rock dissolution (Palmer and Edmond, 1992). The effect of water rock interactions is more pronounced in groundwater due to increased residence time and mineral surface to volume ratio compared to surface water and can be used to identify mixing between groundwaters from variable sources, such as silicate vs. carbonate (Banner et al., 1994; Négrel et al., 2001; Cartwright et al., 2007). Recent estimates of global average riverine Sr concentration and $^{87}Sr/^{86}Sr$ from half of global runoff is 1.2 μM ($4.7*10^{10}$ molSr/yr) and 0.7111, respectively (Peucker-Ehrenbrink and Fiske, 2019). Submarine groundwater discharge could supply less radiogenic $^{87}Sr/^{86}Sr$ to seawater with fluxes ranging from 0.7 to $2.8*10^{10}$ molSr/yr, with an average $^{87}Sr/^{86}Sr$ ratio of 0.7089 (Beck et al., 2013). The oceanic Sr isotope composition reflects the relative fluxes of riverine, SGD, hydrothermal and diagenetic Sr fluxes, and displays a homogenous $^{87}Sr/^{86}Sr$ ratio of 0.70918 (Davis, 2003). The homogenous $^{87}Sr/^{86}Sr$ ratio of the ocean reflects the higher residence time of Sr in the ocean ($5*10^{6}$ years) compared to the interocean mixing time (Broecker, 1997; Banner 2004).

5. General objectives and thesis framework

The research presented in this thesis was inspired by the remarkable variability and distinct nature of $\delta^{30}Si$ signatures observed in groundwater and their potential ability to trace submarine groundwater discharge (Frings et al., 2016; Moore et al., 2010). The thesis focusses on biogeochemical cycling in groundwater systems using multiple tracers, focusing mainly on DSi and Si isotopes in India. Groundwater forms a dynamic system exhibiting spatial and temporal heterogeneity, and acts as an intermediate between subsurface processes occurring in the critical zone and riverine systems, which ultimately delivers solutes from continents to ocean. Complexity in understanding groundwater systems arises from: i) difficulty to access, ii) geogenic and climatic heterogeneity, iii) influence from multiple surfaces as well as subsurface processes, and to add on to all, iv) anthropogenic influence. As water flows through the critical zone, biogeochemical transformations solubilize elements and transport the dissolved products which can be affected by both biotic and abiotic processes before reaching groundwater and then riverine systems. In the thesis we try to address few of the complexities using various elemental and isotopic tracers including $\delta^{30}Si$, $^{87}Sr/^{86}Sr$, $\delta^{44/40}Ca$, $\delta^{2}H$, $\delta^{18}O$ and Ge. Given the broad scope of the topic, we divided the thesis into three major sections, each tackling a specific question/problem in groundwater biogeochemistry using appropriate tracers.

- The first question was to address the impact of land-use and seasonal monsoon precipitation in groundwater Si cycling, which is detailed in **Chapter II**. To achieve the objective, we did extensive groundwater, soil solution and surface water sampling during dry and wet seasons from two contrasting but adjacent watersheds in South India: the intensely cultivated Berambadi watershed and the pristine forested Mule Hole watershed which are part of the French Service National d'Observation (SNO) M-TROPICS observatory. The chapter also touches upon human dimension of Si cycling, and how aboveground agricultural practices impact the groundwater biogeochemistry. We employed different tracers such as $\delta^{30}Si$, $^{87}Sr/^{86}Sr$, $\delta^{2}H$, and $\delta^{18}O$ to delineate abiotic and biotic processes (including anthropogenic) that control the water signatures during the transit through regolith before reaching the saturated zone.

Figure 7. *The field pictures from Berambadi (a, b) and Mule Hole (bottom panel) during March and August sampling 2019.*

- Following the results and understanding we gained from the first question, we discuss the second question pertinent with groundwater complexity in a coastal setting. The broad objective of **Chapter III** was to identify the controls of groundwater and river water biogeochemical cycling in an estuarine region affected by seasonal monsoon precipitation and effect of surface water-groundwater mixing in transition zones. We conducted seasonal sampling during 2019 March (dry season) and August (wet season) from Godavari estuary in India, including river water and groundwater from open wells, handpumps and piezometers next to the estuary. The idea was to assess the spatial variability of groundwaters along the estuarine transect, trying to identify the groundwater discharge patterns in the estuary. In order to tackle the complexity arising from various sources, mixing and processes, we divided the chapter into two sub-chapters based on the tracers we used.

Figure 8. *The field pictures of Godavari river at upstream location during dry season (left) and wet season (right).*

Chapter IIIa emphasis on tracing Si cycling in estuary and groundwater using silicon isotopic composition. Previous works have documented intense phytoplankton blooms and diatoms growth in the estuary during moderate and low discharge periods, which would make $\delta^{30}Si$ an ideal proxy to understand the diatom uptake and its impact on Si delivery to the coast. The work aims to refine our understanding of the role of estuaries in modulating the riverine Si supply and to compare with the behaviour of groundwater in the same environment.

However, attempts to decipher sources *vs.* processes is complicated when source signatures are heavily overwritten by biotic as well as abiotic processes. In **Chapter IIIb** we attempt to remedy this issue using source-specific $^{87}Sr/^{86}Sr$ ratio in conjunction with $\delta^{44/40}Ca$, which can be affected by both source and processes. Since Sr closely follows Ca in biogeochemical cycling, together they provide an ideal toolbox to understand how the fresh river water carrying the signatures from upstream sources traced by $^{87}Sr/^{86}Sr$ is impacted by mixing with seawater which affects both $\delta^{44/40}Ca$ and $^{87}Sr/^{86}Sr$ and also by processes which only impact $\delta^{44/40}Ca$.

- So far, we have been focusing on local hydrologic systems where the lithology and climate remain fairly similar across all the spatial sampling while including seasonal sampling to understand the impact of monsoon. Finally, in **Chapter IV** we focus on a regional study of groundwater systems, where we collected more than 80 coastal groundwater samples from the coastline of Indian subcontinent spanning almost 5500

km. Near coast submarine groundwater discharge (SGD) is documented to be a major source of nutrient transfer to coastal ocean, including dissolved silicon, nitrates and phosphates, which support phytoplankton growth. The chapter attempts to answer two preliminary queries related to silicon cycling groundwater:

i) Can we identify the major processes controlling the Si and $\delta^{30}Si$ behaviour in groundwater by comparing our dataset so far with available database for Si isotopes? Can coupling with Ge/Si ratio help us to disentangle biotic vs abiotic processes?

ii) How does groundwater Si discharge compare with the riverine discharge documented in the Indian subcontinent? Can groundwater discharge modify the isotopic composition of total Si discharge?

Chapter V summarizes overall findings from the research, drawing conclusions related to general patterns of Si behavior in groundwater, associated variability and most importantly, the role in oceanic elemental as well as isotopic budget. This chapter also presents particular perspectives we gained from overall research, problems encountered on the way and recommendations for future research in the field of Si cycling in groundwater and surface water.

II. Deep regolith weathering controls $\delta^{30}Si$ composition of groundwater under contrasting land use in tropical watersheds

Sarath Pullyottum Kavil[1*], Jean Riotte[2,6], Ramananda Chakrabarti[3,4], Arnaud Dapoigny[5], Véronique Vaury[8], Laurent Ruiz[2,6,7], Damien Cardinal[1]

[1] LOCEAN-IPSL, Sorbonne Universite-IRD-CNRS-MNHN, Paris, France
[2] GET-OMP, IRD, Toulouse, France
[3] Centre for Earth Sciences, Indian Institute of Science, Bangalore, India
[4] Interdisciplinary Centre for Water Research, Indian Institute of Science, Bangalore, India
[5] Laboratoire des Sciences du Climat et de l'Environnement, LSCE-IPSL, CEA-CNRS-UVSQ-Université Paris-Saclay, F-91191, Gif-sur-Yvette, France
[6] Indo-French Cell for Water Sciences, ICWAR, IRD, Indian Institute of Science, Bangalore, India
[7] UMR SAS, INRAE, Institut Agro, Rennes, France
[8] IEES, Sorbonne Université, Paris, France

Submitted to Geochimica et Cosmochimica Acta (December 2022)

Abstract

Land use changes are known to alter terrestrial silicon cycling and the export of dissolved silicon from soil to fluvial systems. However, the impact of agricultural practices on groundwater silicon cycle and its isotopic composition remains unclear. In order to assess impact of agricultural processes, we examined multiple isotopic tracers ($\delta^{30}Si$, $^{87}Sr/^{86}Sr$, $\delta^{18}O$ and $\delta^{2}H$) in groundwater and surface water from forested watershed and agricultural watershed. For the present study we choose two contrasting watersheds in South India: Mule Hole (forested) and Berambadi (cultivated with groundwater irrigation). Berambadi groundwater exhibits high Cl and NO_3^- concentrations indicative of fertilizer inputs and evaporative enrichment from multiple groundwater pumping/recharge cycles, evident from water isotopes. While dissolved silicon (DSi) in groundwater is significantly more concentrated in Berambadi (980±313 µM) than in Mule Hole (711±154 µM), the $\delta^{30}Si$ of groundwater ranged from 0.41 to 3.45‰, with no significant differences in average $\delta^{30}Si$ between Berambadi (1.09±0.5‰) and Mule Hole (0.98±0.2‰), indicating limited impact by above-ground land-use patterns. The higher DSi content in groundwater under agricultural land-use mostly results from more intense evapotranspiration during irrigation cycles. The groundwaters also exhibit no seasonal differences, indicating a significant buffer to South West monsoon during wet season. Surface water (1.60±0.3‰) and soil porewater (1.6±0.2‰) exhibit $\delta^{30}Si$ significantly heavier than groundwater. Compared to soil solution, groundwaters in both watersheds displayed significantly lighter $\delta^{30}Si$ signatures and higher DSi, reflecting a lighter silicon source resulting from water rock interaction as soil water percolates through the unsaturated zone. The $\delta^{30}Si$ values of groundwater is primarily driven by silicate weathering and formation of secondary clay minerals such as kaolinite and smectite. The evolution of $\delta^{30}Si$ in most groundwater samples fits a steady state system with fractionation factor ($^{30}\varepsilon$) between -1.0‰ and -2.0‰, indicative of a system receiving a steady input of DSi and a dynamic equilibrium between supply and precipitation of secondary phases. We assign the input to weathering of primary silicate minerals such as plagioclase, biotite and hornblende, with formation of kaolinite and smectites in deeper regolith layers as additional Si fluxes to groundwater, consistent with radiogenic $^{87}Sr/^{86}Sr$ composition of some groundwater. A simple isotopic mass balance suggests that deep regolith weathering contributes on average to 43% and 32% of the total Si concentration in the groundwater of Mule Hole and Berambadi, respectively. We conclude that if silicon cycling in soil porewaters and surface waters are directly impacted by land use, the isotopic composition of groundwater remains unaffected. Our results indicate that Si isotopic

signatures of weathering, adsorption, and plant uptake occurring in the shallow soil and saprolite horizons are partly overprinted and homogenized by the regolith weathering in the deep critical zone, irrespective of land use and seasonality.

Keywords: groundwater, weathering, silicon cycle, forest, agriculture, critical zone.

1. Introduction

Human activities alter the biogeochemical cycling of several elements including carbon (C), nitrogen (N), phosphorus (P), and silicon (Si) thus creating imbalances in the nutrient distribution in aquatic systems (Humborg et al., 1997; Smil, 2000; Galloway et al., 2003). Silicon is one of the essential nutrients in aquatic ecosystems and plays critical role in the growth and distribution of highly productive autotrophs, such as diatoms in both freshwater and marine ecosystems (Street-Perrott and Baker, 2008; Tréguer et al., 2021). It is the second most abundant element in Earth's crust and terrestrial weathering mobilizes Si as dissolved silicon in the form of silicic acid (H_4SiO_4, thereinafter referred to as DSi), which is transported to the ocean majorly through rivers (8.1 Tmol Si yr^{-1}, Tréguer et al., 2021). Land cover and land use changes are one of the major drivers of Si cycling at the global scale (Conley et al., 2008; Struyf et al., 2010; Carey and Fulweiler, 2016). Silicon is considered as a quasi-essential element for many plants and can be found in all photosynthetic plants, with concentration ranging from 0.1 to over 10% by dry weight (Epstein, 2009). Plants can take up DSi from soil solution and precipitate as biogenic silica (amorphous $SiO_2.nH_2O$, hereafter referred to as BSi), in the form of siliceous bodies in cell walls known as phytoliths, which protects the plant from various abiotic and biotic stresses (Alexandre et al., 1997; Epstein, 2009). Globally, terrestrial plants produce 84±29 Tmol Si yr^{-1} as BSi and agricultural plants accounts for almost 35% of the BSi created by land plants (Carey and Fulweiler, 2016). Agricultural crops typically contain elevated levels of BSi, thus agricultural land use can significantly modify the BSi accumulated in soils, resulting in changes in Si export rates (Struyf et al., 2010; Carey and Fulweiler, 2012). Although agricultural Si export through crop harvesting are known to deplete BSi pools in soil, the extent to which agriculture impacts the export of Si from soil to hydrosystems remains to be understood (Ding et al., 2008; Vandevenne et al., 2015).

Agriculture-related land use changes can significantly impact the surface and subsurface hydrogeochemical properties, enhance chemical weathering and erosion (Quinton et al., 2010; Ameijeiras-Mariño et al., 2017). The stable isotopic composition of Si ($\delta^{30}Si$) is a useful tool to evaluate sources of Si and processes controlling Si biogeochemical cycling (Cornelis et al.,

2011; Opfergelt and Delmelle 2012; Frings et al., 2016 and references therein). Silicon solubilized by chemical weathering of the source bedrock (bulk upper continental crust $\delta^{30}Si$ of -0.25±0.16‰, Savage et al., 2014) undergo fractionation during incorporation into secondary phases, which favour lighter ^{28}Si, thereby making the residual solutions (soil waters, groundwaters and rivers) enriched in ^{30}Si (Frings et al., 2016). Silicon uptake by plants is also associated with preferential incorporation of the light isotope, ^{28}Si, followed by further fractionation during translocation, depleting the ^{28}Si from root to leaves (Opfergelt et al., 2006; Frick et al., 2020; Frings et al., 2021). Thus, careful evaluation of pathways and Si interaction with lithosphere, biosphere and hydrosphere is essential to understand output fluxes of Si in a watershed scale, and its subsequent transfer to the oceans. One such evaluation across a land use gradient in a temperate climate showed a significant enrichment in $\delta^{30}Si$ in soil water samples from older intensive cropland cultivated for almost 240 years, compared to those from a forested landscape (Vandevenne et al., 2015) and this isotopic difference was also reflected by difference in $\delta^{30}Si$ of DSi exported to the estuary by sub-watersheds in the same region (Delvaux et al., 2013). High $\delta^{30}Si$ in residual soil solution along with concurrent depletion in the BSi pool of the cropland soil, provides compelling evidence for imprint of land cover changes and related process on silicon isotopic signature on surface a shallow water. However, the chemical composition of streams and rivers do not directly reflect the composition of the water draining below the soil zone as this water does not always directly recharge the groundwater, in particular where deep unsaturated regolith acts as a subsurface reservoir (Ruiz et al., 2010). In deeper aquifers, groundwater underflow plays a significant role in sustaining baseflow in large rivers, especially during dry seasons (Ruiz et al., 2010). The fate of Si in pore water as it travels through the unsaturated zone, often with long residence time, before reaching groundwater is critical in understanding the output fluxes from the watershed. Previously published globally distributed groundwater $\delta^{30}Si$ values exhibits a wide variability, ranging from -1.5 to +2.6‰ (n=66), which is attributed to silicate weathering and dissolution of lighter sources of Si such as secondary minerals (Georg et al., 2009a, 2009b; Strandmann et al., 2014; Frings et al., 2016; Ehlert et al., 2016; Martin et al., 2021). However, the impact of land use changes, anthropogenic activities, and soil processes on groundwater Si cycling and the response to seasonal precipitation changes remains unclear.

In India, the development of intensive agriculture in the past decades is likely to have largely affected Si cycle. India accounts for one third of the world's total irrigated area and about 60% of irrigation results from direct groundwater pumping, leading to rapid decline of the groundwater (Thenkabail et al., 2009; Fishman et al., 2011; Bhaduri et al., 2012). Aquifers in

peninsular India are unconfined and composed of fractured granitic bedrock having a decreasing transmissivity with depth (Dewandel et al., 2006), which limits the area under irrigation from a well to <1 ha (Fishman et al., 2011). Such tube wells are ideal for small farmers dominating Indian agriculture with diverse land use throughout the year, leading to a high density of farming tube wells in the past few decades. Acute pumping for agricultural as well as domestic purposes has led to deterioration of the groundwater quality and lowering of water table (Rodell et al., 2009; Buvaneshwari et al., 2017). Intense pumping and irrigation from borewells and handpumps can lead to multiple groundwater recycling through return flow in cultivated landscapes. This along with excessive use of fertilizers and organic manures can significantly alter the hydrogeochemistry of groundwater (Buvaneshwari et al., 2017, 2020; Robert et al., 2017).

The objective of the present study is to investigate the impacts of contrasting landcover and land use, i.e., forest *vs.* agriculture, on the evolution of groundwater Si isotopic signature from two tropical watersheds. Specifically, we used $\delta^{30}Si$ to understand the Si dynamics and the influence of weathering and biotic controls in groundwater and further utilized groundwater geochemistry to identify geogenic and anthropogenic elemental sources and evaluate their contributions, and water isotopes and $^{87}Sr/^{86}Sr$ to trace the origin and mixing of groundwater in the aquifers.

2. Materials and Methods

2.1. Study area, lithology, and climate

We studied two contrasting watersheds in Southern India: the agricultural watershed of Berambadi (84 km^2) and the pristine forested watershed of Mule Hole (4.1 km^2), both belonging to the Kabini Critical Zone Observatory, the Indian site of M-TROPICS (Sekhar et al., 2016; Riotte et al., 2021), part of OZCAR research infrastructure (Gaillardet et al., 2018) (Fig. 1). The region experiences tropical humid climate and is influenced by both South-West monsoon (June-September) and North-East monsoon (October-December). The bedrock of the region is dominated by the Precambrian peninsular gneiss (85%) and relatively minor (15%) mafic to ultramafic rocks (hornblendite, amphibolite and serpentinite) (Naqvi and Rogers, 1987). Major minerals in granitic-gneiss includes quartz, oligoclase, sericite, biotite and chlorite with accessory minerals such as apatite, epidote, allanite titanite, magnetite, ilmenite, pyrite and zircon (Braun et al., 2009). The average depth of the regolith in Mule Hole region is estimated to be 17 m, comprising 15 m of immature saprolite and a 2 m thick ferralsol (88%) or -vertisol

(12%) system (Barbiero et al., 2007, 2010; Braun et al., 2009). Primary minerals such as oligoclase, biotite and chlorite predominate the saprolite minerology with kaolinite, smectite and Fe-oxyhydroxides occurring as secondary phases (Braun et al., 2009; Violette et al., 2010b). The regolith is underlaid by fissured bedrock, forming the hard rock aquifer typical of aquifers the region (Soumya et al., 2011).

In the semi-arid Berambadi watershed, 60% of the total area is used for agriculture with some reserved forest on the western end (Buvaneshwari et al., 2017). The region receives lower rainfall (800-900 mm/yr) and groundwater undergo continuous pumping which causes depletion of the water table depth and large seasonal and interannual fluctuations depending rainfall and the intensity of pumping. Most of the groundwater sampled for the present study was from actively pumped tube wells in agricultural fields. Increase in the number of tube wells from 1990s led to a shift from low water demand rainfed crops like finger millet, sorghum and pulses to groundwater irrigated agriculture with high water demand cash crops such as sugarcane, banana, turmeric and vegetables (Sekhar et al., 2016; Fischer et al., 2022). Groundwater exhibits an enhanced groundwater hydraulic gradient, with upstream (western side) having shallow groundwater levels and deeper groundwater on the downstream end (eastern side) of the watershed (Buvaneshwari et al., 2017). The Mule Hole watershed is located in sub-humid zone, receiving a mean annual rainfall of 1200 mm distributed from March to October (Gunnell and Bourgeon, 1997). The temperature ranges between 37^{o}C during summer and 17^{o}C during the peak winter, typically in January. The watershed has been preserved from any human activities and belongs since 1974 to the Bandipur national park (Marechal et al., 2009).

2.2. Sampling and measurements

We sampled groundwater and surface water twice in 2019, in March for the dry season and August for the monsoon season. In Mule Hole, groundwater samples were collected from 9 observation wells drilled in 2003 and 2004 (Fig. 1). Three wells P3, P5 and P6 are located along the watershed boundary (300-400 m to the nearest stream) to monitor the background characteristics of the aquifer, far from the stream. The remaining six wells lie in a straight line perpendicular to the stream axis at its outlet with P1 and P7 very near to the stream. In Berambadi, groundwater samples were collected from borewells and handpumps at 17 locations within the watershed. Surface water sample for both watersheds are collected, including Nugu river (a tributary of Kabini almost 1.2 km from Mule Hole watershed, draining mostly the

humid zone of the Kabini Basin and then flowing permanently), few ephemeral streams and a tank very close to the groundwater sampling locations. Prior to sample collection, all sampled wells were purged until the pH and conductivity was stabilised. All water samples were filtered just after collection using 0.4 µm SUPOR PES filters, made aliquots for various analysis and subsequently stored in pre-cleaned containers. The aliquot for major cation and Sr isotope analysis was acidified using few drops of double distilled HNO_3 and aliquot for water isotopes were stored in 10 ml glass tubes. pH and conductivity were measured in the field. Groundwater levels (depth to water table) were measured manually before the groundwater collection using a manual piezometric level sensor (skinny dipper device, Haron instruments), except for handpumps, where such measurement is impossible, and for which water table depth was assumed to lie between 5 m.

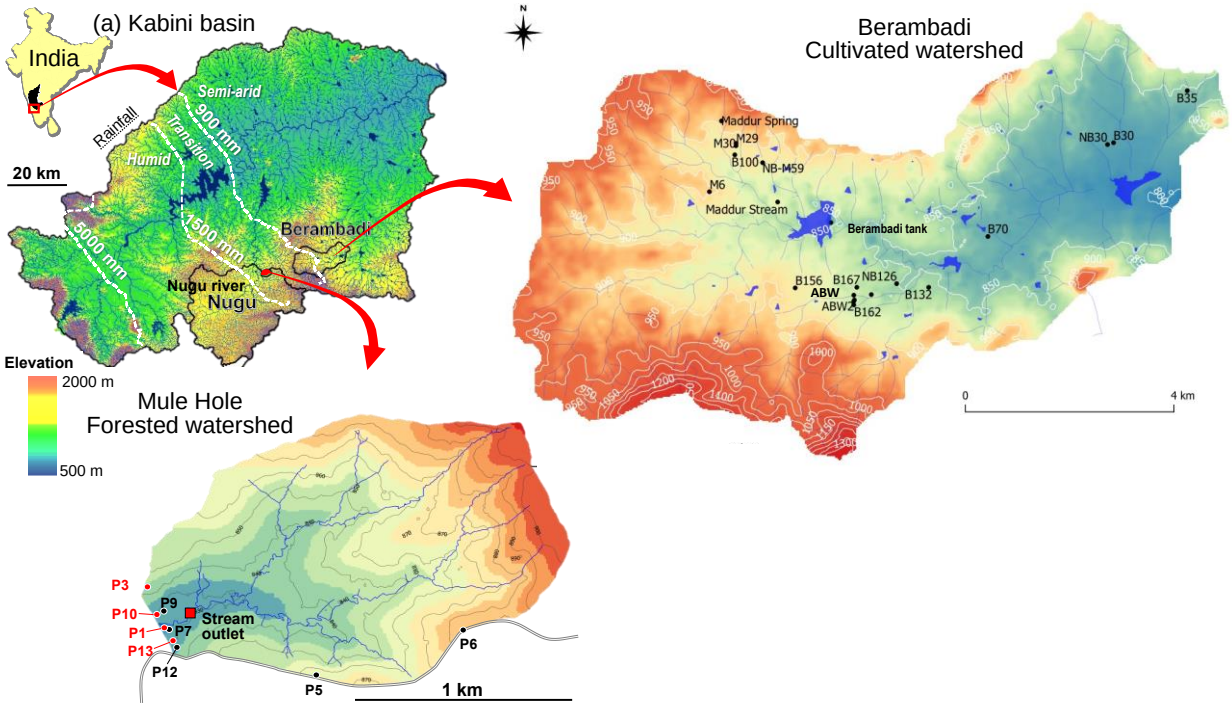

Figure 1. *Kabini watershed map with precipitation levels (mm/yr) and climatic zones marked and the two watersheds sampled for the current study: the cultivated Berambadi watershed and forested Mule Hole watershed. The sampling locations of groundwater and surface water samples are marked in Mule Hole and Berambadi.*

2.3. Elemental concentrations

Major cation and anion concentrations were measured with an Ion Chromatograph (Metrohm COMPACT 861) at IFCWS, IISc, India. The accuracy of measurements was monitored using multiple certified reference materials (AnionWS, ION-96.4, ION 915, SUPER-05 and BIG MOOSE 02) and external reproducibility was better than 5%. Alkalinity was determined with

a titrator Mettler Toledo-DL50 Rondolino. Usual precision obtained on major dissolved species determination was about 5%. Trace elemental concentration (Al, Sr, Fe, Mn) were determined by quadrupole inductively coupled plasma mass spectrometry (ICPMS, 7500cx Agilent) at Alysés analytical platform (IRD-Sorbonne Université, Bondy, France). Samples and standards were diluted and measured in 2% HNO_3. The accuracy of the measured elements was assessed by the measuring certified natural water reference standard, SLRS 6 and the average precision for trace element analysis was within 10%.

2.4 Water isotopes and Sr isotope analysis

Stable isotope (δ^2H and $\delta^{18}O$) compositions were determined by a stable isotope ratio mass spectrometer (Picarro L2130-i Isotopic Water Analyzer, IEES, Paris, France). Results are reported in ‰ with respect to the Vienna Standard Mean Ocean Water (VSMOW2). The analytical uncertainty, estimated from the repeated measurements of the Picarro MID standard, is ±0.1‰ for $\delta^{18}O$ and ±0.5‰ for δ^2H**.**

Strontium was separated from the water samples using a two-stage cation-exchange chromatography technique using BioRad AG50W X8 (100–200 mesh) resin following established protocols (Banerjee et al., 2016). Strontium was eluted in 3N HCl and ~1 μg the purified Sr was loaded on a single degassed Ta filament using phosphoric acid and tantalum oxide. Strontium isotope ratios were and measured using a thermal ionization mass spectrometer (TIMS, Thermo Scientific Triton Plus) at CEaS, IISc. Instrument mass fractionation was corrected using $^{86}Sr/^{88}Sr = 0.1194$ using exponential law. The internal precision for $^{87}Sr/^{86}Sr$ was better than 10 ppm (1 SE). The NIST SRM987 Sr isotopic standard analyzed during this study yielded $^{87}Sr/^{86}Sr=0.710277\pm24$ ppm (1SD, n=10).

2.5. Dissolved silicon and silicon isotope analysis

Silicon concentration (DSi) was measured by spectrophotometer following the Grasshoff et al. (1999) protocol. Analytical quality was assessed using certified reference material, PERADE 09 (supplied by Environment Canada, lot no:0314, with DSi = 110.0±6.8 μM), during each measurement and mean reproducibility was 109.9±3 μM (n=25). We followed a slightly modified two-step pre-concentration method adapted from MAGIC- MAGnesium Co-precipitation technique (Karl and Tien, 1992; Reynolds, 2006; Hughes et al., 2011). To an initial volume of 10 ml of groundwater and surface water samples, we added 0.5 ml of $MgCl_2$ solution to match the seawater Mg concentration and were treated with 2% (v/v) of 1 M NaOH and was shaken and kept undisturbed overnight. The brucite ($Mg(OH)_2$) formed at high pH scavenges

Si which gets adsorbed onto precipitated brucite. The supernatant from the first step was again subjected to second addition of 1% NaOH following, and the precipitate was recovered by centrifugation after 1-2 hrs. Both brucite precipitates were also re-dissolved with 1M HCl and merged. The DSi concentration of the supernatant was analyzed by spectrophotometer (Grasshoff et al., 1999) and found negligible (on average <2%), confirming that all the Si was adsorbed onto the brucite precipitate.

Separation of Si from other cations was carried out using cation exchange resin (BioRad DOWEX 50W-X12, 200 to 400 mesh, in H+ form) following the procedure of Georg et al. (2006). After the purification process, an aliquot was analyzed for major elements analysis (Na, Mg, Ca, K) by ICP-MS (Agilent 7500a) to ensure that the Si/X (Where X= Na, K, Ca or Mg) weight ratio is always >50 to minimize the matrix effects in the plasma. The organic matrix is removed by treatment with 50 µL of 30% H_2O_2 since it has been shown to potentially induce a matrix bias during MC-ICP-MS analyses (Hughes et al., 2011). Analyses performed on a series of 35 groundwater and surface water samples, shows that the preconcentration and H_2O_2 treatment increased the DSi/DOC ratio from 18 to 7000 times, with DSi/DOC ratio > 10 in the final aliquot (Annexe 2). This indicates <0.2‰ shift in Si isotope ratio from isotopic mass bias due to DOC matrix (Hughes et al., 2011). The possible remaining potential matrix effect resulting mainly from Cl^-, NO^-_3 and SO_4^{2-} was corrected by the artificial doping of anions (Merck, Suprapur grade H_2SO_4, HNO_3 and HCl) in all the samples and standards (Hughes et al., 2011). The measurements were performed on MC-ICP-MS (Thermo Neptune+, LSCE-IPSL, Gif-sur-Yvette) in dry plasma mode with Mg doping as described by Closset et al. (2016). Samples were injected into the plasma with an Apex**Ω** HF desolvating nebulization system connected with a PFA nebulizer (100 µL/min uptake rate) and without additional gas. The $\delta^{30}Si$ values were expressed as the permil deviation of the $^{30}Si/^{28}Si$ ratio from the quartz standard NBS28 (RM8546), expressed as:

$$\delta^{30}Si_{sample} = [(^{30}Si/^{28}Si)_{sample}/(^{30}Si/^{28}Si)_{NBS28} - 1] * 1000 \quad \text{(Eq.1)}$$

Blank levels were below 1% of the main signal and were subtracted from each sample and standard analysis. All measurements were carried out in a matrix composed of 0.5 M HNO_3, 0.5 M HCl, 1 mM H_2SO_4 and in medium-resolution mode ($m/\Delta m > 6000$) to optimize the separation of ^{30}Si peak and $^{14}N^{16}O$ interference and were performed on the interference-free left side of the peak (Abraham et al., 2008). The $\delta^{29}Si$ and $\delta^{30}Si$ values were compared to the mass-dependent fractionation line and samples falling outside of its analytical error were excluded from the final dataset. Typical analytical conditions are provided in Table S1. Laboratory

protocol has been intercalibrated for seawater as part as the GEOTRACES intercalibration exercise generated over the entire procedure (Grasse et al., 2017). The analytical precision and accuracy were monitored by the long-term measurements of secondary reference material diatomite ($\delta^{30}Si$ = 1.26‰, Reynolds et al., 2007) indicated an average precision and a long-term analytical reproducibility on $\delta^{30}Si$ values of 1.19±0.18‰ (2SD, n=100). Diatomite solutions processed with MAGIC give average $\delta^{30}Si$ values of 1.07±0.11‰ (2SD, n=12) which is slightly lighter than unprocessed diatomite, but the difference remains within our analytical reproducibility. All samples measured in the present study are chemically replicated at least once (average variability of 0.05±0.15‰), and 23 samples were triplicated (average 2SD of ±0.20 ‰).

2.6. Silicon isotope evolution in water samples

To estimate the fraction of Si released as dissolved phase during weathering, we adopted the normalization proposed by Hughes et al. (2013), where Si to selected elemental ratio (Na*, rainwater corrected) in groundwater and bedrock (Si and Na corrected for inert quartz and sericite) was used as a proxy for weathering congruency (Braun et al., 2009).

$$f_{Si} = Si/(Na^*)_{groundwater} / Si/(Na)_{bedrock} \quad \text{(Eq. 2)}$$

A f_{Si} of 1 corresponds to congruent dissolution of bedrock, i.e. all Si mobilized into dissolved phase with a $\delta^{30}Si$ identical to that of the bedrock. The f_{Si} decrease corresponds to the progressive incorporation of Si into secondary phases, such as clay minerals (Ziegler et al., 2005).

Si isotopic fractionation associated with a removal of DSi from a system can be described using two simple models; i) the Rayleigh model for distillation of isotopes describes a closed system with no further DSi input from external sources, ii) steady state model with continuous supply of DSi and dynamic equilibrium between supply and removal (Bouchez et al., 2013; Frings et al., 2015).

$$\text{Rayleigh: } \delta^{30}Si_{mea} = \delta^{30}Si_o + \varepsilon^* \ln(f_{Si}) \quad \text{(Eq. 3)}$$

$$\text{Steady state: } \delta^{30}Si_{mea} = \delta^{30}Si_o - \varepsilon^* (1 - f_{Si}) \quad \text{(Eq. 4)}$$

f_{Si} indicates the fraction of DSi remaining in the groundwater, obtained using E1. Here $\delta^{30}Si_{mea}$ denotes the measured $\delta^{30}Si$ values of groundwater and surface water samples and $\delta^{30}Si_o$ denotes the initial $\delta^{30}Si$ values before fractionation which is assumed the granitic gneiss bedrock value of -0.34±0.08‰ (Riotte et al., 2018a).

3. Results

3.1. General characteristics and chemical composition

Details of the groundwater and surface water sampling along with the geochemical data are provided in Table 1. Depth to groundwater table ranged from 1.5 to 46 m. The pH of the groundwater varied between 5.8 and 7.8, with Berambadi groundwater showing a slightly alkaline nature. Average groundwater conductivity in Berambadi groundwater was 1500±578 μS/cm (n=33), almost twice as that of Mule Hole (553±201 μS/cm) owing to excess fertilizer input and evapotranspiration. There was no significant seasonal difference observed in conductivity between dry and wet season sampling of the same groundwater (t-test, Table 1). The groundwater table depth fluctuated inconsistently in both watersheds with some wells showing an increase in water table depth between dry and wet and others vice versa. Berambadi groundwater exhibited an average Cl concentration of 4700±3800 μM, one order of magnitude higher than in Mule Hole, indicating chances of fertilizer contamination and also evaporative enrichment. In a plot of Na/Cl vs. Cl concentration, the Berambadi samples exhibited a negative correlation with Na/Cl ratio in certain groundwater samples even lower than the rainwater ratio of ~0.81 (Fig 2), as already observed by Buvaneshwari et al. (2020). To estimate Cl contribution from fertilizers such as potash (KCl), which is routinely applied in Berambadi, we followed the deconvolution method proposed by Buvaneshwari et al, (2020), based on relative proportions of Na and Cl using pristine Mule Hole as a reference. Following which the atmospheric inputs to major cations in groundwater were corrected using the normalization to fertilizer corrected Cl (Cl*) (Stallard and Edmond, 1981) using rainwater composition reported for Mule Hole (Riotte et al., 2014a). For Berambadi groundwater samples, fertilizer inputs accounted on average for 75±25% of the Cl content. On molar basis the concentration of anions in groundwater of both watersheds decreased in the order, $[HCO_3^-] > [Cl^-] > [SO_4^{2-}]$. Concentrations of anions such as Cl^-, NO_3^-, PO_4^{3-} and SO_4^{2-} increased with conductivity, with Berambadi groundwater exhibiting significantly higher nitrate concentration compared to Mule Hole. The cationic load in both watersheds was dominated by Na followed by Ca and Mg, covarying with measured conductivity. Potassium accounted for only a small part of the cationic load despite higher content in fertilizers, suggesting that most of it was exported with crop harvest. Atmospheric input accounted for less than 20% of the cation load in both watersheds. Surface water from small streams exhibited solute concentration similar to the groundwater next to it, while the Nugu river, which partly drains the humid zone of the Kabini basin, exhibited a much more diluted elemental load. The concentration of Sr in groundwater varied

from 1 to 30 µM, with Berambadi groundwater having a higher average of 13 µM compared to Mule Hole (3.9±1.4 µM). Most of the groundwater samples exhibited Al, Fe, and Mn concentrations <1 µM with a few handpumps and piezometers showing extreme Fe enrichment of up to 91µM.

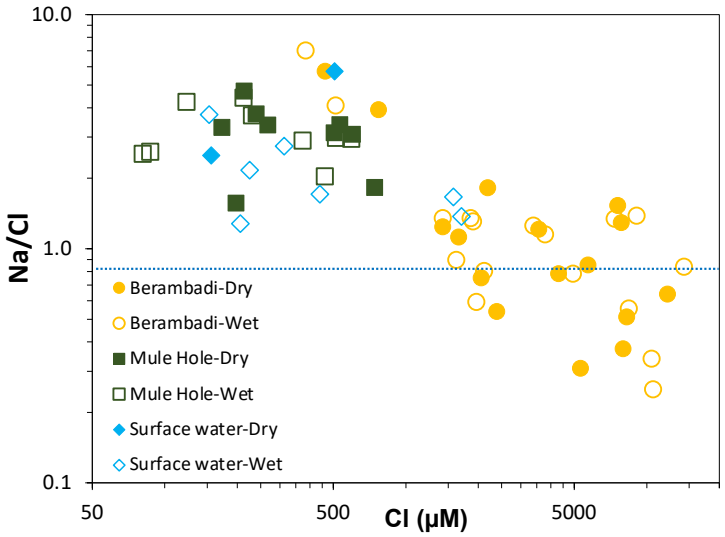

Figure 2*. Plot between Na/Cl and Cl in µM, showing increasing Cl concentration and a concurrent reduction in Na/Cl ratio below rainwater ratio of 0.81 (blue dotted line, Riotte et al., 2014). This trend indicates contamination of Berambadi samples (yellow circles) from fertilizers such as potash, with no such pattern evident in pristine Mule Hole groundwater (green square).*

3.2. Water and Sr isotopes

The results of the isotopic analyses from groundwater and surface water in Berambadi and Mule Hole are given in Table 2. Stable water isotopic composition of Berambadi groundwater ranged from -1.7 to -3.8 ‰ for $\delta^{18}O$ -8.9 to -21.6 ‰ for δD. In Mule Hole groundwater $\delta^{18}O$ ranged from -1.7 to -3.7 ‰ and δD from -2.1 to -18.1‰. On a $\delta^{18}O$ vs. δD plot, all the samples plotted close, but slightly right to the local meteoric water line (LMWL) derived from meteoric water of Mule Hole (Fig 3a, Fig. S1, details of rainwater in Table S2), which itself is superimposed on the global meteoric water line (GMWL, Craig 1961). The deuterium excess (d-excess= $\delta D - 8*\delta^{18}O$) calculated showed consistently lower values in Berambadi compared to Mule Hole and exhibited a general negative trend with conductivity (Fig 3b). No seasonal variability was observed in water isotopic signature of groundwater suggesting significant buffer to seasonal variations in monsoonal rainfall isotopic signature previously documented by Warrier et al. (2010).

Table 1. *The sample details, depth to water table (m), conductivity and elemental composition of groundwater and surface water from Berambadi and Mule Hole. The # denote the Cl concentration corrected for fertilizer input in Berambadi based on Buvaneshwari et al. (2020).*

		Depth m	Conductivity µS/cm	DSi µM	Na* µM	K* µM	Ca* µM	Mg* µM	Sr µM	Al µM	Mn µM	Fe µM	Cl µM	Cl# µM	NO_3 µM	PO_4 µM	SO_4 µM
Berambadi																	
Dry season																	
ABW	Piezometer	6.5	786	111	2577	102	542	2054	2.3	0.2	5.0	<dl	773	529	13	25	294
ABW2	Piezometer	6.0	1423	1150	3402	0	1504	3762	12.5	0.2	<dl	0.1	2196	698	1995	51	511
B100	Borewell	4.5	1890	1000	9858	31	1640	1305	11.8	0.2	<dl	0.1	7580	2024	1779	n.a	378
B132	Borewell	10	2030	1054	2543	138	3976	5348	25.3	0.2	<dl	<dl	7999	522	2664	80	712
B156	Borewell	5.1	1501	995	2863	96	1658	3294	11.7	0.4	0.1	0.2	4312	588	1847	47	503
B167	Borewell	9.4	1011	966	1503	42	2330	2124	6.7	0.2	0.0	0.1	1428	309	1503	45	258
B30	Borewell	46	2310	1301	3591	1055	5747	3489	17.2	0.4	0.0	0.1	8267	737	6085	82	1603
B35	Piezometer	36.3	892	1435	2262	156	1832	1555	6.0	0.4	0.2	<dl	464	464	759	34	190
B70	Borewell	34.5	2460	1060	6640	163	6287	2169	18.7	0.3	0.0	<dl	12219	1363	2688	72	1845
M29	Handpump	5	1336	583	4129	280	2981	1743	10.6	0.2	6.0	25.4	5707	848	102	44	291
M30	Handpump	5	1847	865	8606	131	3437	1314	11.5	0.2	4.0	3.1	7848	1767	2766	44	714
M6	Handpump	5	1098	987	1314	1032	2892	1679	10.2	0.4	13.0	16.1	2060	270	479	35	292
NB-M29	Handpump	5	1200	974	3672	81	2056	1433	10.9	0.1	0.1	0.1	3573	754	1125	43	406
NB126	Borewell	9.5	1170	1088	1093	59	2332	2575	9.1	3.6	<dl	0.2	2390	225	2684	47	474
NB30	Borewell	42.7	1796	1487	1393	357	4607	3904	21.3	0.5	<dl	0.1	5325	286	4928	76	1033
B162	Borewell	9.1	1100	1119	1586	46	3002	1784	10.9	0.2	<dl	0.1	1662	326	1739	47	320
Stream 1	Surface water		1148	868	2471	32	1460	2807	9.33	0.21	2.45	0.12	507	507	711	35	244
Wet season																	
ABW	Piezometer	6.0	663	67	1779	88	351	1343	1.04	0.21	0.69	0.52	512	365	25	16	185
ABW2	Piezometer	6.8	1423	958	2135	13	2022	3674	17.72	0.14	1.01	3.80	1858	438	1147	31	500
B100	Borewell	4.5	2050	1037	10689	38	2800	1202	11.81	0.25	0.02	0.10	9084	2195	1751	29	393
B132	Borewell	10	2180	1002	3028	139	4202	5955	29.65	0.27	0.07	0.59	10492	622	2195	62	715
B156	Borewell	4	1362	1040	3618	52	2466	2479	10.19	0.23	0.02	0.31	3391	743	1747	31	438
B167	Borewell	8	1022	933	1636	43	2305	2227	9.09	0.17	0.10	0.20	1424	336	1290	28	239
B30	Borewell	40.8	2500	1299	3985	1235	6483	3457	18.48	0.24	0.06	0.37	8440	818	3662	51	1783
B35	Piezometer	36.5	934	1396	2296	169	1897	1713	6.76	0.16	0.08	0.16	384	472	631	33	178
B70	Borewell	14.3	2750	1042	10157	45	5291	2254	20.93	0.22	0.09	0.68	14266	2086	1133	66	3305
M29	Handpump	5	1235	672	3296	278	2447	1598	12.12	0.92	5.52	46.36	4947	677	1	28	289
M30	Handpump	5	1808	891	8428	142	2944	956	17.11	0.23	0.66	16.72	7365	1731	1377	41	1044
M6	Handpump	5	984	704	1234	1606	2537	1532	9.72	0.21	17.61	91.16	1620	253	0	28	212
NB-M29	Handpump	5	1162	891	3716	76	2343	1351	n.a	n.a	n.a	n.a	3791	763	773	22	439

		Depth m	Conductivity µS/cm	DSi µM	Na* µM	K* µM	Ca* µM	Mg* µM	Sr µM	Al µM	Mn µM	Fe µM	Cl µM	Cl# µM	NO_3 µM	PO_4 µM	SO_4 µM
NB126	Borewell	10	964	1010	990	45	2657	2189	7.88	0.30	0.04	0.09	1963	203	2143	27	394
NB30	Borewell	40	2580	1259	2267	409	6815	4992	27.24	0.24	0.03	0.16	10628	465	8313	67	2116
B162	Borewell	10	1116	1117	1446	41	3085	1867	n.a	n.a	n.a	n.a	2115	297	1979	29	319
ABW3	Borewell	6.5	1248	893	2119	20	1913	3626	17.98	1.16	1.08	0.19	1905	435	1167	30	502
Stream1	Surface water		1000	597	1275	66	1836	1812	8.18	0.32	1.50	0.08	1576	1576	350	26	235
Stream2	Surface water		530	321	881	51	851	363	3.94	0.23	0.49	0.30	1702	1702	13	16	121
Tank	Surface water		262	179	374	105	504	299	2.35	0.25	0.02	0.25	440	440	1	13	93
Spring	Surface water		72	458	441	4	23	8	0.15	1.11	0.07	0.25	153	153	11	12	36
Mule Hole																	
Dry season																	
P1	Piezometer	7.62	399	588	140	83	1393	798	3.29	0.36	3.74	9.10	198	198	2	19	26
P10	Piezometer	14.13	624	881	1349	83	1512	952	4.83	0.20	9.91	1.69	533	533	1	22	87
P12	Piezometer	10.75	467	477	674	116	1179	837	3.35	0.21	12.28	0.75	268	268	1	19	156
P13	Piezometer	9.77	400	671	696	112	953	805	n.a	n.a	n.a	n.a	240	240	1	17	59
P3	Piezometer	22.48	806	889	721	202	1967	1497	5.46	0.28	7.76	24.48	745	745	1	32	87
P5	Piezometer	31.73	592	759	1145	172	1347	1006	3.75	0.47	0.47	0.10	505	505	1	26	74
P6	Piezometer	33.62	751	689	823	126	1317	1637	3.19	0.43	9.91	1.63	214	214	1	30	180
P7	Piezometer	8.61	584	868	422	40	1677	1346	5.71	0.22	1.60	4.55	173	173	2	28	78
P9	Piezometer	13.26	702	860	1335	128	1798	990	5.42	0.29	13.69	19.25	602	602	2	29	11
Nugu River	Surface water		138	417	257	54	250	237	1.13	0.23	1.65	0.91	156	156	5	10	8
Wet season																	
P1	Piezometer	1.5	172	639	151	37	393	275	1.49	0.55	0.27	0.16	87	87	1	14	32
P10	Piezometer	14.1	624	886	1242	83	1253	819	4.52	0.93	5.26	0.68	595	595	1	27	107
P12	Piezometer	9.2	467	483	546	109	1192	876	4.18	0.85	16.70	0.51	462	462	1	17	188
P13	Piezometer	8.9	452	617	657	118	904	804	2.72	1.06	6.40	0.31	230	230	1	19	69
P3	Piezometer	21.7	150	410	136	122	350	180	1.30	0.74	1.54	1.82	81	81	1	12	16
P5	Piezometer	31.9	722	886	1088	180	1283	1000	3.77	0.29	0.03	0.06	513	513	1	23	71
P6	Piezometer	34.4	910	677	756	121	2081	1584	3.12	0.15	13.04	3.89	212	212	0	26	150
P7	Piezometer	2.4	647	739	416	46	1753	1524	6.55	0.82	0.24	0.24	123	123	0	24	156
P9	Piezometer	13.2	485	776	760	105	1192	655	4.31	0.83	8.09	4.18	373	373	1	20	120
Nugu River	Surface water		107	256	87	64	199	117	0.94	0.30	0.03	0.36	206	206	37	11	20
MH Stream	Surface water		169	453	294	115	336	210	1.20	1.40	0.05	0.50	225	225	1	13	7
Stream 3	Surface water		n.a	299	n.a	n.a	n.a	n.a	1.08	1.19	0.11	0.63	313	313	0	14	21

The $^{87}Sr/^{86}Sr$ ratio showed significant differences in water samples from Berambadi and Mule Hole, ranging from 0.70972 to 0.73077 (Table 2, Fig. S1, Fig 4). $^{87}Sr/^{86}Sr$ and other isotopic signatures of the water compartments measured in the present study and also compiled from a previous study in the region are given in Table 3. Groundwater samples from Berambadi exhibited less radiogenic $^{87}Sr/^{86}Sr$ with an average of 0.71480 compared to Mule Hole (0.71756) (Table 2, Fig. 4). The gneiss bedrock from Mule Hole is reported to have an $^{87}Sr/^{86}Sr$ value of 0.713174, but the composition of the parent gneiss can vary locally from felsic (oligoclase/quartz) to mafic (biotite/chlorite) endmembers (0.713174 to 0.783180, Janardhan and Vidal, 1982; Violette et al., 2010a; Braun et al., 2009).

3.3. Dissolved silicon (DSi) and $\delta^{30}Si$

The average DSi of groundwater water samples was significantly higher in Berambadi (980 ± 313 μM, 1SD, n=33) than in Mule Hole (711±154 μM, 1SD, n=18), with dry season having a higher DSi compared to the wet season for both watersheds (Table 1, 2, Fig. 5). The surface water from both watersheds, including the Nugu river showed a lower DSi compared to groundwater with an average of 427±194 μM (1SD, n=8). The groundwater DSi of the region was generally higher than the previously published terrestrial global average for extrusive igneous (604±192 μM) and granitic (334±255 μM) bedrocks (Rahman et al., 2019). Dissolved $\delta^{30}Si$ of the groundwater ranged from 0.59 to 3.45 ‰, enriched compared to bulk upper continental crust value (−0.25±0.16‰, Savage et al., 2013) and to the local gneiss value reported in Mule Hole (-0.34±0.08‰, Riotte et al., 2018a). Both Berambadi (1.15±0.64‰) and Mule Hole (0.98 ± 0.24 ‰) exhibited comparable $\delta^{30}Si$, and in the higher side of the compiled global groundwater average of 0.5±0.9‰ (n=66) (Figure 5, Ziegler et al., 2005; Georg et al., 2009a; 2009b; Opfergelt et al., 2013; Pokrovsky et al., 2013; Strandmann et al., 2014; Ehlert et al., 2016; Riotte et al., 2018a; Martin et al., 2020). The $\delta^{30}Si$ values of surface water samples collected from small streams close to the groundwater samples and of Nugu river (part of Kabini river a tributary of Kaveri) showed an average value of 1.69±0.54‰, which was significantly heavier than the groundwater values in the watershed (*p* value <0.05, Fig 5). We do not observe any seasonal differences in $\delta^{30}Si$ values measured in groundwater samples from both watersheds. A weak negative correlation was found between DSi and $\delta^{30}Si$, with heavier $\delta^{30}Si$ corresponding to a loss of DSi from the system (R^2=0.42, *p* value<0.05, Fig 6). The average $\delta^{30}Si$ of soil solution from Berambadi was 1.55±0.3‰, significantly higher than groundwater (*p*-value<0.005).

Table 2. *The isotope ratios of the H, O, Sr and Si from Berambadi and Mule Hole during dry and wet season. The '*' denotes the standard deviation of triplicated samples and the rest is only duplicated and denote variability.*

	$\delta^{18}O$ ‰	$\delta^{2}H$ ‰	$^{87}Sr/^{86}Sr$	$\delta^{30}Si$ ‰	1SD ‰
Berambadi- *Dry season*					
ABW	-3.8	-21.6	0.716358	2.959	0.04
ABW2	-2.9	-17.7	0.711203	1.133	0.13*
B100	-2.6	-13.1	n.a	0.681	0.06*
B132	-3.0	-18.6	0.71276	0.973	0.02
B156	-3.2	-18.4	0.712819	0.736	0.08
B167	-3.5	-20.6	0.715044	1.096	0.14
B30	-2.6	-14.2	n.a	0.763	0.09
B35	-3.4	-19.5	0.725742	1.060	0.03
B70	-1.7	-10.8	0.709721	0.927	0.05
M29	-3.0	-16.2	0.715262	1.490	0.10*
M30	-2.4	-12.5	n. a	1.478	0.10*
M6	-2.4	-11.8	n.a	0.694	0.08*
NB-M29	-2.0	-9.8	0.713611	1.020	0.11*
NB126	-3.2	-19.0	0.718218	1.022	0.13*
NB30	-3.2	-18.1	0.713255	0.630	0.05
B162	-3.5	-21.1	n.a	0.844	0.08
Stream 1	-3.4	-19.6	0.715256	1.636	0.04
Berambadi- *Wet season*					
ABW	-3.8	-19.7	0.716354	3.451	0.01
ABW2	-3.1	-17.7	0.711222	1.414	0.10*
B100	-2.7	-12.7	0.713536	0.877	0.04
B132	-3.4	-19.8	0.712892	0.702	0.12*
B156	-3.4	-18.8	n. a	0.593	0.06
B167	-3.6	-20.8	n. a	1.204	0.08*
B30	-2.2	-9.6	0.714732	0.833	0.05
B35	-3.5	-19.0	0.730778	0.893	0.10*
B70	-1.8	-8.9	0.710274	1.080	0.09*
M29	-3.2	-16.0	0.713521	1.815	0.11*
M30	-3.0	-13.0	0.71242	1.585	0.12*
M6	-2.7	-12.4	n. a	1.440	0.07
NB-M29	-1.9	-9.3	n. a	0.749	0.02
NB126	-3.3	-19.1	0.714888	0.847	0.08
NB30	-2.6	-14.9	0.714703	0.795	0.02
B162	-3.5	-20.4	n. a	0.903	0.10*
ABW3	-3.1	-17.6	0.711163	1.198	0.04
Stream1	-3.1	-16.1	0.715242	1.780	0.15
Stream2	-2.5	-10.5	n. a	1.891	0.08*
Tank	-2.3	-10.1	0.713966	1.596	0.06
Spring	-3.1	-12.8	n. a	0.967	0.06
Mule Hole-*Dry season*					
P1	-2.4	-6.8	0.716582	1.465	0.15
P10	-3.3	-14.8	n. a	1.061	0.02
P12	-2.5	-9.2	n. a	1.071	0.18*
P13	-2.9	-12.9	n. a	1.142	0.13
P3	-3.4	-16.4	0.717517	0.589	0.11
P5	-3.6	-16.7	0.719834	0.970	0.12
P6	-2.8	-16.9	0.714836	0.851	0.10
P7	-2.7	-9.4	0.716777	1.225	0.10*
P9	-3.6	-17.0	0.718167	1.033	0.03
Nugu River	-1.8	-6.9	0.711591	2.186	0.09*
Mule Hole-*Wet season*					
P1	-2.2	-4.9	0.716500	1.307	0.13
P10	-3.3	-14.1	n. a	0.878	0.04
P12	-1.7	-2.1	0.718185	0.965	0.04
P13	-3.3	-13.8	n. a	0.752	0.03
P3	-3.2	-13.8	0.715977	0.928	0.07
P5	-3.7	-17	0.720013	0.651	0.06
P6	-3.3	-18.1	0.718298	0.602	0.01
P7	-2.5	-6.4	0.716795	1.087	0.09*
P9	-2.7	-8.3	0.718823	1.077	0.01
Nugu River	-2.8	-10.1	0.71089	1.469	0.08*
MH Stream	-2.5	-7.9	0.721681	1.524	0.06
Stream 3	-2.1	-6.3		1.507	0.11
NIST SRM987	-		0.710277 (±24 ppm, 1SD, n=10)		-
Diatomite	-	-	-	1.19	0.09 (n=100)

4. Discussion

4.1 Groundwater geochemistry: weathering vs. anthropogenic sources

The chemistry of water in aquifer is influenced by the rainfall, throughfall, water-rock interactions when infiltrating through vadose zone and aquifer, and the contributions from direct and indirect anthropogenic inputs. Weathering reactions in soil and saprolite layers occurring during infiltration is the major source of DSi in the groundwater, with negligible input from throughfall in Mule Hole (Soumya et al., 2011, 2013; Riotte et al. 2014a). In the case of Mule Hole, most of the DSi in the soil- infiltrating solution and overland flow is controlled by amorphous silica (ASi) dissolution (Riotte et al., 2014a; Riotte et al., 2018a). In absence of human activities, water-rock interactions in the regolith and fractured zone contribute to much of the DSi, Na^+, Ca^{2+}, Mg^{2+}, and alkalinity in groundwater with very limited SO_4^{2-} and NO_3^- (Soumya et al., 2013) This is evident in Mule Hole with low concentration and limited variability of sulphate and nitrate in the groundwater (Table 1). Na^+ in groundwater can originate from atmospheric inputs and from the Na-plagioclase weathering, while Ca and Mg primarily comes from water rock interactions (e.g., biotite, apatite, hornblende, chlorite and calcite weathering, Braun et al., 2009). The presence of pedogenic carbonates, previously documented in Mule Hole, is also a potential source for Ca and Mg in the groundwater (Violette et al., 2010b; Braun et al., 2009). Potassium-bearing minerals such as biotite and chlorite are the likely sources of K^+ in groundwater and are heavily recycled through vegetation. In Berambadi, solutes in groundwater can originate from atmospheric input, weathering, and anthropogenic inputs as fertilizers, which can further be concentrated through processes such as evapotranspiration due to successive pumping (Buvaneshwari et al., 2017, 2020). Additional anthropogenic input was evident from the drastic increase in all the cations and anions in groundwater for both seasons compared to Mule Hole (Table 1). Groundwater from Berambadi exhibits a decrease in Na/Cl ratio with increasing Cl concentration, even below the rainwater ratio, consistent with a input of fertilizers such as Potash (KCl) (Figure 2) as already discussed by Buvaneshwari et al. (2020). Groundwater in Berambadi exhibited high nitrate concentrations compared to negligible amounts in Mule Hole, indicating the effect of excessive fertilizers usage for irrigated agriculture in the region (Buvaneshwari et al., 2017). More detailed studies and modelling frameworks of geochemistry of groundwater samples from Mule Hole and Berambadi can be found elsewhere (Soumya et al., 2013; Riotte et al., 2014a; Buvaneshwari et al., 2017, 2020).

4.2 Stable isotopes of water: evaporation, recharge, and irrigation

Stable water isotopes in groundwater primarily reflect the average isotopic signature of local precipitations and recharge occurring in the aquifer. The differences in water isotopic signatures in groundwater arise due to variability in isotopic signatures of local rainfall, evaporation during percolation through vadose zone, and from mixing with pre-existing water mass (Clark, 2015). In Mule Hole forested watershed with an average rainfall of 1100 mm/year, evapotranspiration accounts for about 900 mm/year, including about 100 mm/year resulting from deciduous tree uptake from the deep saprolite layers (Ruiz et al., 2010). Meteoric water undergoing such high rates of evapotranspiration during the transit in the deep vadose zone leads to a groundwater underflow of just 80 mm/year, and a buffered response to precipitation events (Ruiz et al., 2010). The δ^2H and $\delta^{18}O$ of groundwaters plotted close to the local meteoric water line (LMWL) indicating that source of groundwater can be considered within the domain of modern precipitation and recharge (Figure 3a). The weighted average value of $\delta^{18}O$ reported for annual precipitation in Mule Hole was -4.3±0.28 ‰ (n=23), which is lighter than the weighted mean of South-West monsoon value of -2.9 ‰ (Table S2, Warrier et al., 2010). Based on the water level fluctuations and distance from the stream in Mule Hole, Marechal et al., (2009) partitioned the groundwater into two major groups; direct discharge dominated (group 1), and indirect discharge dominated (group 2). Direct recharge from precipitation dominates the wells in group 1 (P3, P5, P6), since they are far away from the stream (Marechal et al., 2009). Observed deficit in recharge is attributed to high evapotranspiration in the watershed, and the groundwater exhibits a heavier $\delta^{18}O$ compared to rainwater, which can be attributed to evaporative enrichment (Barnes and Allison, 1983; Marechal et al., 2009; Wenninger et al., 2010). Group 2 piezometers (P1 and P7) are shallow aquifers located in close vicinity of the stream with high seasonal water level fluctuations due to indirect recharge from the ephemeral stream during wet season (>7 m water table fluctuation, Marechal et al., 2009). δ^2H and $\delta^{18}O$ are distinctly heavier in the group 2 piezometers and they lie very close to the Mule Hole stream during monsoon in dual isotope plot, indicating direct signatures of local precipitation (Figure 3a). Almost all the groundwater exhibits a low conductivity and d-excess value between 10.4 and 13.6, except P6 which is the deepest piezometer close to watershed boundary (Fig. 3b).

In the intensely cultivated Berambadi watershed, the recharge process is not straightforward due to irrigation return flows, which can vary in different areas depending on the water requirements for specific crops (Dewandel et al., 2008; Négrel et al., 2011). As pumped water

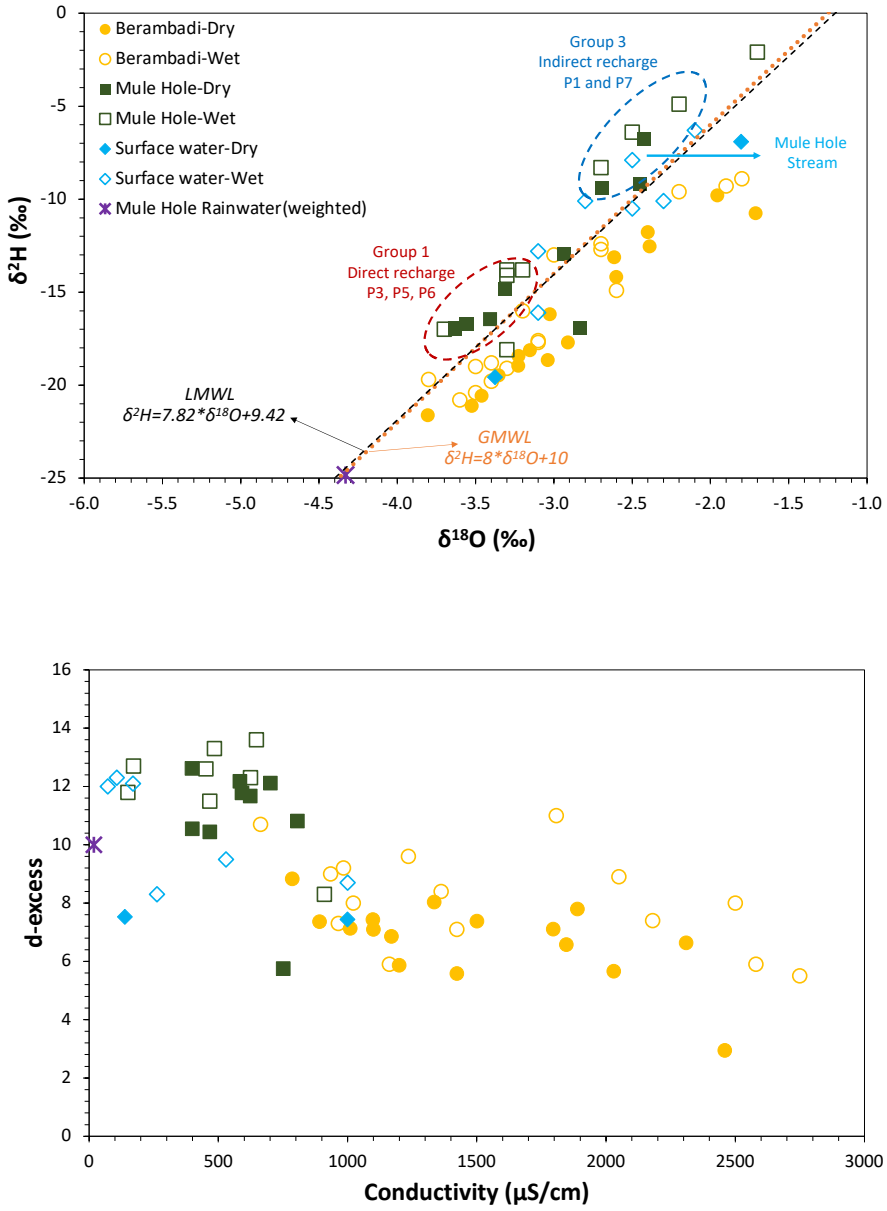

Figure 3. *a) $\delta^{18}O$ and $\delta^{2}H$ bivariate plots for groundwater and surface water from Mule Hole and Berambadi along with the local meteoric water line (LMWL, black dashed line) from local precipitation signal and global meteoric water line (GMWL, orange dashed line) from Craig (1961). Equations for linear relationship between $\delta^{18}O$ and $\delta^{2}H$ for each watershed during both seasons are: Berambadi-Dry ($\delta^{2}H$=6.4 (±0.4)*$\delta^{18}O$+ 2.3 (±1.3)), Berambadi-Wet ($\delta^{2}H$=6.6 (±0.6)*$\delta^{18}O$+ 3.8 (±1.8)), Mule Hole-Dry ($\delta^{2}H$=7.3 (±1.6)*$\delta^{18}O$+ 8.7 (±5.1)), Mule Hole-Wet ($\delta^{2}H$=8.4 (±0.9)*$\delta^{18}O$+ 13.3 (±2.6)) and surface water-wet ($\delta^{2}H$=7.1 (±1.9)*$\delta^{18}O$+ 8.1 (±5.1)) (note that surface water during dry season was omitted since only two data points are available), b) d-excess vs. conductivity measured on site of groundwater and surface water from Mule Hole and Berambadi.*

returns to the aquifer, the δD and $\delta^{18}O$ vary depending on the source of irrigation water, depth of unsaturated zone and evapotranspiration rates (Négrel et al., 2011). In Berambadi watershed, the deepest groundwater levels, below the saprolite layer (typically >17m) are located in areas

with low hydraulic gradient and the recharge is mostly vertical with negligible lateral flow (Buvaneshwari et al., 2017). Berambadi groundwater from both season plots on the right of LMWL in dual isotope plot indicating larger influence of evaporation and intercepts the LMWL between -4.5 and -5‰, comparable with the weighted $\delta^{18}O$ of modern precipitation in the region (Figure 3a). This is further shown by the plot of d-excess vs. conductivity, with Berambadi groundwater exhibiting consistently low d-excess (between 2.9 and 11) compared to Mule Hole (11.5 to 13.6) and shows a weak negative correlation with conductivity (R^2= 0.3, $p<0.05$, Fig. 3b). Increased conductivity associated with lower d-excess indicates evaporative enrichment associated with irrigation return flow in Berambadi. To summarize, contrasting land-use with anthropogenic involvement significantly impact the geochemical signatures of the groundwater, where multiple cycles of pumping and return flow in Berambadi watershed lead to intense leaching of solutes with additional human inputs and/or significant evaporative enrichment. On the other hand, water isotopes in forested Mule Hole are consistent with different recharge processes of the watershed estimated by earlier studies using geochemistry and modelling (Marechal et al., 2009; Ruiz et al., 2010).

4.3 Lithological and anthropogenic controls on $^{87}Sr/^{86}Sr$ of groundwater

$^{87}Sr/^{86}Sr$ is used as a tracer in hydrologic systems to understand water rock interactions, source delineation and mixing (Blum et al., 1993; Brantley et al., 1998; Négrel et al., 2018). Strontium-bearing primary (rock-forming) minerals such as plagioclase, apatite, amphibolites, micas and secondary weathering products such as carbonates, evaporates, are the major sources of Sr in groundwater with minor inputs from rainwater and anthropogenic activities (Blum et al., 1994; Pett-Ridge et al 2009; Négrel et al., 2018). A plot of Ca/Sr molar ratio versus $^{87}Sr/^{86}Sr$ is used to decipher contributions rock/mineral weathering endmembers and anthropogenic sources of Sr to groundwater (Fig 4a). Observed variations in $^{87}Sr/^{86}Sr$ of groundwater samples of this study can be explained by contributions from three endmembers: i) a low Ca/Sr and less radiogenic $^{87}Sr/^{86}Sr$ source, ii) high Ca/Sr and less radiogenic $^{87}Sr/^{86}Sr$ source, and iii) more radiogenic $^{87}Sr/^{86}Sr$ bearing source with high/intermediate Ca/Sr (Figure 4a). The only reported $^{87}Sr/^{86}Sr$ value for Precambrian gneiss from Mule Hole is 0.7132 with a Ca/Sr molar ratio of ~250, which can be the bulk silicate rock weathering endmember (E1) and labile pedogenic carbonates with $^{87}Sr/^{86}Sr$ of 0.7145 (±0.0014, n=23) and Ca/Sr>1000 (Violette et al., 2010a) can be carbonate weathering endmember (E2). One possibility for a radiogenic endmember is increased contribution from weathering of primary phases such as biotite and/or K-feldspars ($^{87}Sr/^{86}Sr$ of 0.72 to 4.3, Meißner et al., 2002; Pett-Ridge et al., 2009). Abundance of highly

radiogenic primary mineral phase such as biotite (~10% on average but extremely variable laterally) in bedrock can be a potential third endmember (E3) (Braun et al., 2009). Significantly radiogenic $^{87}Sr/^{86}Sr$ of 0.725 and 0.730 was observed in a deep piezometer sample B35 (>35 m) in Berambadi during both dry and wet seasons, suggesting contribution from a local lithology containing higher proportions of radiogenic $^{87}Sr/^{86}Sr$-bearing phases such as biotite and K-feldspars. Deeper groundwater such as B35 with higher fluid residence time and water-rock interaction time within the bedrock aquifer along with negligible lateral flow can capture more intense signatures of radiogenic silicate phases. Interestingly, several Berambadi groundwaters exhibit less radiogenic $^{87}Sr/^{86}Sr$ relative to the parent gneiss endmember (E1), which can be due to two factors, i) heterogeneity in whole rock composition locally (0.7027 to 0.7573, Meißner et al., 2002), ii) additional input of Sr from fertilizers. We measure a Sr concentration of 350 ppm with a less radiogenic $^{87}Sr/^{86}Sr$ (0.7085) and Ca/Sr of 2500 in a fertilizer mixture routinely applied in Berambadi. Thus, fertilizer input can also explain relatively lower $^{87}Sr/^{86}Sr$ and higher Sr concentration in Berambadi compared to Mule Hole. Similar observation was previously documented in groundwaters from heavily cultivated Maheshwaram catchment in India and other watersheds (Négrel et al., 2004, 2018). Finally, combining δD-$\delta^{18}O$ and $^{87}Sr/^{86}Sr$ compositions, we also observe that the groundwater with lower d-excess values are associated with a less radiogenic $^{87}Sr/^{86}Sr$, except the deep piezometer sample B35 (Fig. 4, Fig S2). Such a pattern in Berambadi points towards aquifer systems undergoing intense pumping and return flow, leading to lower d-excess values due to evaporative enrichment and accumulating fertilizer leachate through successive cycles. Overall, in both watersheds, whole rock weathering dominated by non-radiogenic $^{87}Sr/^{86}Sr$ bearing phases such as Na-plagioclase, controls $^{87}Sr/^{86}Sr$ ratio in groundwater, along with minor contribution from weathering of residual radiogenic primary minerals such as micas and less radiogenic carbonates. In addition to such water rock interactions, Berambadi groundwater is also influenced by extensive anthropogenic inputs through fertilizers application.

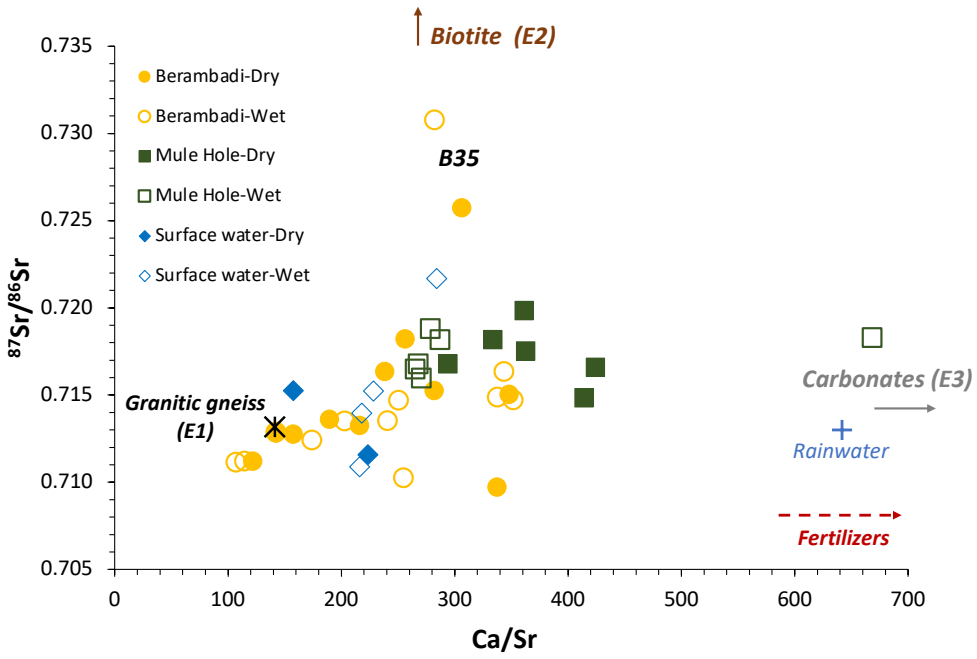

Figure 4. *Plot between Ca/Sr ratio and $^{87}Sr/^{86}Sr$ of the groundwater and surface water samples from Berambadi and Mule Hole. The data for potential endmembers (E1-E3) and rainwater water data are from published in Meißner et al, (2002) and Violette et al. (2010a). The fertilizer sample from Berambadi analysed exhibits an $^{87}Sr/^{86}Sr$ of 0.7085 (Table 2).*

4.4. δ^{30}Si signatures in groundwater and surface water

4.4.1 Climatic and land use controls of groundwater δ^{30}Si

The journey of Si to groundwater starts as it is solubilized during primary mineral weathering in the regolith, but soon to encounter various processes that can immobilize the element throughout the weathering zone. Processes such as precipitation/dissolution reactions of secondary clay minerals, adsorption/desorption kinetics of oxy-hydroxides and biotic uptake forming biogenic silica (BSi, primarily phytoliths in our case) can alter the fate of solubilized silicon in the regolith (Frings et al., 2016 and the references therein). The remaining fraction of dissolved silicon (DSi) is transferred to fluvial systems through (sub-)surface flow or groundwater. One should note here that the timescales of such processes are very different: clay mineral formation happens over a long period of time (decades to millions of years), but the adsorption and biologic uptake can happen in a span of few days (Cornelis et al., 2011; Thiry, 2000; Price et al., 2005). Tracing the source of such dissolved silicon in groundwater is further complicated by water rock interaction that happens in deep regolith, which is necessarily independent of the aboveground and shallow soil processes. Incongruent weathering signature is evident in both watersheds, with heavier average groundwater δ^{30}Si

value in both Berambadi and Mule Hole compared to the granitic gneiss bedrock value of -0.34‰ reported previously (Figure 5 and Riotte et al., 2018a). Overall, based on the watershed level $\delta^{30}Si$ of different hydro compartments, three major inferences can be reached. Firstly, the absence of seasonal differences in groundwater $\delta^{30}Si$ composition despite variable and significant differences in DSi contents with season, both in Mule Hole and Berambadi. This indicates that the immediate monsoonal precipitation imparts very little influence on the abiotic as well as biotic processes controlling the dynamics of Si in groundwater (Fig. 5). This can be contrasted with nearby Nugu river, showing cation dilution and a lower silicon isotopic composition during the wet season owing to excess runoff from monsoonal precipitation. High discharge in surface waters also limits diatom growth due to high turbidity, fitting the overall trend observed earlier in the Kaveri river basin (Meunier et al., 2015; Sarath et al., 2022). Secondly and rather surprisingly, two watersheds under strong contrasting land use and land cover exhibits no differences in groundwater $\delta^{30}Si$ signatures (Fig. 5). Such a behaviour of groundwater can be contrasted to the observation from soil solution and rivers in temperate land use gradients, where $\delta^{30}Si$ was significantly heavier in old cropland compared to forested landscapes, owing to efficient harvest in cropland and subsequent reduction in soil biogenic Si (BSi) turnover (Ding et al. 2004; Delvaux et al., 2013; Vandevenne et al., 2015). Despite more than 30 years of irrigated agriculture and continuous cultivation of Si accumulating crops such as sugarcane, banana and maize, with significant changes in geochemistry due to fertilizer use, Si isotopic signature in Berambadi groundwater remains unaltered. One possible explanation is that the impact of such land use changes, evident in the soil solution, is overwritten by water rock interactions in the deep regolith and in the subsequent sections we look in detail to the processes that can impact the Si cycling in groundwater in both watersheds. Thirdly, groundwater $\delta^{30}Si$ values are on average lighter than the surface water samples (1.60±0.33‰) and soil solutions (1.60±0.21‰), hinting towards a differential controls of silicon isotopic fractionation processes in the two hydrosystems (Riotte et al., 2018a). The ephemeral nature of the streams prevents diatom growth and can be neglected, with amorphous silica (ASi) fraction in the suspended loads dominated by phytoliths (Riotte et al., 2018a). During the dry season, most streams are dried up except the Nugu river, which drains the humid part of the Kabini Basin, with $\delta^{30}Si$ of 2.2‰, indicating impacts of upstream agriculture in the upper Kabini basin.

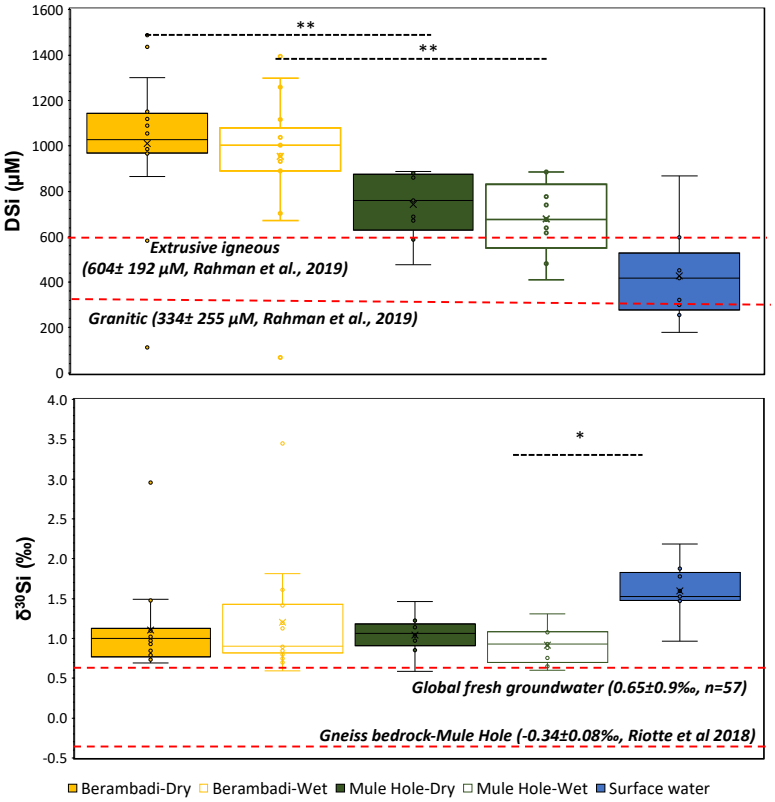

Figure 5. *Box plot showing the variability of a) dissolved silicon (DSi), b) silicon isotopic composition of groundwater and surface water from the present study and also the published DSi values of groundwater globally (Rahman et al., 2019) and δ^{30}Si (Frings et al., 2016, Ehlert et al., 2016 and Martin et al., 2020) with different compartments in Mule Hole published by Riotte et al. (2018a). The * represent the level of significance and DSi was significantly high for Berambadi compared to Mule Hole and surface water. Significance differences in δ^{30}Si between surface water and groundwater was only found between during Mule Hole in wet season.*

4.4.2 First order weathering controls: Si incorporation into secondary phases

Previous studies have reported that the majority of the soil silicon pool in the region is still located in primary minerals (86-95%) and a small proportion in secondary minerals (4-13%), mainly as kaolinites (Braun et al., 2009, Riotte et al., 2018a). Elemental mass balance inferred from isotopes confirms that Si infiltrating the soil from overland flow and seepage is originating from dissolution of ASi fraction (1.25‰), primarily phytolith due to the high solubility and dissolution rates (Fraysse et al., 2009; Riotte et al., 2018a). During transit through shallow soil and saprolite, the water incorporates signatures from Na-plagioclase weathering leading to kaolinite formation and subsequent plant uptake both favouring light ^{28}Si, leaving soil solution heavier in δ^{30}Si in Mule Hole (1.64±0.15‰, Riotte et al., 2018a). However, as observed in Fig. 6a, relationship between δ^{30}Si and DSi in groundwater is not straightforward, due to multiple processes, such as formation and dissolution of secondary minerals, plant

uptake, and adsorption impacting silicon isotopic composition in Berambadi and Mule Hole. This can be contrasted with the study of surface water from Kaveri and Netravathi river basins, where the $\delta^{30}Si$ was positively correlated with DSi, in agreement with what is generally observed in rivers, indicating prominent weathering control of silicon isotopic composition (Sarath et al., 2022). Based on the assumption and normalization procedure based on equation Eq. 2 detailed in section 2.4, we estimate that on average 80±25% of the Si mobilized from the parent gneiss is incorporated into secondary minerals, similar to the estimate by Frings et al. (2016) for global river water and groundwater compilation. We employed two simple conceptual models: Rayleigh distillation and steady state or batch equilibrium system, to understand the evolution of the groundwater silicon isotopic composition due to removal of DSi from the solution Eq. 3 and Eq. 4 (Bouchez et al., 2013; Frings et al., 2015). Interestingly, most of the groundwater samples fit a steady state system with fractionation factors (ε) between -1.0‰ and -2.0‰, which can be contrasted with Rayleigh or mixed behaviour commonly observed in surface waters (Frings et al., 2014, 2016) (Fig 6b). The fractionation factors are consistent with the reported values of ε_{prec} for precipitation of kaolinite type clays (-1‰ to -2‰, Riotte et al., 2018a; Frings et al., 2021) and smectite type clays (-0.1 to -0.7‰, Opfergelt et al., 2012, Frings et al., 2021), which are the dominant clay types in the watershed (Braun et al., 2009). Groundwater receives steady supply of Si from weathering reactions in regolith, a fraction of which is immobilized by precipitation of secondary phases, incorporating a unidirectional kinetic signature (Geilert et al., 2014; Oelze et al., 2015). However, water rock interactions can re-equilibrate precipitated amorphous phases, depending on the surface area of the precipitated phase and the extend of interaction with the groundwater and/or soil solution (Fernandez et al., 2019). In order to attain a steady state behaviour, a dynamic equilibrium must be established through balancing silicon supply to the groundwater and Si removal through precipitation of the secondary phases. Few groundwaters and surface waters fit more to a Rayleigh model in Fig. 6b, including hyporheic piezometers receiving stream water input during wet season in Mule Hole (P1 and P7) and previously reported Kaveri and Netravathi river water signatures (Fig 6b; Sarath et al., 2022). Exceptionally heavy $\delta^{30}Si$ found in an abandoned bore well in Berambadi (3.0 and 3.4‰ respectively for both dry and wet season) shows an intermediate behaviour fitting neither Rayleigh nor steady state model with the chosen fractionation factors (discussed in the section 4.4.4). However, it may be noted that such simple conceptual models, taking into consideration a single process (secondary clay

precipitation) and also a single fractionation factor for the whole watershed, only provides a crude picture of δ^{30}Si distribution in groundwater.

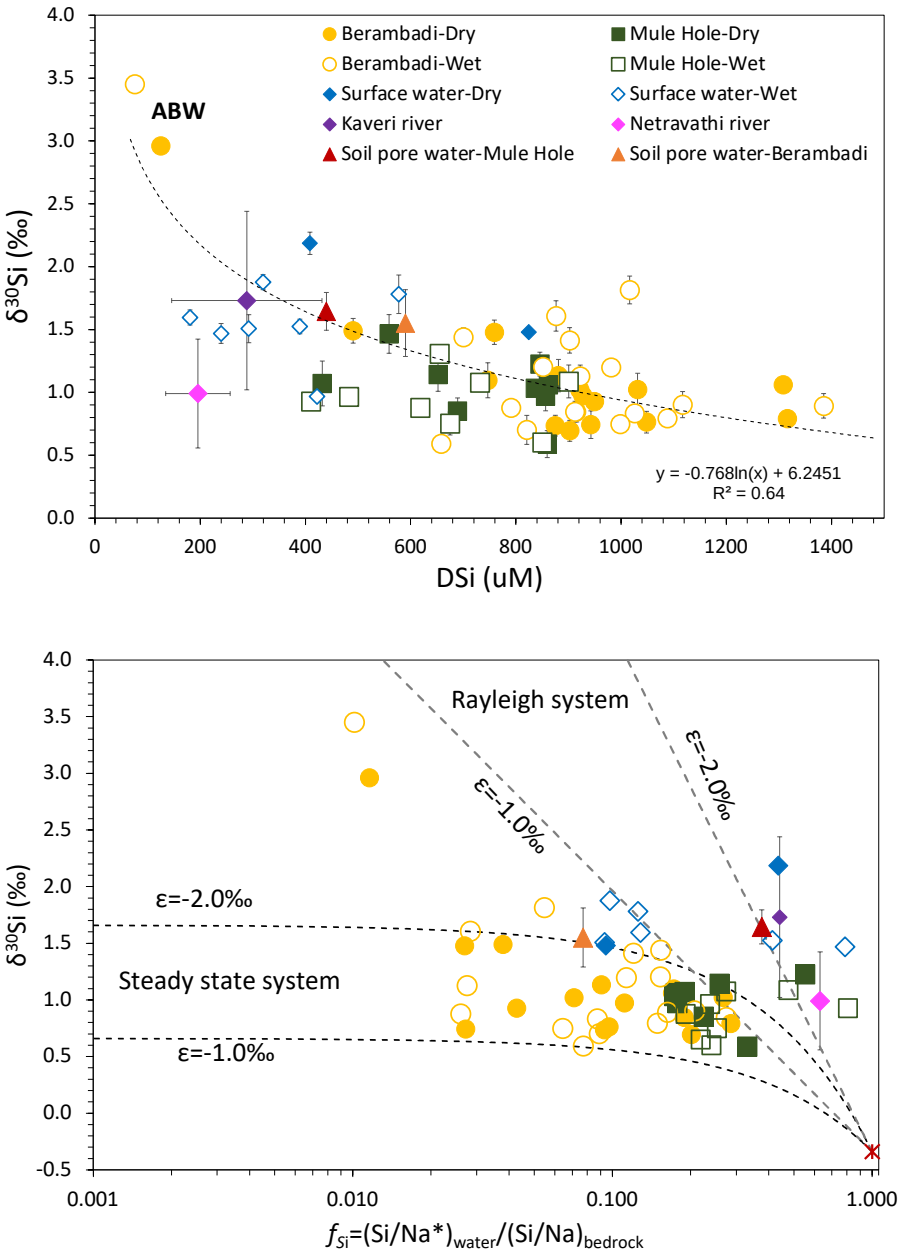

***Figure 6**. The relationship between δ^{30}Si and a) dissolved silicon in groundwater and surface water from Mule Hole and Berambadi, (the error bar indicates 1SD or the variability range when n=2 based on full chemical replicate), b) Evolution of δ^{30}Si with fraction of Si mobilized into dissolved phase (f_{Si}) during weathering (see section 4.4.2 for more details). Dashed and dotted lines represent the evolution of δ^{30}Si expected from Si removal under two model scenarios: i) Rayleigh distillation from a finite Si pool, ii) steady state or open system. The Kaveri and Netravathi data from Sarath et al. (2022).*

Table 3. *The Si and Sr isotope ratio of various endmembers from the present study and from Violette et al 2010a (#) and Riotte 2018a (*), both from the same region. The soil pore water collection for Berambadi was performed earlier in 2015 March.*

Compartments	Location	$\delta^{30}Si$ ‰	$^{87}Sr/^{86}Sr$	Reference
Granitic gneiss	Mule Hole	-0.34±0.08	0.713174	# *
Soil pore water	Berambadi	1.55±0.26 (n=8)	-	Present study
	Mule Hole	1.64±0.15 (n=9)	-	*
Clay fraction	Mule Hole	-1.3±0.03 (n=3)	-	*
Pedogenic Carbonate	Berambadi and Mule Hole	-	0.714469 (n=23)	#
Rainwater	Mule Hole	-	0.713945 (n=8)	#
Fertilizer	Berambadi	-	0.708518 (n=2)	Present study

4.4.3 Evolution of $\delta^{30}Si$ from pore water to groundwater

Given the comparable lithology and climate of Berambadi and Mule Hole, we expect the abiotic weathering processes to be similar but crop harvest can severely disrupt the biological Si feedback loop (Struyf et al., 2010; Keller et al., 2012; Vandevenne et al., 2012). However, as discussed earlier, the groundwater signature is unable to capture any such land cover changes in terms of Si isotopes. $\delta^{30}Si$ values of groundwater in both watersheds were similar and consistently lower than the reported porewater values, with groundwater exhibiting a higher DSi concentration (Table 1, Riotte et al., 2018a, 2018b). Such a pattern in groundwater from both watersheds indicates that soil water undergoes further water-rock interactions as it percolates through the unsaturated zone before reaching groundwater. In Mule Hole, even with average rainfall input of 1100 mm/year, intense evapotranspiration during the percolation up to deep vadose zone limits the groundwater recharge, leading to the disconnection of groundwater with the surface runoff (Ruiz et al., 2010; Marechal et al., 2009). A significant lag in water table response to the precipitation events is also observed in Mule Hole, indicating long vertical travel time through vadose zone, up to 20 years according to the COMFORT model (Riotte et al., 2014b). A longer residence time of water in the unsaturated zone implies that different abiotic as well as biotic processes can affect the transit of Si from the upper soil to the groundwater table in the fractured bedrock. The thick vadose zone also constitutes a major water stock for the deep-rooted deciduous trees in the watershed (Ruiz et al., 2010; Chitra-Tarak et al., 2018). One possible explanation is deep root uptake by deciduous trees, but

it can be discarded here, as plants preferentially take up lighter silicon isotope leading to an enrichment in $\delta^{30}Si$ as well as loss of Si from the soil solution, which is not coherent with a Si source and lower groundwater Si isotopic composition (Linden and Delvaux, 2019). Moreover, this would hold true only in Mule Hole, since deep rooted trees are marginal in the Berambadi watershed. Therefore, we propose that long water-rock interactions in the deeper regolith layers, involving particularly plagioclase, biotite and hornblende weathering with formation of secondary products such as kaolinites and smectites, can explain the observed DSi and isotopic composition of groundwater. This interpretation is also in accordance with steady-state behaviour in groundwater (Fig. 6b), with the Na-plagioclase, hornblende and biotite abundances in parent gneiss (Braun et al., 2009) and from Sr isotopic signatures discussed in section 4.3. In order to estimate the $\delta^{30}Si$ of DSi released by weathering of plagioclase and formation of kaolinite/smectite, we used a simple mass balance (Bouchez et al., 2013);

$$\delta^{30}Si_{released}=\delta^{30}Si_{prim.\ sili.}*fSi_{prim.\ sili.} - \delta^{30}Si_{clay}*fSi_{clay}/(1- fSi_{clay}) \quad \text{(Eq. 5)}$$

Here, we assume Si isotopic composition of primary silicate minerals ($\delta^{30}Si_{prim.\ sili.}$) to be similar to that of the whole gneissic bedrock (-0.34±0.08‰). The $\delta^{30}Si_{clay}$ of kaolinite in Mule Hole is also known (-1.3±0.03‰; Riotte et al., 2018a). However, the $\delta^{30}Si_{clay}$ of smectites was not available for the study region and we opted published $\Delta^{30}Si_{smectite\text{-}bedrock}$ to recalculate $\delta^{30}Si_{smectite,}$ which ranged from -1.05 (volcanic soils of Guadeloupe, Opfergelt et al., 2012) to -0.44 (Central Swiss Alps Frings et al 2021). We assign the fSi_{clay} values to the typical weathering reaction stoichiometry at equilibrium for; i) Na-plagioclase to kaolinite weathering (Eq. 6), ii) biotite to smectite (Eq. 7), and, iv) hornblende to smectite (Eq. 8) (Table S3).

$$2*Na_{0.92}Ca_{0.08}Al_{1.07}Si_{2.93}O_8 + 2H^+ + 9H_2O \rightarrow 1.07Si_2Al_2O_5(OH)_4 + 1.84Na^+ + 0.16Ca^{2+} + 3.72H_4SiO_4 \quad \text{(Eq. 6)}$$

$$1.67*KMg_{1.5}Fe_{1.5}AlSi_3O_{10}(OH)_2 + 6.7H^+ + 3.5H_2O \rightarrow Si_4O_{10}(OH)_2Mg_{0.33}Al_{1.67}Mg_{0.165} + 2Mg^{2+} + 2.5Fe(OH)_3 + 1.01H_4SiO_4 \quad \text{(Eq. 7)}$$

$$1.67*(Ca_{1.76}Na_{0.29}K_{0.07})(Mg_{2.66}Fe_{1.99}Al_{0.33}Ti_{0.11}Mn_{0.09})(Si_{7.21}Al_{0.79})O_{22}(OH)_2 + 18.16H^+ + 3.58H_2O \rightarrow 1.12*Si_4O_{10}(OH)_2Mg_{0.33}Al_{1.67}Mg_{0.165} + 8.29Mg^{2+} + 0.15Mn^{2+} + 0.48Na^+ + 0.12K^+ + 2.93Ca^{2+} + 3.32Fe(OH)_3 + 7.56H_4SiO_4 \quad \text{(Eq. 8)}$$

The estimated $\delta^{30}Si_{released}$ of the DSi produced by plagioclase weathering is estimated using Eq. 5 as 0.21‰. The estimate using $\delta^{30}Si_{smectite}$ of -1.05‰ yield a $\delta^{30}Si_{released}$ of +2.5‰ for biotite to smectite transformation, which cannot account for a lighter $\delta^{30}Si$ for groundwater (Table S3). This can be due to two possibilities, i) the $\Delta^{30}Si_{smectite\text{-}bedrock}$ approximation does hold true for our study site and volcanic soils of Guadeloupe, ii) biotite to smectite transformation plays minor role in groundwater DSi concentration. Using a $\Delta^{30}Si_{smectite\text{-}bedrock}$ value from Frings et al, (2021), we obtain a $\delta^{30}Si_{released}$ of 0.06‰ and -0.24 for biotite to smectite and hornblende to smectite respectively (Table S3). From these signatures, we can estimate the fraction of Si potentially released from each primary mineral weathering to groundwater DSi using a simple isotopic balance:

$$f_{released}*\delta^{30}Si_{released}+(1- f_{released})*\delta^{30}Si_{porewater}= \delta^{30}Si_{groundwater} \quad \text{(Eq. 9)}$$

In Mule Hole, considering that the $\delta^{30}Si_{groundwater}$ of 0.98±0.2‰ results from a mixing between an infiltrating soil solution at 1.64±0.15‰ (n=9) and $\delta^{30}Si_{released}$ from primary silicates weathering, the primary silicate weathering would contribute from 34 to 46% of the total DSi (and the rest is coming from of the upper soil porewater; Table S3). We must be cautious here regarding possible deep root uptake, which is not yet quantified and could take up DSi from soil solution as well as shallow groundwaters (Ding et al., 2008; Frings et al., 2021). In Berambadi, such calculations are complicated by the fact that groundwater is routinely used for crop irrigation, which can undergo subsequent Si uptake in the shallow soil depending on crop type. We measured $\delta^{30}Si$ of soil porewater from Berambadi under cultivation of cabbage and garlic which was 1.55±0.25‰ (n=8), i.e. significantly lighter than reported soil water values from paddy fields irrigated with groundwater in similar gneiss bedrock complex (ranged from 2.1 to 3.3‰, Riotte et al., 2018b). Riotte et al, (2018b) attributed such heavy $\delta^{30}Si$ values in soil solution and stagnant water in paddy fields to active DSi uptake by rice with a fractionation factor close to -1‰. Unlike Mule Hole, the soil porewater in Berambadi fits the steady state model with low f_{Si} values, indicative of groundwater origin through multiple cycles of irrigation and return flow (Fig. 6b). Using similar $\delta^{30}Si_{released}$ from primary silicates weathering, and average groundwater and porewater values from Berambadi in Equation Eq. 9, we estimate an average Si contribution ranging from 25 to 34% resulting from deeper layers of regolith. Such deeper silicate weathering contributions are enhanced by greater extend of water-rock interaction in unsaturated zone, which is also evident from the higher DSi

concentration in deeper groundwater (1285±163 μM) compared to shallow groundwater (884±275 μM) in Berambadi and Mule Hole (710±150 μM) (Table 2). Overall, given the consistently low $\delta^{30}Si$ in groundwater compared to soil waters in both Berambadi and Mule Hole reflects that the signatures of weathering, adsorption and biotic uptake in the shallow soil horizons is partly overwritten and homogenized by the weathering Si fluxes in the deep critical zone.

4.4.4. Deep vs. shallow groundwater processes

In shallow regolith, groundwater is susceptible to be influenced by local recharge which includes rainfall, regolith weathering processes which are governed by local lithology and plant uptake (Opfergelt and Delmelle, 2012). In both Mule Hole and Berambadi, $\delta^{30}Si$ shows more variability in the shallow groundwaters (<10m), from 0.5 to 3.5‰, arising from multiple shallow aquifer processes controlling the isotopic composition (Fig.7). Shallow groundwaters in Mule Hole (P1 and P7) located close to the stream are ~0.4% heavier than the rest of the groundwater. Shallow regolith layers within hyporheic zones are recharged by stream water during flow period and indicate surface water signatures. In Berambadi, ABW is a shallow abandoned borewell (water level at 6m) in a field (maize at the time of sampling) which exhibits both the highest $\delta^{30}Si$ during both seasons, and lowest DSi concentration. Such consistent peculiar behaviour can indicate a primary control of Si plant uptake in the recharge water, comparable with stagnant surface water and porewater values in agricultural lands reported earlier (Vandevenne et al 2015; Riotte et al., 2018b). We can estimate the fractionation factor ($^{30}\varepsilon$) for plant uptake assuming that groundwater composition results from an excess DSi uptake from shallow soil solution. The fraction of Si remaining can be estimated by as

$$f_{Si(ABW)} = DSi_{ABW}/DSi_{soil\ solution} \quad \text{(Eq. 10)}$$

Assuming plant uptake follows a Rayleigh, model and applying equation Eq. 3, we can obtain a $^{30}\varepsilon$ value of -0.84‰ for dry season and -0.87‰ for wet season, within the reported fractionation factors of crop uptake (Sun et al., 2017; Frick et al., 2020; Frings et al., 2021). Thus, ABW represents an isolated or stratified aquifer with negligible lateral flow, which has accumulated signatures from soil solution impacted by plant uptake through irrigation cycles and has not been overwritten by local weathering. However, the exact reason why the signatures of plant uptake from shallow soil layers dominates ABW remains unclear.

On the other hand, deep groundwaters (>10 m), with water table at deeper layers of saprolite and fracture/hard bedrock zone exhibit a higher DSi (~1300 µM in Berambadi) and relatively lighter with restricted range of δ^{30}Si (0.86±0.17‰), which can be indicative of equilibration of water-rock interaction due to long residence time in deep aquifers. Higher residence time of the water in the deeper regolith layers lead to dominant control of deep weathering Si fluxes, diminishing the impact from the overlaying local heterogeneity and processes and a higher Si input to groundwater (Calmels et al., 2011). Such a pattern in both watersheds is coherent with our earlier interpretation of plagioclase weathering in deep regolith layers controlling the δ^{30}Si of groundwater. Previous works in groundwater δ^{30}Si also noted an evolution towards lighter silicon isotopic composition in deeper and older groundwater, even below the bedrock values, which they attributed to shift from primary to secondary Si sources such as clays and silcretes (Georg et al., 2009a, 2009b, Strandmann et al., 2014). However, we note that such extreme cases of dissolution of shift from primary to secondary sources of Si is recorded in groundwater with a depth greater than 100 m. Future work could seek to validate such a trend by extending the sampling to deep fissured aquifers, as the factors controlling such shifts in weathering pattern remain unclear.

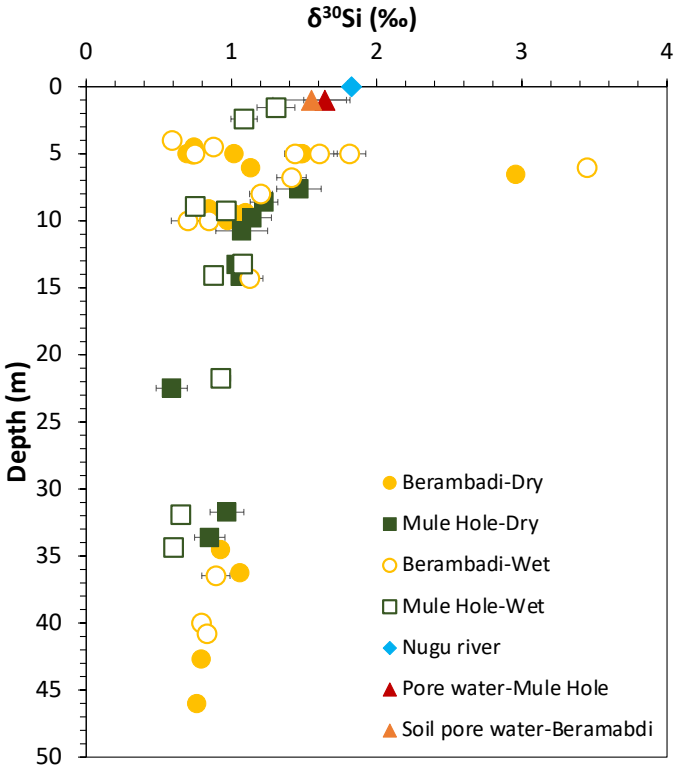

Figure 7. *Variations in a) δ^{30}Si in groundwater from Mule Hole and Berambadi collected from different depths (depth to the water table). Also plotted are the compositions of the Nugu hole river, part of Kabini basin, (blue filled diamond) and soil porewater data from Mule Hole (Riotte et al. 2018a) and Berambadi (present study) (assumed average depth of 1m).*

5. Conclusion

We assessed the impact of land use changes on silicon isotopic composition of groundwater by comparing two contrasting watersheds, forested Mule Hole watershed and intensely cultivated Berambadi watershed. Contrary to dissolved Si concentration, $\delta^{30}Si$ signatures of groundwater indicates no significant impact of land use changes, despite continuous cultivation for more than 30 years in Berambadi. Moreover, groundwater also exhibits no seasonal differences in terms of $\delta^{30}Si$ and $^{87}Sr/^{86}Sr$, indicating that immediate monsoonal precipitation imparts very little influence on the groundwater composition. Silicate weathering and formation of secondary minerals exerts dominant control over the silicon isotopic composition of groundwater, fitting the steady state model proposed for weathering zone. Apart from weathering controls, shallow aquifers are impacted by plant uptake, adsorption/desorption of oxyhydroxides and dissolution of amorphous and secondary phases and exhibits variable $\delta^{30}Si$. $\delta^{30}Si$ values of groundwater were consistently lighter than the soil pore water composition (1.6±0.2‰), reflecting contribution from deep weathering Si fluxes homogenizing the Si isotopic composition. Overall, weathering of silicate minerals and formation of kaolinite and smectite type clay minerals in deeper layers of regolith contributes to 34 to 46% of total Si flux in the forested Mule Hole and 25 to 34% in Berambadi under intensive agriculture. The much higher variability in Si concentration and Si isotopes is reflected by higher errors in our Si budget in Berambadi compared to Mule Hole. This results from high spatio-temporal variability in agricultural practices, which was also evident from nitrate concentrations. Groundwater support baseflow of rivers, especially during dry season, with a chemical composition and isotopic signature very different from shallow surface and subsurface runoff. Such different isotopic signature could be used in future studies to track the fate of groundwater DSi with surface water interaction downstream. Our results highlight the importance of deep regolith weathering in determining groundwater silicon isotopic composition, overwriting the signatures of aboveground land use, human alterations and shallow regolith processes.

Acknowledgments

The work is funded by CEFIPRA-IFCPAR support (NUNDERGROUND, project #5907). We acknowledge SNO M-TROPICS for providing necessary support for field campaign and sampling. Isotopic composition of rainwater from Mule Hole were supported by the French programme INSU EC2CO. The authors thank Benjamin Baud for the water sampling during field work, Pierre Burckel and Irina Djouraev for the help with ICPMS to check for Si chemistry and the ALYSES facility (IRD-SU). We thank Julien Amelin for providing the sampling map for Berambadi. SPK thank IRD-Campus France for providing Ph.D. scholarship and constant support to carry out the work. SPK also thanks Sourav Ganguly for helping with Sr isotope analysis in IISc. The authors would like to thank M. Benrahmoune (LOCEAN-IPSL) for help in sample processing and clean lab management.

Supplementary tables

Table S1. *Analytical settings for the measurement of Si isotopic composition in MC-ICPMS.*

Parameters	Settings
Resolution	Medium
Forward Power	1100-1300 W
Accelerating voltage	10 kV
Plasma Mode	Dry plasma
Plasma Ar Flow Rate	16 L/min
Auxiliary Ar Flow Rate	0.8-1.9 L/min
Ar carrier gas flow rate	0.8-0.95 L/min
Cones type	Nickel X-Skimmer cone + Jet Ni-Sample cone
Desolvator	Apex Ω / Apex Ω HF (ESI)
Nebulizer	Apex MicroFlow PFA-ST nebulizer 100µl/min
Running Concentrations	Si = 1-2 ppm, Mg = 0.5-1 ppm
Sensitivity	10-35 V/ppm
Blank Level	≤ 1% signal
^{30}Si Interference	≤ 100 mV

Table S2. *The H and O isotopic composition of rainwater samples from the Mule Hole region collected and analyzed as a part of previous field campaign supported by INSU EC2CO.*

ID	Date	Location	Rainfall	$\delta^{18}O$	$\delta^{2}H$	d-excess
			mm	‰	‰	‰
886	15-04-05	Mule Hole	23.2	-0.02	14.5	14.6
899	28-07-05	Mule Hole	10.6	-1.50	-5.1	6.8
897	30-07-05	Mule Hole	26.4	-1.78	-4.2	10.1
883	02-08-05	Mule Hole	7.6	-0.90	-6.2	1.0
896	03-08-05	Mule Hole	7.4	-0.92	3.5	10.9
902	04-08-05	Mule Hole	9.6	-0.63	4.0	9.0
900	07-10-05	Mule Hole	21	-1.98	-5.0	10.8
893	12-10-05	Mule Hole	10.5	-6.71	-41.9	11.8
901	14-10-05	Mule Hole	33.5	-13.03	-93.0	11.3
892	20-10-05	Mule Hole	2.4	-0.24	11.3	13.2
884	21-10-05	Mule Hole	43.46	-4.17	-28.0	5.4
894	05-03-06	Mule Hole	16.5	-11.14	-77.5	11.7
898	07-03-06	Mule Hole	5.2	-7.36	-48.5	10.4
889	10-03-06	Mule Hole	14.5	-6.82	-42.3	12.2
887	31-03-06	Mule Hole	12.5	-2.71	-10.7	11.0
895	14-04-06	Mule Hole	13	-0.81	6.7	13.2
888	16-04-06	Mule Hole	6.2	-1.62	-0.8	12.1
904	03-05-06	Mule Hole	18	0.25	7.1	5.1
903	17-05-06	Mule Hole	18.5	0.91	13.5	6.2
890	19-05-06	Mule Hole	26.5	-0.79	5.2	11.5
891	28-05-06	Mule Hole	22.4	-6.19	-36.7	12.8
885	29-05-06	Mule Hole	34.6	-9.14	-64.3	8.8
905	30-05-06	Mule Hole	11.4	-5.74	-34.7	11.2

Table S3. *The weathering reaction that can contribute to deep regolith Si fluxes and the associated $\delta^{30}Si_{released}$. The percentage contribution for Mule Hole and Berambadi is from a simple isotopic mass balance described in section 4.4.3 ('$' denote value from Riotte et al., 2018a, '*' from Opfergelt et al., 2012 and '#' from Frings et al., 2021.*

Weathering reaction	**Plagioclase to kaolinite**	**Biotite to smectite**		**Hornblende to smectite**	
$f Si_{clay}$	0.36	0.8		0.37	
$\delta^{30}Si_{clay}$	-1‰$^{\$}$	-1‰*	-0.4‰$^{\#}$	-1‰*	-0.4‰$^{\#}$
$\delta^{30}Si_{released}$	0.21‰	2.5‰	0.06‰	-0.08‰	-0.28‰
% weathering (Mule Hole)	46%	-	42%	42%	34%
% weathering (Berambadi)	34%	-	31%	31%	25%

Supplementary figures

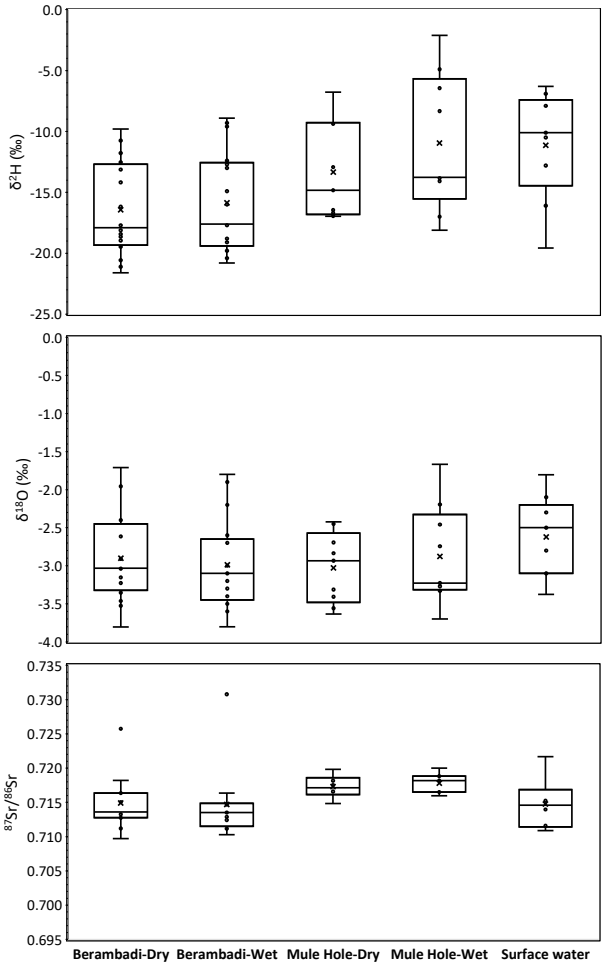

Figure S1. *Box plots of $^{87}Sr/^{86}Sr$, $\delta^{18}O$ and $\delta^{2}H$ of groundwater and surface water from Mule Hole and Berambadi plotted for both dry and wet season.*

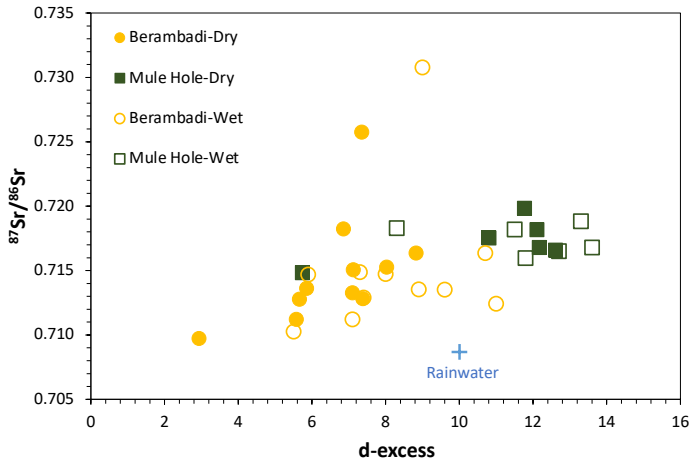

Figure S2. *Plot between $^{87}Sr/^{86}Sr$ and d-excess (d-excess=$\delta^{2}H$ - 8*$\delta^{18}O$) plotted for Mule Hole and Berambadi. The rainwater data is from Pearce et al. (2015).*

III. Biogeochemical cycling in tropical Godavari estuary and groundwater

IIIa. Spatio-temporal dynamics of silicon cycling in tropical monsoonal Godavari estuary and coastal groundwater

IIIb. Calcium and strontium transport across the land-ocean interface and implications on coastal groundwater

IIIa. Spatio-temporal dynamics of silicon cycling in tropical monsoonal Godavari estuary and coastal groundwater.

Sarath Pullyottum Kavil, Jean Riotte, Ramananda Chakrabarti, Arnaud Dapoigny, V.V.S.S Sarma, Damien Cardinal, *et al.*

Article in preparation

Abstract

Riverine supply is the primary source of dissolved silicon (DSi) to the ocean and is crucial in determining diatom productivity in coastal regions. The objective of this study is to identify the major drivers of Si cycling in the Godavari estuary, and their implications for Si delivery to the Bay of Bengal (BoB). For this we analysed the DSi and δ^{30}Si composition from the Godavari estuary and adjacent groundwater during dry (pre-monsoon) and wet (monsoon) seasons. The DSi and δ^{30}Si exhibit non-conservative mixing during the dry season, with a significant removal of Si (65±6%) and an enrichment in δ^{30}Si (1.0±0.4‰) compared to the theoretical mixing line. Based on correlation with diatom marker pigment, fucoxanthin, and Scanning Electron Microscope (SEM) observation of diatoms in suspended matter we confirmed that the diatom uptake imparts major control over the δ^{30}Si composition of the estuary during dry season. River flow retention by dams limits the discharge during dry season, forming a stable water column with high residence time, favouring diatom growth. On the other hand, monsoonal precipitation and the opening of dam gates lead to high river water influx during the wet season, resulting in low salinity (<0.2) throughout the estuary. High suspended matter (175±50 mg/l) in the water column limits diatom growth during the wet season. During wet period, the δ^{30}Si signature in the estuary reflect the silicate weathering and formation of secondary clays that occurred in the river basin. Overall, the Godavari river supplies 21.5±0.3 GmolSi/yr with a weighted δ^{30}Si isotopic composition of 0.92±0.2‰ to the Bay of Bengal. Almost 3.4±0.4 GmolSi/yr (~15%) is sequestered within estuary as biogenic silica by diatoms during low discharge periods. The groundwater exhibits no seasonal variability in DSi and δ^{30}Si with an average of 570±160 µM and 0.99±0.82‰ respectively. The Si cycling in groundwater is primarily controlled by weathering and formation of secondary clays such as smectites, with minor impact from plant uptake by agriculture and adsorption onto Fe oxyhydroxides. Based on the previous estimate of SGD rates, annual groundwater discharge into the Godavari estuary accounts for 3.5% of the riverine Si flux to the Bay of Bengal.

Keywords: δ^{30}Si, dissolved silicon, diatoms, riverine Si supply, submarine groundwater discharge.

1. Introduction

Rivers transport essential nutrients released during terrestrial silicate weathering as dissolved and particulate load into the ocean (Chester and Jickells, 2012). Continental silicate weathering and land-to-ocean silicon flux are of great interest since, i) it is a major sink for atmospheric CO_2 and regulates the long-term climate of the Earth through a negative feedback loop (Walker, 1981, Berner et al., 1983) and ii) dissolved silicon is an essential macronutrient for marine diatoms which accounts for 40% of the oceanic primary productivity (Field et al., 1998, Tréguer et al., 2018). Terrestrial Si fluxes through rivers contribute almost 8.1±2 Tmol Si/yr, forming 55% of the annual total dissolved silicon (DSi) flux to the global coastal ocean (Tréguer et al. 2021). Estuary serves as an interface between terrestrial and marine systems, where the solutes and reactive solids can undergo significant biogeochemical modifications (Meybeck and Vorosmarty, 2005, Bianchi, 2007), and have been often referred to as the estuarine filter for the geochemical fluxes along the land-to-ocean continuum (Meybeck and Vörösmarty, 2005). Indeed, before entering the oceanic systems, Si passes through fluvial filters such as estuaries, wetlands, and marshes, where biogeochemical alterations and sedimentation can modify both the elemental fluxes and isotopic composition (Weiss et al., 2015, Zhang et al., 2020). Estuaries and continental shelf regions are highly productive and can act as a permanent or at least transient storage system for Si reaching the ocean (Struyf et al., 2007, Carey and Fulweiler, 2014, Zhang et al., 2015). Through biogenic silica (BSi) production by diatoms, burial, and subsequent formation of authigenic clay minerals (referred to as 'reverse weathering'), deltaic and estuarine environments can form a significant sink for DSi transported by rivers (Michalopoulos & Aller 2004; Presti & Michalopoulos 2008, Tréguer et al., 2013). Groundwater-derived solute fluxes are now identified as a major source of nutrients to the coastal ocean, which can significantly enhance the productivity and impact the water and elemental budgets of the global ocean (Taniguchi et al 2002; Moore et al 2010). Recent estimates suggest that submarine groundwater-derived Si fluxes can account for 4 to 25% of the total annual Si flux to the ocean (Cho et al., 2018, Rahman et al., 2019, Tréguer et al., 2021). In addition to these natural processes being poorly constrained, anthropogenic activities disturb the natural silicon cycle: cultivation and Si export through food crops can reduce DSi fluxes from land to ocean (Struyf et al., 2010, Carey and Fulweiler, 2012) as well as, dams and reservoirs that can alter the water, sediment, and nutrient discharge to the sea, and are known to reduce the Si flux and disrupt the Si: N and Si:P ratio in estuaries and coastal sea (Humborg et al., 1997, Garnier et al., 2010, Maavara et al 2015).

Indian estuaries exhibit spatial and temporal variability in biogeochemical parameters, with Si cycling driven by land use, weathering and lithogenic supply during the wet season and dominated by diatom uptake during the dry season (Mangalaa et al., 2017, Bharathi et al., 2022). In the present work, we evaluated the spatial and temporal variability of the elemental and isotopic composition of Godavari estuary and coastal groundwater to understand the impacts of estuarine processes on marine isotope budgets. Godavari estuary-the largest monsoonal river in peninsular India, exhibits significant intra-annual variability in nutrient concentrations (Sarma et al., 2010), seasonal phytoplankton blooms (Acharyya et al., 2012), and significant submarine groundwater discharge (Rengarajan and Sarma, 2015, Damodararao and Singh, 2022). The riverine discharge to Godavari estuary is regulated by both seasonal monsoon precipitation and dams, providing a suitable setting to understand the impact of discharge dynamics on estuarine biogeochemistry (Sarma et al., 2010, Acharyya et al., 2012). Recently, submarine groundwater discharge through the major estuaries on the east coast of India was estimated to be 11000 m^3/s (Damodararao and Singh, 2022). The Si fluxes by groundwater discharge to the Bay of Bengal was estimated to be almost 40% of the Ganga-Brahmaputra Si flux, which may modify the silicon isotopic signature of the rivers up to 0.4‰ (Georg et al 2009b). However, the submarine groundwater fluxes are poorly constrained and exhibit significant spatial and temporal variability (Rengarajan and Sarma 2015, Cho et al 2018). Understanding the temporal variability associated with groundwater and riverine fluxes is essential to interpret the past changes in elemental biogeochemical cycling. Through the study of the Godavari estuary, we aim to understand i) the seasonal variability and associated drivers of Si cycling in Godavari estuary and coastal groundwater, ii) the impact of variability in Si fluxes and isotopic composition of Godavari river to the Bay of Bengal.

2. Materials and Methods

2.1. Godavari estuary

Godavari is the second largest river and largest peninsular river in India, originating from the Western Ghats mountain ranges and flowing eastwards through the Indian peninsular shield. The river drains successively Deccan basalts (48% of the drainage area), peninsular gneiss (39%), and sedimentary rocks (11%) before discharging into the Bay of Bengal (Biksham and Subramanian 1988). Climate evolves from semi-arid in the rain shadow region of Western Ghats to sub-humid in the lower basin. The river water levels are largely monsoon-driven: the basin receives rainfall from both Southwest and Northeast monsoons, with the majority of the

rainfall occurring from July to September (Sarma et al., 2010). Godavari estuarine system covers an area of 330 km^2. The river flow to the estuary is regulated by a century-old dam in Dowleiswaram (~80 km upstream of the river mouth) and after the dam the river splits into two branches, Gautami and Vasista Godavari, both flow towards the east to the Bay of Bengal (Fig. 1). The annual discharge of Godavari river is 111 km^3, with 93-96% of the annual flow occurring during monsoon season (Gupta et al., 1997, Mangalaa et al 2017). Based on the discharge patterns driven by monsoon and opening and closing of the dams, Sarma et al. (2010) classified annual discharge into three main periods: i) peak flow (typically>2000 m^3/s) between June and September, ii) moderate discharge (between 0 and 2000 m^3/s) from October to December and iii) limited or no discharge when the dam is closed from January to May. The tides in the estuary are semi-diurnal in nature with an amplitude of 1.5 m, and an average current speed of 1-2 m/s (Acharyya et al., 2012). Estuary has an average depth and width of 8 m and 1200 m respectively (Sridevi et al., 2015). The deltaic plains surrounding the estuary region are intensely cultivated, dominantly by rice and rain-dependent crops, with extensive fertilizer application.

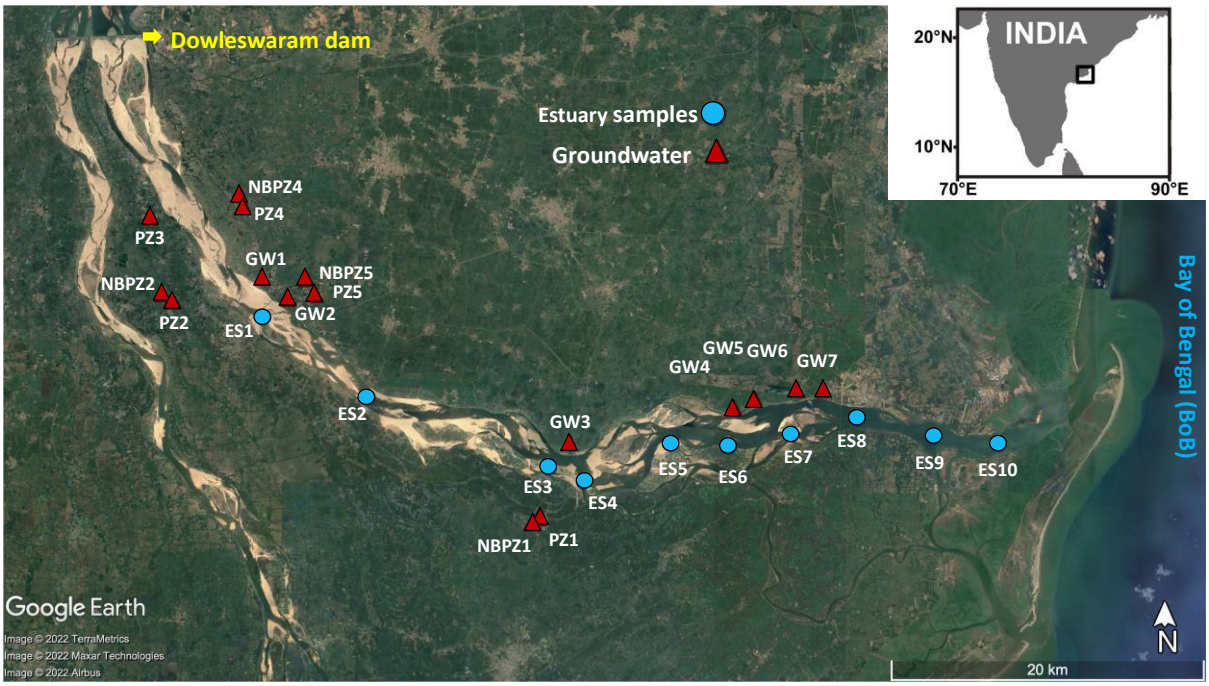

Figure 1. *Google Earth image of Godavari estuary region with sampling locations marked on the Gautami Godavari branch. The estuary samples are marked as blue circles and the groundwaters as red triangles, the location of the Dowleiswaram dam and Bay of Bengal is also marked in the figure (Google Earth version 6, 2022, Godavari).*

2.2. Sampling

Estuary samples were collected from ten locations in the Gautami branch of the Godavari river, downstream of the damming site during March (dry season) and August (wet season) 2019. Sampling was carried out from both boat and direct sampling from the river using a 5 L Niskin bottle connected to a plastic rope. Surface and bottom water samples were collected whenever possible from the same location. Groundwater samples were collected from borewells and handpumps at seven locations adjacent to the estuary on the northern bank during both March and August. We collected nine additional groundwater from piezometers and handpumps exclusively during August (Fig. 1, Table 1). Temperature, pH, conductivity, and salinity (for estuary) were measured on-site using portable sensors (CTD; SBE-19plus, Sea-Bird Electronics, USA). The error in salinity and temperature measurement was 0.001 and 0.001 ^{o}C respectively. Groundwater depth for open wells and borewells was estimated as depth below ground level using a skinny dipper device and the depth for hand pumps was assumed to be 5m. Almost 100mL of water samples were filtered through 0.4 µm SUPOR PES filters and stored. The chlorophyll-*a* and fucoxanthin concentrations were measured for estuary samples for both seasons. The details of sampling, storage and analysis for chlorophyll and pigment analysis were already published elsewhere (methods detailed in Roy et al., 2015). Scanning electron microscope (SEM, EVO LS15, ZEISS) observations were made on selected samples, with suspended matter filtrate available, at ALYSES facility (IRD-SU), IRD Bondy.

2.3. Elemental analysis

The concentrations of major cations (Na, K, Mg, Ca) were measured by quadrupole inductively coupled plasma mass spectrometry (ICPMS Agilent 7500) at IRD, at Alysés analytical platform (IRD-Sorbonne Université, Bondy, France) and ICPMS (Thermo Scientific X-Series II) at CEaS, IISc. Trace elemental concentrations (Al, Fe, Mn) were determined by ICPMS (7500 Agilent) at Alysés analytical platform (IRD-Sorbonne Université, Bondy, France). The accuracy of the cation analyses was checked using certified river water reference material, SLRS-6 (NRC-CNRC, Canada) and rock standard AGV-2 (Guano-valley Andesite), and the obtained precision was better than 10%. Major anion concentrations were measured with an Ion Chromatograph (Metrohm COMPACT 861) at the Indo-Fench Cell for Water Sciences (IFCWS, IISc, Bangalore, India). The accuracy of measurements was monitored using multiple certified reference materials (AnionWS, ION-96.4, ION 915, SUPER-05 and BIG MOOSE

02). The saturation indices were estimated using PHREEQC software with llnl.dat thermodynamic database (Parkhurst and Appelo, 1999).

2.4. DSi and Si isotope analyses

Dissolved silicon concentration (DSi) was measured by spectrophotometer following the Grasshoff et al. (1999) protocol. Analytical quality was assessed using certified reference material, PERADE 09 (supplied by Environment Canada, lot no:0314, with DSi = 110.0±6.8 µM), during each measurement and mean reproducibility was 109.9±3 µM (n=25). We followed a slightly modified two-step pre-concentration method adapted from MAGIC-MAGnesium Co-precipitation technique (Karl and Tien, 1992; Reynolds, 2006; Hughes et al., 2011). To an initial volume of 10 ml of groundwater and surface water samples, we added 0.5 ml of $MgCl_2$ solution to match the seawater Mg concentration and were treated with 2% (v/v) of 1 M NaOH and was shaken and kept undisturbed overnight. The brucite ($Mg(OH)_2$) formed at high pH scavenges Si which gets adsorbed onto precipitated brucite. The supernatant from the first step was again subjected to second addition of 1% NaOH following, and the precipitate was recovered by centrifugation after 1-2 hrs. Both brucite precipitates were also re-dissolved with 1M HCl and merged. The DSi concentration of the supernatant was analyzed by spectrophotometer (Grasshoff et al., 1999) and found negligible (on average <2%), confirming that all the Si was adsorbed onto the brucite precipitate.

Separation of Si from other cations was carried out using cation exchange resin (BioRad DOWEX 50W-X12, 200 to 400 mesh, in H+ form) following the procedure of Georg et al. (2006). After the purification process, an aliquot was analyzed for major elements analysis (Na, Mg, Ca, K) by ICP-MS (Agilent 7500a) to ensure that the Si/X (Where X= Na, K, Ca or Mg) weight ratio is always >50 to minimize the matrix effects in the plasma. The organic matrix is removed by treatment with 50 µL of 30% H_2O_2 since it has been shown to potentially induce a matrix bias during MC-ICP-MS analyses (Hughes et al., 2011). Analyses performed on a series of 35 groundwater and surface water samples, shows that the preconcentration and H_2O_2 treatment increased the DSi/DOC ratio from 18 to 7000 times, with DSi/DOC ratio > 10 in the final aliquot (Annexe 2). This indicates <0.2‰ shift in Si isotope ratio from isotopic mass bias due to DOC matrix (Hughes et al., 2011). The possible remaining potential matrix effect resulting mainly from Cl^-, NO^-_3 and SO_4^{2-} was corrected by the artificial doping of anions (Merck, Suprapur grade H_2SO_4, HNO_3 and HCl) in all the samples and standards (Hughes et al., 2011). The measurements were performed on MC-ICP-MS (Thermo Neptune+, LSCE-

IPSL, Gif-sur-Yvette) in dry plasma mode with Mg doping as described by Closset et al. (2016). Samples were injected into the plasma with an ApexΩ HF desolvating nebulization system connected with a PFA nebulizer (100 µL/min uptake rate) and without additional gas. The $\delta^{30}Si$ values were expressed as the permil deviation of the $^{30}Si/^{28}Si$ ratio from the quartz standard NBS28 (RM8546), expressed as

$$\delta^{30}Si_{sample} = [(^{30}Si/^{28}Si)_{sample}/(^{30}Si/^{28}Si)_{NBS28}-1] *1000 \quad E(1)$$

Blank levels were below 1% of the main signal and were subtracted from each sample and standard analysis. All measurements were carried out in a matrix composed of 0.5 M HNO_3, 0.5 M HCl, 1 mM H_2SO_4 and in medium-resolution mode ($m/\Delta m > 6000$) to optimize the separation of ^{30}Si peak and $^{14}N^{16}O$ interference and were performed on the interference-free left side of the peak (Abraham et al., 2008). The $\delta^{29}Si$ and $\delta^{30}Si$ values were compared to the mass-dependent fractionation line and samples falling outside of its analytical error were excluded from the final dataset. Typical analytical conditions are provided in Table S1(Chapter II). Laboratory protocol has been intercalibrated for seawater as part as the GEOTRACES intercalibration exercise generated over the entire procedure (Grasse et al., 2017). The analytical precision and accuracy were monitored by the long-term measurements of secondary reference material diatomite ($\delta^{30}Si$ = 1.26‰, Reynolds et al., 2007) indicated an average precision and a long-term analytical reproducibility on $\delta^{30}Si$ values of 1.19±0.18‰ (2SD, n=100). Diatomite solutions processed with MAGIC give average $\delta^{30}Si$ values of 1.07±0.11‰ (2SD, n=12) which is slightly lighter than unprocessed diatomite, but the difference remains within our analytical reproducibility. All samples measured in the present study are chemically or analytically replicated at least once (average variability of 0.05±0.15), and 9 samples were triplicated with an average 2SD of ±0.20‰.

3. Results

The results of all the chemical and isotopic measurements for the Godavari estuary and groundwater is displayed in Table 1.

Table1. *The results from various chemical and isotopic measurements estuary and Groundwater during dry and wet season.*

	Feature	Salinity	pH	TSM mg/l	Fucoxanthin ug/l	Chl a mg/m^3	DSi µM	δ^{30}Si ‰	1SD ‰	Na µM	K µM	Ca µM	Mg µM
Godavari estuary- *Dry season (March 2019)*													
ES1	Surface	0.4	7.48	5.9	1.443	20.8	276.3	1.88	0.1	3234	155	817	1046
ES2	Surface	0.9	7.64	14.5	0.167	5.7	256.4	1.08	0.0	12475	272	1065	1686
ES3	Surface	9.3	7.24	28.1	0.068	1.2	75.8	1.69	0.1	139888	3171	4129	15935
ES3	Bottom	9.9	7.31	9.7	0.267	2.8	65.5	1.77	0.0	159419	3573	4384	18177
ES4	Surface	11.7	7.36	10.0	0.079	0.3	63.0	1.77	0.0	162986	3622	4440	18383
ES4	Bottom	11.7	7.39	4.8	0.095	1.5	61.0	1.79	0.1	169684	3790	4533	19214
ES5	Surface	20.3	7.43	8.5	1.152	7.0	38.2	2.20	0.1	278167	6274	6576	31952
ES5	Bottom	20.2	7.41	10.4	1.564	9.3	38.8	-	-	277819	6348	6654	31816
ES6	Surface	24.7	7.28	12.5	5.010	21.5	18.8	2.29	0.1	344414	7704	7864	39630
ES7	Surface	25.5	7.33	11.2	2.265	12.9	16.4	2.44	0.1	345458	7727	8038	39918
ES7	Bottom	27.3	7.45	20.2	4.066	20.7	13.0	2.65	0.2	359290	7988	8148	41638
ES8	Surface	27.3	7.51	32.1	1.745	1.1	7.3	-	-	371948	8381	8540	43036
ES8	Bottom	28.0	7.50	42.6	1.874	6.8	7.3	2.22	0.1	374688	8361	8549	43366
ES9	Surface	28.4	7.71	32.4	2.394	17.0	6.7	2.45	0.1	383910	8581	8844	44518
ES9	Bottom	28.7	7.74	44.0	2.694	14.3	6.1	2.50	0.1	392696	8783	9002	44970
ES10	Surface	29.6	7.61	28.8	1.668	12.9	6.1	3.03	0.0	396959	8801	8975	45094
ES10	Bottom	29.6	7.53	70.0	1.525	16.0	5.5	2.68	0.1	400874	8957	9296	46040
Groundwater- *Dry season (March 2019)*													
GW1	Open Well	3.3	6.90	-	-	-	501	0.71	0.0	4243	20	1283	1478
GW2	Borewell	23	6.97	-	-	-	586	0.42	0.0	3185	76	1112	1632
GW3	Open Well	4	7.02	-	-	-	847	1.07	0.0	1924	1010	1392	549
GW4	Open Well	2	7.11	-	-	-	474	1.18	0.0	20880	1837	504	5296
GW5	Handpump	5	6.93	-	-	-	439	0.38	0.1	21023	253	250	549
GW7	Open Well	3.3	6.92	-	-	-	479	1.01	0.0	7425	752	1436	1678
GW6	Open Well	-	7.02	-	-	-	438	1.06	0.0	1598	76	384	1087
Godavari estuary-*Wet season (August 2019)*													
ES1	Surface	0.181	-	150	0.315	4.04	202.8	1.14	0.1	386.7	61.0	488.6	206.9
ES2	Surface	0.087	6.7	54	0.154	6.10	203.9	1.02	0.0	350.6	54.8	472.6	199.3
ES3	Surface	0.014	6.6	212	0.088	2.14	199.5	0.86	0.0	293.6	50.0	425.0	174.9
ES3	Bottom	0.075	6.6	-	0.730	4.10	199.0	0.72	0.1	267.4	48.6	408.2	168.9
ES4	Surface	0.014	6.8	148	0.459	3.10	200.3	0.78	0.0	265.5	47.3	407.2	168.0
ES5	Surface	0.014	6.6	236	0.079	2.30	198.5	0.81	0.0	295.8	50.1	425.0	175.6
ES6	Surface	0.014	6.8	180	0.126	3.11	197.2	0.81	0.0	291.6	47.9	401.6	168.5
ES7	Surface	0.014	6.7	168	0.058	-	162.1	0.81	0.2	292.7	48.5	406.1	170.8
ES7	Surface	0.077	-	-	-	-	156.4	0.85	0.0	333.8	50.9	426.6	180.4
ES8	Surface	0.014	-	190	0.182	1.34	152.8	0.81	0.0	337.8	50.9	433.6	183.1
ES8	Surface	0.082	-	-	-	3.22	169.7	0.90	0.0	331.9	50.0	419.8	179.5
ES9	Surface	0.014	6.6	200	0.061	1.06	169.6	0.81	0.1	327.6	49.8	415.5	178.6
ES10	Surface	0.014	-	212	0.060	1.87	151.5	0.92	0.1	752.0	51.6	431.6	184.0

	Feature	Depth m b.g.l	pH	TSM mg/l	Fuco. ug/l	Chl a mg/m^3	DSi µM	δ^{30}Si ‰	SD ‰	Na µM	K µM	Ca µM	Mg µM
Wet season (August 2019)													
GW1	Open Well	1.3	7.12	-	-	-	522	0.50	0.1	4753	72	1900	1387
GW3	Open Well	1.3	6.97	-	-	-	881	0.74	0.1	2208	1240	2250	839
GW4	Open Well	1.07	7.46	-	-	-	549	0.61	0.1	42168	4963	3213	8183
GW5	Handpump	5	7.35	-	-	-	545	0.20	0.1	20928	260	277	582
GW6	Open Well	1.9	7.25	-	-	-	540	1.08	0.1	2295	98	1659	1442
GW7	Open Well	0.53	7.12	-	-	-	614	0.58	0.0	3428	1173	2717	903
PZ1	Piezometer	4.31	7.55	-	-	-	602	1.06	0.1	17701	470	4979	5046
NBPZ1	Handpump	5	7.02	-	-	-	704	1.11	0.0	4434	119	1252	3122
PZ2	Piezometer	7.69	6.84	-	-	-	498	1.15	0.1	1688	152	1501	1103
NBPZ2	Open Well	1.98	7.55	-	-	-	796	0.94	0.0	23886	22	1011	3010
PZ3	Piezometer	3.93	7.38	-	-	-	226	4.05	0.0	5914	5354	419	2064
PZ4	Piezometer	7.2	7.02	-	-	-	739	0.62	0.0	1504	184	1446	1251
NBPZ4	Handpump	20	6.99	-	-	-	674	0.75	0.1	6608	531	2110	1893
PZ5	Piezometer	4.86	6.87	-	-	-	303	2.27	0.0	1410	60	1636	1180
NBPZ5	Handpump	5	6.8	-	-	-	590	0.65	0.1	2226	103	1898	1188

3.1. Chemical characterization of Godavari estuary and groundwater

Godavari estuary samples exhibited a salinity gradient during the dry season ranging from 0.4 in the most upstream sampling location to 29.6 in the most downstream location. Wet season estuary exhibited very low salinity across the estuary with an average of 0.05±0.05. The pH in the estuary ranged from 7.24 to 7.74 during the dry season and 6.56 to 6.78 during the wet season. Groundwater samples exhibited a pH range from 6.83 to 7.53 with no significant seasonal differences (t-test, Table 1). Obviously, the major cation (Na, K, Mg, Ca) concentrations in the estuary increased with the salinity gradient during the dry season, while the wet season chemical composition remained relatively homogenous throughout the estuary (Table 1). During the wet season, the dominant major cation was Ca^{2+}, followed by Na^{+}, Mg^{2+} and K^{+}. The cation concentration in groundwater reduced in the order $Na^{+} > Mg^{2+} > Ca^{2+} > K^{+}$ (Table 1). The total suspended matter (TSM) in the estuary was higher during the wet season (170±50 mg/l) compared to the dry season (22±17 mg/l). The mean Chlorophyll-*a* was 10.1±7.5 mg/m^3 during the dry season and 2.9±1.4 mg/m^3 for the wet season. The fucoxanthin also exhibited a higher value during the dry season, 1.6±1.4 µg/l, than during the wet season, 0.2±0.2 µg/l. The highest fucoxanthin and chlorophyll-*a* concentrations were observed at salinity of 24.7 during the dry period.

3.2. Variability of DSi and $\delta^{30}Si$ in estuary and groundwater

The DSi concentration in the estuary ranged from 5.5 to 275 µM, with a decreasing trend along the salinity gradient during the dry season while it was homogenous during the wet season, 181±21 µM. No significant differences exist between surface and bottom water DSi for dry and wet season. The $\delta^{30}Si$ values in Godavari estuary during the dry season ranged from 1.08 to 3.0‰ with the lowest $\delta^{30}Si$ located at an upstream location with a salinity of 0.9 (ES2) and the highest in the most downstream location at a salinity of 29.6 (ES10) (Fig. 2). The rationale behind choosing ES2 instead of ES1 is described in discussion. During the wet season, the estuary exhibited uniformly lower $\delta^{30}Si$, which was comparable with the upstream estuarine value during the dry season, with an average $\delta^{30}Si$ of 0.86±0.1‰. Overall, groundwater exhibited higher DSi concentration (570±160 µM) and a highly variable $\delta^{30}Si$ ranging from -0.21 to 4.05‰, with an average of 0.99±0.82‰ (Table 1). Groundwater exhibited no significant differences in $\delta^{30}Si$ between dry (0.83±0.3‰) and wet (1.1±1.0‰) seasons (t-test).

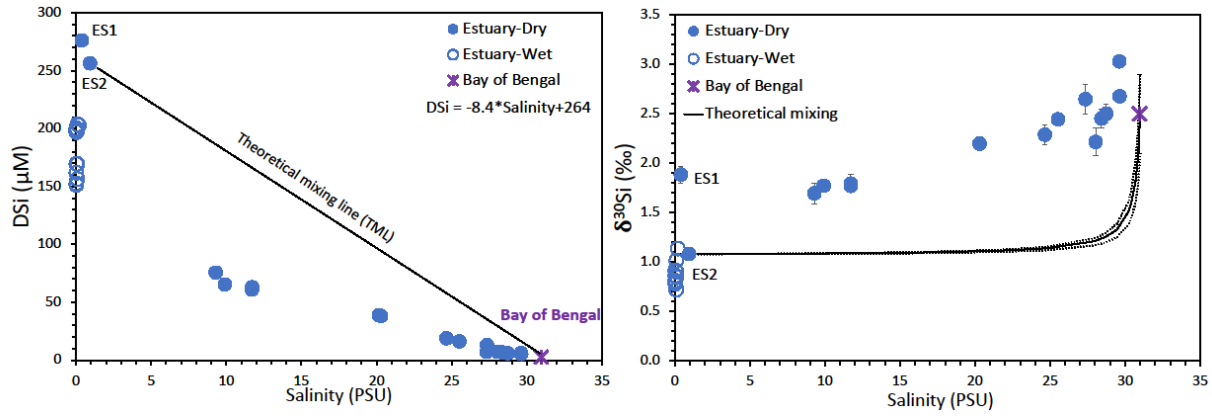

Figure 2. *Variability of DSi (a) and $\delta^{30}Si$ (b) with salinity in the Godavari estuary during dry and wet seasons. The black lines represent the theoretical mixing between fresh water and seawater and the dashed line of $\delta^{30}Si$ vs. salinity plot represents the sensitivity for mixing based on the error of $\delta^{30}Si$ (seawater data from Singh et al. (2015))*

4. Discussion

Estuaries play a crucial role in determining the fluxes and composition of elements entering the coastal ocean. Godavari estuary exhibited significant spatial and temporal variability with reference to discharge: strong salinity gradient was observed during the dry period due to weak/no discharge, whereas freshwater dominated during the wet period due to high discharge (Table 1). Previous works have also documented substantial temporal variability in nutrient fluxes (Sarma et al., 2010), phytoplankton growth (Bharathi et al., 2018, Acharyya et al., 2012)

and submarine groundwater discharge (Rengarajan and Sarma, 2015, Damodararao and Sarma, 2022) in Godavari estuary. The variability of DSi and $\delta^{30}Si$ signatures in the estuary can result from the cumulative effects of source variability, mixing of water masses and abiotic as well as biotic processes in the estuary. The discussion of the results will broadly emphasize on i) seasonal distributions in concentration and isotopic composition of DSi in the estuary (sections 4.1 and 4.2), ii) factors controlling DSi distribution in the groundwater (section 4.2), and iii) implications for riverine transport and groundwater discharge (section 4.3).

4.1. Diatom uptake during the dry season

The estuary exhibited a salinity gradient ranging from 0.4 upstream to 29.6 downstream indicating the occurrence of active freshwater-seawater mixing. However, DSi and $\delta^{30}Si$ displayed non-conservative behaviour between low salinity fresh river water and Bay of Bengal seawater (Singh et al. 2015) end-members, with significant removal of DSi accompanied by enrichment in ^{30}Si in the dissolved load (Fig. 2). The most upstream sample with the lowest salinity was impacted by significant diatom growth, as evidenced from high $\delta^{30}Si$ (1.9‰), fucoxanthin content and abundance of diatoms from SEM imaging of suspended matter (Fig. 4). Therefore, we used the ES2 as the fresh river water endmember with low $\delta^{30}Si$ (1.1‰) and low fucoxanthin content, similar to upstream river water $\delta^{30}Si$ during the wet season and fresh groundwater (Fig. 2 and Table 1). We observed an increase in diatom marker pigment, fucoxanthin (normalized to DSi, Fig 3) and Chl-*a* concentration (upto 21 mg/m^3, Fig 3) with $\delta^{30}Si$ in dry period, suggesting DSi uptake by diatoms in the estuary. During the low discharge period, the closure of the Dowaleiswaram dam gates limits the fresh river flow resulting in an increase of water residence time in the estuary to >30 days (Fig. 1; Sridevi et al 2015). The high residence time, controlled by tidal influence, leads to the formation of a stable shallow water column with low turbidity that promotes the growth of diatoms and other phytoplanktons in the Godavari estuary (Acharyya et al 2012, Bharati et al., 2018). Diatom communities in the estuary are dominated by Melosira *sp.*, Fragellaria *sp.*, Navicula *sp.*, Amphiprora *sp.*, Synedra *sp*., Amprora *sp.*, Pinnularia *sp.*, Thalassionema *sp.*, Coscinodiscus *sp.*, and Nitzschia *sp.* (Acharyya et al 2012; Bharathi et al 2018) and SEM observations on our samples confirm the presence of diatoms (Fig. 4). Thus, diatom uptake imparts significant control over the DSi loss and subsequent heavier $\delta^{30}Si$. The Si isotopic fractionation associated with the removal of DSi from a system can be described using two simple models; a Rayleigh model for distillation of isotopes describing a closed system with no further DSi exchange with the source and a steady

state model describing an open system where there is a continuous input of DSi from external sources (Fripiat et al., 2011 and references therein).

$$\text{Rayleigh: } \delta^{30}Si_{diss} = \delta^{30}Si_{mix} + \varepsilon * \ln(f) \quad \text{(E2)}$$

$$\text{Steady state: } \delta^{30}Si_{diss} = \delta^{30}Si_{mix} - \varepsilon * (1-f) \quad \text{(E3)}$$

$$f_{Si} = DSi_{mea}/DSi_{mix} \quad \text{(E4)}$$

Here f_{Si} indicates the fraction of DSi remaining in the estuary after diatom uptake, relative to the DSi expected from simple two-endmember mixing between freshwater and seawater for a given sample. $\delta^{30}Si_{diss}$ denotes the $\delta^{30}Si$ of the dissolved phase resulting from Si removal and $\delta^{30}Si_{mix}$ denotes the expected Si isotopic composition by two endmember mixing model. Applying equation E4, we estimated the fraction of DSi remaining in the system after diatom uptake to be 35±6% and exhibited no trend with salinity gradient (Table 2). Using equations E2 and E3, we can estimate the $\delta^{30}Si_{diss}$ for each estuary location using calculated f_{Si} (E4), assuming a constant fractionation factor ($^{30}\varepsilon$) of -1.1‰ and a $\delta^{30}Si_{mix}$ obtained from a two-endmember isotope mixing (Table 2). The assumption is based on the average $^{30}\varepsilon$ reported in the literature, -1.1‰, for diatoms assemblage in seawater (Fripiat et al 2011) and freshwaters (Alleman et al., 2005). Comparing the results of $\delta^{30}Si_{diss}$ from Rayleigh and steady-state models with the measured $\delta^{30}Si_{mea}$, we conclude that diatom uptake explains a part of the deviation from binary mixing, and there remains some unaccounted deviation. We can also argue that the Rayleigh fractionation behaviour during diatom uptake is appropriate in Godavari estuary during dry season given that steady state fractionation with $^{30}\varepsilon$ of -1.1‰ cannot explain any of the $\delta^{30}Si_{mea}$ greater than 2.36‰. The unexplained deviations based on Rayleigh fractionation are heterogeneous spatially, with values generally lighter than expected at low salinity and few samples heavier than expected at high salinity (Table S1).

We hypothesize that such deviations may result from three possible causes: i) groundwater contribution to the estuary during the dry season which can lead to an underestimation of f_{Si} and also depletion in $\delta^{30}Si$ (due to consistently lighter $\delta^{30}Si$ of adjacent groundwater; Fig. 2), ii) the assumption of a single $^{30}\varepsilon$ throughout the estuary and, iii) dissolution of precipitated biogenic silica (BSi) and/or lithogenic particles in sediment.

Table 2. *The results of calculation for mixing and diatom uptake described in section 4.1. The subscript 'mea' indicate measured values in estuary, 'mix' indicates expected values from two endmember mixing and 'diss' indicates the values obtained for dissolved phase from Rayleigh and steady state models with a constant fractionation factor of -1.1‰ for diatom uptake. [#]The seawater endmember is Bay of Bengal (BoB) surface water average from Singh et al (2015).*

Sample		**Salinity**	**DSi_{mea}**	**DSi_{mix}**	f_{Si}	**$\delta^{30}Si_{mea}$**	**$\delta^{30}Si_{mix}$**	**$\delta^{30}Si_{diss}$ Rayleigh**	**$\delta^{30}Si_{diss}$ Steady**	**$\delta^{30}Si_{diss}$ - $\delta^{30}Si_{mix}$ Rayleigh**	**$\delta^{30}Si_{diss}$ - $\delta^{30}Si_{mix}$ Steady**
			µM	µM		‰	‰	‰	‰	‰	‰
ES1	Surface	0.4	276.3	-	-	1.88	-	-	-	-	-
ES2	Surface	0.9	256.4	256.4	1.00	1.08	-	-	-	-	-
ES3	Surface	9.3	75.8	185.8	0.41	1.69	1.09	2.07	1.74	**-0.38**	-0.04
ES3	Bottom	9.9	65.5	180.6	0.36	1.77	1.09	2.20	1.79	**-0.43**	-0.02
ES4	Surface	11.7	63.0	165.3	0.38	1.77	1.09	2.15	1.77	**-0.38**	0.00
ES4	Bottom	11.7	61.0	165.5	0.37	1.79	1.09	2.19	1.78	**-0.39**	0.01
ES5	Surface	20.3	38.2	92.8	0.41	2.20	1.11	2.09	1.76	0.11	**0.44**
ES6	Surface	24.7	18.8	56.0	0.34	2.29	1.14	2.34	1.87	-0.05	**0.42**
ES7	Surface	25.5	16.4	48.7	0.34	2.44	1.15	2.35	1.88	0.09	**0.56**
ES7	Bottom	27.3	13.0	33.3	0.39	2.65	1.19	2.22	1.86	**0.43**	**0.79**
ES8	Surface	28.0	7.3	27.5	0.26	2.22	1.22	2.68	2.02	**-0.46**	**0.19**
ES9	Surface	28.4	6.7	24.3	0.27	2.45	1.23	2.66	2.03	-0.21	**0.42**
ES9	Bottom	28.7	6.1	21.6	0.28	2.50	1.26	2.65	2.05	-0.15	**0.45**
ES10	Surface	29.6	6.1	14.2	0.43	3.03	1.35	2.29	1.98	**0.74**	**1.05**
ES10	Bottom	29.6	5.5	14.0	0.39	2.68	1.36	2.39	2.03	**0.28**	**0.65**
BoB[#]	Surface	30.9	2.9	2.9	-	2.48	-	-	-	-	-

Firstly, to check for groundwater mixing, we considered the $\delta^{30}Si$ of groundwater adjacent to estuarine location in the dry season and estimated the proportion of groundwater contribution to estuary using a isotopic balance (Table S1). Here note that all the adjacent groundwater exhibit a $\delta^{30}Si$ lighter than estuary, thus cannot account for heavier than expected $\delta^{30}Si$. Therefore, we restrict our calculation to samples with $\delta^{30}Si$ lighter than expected after correcting for mixing and diatom uptake, and having deviation larger than our analytical uncertainty of ±0.2‰. Our estimate suggest that groundwater contribution to DSi in estuary ranges from 9 to 36%, with higher contribution in low salinity samples (Table S1). The estimates are within the dry season submarine groundwater discharge (SGD) Si flux calculated for the Gautami Godavari branch using Radium isotopes but lower than the groundwater discharge calculated using Sr isotopes (Chapter IIIb, Rengarajan and Sarma 2015).

However, mixing with a lighter source of Si (i.e. groundwater) cannot explain the heavier than expected $\delta^{30}Si_{mea}$ observed in ES7 and ES10 (Table S1). Species-dependent differences in fractionation factors are documented for marine diatoms, ranging from -0.54 to -2.09‰ (Sutton et al., 2013). Given that such overestimation of $\delta^{30}Si_{mea}$ is confined to the high salinity region, one possibility is change in diatom species with more negative $^{30}\varepsilon$ (Fripiat et al., 2012). However, we have no real evidences to support the argument and the previous literatures suggest a possible inverse relationship between fractionation factor and DSi in marine diatoms and sponges (Cardinal et al., 2007, Hendry and Robinson, 2012). Thus variable $^{30}\varepsilon$ is unlikely to explain the heavy Si isotopic signature. We can also neglect a benthic source of Si from biogenic silica and sediment dissolution, given the water column is stable with a salinity gradient and hence it is unlikely to be contributing during dry season. In addition biogenic silica dissolution in sediment can lead to the formation of authigenic clay minerals (Michalopoulos and Aller 2004, Tatzel et al 2015), and can increase the pore water $\delta^{30}Si$ up to 2‰ (Ehlert et al 2016; Rahman et al 2016). Abiotic removal of Si from the sediments is favoured under high productivity and burial, but the DSi fluxes from the sediment to the water column remain questionable given we don't observe significant differences in DSi and $\delta^{30}Si$ between surface and bottom (Table 1). Overall, in Godavari estuary diatom uptake and formation of biogenic silica drive the Si dynamics during the dry period, when fresh river water discharge is minimal with contribution from groundwater at low salinity.

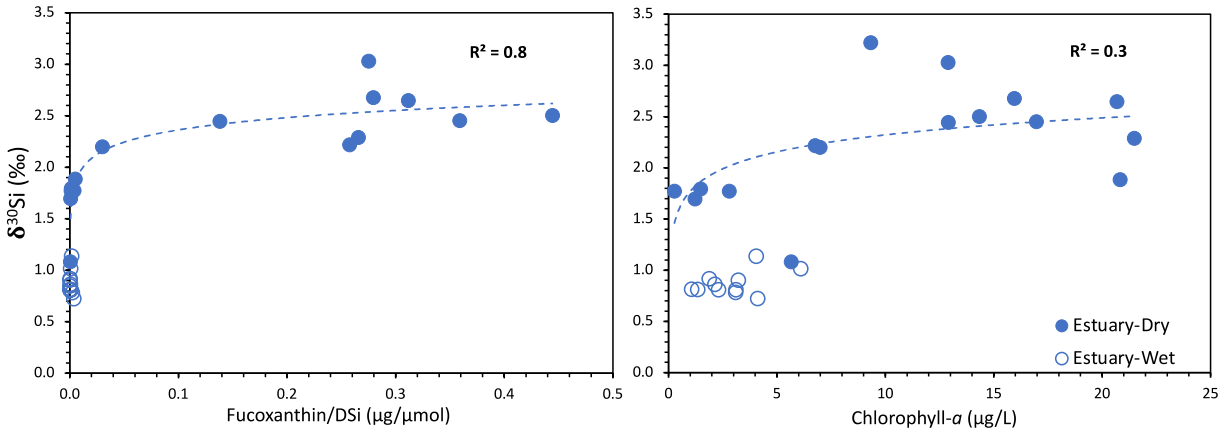

Figure 3. *$\delta^{30}Si$ plotted against a) fucoxanthin/DSi and b) chlorophyll-a, indicating the increase in phytoplankton and diatom blooms at high $\delta^{30}Si$ in estuary during dry season. Wet season exhibits low fucoxanthin and chlorophyll-a.*

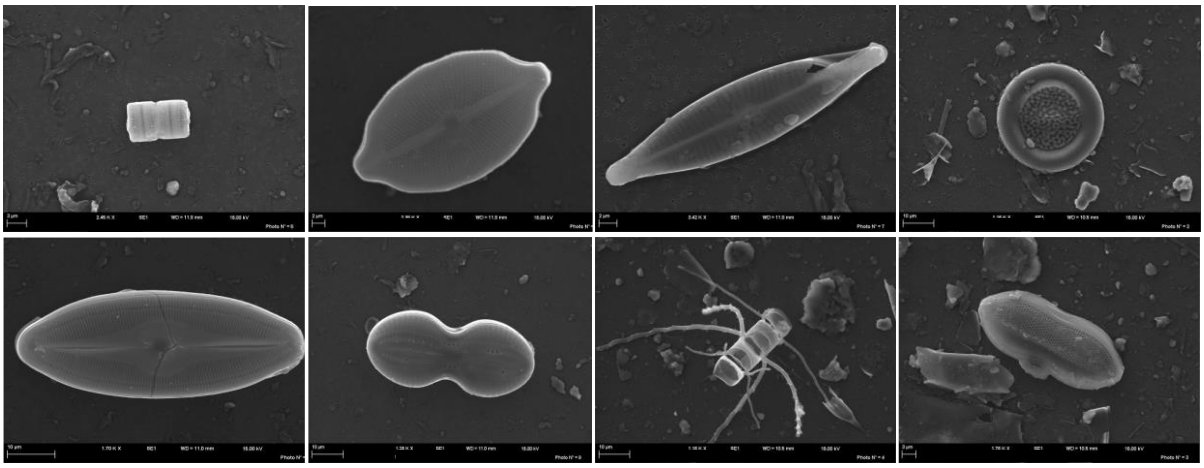

Figure 4. *Scanning electron microscopy (SEM) images of diatom frustules found in suspended fraction of Godavari estuary during dry season.*

4.2. Weathering controls on Si cycling

4.2.1. Weathering signatures recorded in wet season estuary

Unlike the dry season, the estuary during the wet season exhibited a homogenous signature in DSi (181±21 µM) and δ^{30}Si (0.87±0.1‰), resulting from a huge influx of fresh river water (salinity<0.5), due to heavy monsoonal precipitation and weak tidal mixing. During months of South West monsoon, the dam gates are open and the residence time of water in the estuary is typically less than a day (Sridevi et al., 2015). High suspended particulate load (175±50 mg/l) resulting from increased river discharge significantly reduces the light penetration depth, limiting phytoplankton growth (Sarma et al., 2009). This is evidenced by a low Chl-*a* and fucoxanthin content and light δ^{30}Si signatures comparable to groundwater (Table 1 and Fig 3). SEM observations confirm also the absence of well-preserved diatoms frustules in wet season (Fig. S1). Given the absence of diatoms and dominant fresh river water influx, δ^{30}Si signatures during the wet season can be driven by; i) dissolution of amorphous phases (ASi, dominated by biogenic silica and Al-rich amorphous phases) and suspended as well as resuspended matter that can dissolve within the estuary (Ronchi et al., 2013), ii) soil weathering signatures in the Godavari basin resulting from the surface and subsurface runoff. During the Southwest monsoon, the water mass leaching superficial soil layers dominate the river flow, carrying a higher load of soil derived ASi and other lithogenic components (primary and secondary minerals) compared to the dry season (Frings et al 2014; Mangalaa et al 2017). The ASi fraction in the soils and suspended matter can be subdivided into, i) BSi (biogenic silica) originating from phytoliths as well as diatoms, ii) non-crystalline inorganic fraction formed by pedogenic processes (Saccone et al., 2007, Ronchi et al., 2015). The total flux of particulate silica to the

ocean is estimated to be 147±44 TmolSi/yr with a fairly soluble ASi flux of 1.9±1 TmolSi/yr (Dürr et al., 2011, Frings et al., 2016). Moreover, the ASi fraction can be a readily available source of DSi to the rivers due to its high solubility compared to primary minerals and undersaturation in river water (Table S2, Fraysse et al., 2009). Only available soil ASi $\delta^{30}Si$ data from the Indian subcontinent puts $\delta^{30}Si_{ASi}$ at 1.25±0.28‰ (Riotte et al., 2018), which is heavier than the reported $\delta^{30}Si$ values of the estuary water during wet season (Table 1). In the absence of any measured $\delta^{30}Si$ of diatoms, we can recalculate the $\delta^{30}Si_{diatom}$ grown during the dry season using the Rayleigh fractionation equation given by:

$$\delta^{30}Si_{diatom} = \delta^{30}Si_{mix} - {}^{30}\varepsilon * f * \ln(f)/(1-f) \quad \text{(E5)}$$

An estimate shows that $\delta^{30}Si_{diatom}$ could have accumulated in the estuarine sediments during the dry season which can range between 0.41 and 0.71‰. Previous studies reported an overall fractionation during the dissolution of diatoms, with a fractionation factor ranging from -0.55 to -0.12‰ (Demarest et al., 2009, Sun et al., 2016). Moreover, the fractionation associated with dissolution must be transient and is unlikely to have any significance. Thus, DSi resulting from the dissolution of diatoms also cannot account for the observed $\delta^{30}Si$ values in the estuary during the high discharge season.

The geology of the Godavari basin mainly consists of Deccan trap basalts (55%, upstream) and Precambrian granitic gneiss (28%, downstream), with clay mineral distribution dominated by smectites (~68% in the shelf sediments, Biksham and Subramanian, 1988, Raman et al., 1995). The $\delta^{30}Si$ of the Godavari river during the wet season (0.87±0.1‰) was lighter than reported values of the Kaveri river (1.98‰, also east flowing river), but more similar to intensely weathered Netravathi river (0.98‰, west-flowing river of the peninsula), reflecting differences in weathering regimes and land use (Sarath et al., 2022). We can use the similar Rayleigh and steady state models (Equations E2 and E3) to understand the evolution of $\delta^{30}Si$ signatures in the estuary during the wet season because of weathering and incorporation of Si into secondary precipitates. The initial $\delta^{30}Si$ is assumed to be the peninsular gneiss value (-0.34±0.1‰, Riotte et al 2018a). The fraction of weathering solubilized Si remaining in the solution (f_{Si}) is calculated using the equation:

$$f_{Si} = (DSi/Na)_{mea}/(Si/Na)_{bedrock} \quad \text{(E6)}$$

Here we assume that silicate weathering stoichiometrically releases Si and Na, and Na behaves conservatively in the solution after solubilization. The Si/Na ratio of the bedrock was obtained from peninsular gneiss and corrected for quartz content (Braun et al., 2009). A f_{Si} value of 1 indicates all the solubilized Si remains in the solution and decreases as Si is immobilized into secondary phases. For the sake of simplicity, we assume the Si in the river water is sourced from the integration of multiple flow paths, with a single fractionation factor associated with the dominant clay mineral, i.e., smectite and kaolinites in the Godavari basin. As shown in Fig 5, the wet season estuary plots at a high f_{Si}, between the fractionation factor ($^{30}\varepsilon$) of -1.75 and -1.1‰ fitting more to a steady state or open system fractionation (Fig. 5). This can be contrasted with more Rayleigh type evolution in Himalayan River Ganges and tributaries, controlled by incongruent weathering in the alluvial plains (Fontorbe et al., 2013, Frings et al., 2015). The $^{30}\varepsilon$ range is within the reported values for smectites elsewhere (-0.1‰ to -0.7‰ Opfergelt et al., 2012, Frings et al., 2021) and kaolinites from peninsular India and Sri Lanka (-1‰ to -2‰, Riotte et al., 2018, Frings et al., 2021). Interestingly, groundwater from Godavari estuary also plots in a similar trend with lower f_{Si}, indicating that δ^{30}Si signatures in both coastal groundwater and fresh river during monsoon are driven by chemical weathering of primary silicate minerals and smectite type clay formation occurring in soil and saprolite layers. However, it is hard to discern any interactions between surface water and groundwater during the wet season owing to the similarity in δ^{30}Si composition. This can be contrasted with our observation from Karnataka, where surface streams and Nugu river exhibited a higher δ^{30}Si compared to groundwater (Chapter II). The DSi fluxes in river water can integrate the signatures from surface and subsurface flow in the basin, typically exhibiting a low residence time and can result in lower f_{Si} compared to groundwater (Maher et al., 2011, Chapter II). To summarise, we attribute the δ^{30}Si signatures in the river water in the Godavari estuary during the wet season to incongruent weathering in the Godavari basin.

4.2.2. Coastal groundwater Si cycling

Groundwater Si is ultimately sourced from weathering of silicate minerals and can undergo multiple abiotic as well as biotic processes including secondary mineral precipitation, plant uptake from shallow soil layers, and adsorption onto Fe and Al oxyhydroxides (Frings et al., 2016 and references therein).

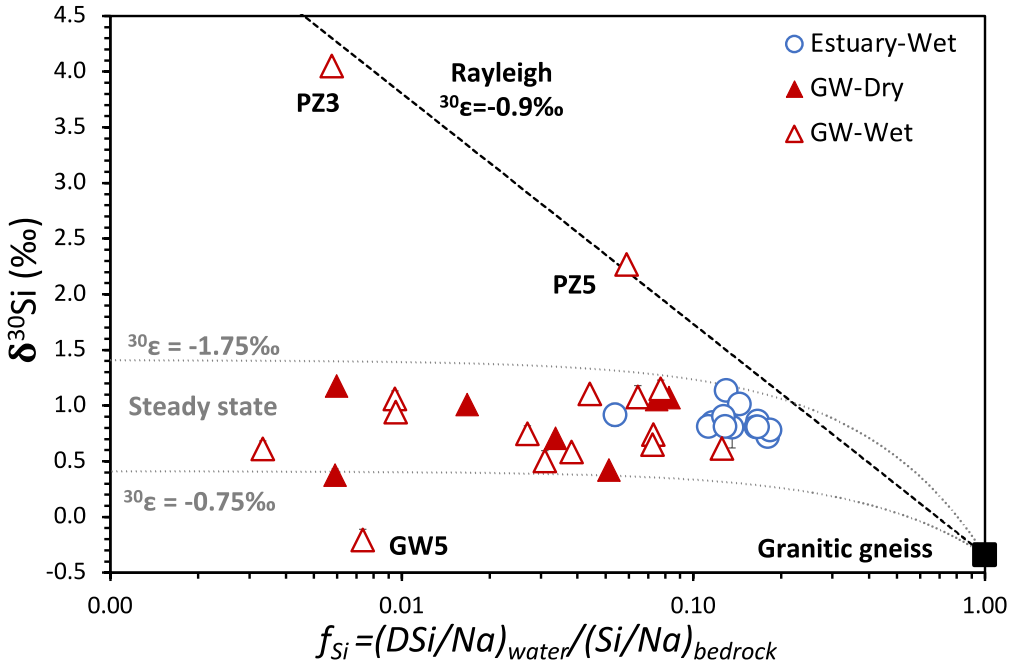

Figure 5. *δ^{30}Si composition plotted against f_{Si} (fraction of Si remaining in the solution) estimated using the normalization procedure described in Hughes et al. (2013) for wet season estuary and groundwater. The fractionation factors for the Rayleigh and steady-state models with various fractionation factors (see section 4.2) and granitic gneiss endmember from Riotte et al. (2018).*

Using a similar approach as discussed in section 4.2, we can use Rayleigh and steady-state fractionation models to understand the evolution of δ^{30}Si in the aquifers (Fig. 5). Majority of groundwater samples plot within a steady-state fractionation model, between the fractionation factors of -0.75 and -1.75‰. Such variability can result from, i) different fractionation factors associated with biotic as well as abiotic incorporation of Si, ii) assumption of a single source of Si to calculate f_{Si} which can be an oversimplification. Assuming that incorporation of Si into secondary clays dominates the Si loss from the groundwater system, the $^{30}\varepsilon$ of observed groundwater samples are consistent with the published fractionation factor of smectite-type and kaolinite type clays (Opfergelt et al., 2012, Frings et al., 2021). Groundwater δ^{30}Si in other contexts are also consistent with dominant weathering control of Si cycling and the variability determined by the source of Si (primary *vs.* secondary minerals) and also the type of clay mineral formed (Georg et al., 2009a, Georg et al., 2009b, Strandmann et al., 2014). Plant uptake also exhibits a wide range of fractionation factors, with $^{30}\varepsilon$ ranging from +0.3 to -1.7‰, but typically follows a Rayleigh model fractionation during Si uptake from soil solution (Opfergelt et al., 2006, Ding et al., 2008, Sun et al., 2016). Silicon can also be readily adsorbed onto Fe oxyhydroxides, with known fractionation factors ranging from -1.1 to -1.5‰ following better Rayleigh model behaviour (Delstanche et al., 2009, Opfergelt et al., 2009). Thus, given the

similar behaviour of the majority of the groundwater in both seasons, following a steady state system, we can attribute the clay formation as the dominant process controlling the $\delta^{30}Si$ variability. The observation is consistent with the behaviour of groundwater from watersheds in peninsular India, where soil solution percolates through a thick unsaturated zone composed of an immature regolith (Chapter II from the thesis).

From Fig. 5 we also observe three outliers, two piezometers PZ3 and PZ5 exhibiting a heavier $\delta^{30}Si$ and GW5 a handpump with lighter $\delta^{30}Si$ composition of -0.21‰ during the wet season. Both piezometers PZ3 and PZ5 are shallow (4 and 5m deep respectively, Table 1) and sampled only during the wet season. They exhibited $\delta^{30}Si$ of 4.0‰ and 2.3‰ respectively, along with significant loss of DSi (~50% less than the average DSi in groundwater, Table 1). Thus, they are affected by near-surface/sub-surface processes occurring in shallow soil and saprolite, which can significantly fractionate Si isotopes (Opfergelt and Delmelle, 2012), such as plant uptake. They indeed fit a Rayleigh model with $^{30}\varepsilon$ of -0.9‰. Deltaic plains of Godavari are heavily cultivated for rice, which is known to have a fractionation factor close to -1‰, coherent with our estimate (Ding et al., 2008, Sun et al., 2016) and with $\delta^{30}Si$ signatures of paddy fields porewater (2.8 to 3.2‰, Riotte et al. 2018b). On the other hand, lighter Si isotopic composition in GW5 (+0.38 and -0.21‰ dry and wet season) is associated with a high Fe concentration, 14 µM and 12 µM, respectively, for dry and wet seasons (Table S2). The anoxic conditions existing in the aquifer (DO<0.5 mg/L, Table S2) can lead to the reductive dissolution of Fe-oxyhydroxides, thereby preferentially releasing lighter ^{28}Si into the groundwater (Delstanche et al., 2009, He and Liu, 2015). However, the interpretation is speculative at this point given the significant overlap in the fractionation factor associated with the processes (Opfergelt and Delmelle, 2012). To summarize the groundwater $\delta^{30}Si$ is primarily controlled by weathering and formation of secondary clays during both wet and dry seasons with minor impact from plant uptake and adsorption-desorption processes. The similarity in the $\delta^{30}Si$ composition and behaviour of groundwater and estuary during the wet season can result from similar Si sources in both fluvial systems, controlled by the lithology and weathering in the region.

4.3. Implication of riverine and groundwater discharge in Godavari estuary

In the Godavari estuary, the behaviour of the Si during estuarine mixing is modulated by river discharge, which in turn modifies the riverine DSi fluxes and isotopic composition. As evident from the discussion above, the estuarine Si cycling during the dry season is significantly modified by diatom uptake and groundwater discharge during the dry season. Firstly,

considering fresh river water endmember for the dry and wet seasons, Godavari river supplies almost 21.5±0.3 GmolSi/yr (Mangalaa et al., 2017) with a weighted $\delta^{30}Si$ isotopic composition of 0.92±0.2‰ to Bay of Bengal (this study). Here, dry season accounts for almost 24% of the annual Si flux to the ocean. Moreover, assuming that the diatom growth persists throughout the low discharge periods (Acharyya et al., 2012), the fraction of Si taken up by diatoms as 0.65±0.06 (calculated from 1-f_{Si}, Table 2), corresponds to 3.4±0.4 GmolSi/yr. Thus, annually almost 15.8% of DSi is precipitated as BSi, higher than the estimate of 10% by DeMaster, (2002). Highly productive coastal shelf and estuarine environments can act like a fluidized bed reactor, acting as a potential sink for terrestrial DSi as biogenic deposition into sediments and storage via authigenic clay formation, altering the flux and isotopic composition DSi entering the open ocean (DeMaster, 2002, Frings et al., 2016, Zhang et al., 2020). We can also estimate the isotopic effect of estuarine removal (change in the isotopic composition of river water that occurs in estuary before being discharged to sea) assuming Rayleigh model for the diatom uptake:

$$\delta^{30}Si_{sea} - \delta^{30}Si_{river} = {}^{30}\varepsilon * \ln(f_{Si}) \quad \text{(E6)}$$

Here f_{Si} is the fraction of DSi remaining after the estimated loss of 15.8%, and ${}^{30}\varepsilon$ is assumed to be -1.1±0.4‰, consistent with known diatom uptake (Sutton et al., 2013, 2018). The estimated isotopic effect on diatom removal for Godavari estuary during the dry season is +0.16±0.1‰, i.e. almost +0.16‰ enrichment in the riverine $\delta^{30}Si$ occurs before it reaches the Bay of Bengal. This estimate is heavier than the previous one of +0.1‰ by Frings et al, (2016) but lower than the +0.2‰ to +0.3‰ by Zhang et al, (2020) for the Amazon river estuary, due to the lower estimate of the fraction of Si lost from the estuary (also known as estuarine filter capacity). However, calculations carry two major drawbacks: we did not consider BSi dissolution during the high discharge period and neglected the impact of groundwater discharge. Increased suspended matter during high discharge in the estuary can result from sediments resuspension, where the BSi fraction in the sediment can be flushed to the ocean leading to dissolution, releasing the lighter Si (Rickert et al., 2002, Loucaides et al., 2008). The fraction of BSi resuspended in the following season and solubilized remains to be quantified.

Rengarajan and Sarma (2015) estimated an average SGD flux of $3.6*10^6$ m^3/day and based on the average DSi of groundwater from the region (Table 1), we can estimate an SGD Si flux of 0.76±0.5 GmolSi/yr with a $\delta^{30}Si$ of 0.99±0.82‰. The estimate is just 3.5% of the annual riverine Si flux and both spatially and temporally variable across the estuary (Rengarajan and

Sarma, 2015). Given the similarity in Si isotopic composition between groundwater and estuary during wet season and low Si flux compared to the Godavari river, the estimated isotopic effect of groundwater discharge is lower than our analytical uncertainty, and cannot be distinguished from the weighted δ^{30}Si of Godavari river. However, without estimation of recycled marine groundwater, which accounts for almost 90% of the total SGD to the coast, the total SGD fluxes to the Bay of Bengal coast cannot be estimated (Taniguchi et al., 2002, Moore et al., 2010, Rahman et al., 2019). Overall, the diatom uptake during low discharge periods in Godavari estuary have a significant impact on the Si supply to the Bay of Bengal, however, the possible resuspension and dissolution of BSi during high discharge period remain to be accounted for the estimates.

5. Conclusion

The δ^{30}Si signatures of dissolved silicon in the Godavari estuary exhibited significant seasonal and spatial differences with strong salinity gradients during the dry and fresh river water influx during wet seasons. The DSi and δ^{30}Si exhibits a non-conservative mixing during dry season, consistent with Si uptake and enrichment of estuary water resulting from diatom growth. We estimate an average isotopic enrichment of 1.0±0.4‰ and an average DSi loss of 65±7% from the estuary during dry season. The low discharge and stable water column with high residence time aided by closure of dams gates provide favourable condition for diatom growth, evident from high chlorophyll-*a* content and fucoxanthin. During wet season the high suspended matter flux limits the diatom growth and the estuary exhibits a homogenous DSi (181±21 µM) and δ^{30}Si (0.86±0.1‰) with low salinity (<0.2), reflecting signatures of river water. The δ^{30}Si in Godavari river water is primarily controlled by weathering in the river basin, exhibiting signatures comparable to groundwater (0.99±0.82‰) in the basin. Unlike estuary, groundwater exhibited no significant temporal variability in DSi and δ^{30}Si, with a large range in δ^{30}Si ranging from -0.2 to 4.0‰. The silicon isotopic composition in groundwater is controlled by weathering and formation of secondary clay minerals such as smectites and follows a steady state fractionation model with $^{30}\varepsilon$ between -0.75 to -1.75‰. Overall, Godavari river supplied almost 21.5±0.3 GmolSi/yr with a weighted δ^{30}Si isotopic composition of 0.92±0.2‰ and groundwater discharge into the estuary accounts for less than 3.5% of the riverine Si flux to the Bay of Bengal during 2019.

Acknowledgements

The work is funded by CEFIPRA-IFCPAR support (NUNDERGROUND, project #5907). We acknowledge National Institute of Oceanography (NIO) for providing necessary support for field campaign and sampling. SPK and DC thank Sandrine Caquineau for the support and insights for SEM investigations at ALYSES facility (IRD-SU). The authors thank B.S.K Kumar for the help with field sampling and pigment analysis, Irina Djouraev and Pierre Burckel for the help with ICPMS analysis and the ALYSES facility (IRD-SU). SPK thank IRD and Campus France for providing Ph.D. scholarship and constant support to carry out the work. The authors would like to thank M. Benrahmoune (LOCEAN-IPSL) for help in sample processing and clean lab management.

Supplementary table

Table S1. *The estimation of fractional contribution of groundwater discharge to balance the isotopic depletion after diatom uptake in the estuary. The $\delta^{30}Si_{GW}$ are from adjacent groundwater close to estuary location.*

Sample		**Salinity**	**$\delta^{30}Si_{mea}$**	**$\delta^{30}Si_{mix}$**	**$\delta^{30}Si_{diss}$ - $\delta^{30}Si_{mix}$ Rayleigh**	**$\delta^{30}Si_{GW}$**	**f_{GW}**
			‰	‰	‰		
ES1	Surface	0.4	1.88	-	-	-	-
ES2	Surface	0.9	1.08	-	-	-	-
ES3	Surface	9.3	1.69	1.09	**-0.38**	1.07	0.36
ES3	Bottom	9.9	1.77	1.09	**-0.43**	1.07	0.36
ES4	Surface	11.7	1.77	1.09	**-0.38**	1.07	0.33
ES4	Bottom	11.7	1.79	1.09	**-0.39**	1.07	0.34
ES5	Surface	20.3	2.20	1.11	0.11	-	-
ES6	Surface	24.7	2.29	1.14	-0.05	-	-
ES7	Surface	25.5	2.44	1.15	0.09	-	-
ES7	Bottom	27.3	2.65	1.19	0.43	-	-
ES8	Surface	28.0	2.22	1.22	**-0.46**	1.01	0.28
ES9	Surface	28.4	2.45	1.23	**-0.21**	1.01	0.13
ES9	Bottom	28.7	2.50	1.26	**-0.15**	1.01	0.09
ES10	Surface	29.6	3.03	1.35	0.74	-	-
ES10	Bottom	29.6	2.68	1.36	0.28	-	-
BoB[#]	Surface	30.9	2.48	-	-	-	-

Table S2. *Table with results of dissolved oxygen, trace element and saturation index using PHREEQC for Godavari estuary and groundwater.*

	Feature	DO	Al	Fe	Mn	SI index		
		ml/l	µM	µM	µM	Ca-montmorillonite	Kaolinite	Amorphous silica
Godavari estuary								
Dry season (March 2019)								
ES1	Surface	7.3	0.30	0.38	0.30	2.93	4.2	-0.85
ES2	Surface	7.2	0.23	0.11	0.08	0.79	2.35	-0.88
ES3	Surface	4.5	0.48	0.03	0.21	-0.66	1.75	-1.39
ES3	Bottom	4.1	0.39	0.02	0.07	-0.34	2.07	-1.46
ES4	Surface	4.4	0.32	0.02	0.10	-0.61	1.85	-1.47
ES4	Bottom	4.5	0.26	0.01	0.06	-1.8	1.05	-1.68
ES5	Surface	4.4	0.30	0.03	0.11	-1.99	0.86	-1.68
ES5	Bottom	3.9	0.46	0.07	0.09	-1.82	1	-1.67
ES6	Surface	6.7	0.27	0.05	0.14	-2.33	0.93	-1.98
ES7	Surface	5.5	0.42	0.17	0.17	-3.09	0.35	-2.04
ES7	Bottom	4.7	0.23	0.05	0.14	-3.3	0.24	-2.14
ES8	Surface	4.9	0.28	0.02	0.10	-4.93	-0.88	-2.39
ES8	Bottom	4.6	0.27	0.03	0.08	-4.73	-0.71	-2.39
ES9	Surface	6.2	0.44	0.08	0.10	-5.3	-1.21	-2.42
ES9	Bottom	4.8	0.36	0.02	0.14	-4.95	-0.87	-2.46
ES10	Surface	4.9	0.69	0.04	0.08	-5.15	-1.05	-2.46
ES10	Bottom	4.6	0.30	0.11	0.16	-4.26	-0.17	-2.51
Wet season (August 2019)								
ES1	Surface	5.1	0.46	0.01	0.04	2.47	4.2	-0.98
ES2	Surface	4.9	0.38	0.02	0.06	2.28	4.04	-0.98
ES3	Surface	5.4	0.43	0.03	0.09	2.48	4.25	-0.99
ES3	Bottom	4.8	0.41	0.03	0.06	2.43	4.21	-0.99
ES4	Surface	5.1	0.59	0.01	0.07	2.56	4.26	-0.99
ES5	Surface	4.5	0.58	0.01	0.23	2.78	4.51	-0.99
ES6	Surface	4.9	0.43	0.01	0.04	2.21	3.97	-0.99
ES7	Surface	4.8	0.68	0.02	0.20	2.36	4.2	-1.08
ES7	Surface		0.47	0.01	0.06	1.93	3.85	-1.09
ES8	Surface	5.1	0.46	0.01	0.08	1.88	3.81	-1.1
ES8	Surface		0.39	0.01	0.07	2.01	3.9	-1.06
ES9	Surface	4.9	0.33	0.01	0.06	1.84	3.76	-1.06
ES10	Surface	5.1	0.38	0.01	0.07	1.8	3.78	-1.11
Groundwater								
Dry season (March 2019)								
GW1	Open Well	1.8	0.36	0.73	0.10	3.37	4.42	-0.59
GW2	Borewell	1.3	0.33	4.79	0.08	3.42	4.37	-0.52
GW3	Open Well	0.8	0.36	0.22	0.47	4.03	4.68	-0.36
GW4	Open Well	0.4	0.28	19.9	0.16	2.53	3.74	-0.61
GW5	Handpump	0.3	0.81	0.51	14.42	3.78	4.94	-0.64
GW7	Open Well	0.5	0.36	32.9	0.28	3.26	4.33	-0.61
GW6	Open Well	0.2	0.21	9.27	0.55	2.33	3.63	-0.65
Wet season (August 2019)								
GW1	Open Well	0.9	0.74	0.75	0.58	3.81	4.69	-0.57
GW3	Open Well		0.31	0.27	0.07	4.05	4.66	-0.34
GW4	Open Well	0.6	0.19	5.43	0.07	1.83	2.85	-0.54
GW5	Handpump	0.5	0.43	0.56	12.58	2.72	3.8	-0.55
GW6	Open Well	0.8	0.17	3.35	0.05	2.19	3.28	-0.55
GW7	Open Well	0.7	0.74	5.66	0.38	4.09	4.83	-0.5
PZ1	Piezometer	0.6	0.29	2.96	0.10	2.37	3.23	-0.51
NBPZ1	Handpump	0.6	0.30	8.06	0.10	3.54	4.37	-0.44
PZ2	Piezometer		0.37	4.90	0.17	3.57	4.61	-0.59
NBPZ2	Open Well	3.4	0.28	0.08	0.04	2.68	3.45	-0.39
PZ3	Piezometer	0.6	0.26	2.88	0.09	0.76	2.51	-0.93
PZ4	Piezometer	0.6	0.21	7.52	0.12	3.26	4.09	-0.42
NBPZ4	Handpump	0.5	0.23	4.19	0.06	3.27	4.14	-0.46
PZ5	Piezometer	0.4	0.16	1.78	0.08	1.94	3.45	-0.81
NBPZ5	Handpump	0.6	0.31	2.95	0.22	3.67	4.60	-0.52

Supplementary figures

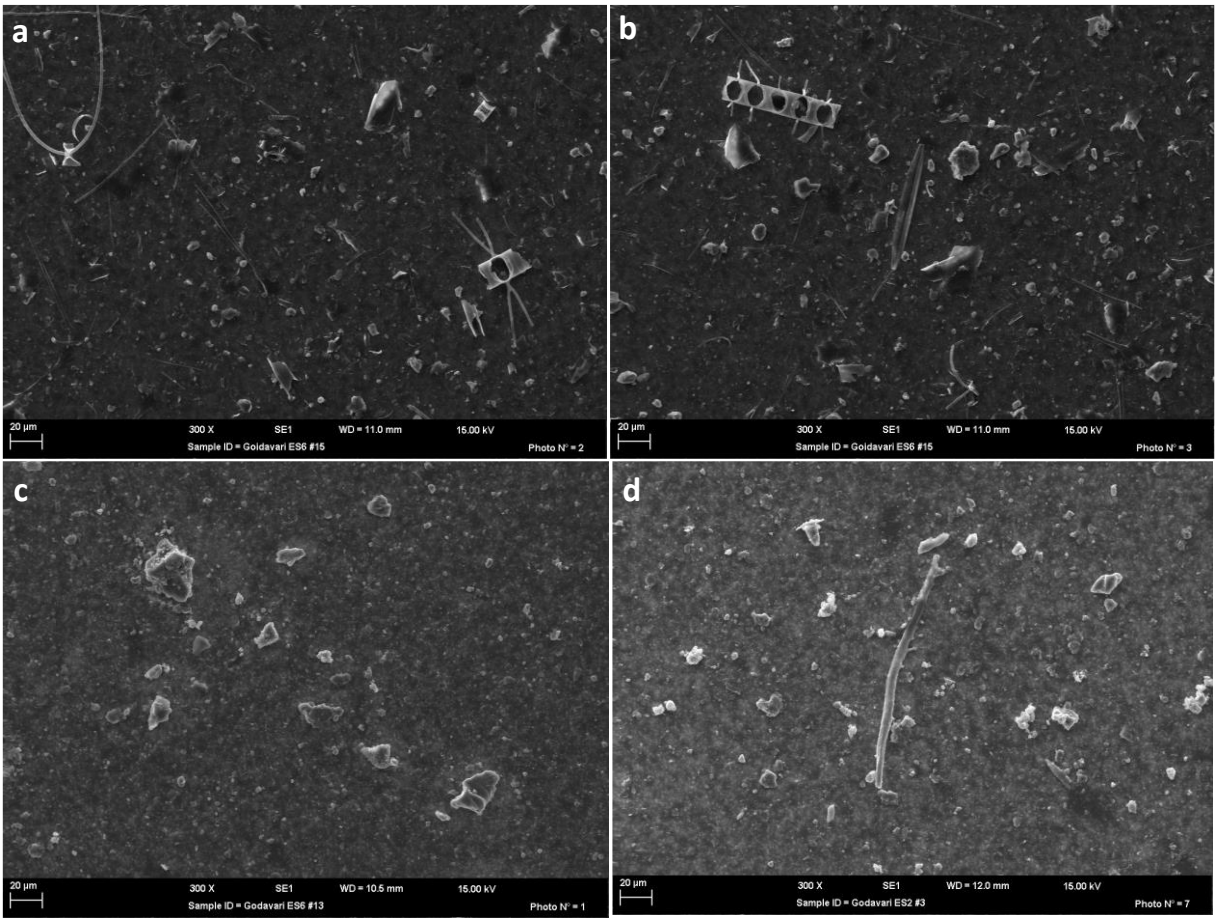

Figure S1. *The SEM images of suspended matter from Godavari estuary; a and b during dry season with diatom frustules clearly visible, c and d wet season with a lot of lithogenic particles with little or no diatom frustule identified.*

IIIb. Calcium and strontium transport across the land-ocean interface and implications on coastal groundwater

Sarath Pullyottum Kavil, Ramananda Chakrabarti, Jean Riotte, Arnaud Dapoigny, V.V.S.S Sarma, Damien Cardinal, *et al.*

Article in preparation

Abstract

The present study investigated the impact of sources and of processes in controlling Ca and Sr isotopic compositions of the tropical monsoonal Godavari estuary. Sampling was carried out during the dry and wet seasons to understand the variability associated with hydrological condition. We also analyzed the composition of groundwater adjacent to the estuary to assess the contribution of local groundwater to the estuary. During the dry season, the $^{87}Sr/^{86}Sr$ ratio in the estuary decreased from 0.71477 in the upstream river water endmember to 0.70926 at salinity of 30, also exhibiting a non-conservative mixing between seawater and river water. We attributed the deviation from binary mixing to groundwater discharge with an average $^{87}Sr/^{86}Sr$ ratio of 0.71187, with contributions ranging from 75% in the upper estuary to 6% in the lower estuary. Similar to $^{87}Sr/^{86}Sr$, $\delta^{44/40}Ca$ also exhibited a non-conservative mixing during the dry season, with a lower $\delta^{44/40}Ca$ compared to the mixing line in the upper estuary and higher $\delta^{44/40}Ca$ in some downstream locations. The input of Ca sourced from isotopically light groundwater adjacent to the upper estuary could explain the deviation from mixing line, while the excess $\delta^{44/40}Ca$, heavier than seawater, was explained by the precipitation of carbonates induced by diatom growth and photosynthesis. During the wet season, low salinity, Sr concentration and radiogenic $^{87}Sr/^{86}Sr$ ratio (0.715 to 0.717) were observed throughout the estuary. The more radiogenic composition is driven by the opening of dam and water influx from the main river channel and tributaries draining the Archean-Proterozoic gneiss complexes in the middle and lower reaches of Godavari basin. The $\delta^{44/40}Ca$ composition of the estuary was relatively low during the wet season with a higher Ca/Sr ratio, indicating increased contribution from carbonate weathering due to high discharge during monsoon. Groundwater exhibited no significant differences in $\delta^{44/40}Ca$ and $^{87}Sr/^{86}Sr$ ratio between dry and wet seasons, with $\delta^{44/40}Ca$ ranging from 0.57 to 3.48‰ and $^{87}Sr/^{86}Sr$ from 0.710 to 0.715. The variable $\delta^{44/40}Ca$ in groundwater was mainly driven by calcium carbonate precipitation in the aquifer with minor impact from plant uptake and adsorption onto phyllosilicates.

1. Introduction

Estuaries are highly dynamic transition zones between freshwater and oceans, exhibiting significant spatial and temporal variability in physicochemical properties depending on the extent of mixing and estuarine processes. Rivers deliver a considerable amount of terrestrial materials, such as suspended sediments and nutrients in both dissolved and particulate phases, into the estuarine system. A range of physical, chemical and biological processes occurring in the estuary can influence the elemental as well as sediment fluxes (Nedwell, 1999, Statham, 2012, Teuchies et al., 2013). Calcium is the fifth most abundant element in the upper continental crust, and an essential nutrient for biogeochemical cycling on Earth's surface (Rudnick and Gao, 2003). The weathering of Ca-bearing primary minerals, releases divalent cations and bicarbonate in the critical zone, and subsequent precipitation and burial of calcium carbonates in the ocean result in the net removal of CO_2 from the atmosphere (Walker et al., 1981, Berner et al., 1983). Calcium is also an essential macronutrient for plants and take part in intracellular signalling, cell wall stabilization and regulation of stomata (White and Broadley, 2003). Rivers and groundwater form a major link between continents and oceans in terms of elemental fluxes, and together supply the majority of Ca to the global ocean (Milliman, 1993, Holmden et al., 2012). Both riverine and groundwater solute fluxes are a major sources of nutrients to the coastal ocean and can significantly alter the oceanic biosphere and also the oceanic water and elemental budgets (Chester, 1990, Moore et al., 2010). The strontium isotope ratio, $^{87}Sr/^{86}Sr$ are routinely used to trace Ca cycling in continental systems due to the similar chemical behaviour of Ca and Sr (Jacobson et al., 2002, Pett-Ridge et al., 2009, Meek et al., 2016, Novak et al., 2020). The $^{87}Sr/^{86}Sr$ ratio is a conservative tracer for understanding solute sources, hydrological pathways and mixing of water masses (Bain and Bacon, 1992, Négrel et al., 2001, Shand et al., 2007).

A stable calcium isotopic ratio ($\delta^{44/40}Ca$) has been used to trace the Ca sources, understand biogeochemical processes, and quantify biogeochemical budgets in a variety of Ca reservoirs on the Earth's surface (Tipper et al., 2006, Holmden et al., 2012, Jacobson et al., 2015). In fluvial systems, Ca is sourced from weathering of both silicate and carbonate rocks, and the riverine budget of Ca is generally dominated by carbonate weathering (Meybeck, 1987, Gaillardet et al., 1999). However, an isotopic imbalance exists in the river system with the average estimated $\delta^{44/40}Ca$ of the riverine flux (0.88‰) to the oceans being closer to the isotopic signature of the bulk silicate Earth (BSE, 0.94 ‰, Kang et al., 2017) than carbonates (0.6‰),

indicating the relevance of secondary biogeochemical processes in terrestrial systems (Fantle and Tipper, 2014, Tipper, 2016). Calcium isotopic fractionation can occur during the precipitation of calcite (Lemarchand et al., 2004, Gussone et al., 2005, Tang et al., 2012), biotic uptake (Cenki-Tok et al., 2009, Cobert et al., 2011, Schmitt et al., 2013), adsorption onto phyllosilicates and ion exchange (Ockert et al., 2013, Brazier et al., 2019). Calcium has a long residence time of ~1 Myr in the modern ocean; due to the high concentration of Ca in seawater and relatively small input fluxes. Modern ocean exhibits a relatively homogenous $\delta^{44/40}$Ca value of 1.89±0.16‰ (2SD, n=62) which is primarily controlled by precipitation of biogenic and abiotic carbonates from the seawater (Fantle and Tipper, 2014, Griffith et al., 2020). Despite having similar biogeochemical controls on Ca cycling, groundwaters and spring waters are less constrained in $\delta^{44/40}$Ca and exhibit variability ranging from 0.17 to 2.08‰ (Tipper, 2016, Nelson et al., 2022). Recent studies suggest that the submarine groundwater discharge (SGD) is a dominant pathway for solute delivery to the coastal ocean, thus forming a significant component of oceanic biogeochemical cycling (Cho et al., 2018, Santos et al., 2021). However, SGD remains overlooked in ocean elemental budgets and is difficult to quantify given large spatial and temporal variability. Globally, groundwater-derived Ca contribution to the global ocean ranges from 5 to 39% of the global river discharge, with a distinct isotopic signature compared to rivers signifying its relevance in oceanic isotope budgets (Beck et al., 2013; Luijendijk et al., 2020; Mayfield et al., 2021). Measurements of $^{87}Sr/^{86}Sr$ in Indian estuaries and coastal oceans have been used to detect submarine groundwater discharge (SGD) signatures and to estimate SGD-derived Sr fluxes to the ocean (Basu et al., 2001, Rahaman and Singh, 2012, Chakrabarti et al., 2018, Damodararao and Singh, 2022). The estimated SGD derived Sr fluxes along Indian coast are similar to or higher than riverine fluxes, accounts for almost 0.3 to 0.7% of the global SGD Sr flux, with more radiogenic $^{87}Sr/^{86}Sr$ ratio (Beck et al., 2013, Damodararao and Singh, 2022). However, the SGD fluxes to the estuary and coastal ocean are poorly constrained and can be spatially and temporally variable and complex, depending on the extent of tidal influence, groundwater-surface water interactions and other estuarine processes (Moore et al., 2010).

Past investigations in the Godavari estuary have documented intra-annual variability in nutrient concentration depending on discharge (Sarma et al., 2010), seasonal phytoplankton blooms (Acharyya et al., 2012), and significant groundwater discharge (Rengarajan and Sarma, 2015, Damodararao and Singh, 2022). The $^{87}Sr/^{86}Sr$ and $\delta^{44/40}$Ca are also reported for upper Godavari river draining Deccan traps, which indicated dominance of basaltic weathering and carbonate

precipitation (Valens, 2021). The primary objective of the present study is to investigate the impact of estuarine processes on the elemental and isotopic composition of Ca and Sr in the Godavari estuary. Through seasonal sampling during monsoon and pre-monsoon, we also aim to capture the temporal variability associated with immediate monsoonal precipitation in estuarine processes. We employed Sr and $^{87}Sr/^{86}Sr$ to elucidate the sources and mixing of between river water, seawater, and groundwater, following which we interpret the associated variability in $\delta^{44/40}Ca$ of the estuary. Additionally, the composition of groundwater adjacent to the estuary are compared to decipher the groundwater mixing processes and their impact on the estuarine Ca and Sr cycling. Finally, we evaluate the roles of various biogeochemical processes occurring in the estuary and groundwater to explain the $\delta^{44/40}Ca$ composition.

2. Materials and Methods

2.1. Regional setting

Godavari is the second largest river and largest peninsular river in India, originating from Western Ghats and flowing eastwards through the Indian peninsular shield. The river traverses almost 1480 km, draining Deccan basalts (dominant upstream, 48% of the drainage area), peninsular gneiss (39%), and sedimentary rocks (11%) before discharging into the Bay of Bengal (Biksham and Subramanian 1988). The river basin climate varies from semi-arid in the rain shadow region of Western Ghats to sub-humid in the lower basin. The river water levels are largely monsoon driven and the river receives rainfall from both Southwest and Northeast monsoons, with the majority of the rainfall occurring from July to September (Sarma et al., 2010). Godavari estuarine system covers an area of 330 km^2, and the river flowing to the estuary is regulated by a century-old dam in Dowleiswaram (~80 km upstream of the river mouth). After the dam, the river splits into two branches, Gautami and Vasista Godavari branch (Fig. 1). The annual discharge of the Godavari river is 105 km^3, with 93-96% of the annual flow occurring during the monsoon season (Rao, 1975, Gupta et al., 1997). Based on the discharge patterns driven by monsoon and opening and closing of the dams, Sarma et al, (2010) classified annual discharge into three main discharge periods: i) peak discharge (typically>2000 m^3/s) between June and September, ii) moderate discharge period (between 0 and 2000 m^3/s) from October to December and iii) "no discharge" period when the dam is closed from January to May. The tides in the estuary are semi-diurnal with an amplitude of 1.5 m, and an average current speed of 1-2 m/s (Acharyya et al., 2012). Estuary has average depth and width of 8 m and 1200 m, respectively (Sridevi et al., 2015). The deltaic plains surrounding

the estuary region are extensively cultivated, dominated by rice and rainfed crops, with extensive fertilizer application.

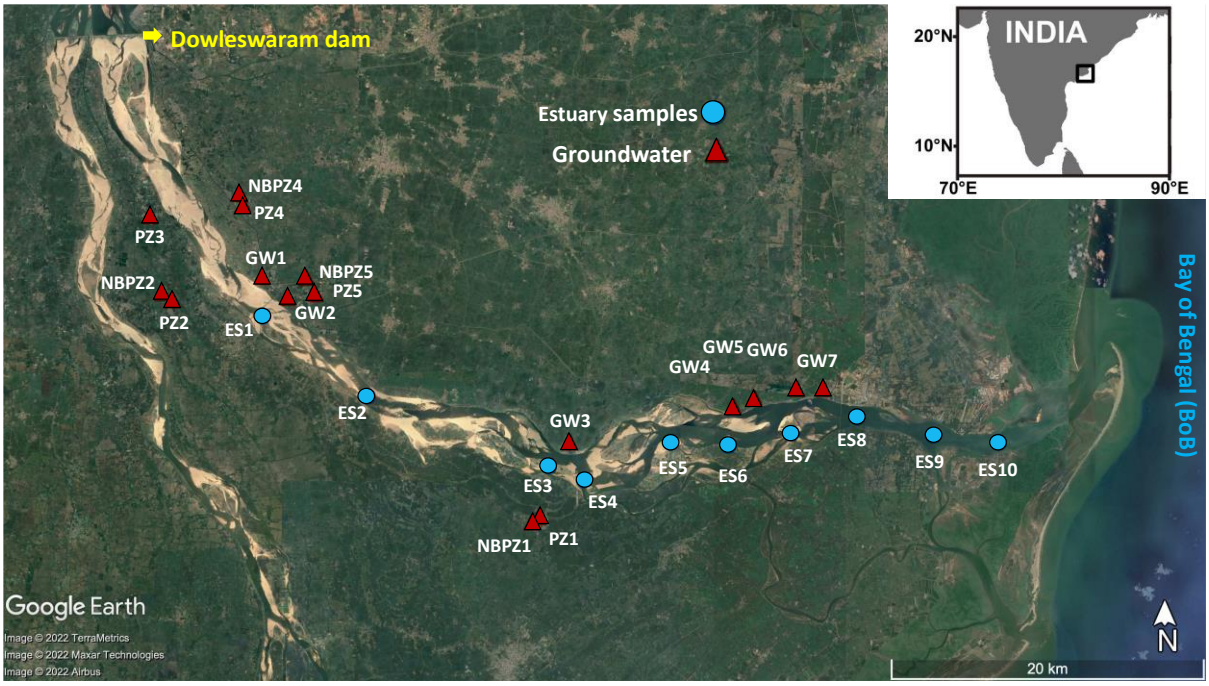

Figure 1. *Google Earth image of Godavari estuary region with sampling locations marked on the Gautami Godavari branch. The estuary samples are marked as blue circles and the groundwaters as red triangles, the location of the Dowleiswaram dam and Bay of Bengal is also marked in the figure (Google Earth version 6, 2022, Godavari).*

2.2. Sampling and elemental analysis

Estuary samples were collected from ten locations in the Gautami branch of the Godavari river, downstream of the Dowleiswaram dam, during March (dry season) and August (wet season) 2019. Sampling was carried out by mechanized boat and samples were collected using a 5 L Niskin bottles. Both surface and bottom water were collected wherever the water column is deeper than 5 m. Groundwater samples were collected from borewells and handpumps at seven locations adjacent to the estuary along the left bank during both March and August. We collected an additional nine groundwater samples from piezometers and handpumps exclusively during August from the estuarine region (Fig. 1). Temperature, conductivity, and salinity (for estuary) were measured on-site using portable sensors (CTD; SBE-19plus, Sea-Bird Electronics, USA). The precision of the salinity and temperature sensor was ±0.001 and ±0.001 ^{o}C, respectively. The depth of groundwater level for open wells and borewells was measured as depth below ground level using a skinny dipper device. The groundwater depth for hand pumps was assumed to be 5m. Almost 100 mL of water samples were filtered through

0.45 μm PES filters (SUPOR) and acidified using double distilled HNO_3 to pH<2 before storage. The details of sampling and storage for phytoplankton pigment analysis were already published elsewhere (Roy et al., 2015). The concentration of major cations (Na, K, Mg, Ca) and Sr were measured by quadrupole ICPMS at IRD, Bondy (Agilent 7500) and at CEaS, IISc (Thermo Scientific X-Series II). The accuracy of the cation analyses was checked using certified river water reference material, SLRS-6 (NRC-CNRC, Canada) and rock standard AGV-2 (Guano-valley Andesite). Scanning electron microscope (SEM, EVO LS15, ZEISS) observations were made on selected samples were suspended matter filtrate was available at ALYSES facility (IRD-SU), IRD Bondy. The obtained precision was better than 10%. Saturation indices were estimated using PHREEQC software with llnl.dat thermodynamic database (Parkhurst and Appelo, 1999).

2.3. Ca and Sr isotope analysis

Strontium was separated from water matrix using cation-exchange chromatography following established protocols (Banerjee et al., 2016). The separation protocol follows two steps of Sr purification using BioRad AG50W X8 (100–200 mesh) resin where Sr is eluted in 3N HCl. The purified Sr was loaded on a single-degassed Ta filament and using orthophosphoric acid and Ta_2O_5 was added as an activator. Subsequently, Sr isotopes were measured using a thermal ionization mass spectrometer (TIMS, Thermo Scientific Triton Plus) at CEaS, IISc. Instrument mass fractionation was corrected using $^{86}Sr/^{88}Sr$ ratio=0.1194 following an exponential law. The average uncertainty in the measured $^{87}Sr/^{86}Sr$ was better than 10 ppm. The NIST SRM987 Sr isotopic standard analyzed during this study yielded $^{87}Sr/^{86}Sr$ ratio of 0.710277±0.000020 (1SD, n=10).

For calcium isotope analysis, an aliquot of water sample containing around 10 μg of Ca was mixed with an optimal amount of ^{43}Ca-^{48}Ca double spike in a Teflon beaker and the mixture was kept on a hot plate for 8 hours at 80 ^{o}C to ensure equilibration between sample and spike, following which the mixture was evaporated. Calcium was purified using cation exchange chromatography (AG50W X8, 200-400 mesh resin), and Ca was eluted in 2.5 N HCl. For all samples, the separation procedure was repeated for eluted Ca to ensure the complete removal of the rest of the elements present in the sample matrix. Post evaporation the purified Ca cut was treated with a few drops of double distilled HNO_3 to oxidize leaked organic resins from the columns. Approximately 2.5 μg of purified Ca was loaded onto a degassed Ta filament using 0.8M HNO_3, followed by the addition of Ta_2O_5 activator while degassed Re filaments

were used as ionization filaments. Calcium isotopic ratios were also measured using a thermal ionization mass spectrometer (TIMS, Thermo Scientific Triton Plus) at CEaS, IISc following established laboratory protocol (Mondal and Chakrabarti, 2018, Banerjee and Chakrabarti, 2018). The $\delta^{44/40}$Ca calcium values are reported relative to NIST SRM 915a; the accuracy of the data is based on multiple measurements of NASS-6 seawater (1.87±0.1‰, 2SD, n=5) and NIST SRM 915a (-0.01±0.1‰, n=3), which is consistent with published results (e.g., Chakrabarti et al., 2021) while the external reproducibility, also based on multiple measurements of standards is better than 0.1‰ per mil (2SD).

3. Results

All measured physiochemical measurements, concentration and isotopic data for Godavari estuary and groundwater samples are given in Table 1.

3.1. Ca and Sr variability estuary and groundwater

During the dry season in the estuary, Ca and Sr concentration increases along the salinity gradient from 817 μM and 3.5 μM in most upstream samples at a salinity of 0.4, to 8975 μM and 80.1 μM in the most downstream station at a salinity of 29.6 respectively (Table 1, Fig. S1). Wet season samples in the estuary exhibit homogenously low Ca, Sr concentrations and salinity (<1) throughout the estuary, with an average of 428±28 μM for Ca and 0.9±0.04 μM for Sr (Fig. S1). Overall, Ca and Sr concentrations in the most upstream river water endmember was diluted during the wet season compared to the dry season. The Ca concentration in groundwater varies between 172 to 4786 μM, with an average of 832±563 μM during the dry season and 1806 ±1126 μM during the wet season (Table 1).

3.2. Variability in $^{87}Sr/^{86}Sr$ composition

The $^{87}Sr/^{86}Sr$ ratio of estuary samples decreases along the salinity gradient, with the most radiogenic value from estuary water collected farthest upstream (0.71477, sample ES1), least radiogenic value of 0.70926 in the most downstream (sample ES10). The fresh river water endmember is close to the reported $^{87}Sr/^{86}Sr$ ratio of Godavari river by Sharma et al, (2007) and the most downstream sample value is similar to modern seawater ratio of Bay of Bengal (Chakrabarti et al., 2018; Danish et al., 2020). During the wet season, the entire estuary exhibited a more radiogenic $^{87}Sr/^{86}Sr$ ratio, ranging from 0.715 to 0.717, with no trend along the estuarine transect. The average $^{87}Sr/^{86}Sr$ of the estuary samples in the wet season was

0.716, similar to the fresh Godavari River water endmember reported by Sharma et al (2007). Groundwater exhibits a narrow range of variability in $^{87}Sr/^{86}Sr$ from 0.71016 to 0.71254, with a single outlier piezometer, PZ3, with $^{87}Sr/^{86}Sr$ of 0.71500. The $^{87}Sr/^{86}Sr$ ratio in PZ3 groundwater was similar to upstream estuarine water at ES1. We observed no significant seasonal variability in $^{87}Sr/^{86}Sr$ of groundwater (Table 1).

Table 1. *Salinity, Na, Ca, Sr, Ca isotopes and Sr isotope ratio of estuary and groundwater from Godavari during dry and wet season. The '*' indicates that the depth to water table (below ground level in meters) with handpumps assumed to be 5 m deep, and '#' indicates 2 standard deviations for internal errors associated with δ44/40Ca measurement with atleast 20 blocks of data.*

		Salinity	Na µM	Ca µM	$\delta^{44/40}Ca$ ‰	$2SD^{\#}$ ‰	Sr µM	$^{87}Sr/^{86}Sr$
Godavari estuary								
Dry season								
ES1	Surface	0.4	3234	817	1.29	0.1	3.5	0.714772
ES2	Surface	0.9	12475	1065	1.13	0.17	4.2	0.712314
ES3	Surface	9.3	139888	4129	1.66	0.11	29.0	0.709977
ES3	Bottom	9.9	159419	4384			31.8	0.709917
ES4	Surface	11.7	162986	4440	1.39		33.3	0.709851
ES4	Bottom	11.7	169684	4533			34.5	0.709857
ES5	Surface	20.3	278167	6576	1.69	0.09	55.3	0.709433
ES5	Bottom	20.2	277819	6654			55.4	0.709439
ES6	Surface	24.7	344414	7864	2.40	0.15	71.3	0.709340
ES7	Surface	25.5	345458	8038	2	0.12	70.9	0.709399
ES7	Bottom	27.3	359290	8148			71.4	0.709321
ES8	Surface	27.3	371948	8540			72.9	0.709296
ES8	Bottom	28.0	374688	8549			75.3	
ES9	Surface	28.4	383910	8844			79.2	0.709268
ES9	Bottom	28.7	392696	9002			78.7	
ES10	Surface	29.6	396959	8975	1.89	0.1	80.1	0.709284
ES10	Bottom	29.6	400874	9296	1.81	0.1	77.5	0.709262
Wet season								
ES1	Surface	0.2	386.7	488.6	0.9	0.1	1.0	0.716246
ES2	Surface	0.1	350.6	472.6	1.24	0.15	0.9	0.7158
ES3	Surface	0.0	293.6	425.0	1.14	0.1	0.8	0.715626
ES3	Bottom	0.1	267.4	408.2			0.8	0.715933
ES4	Surface	0.0	265.5	407.2			0.8	0.715651
ES5	Surface	0.0	295.8	425.0	0.76	0.13	0.8	0.716163
ES6	Surface	0.0	291.6	401.6			0.9	0.715792
ES7	Surface	0.0	292.7	406.1	0.84	0.13	0.8	0.716009
ES7	Surface	0.1	333.8	426.6			0.9	
ES8	Surface	0.0	337.8	433.6			0.9	
ES8	Surface	0.1	331.9	419.8			0.9	0.715757
ES9	Surface	0.0	327.6	415.5	0.71	0.12	0.9	0.715791
ES10	Surface	0.0	752.0	431.6	0.83	0.11	0.9	0.717084

		Depth* (m)	Na µM	Ca µM	$\delta^{44/40}$Ca ‰	2SD# ‰	Sr µM	$^{87}Sr/^{86}Sr$
Groundwater								
Dry season								
GW1	Open well	3.3	2584	1248	1.73	0.13	6.5	0.711092
GW2	Borewell	23	2042	1088			5.7	0.712506
GW3	Open well	4	1255	1378	0.97	0.13	2.9	0.711554
GW4	Open well	2	5404	176	2.41	0.12	15.4	0.711476
GW5	Handpump	5	17317	172	1.08	0.13	1.2	0.710173
GW7	Open well	3.3	4766	1380			6.0	0.711695
GW6	Open well	n.a	1598	384	2.02	0.12	4.1	0.712137
Wet season								
GW1	Open well	1.3	2168	1845	0.99	0.11	6.0	0.712792
GW3	Open well	1.3	111	2206	1.23	0.11	4.7	0.711575
GW4	Open well	1.1	32265	3003	2.16	0.11	22.2	0.711189
GW5	Handpump	5	16491	183	1.54	0.16	1.3	0.710163
GW6	Open well	1.9	1223	1636			5.0	0.712071
GW7	Open well	0.5	1166	2669	0.57	0.16	3.8	0.712685
PZ1	Piezometer	4.3	8583	4786	1.51	0.11	17.3	0.711329
NBPZ1	Handpump	5	1233	1184			7.9	
PZ2	Piezometer	7.7	1379	1494	0.95	0.14	2.8	0.711358
NBPZ2	Open well	2.0	12786	776	2.1	0.13	7.1	0.712225
PZ3	Piezometer	3.9	2744	352	3.48	0.17	3.7	0.715004
PZ4	Piezometer	7.2	1003	1435			3.6	0.712547
NBPZ4	Handpump	20	2777	2029	1.26	0.1	5.0	0.711757
PZ5	Piezometer	4.9	408	1615			7.8	0.712061
NBPZ5	Handpump	5	1050	1873			4.9	

3.3. $\delta^{44/40}$Ca variability in estuary and groundwater

The $\delta^{44/40}$Ca values of Godavari estuary water are reported in Table 1. During the dry season, $\delta^{44/40}$Ca values vary between 1.13 to 2.40‰, with high saline endmember exhibiting a $\delta^{44/40}$Ca ratio close to modern global seawater (1.89±0.16‰) (Tipper et al 2016). The highest $\delta^{44/40}$Ca value of 2.4‰ was observed at a salinity of 25 (ES6) and the lowest at ES2 (Table 1). The $\delta^{44/40}$Ca of the surface and bottom samples were analysed only at ES10 (1.89‰ and 1.81‰ for surface and bottom) and remained within the analytical uncertainty. Similar to $^{87}Sr/^{86}Sr$, $\delta^{44/40}$Ca values of wet season samples was more homogenous with an average of 0.92±0.2‰ and significantly lower than the seawater. The groundwater $\delta^{44/40}$Ca values exhibit a large variability from 0.57 to 3.48‰ with an average $\delta^{44/40}$Ca of 1.6 ‰. The groundwater exhibited insignificant seasonal differences in $\delta^{44/40}$Ca, despite exhibiting significantly high Ca concentrations during the wet season (p-value <0.05).

4. Discussion

The discussion of the results from this study is presented as three sections. First, we look at the variability and mixing between water masses in the Godavari estuary based on Sr and $^{87}Sr/^{86}Sr$, and estimate the proportion of mixing using source-specific $^{87}Sr/^{86}Sr$ ratio. Following this, we considered various sources of Sr and Ca in the estuary, focusing on lithological endmembers from the region. Finally, we decipher processes that can explain the observed variability of $\delta^{44/40}Ca$ in the estuary and groundwater.

4.1. Mixing between water sources in the dry season

Previous studies documented non-conservative mixing in Sr isotopes from western estuaries in India (Rahaman and Singh, 2012), and from the same branch of Godavari estuary, further downstream during post-monsoon (Damodararao and Singh, 2022). The $^{87}Sr/^{86}Sr$ vs. 1/Sr plot shows that estuary samples during the dry season deviated from the theoretical mixing line between river water and seawater, indicating a non-conservative behaviour in the estuary (Fig 2). The deviation from simple mixing can be due to the supply of Sr from additional sources, such as groundwater, dissolution of silicates and carbonates, and/or desorption from particulate Fe-Mn oxyhydroxides (Andersson, 1994, Rahaman and Singh, 2012, Beck et al., 2013). Submarine groundwater discharge is documented in Godavari estuary using Ra isotopes, with an SGD flux ranging from 1.3 to 7.4 $*10^6$ m^3/day (post monsoon and pre monsoon sampling, Rengarajan and Sarma, 2015). Thus, groundwater discharge can be considered as a significant source of Sr to the estuary. From Fig. 2, it is clear that compared to the theoretical mixing line, we observe a lower $^{87}Sr/^{86}Sr$ at low salinity sample ES2, and higher $^{87}Sr/^{86}Sr$ than expected at higher salinity samples. All the groundwaters sampled from the Godavari estuary region exhibited a narrow range of $^{87}Sr/^{86}Sr$ from 0.710 to 0.712 with no seasonal differences (Fig. 2). We suspect the radiogenic value in the outlier shallow piezometer (PZ3) results from leaching of irrigated canal water, which originates from the Dowleiswaram dam. This explains why PZ3 plots were almost identical to the ES1 (most upstream samples) in Figure 2. One possibility of a less radiogenic Sr source to the groundwater is fertilizers, which are extensively applied in the cultivated areas of the Godavari estuarine region. Previously documented values of $^{87}Sr/^{86}Sr$ for fertilizers globally range from 0.7066 to 0.7095, and a consistent value was also observed in fertilizer mix from Berambadi (Sr of 350 ppm and $^{87}Sr/^{86}Sr$ ratio of 0.708, Chapter II) (Vitòria et al., 2004, Zou et al., 2018, Acharya et al., 2022). Homogeneity in Sr isotopic composition in majority of groundwater samples, higher than fertilizers and seawater, indicates

that coastal aquifer signatures may be driven by local aquifer lithology and water-rock interactions (Santoni et al., 2016). However, in order to calculate the SGD flux using inverse modelling, Damodararao and Singh, (2022) assumed an $^{87}Sr/^{86}Sr$ of 0.718 as SGD endmember (based on $^{87}Sr/^{86}Sr$ of a tributary of Godavari). This value does not correspond to the groundwater composition in Godavari estuary, varying between 0.710 to 0.715 (Fig 2). Thus, we re-estimated the SGD fluxes for Godavari estuary using adjacent coastal groundwater $^{87}Sr/^{86}Sr$ as an endmember composition.

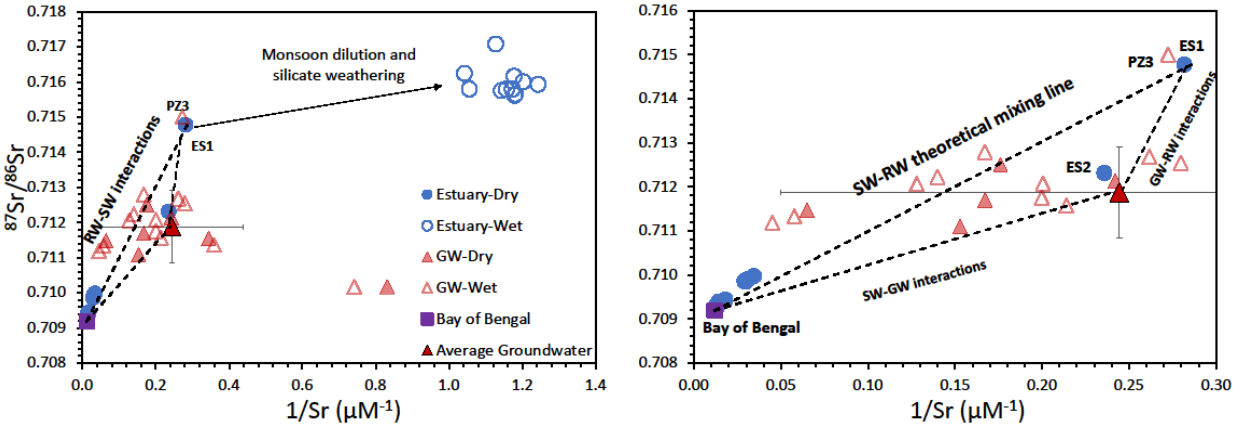

***Figure 2**. Plot of, a) $^{87}Sr/^{86}Sr$ vs. 1/Sr (μM^{-1}) for estuary and groundwater sample in Godavari. The dotted lines represent mixing lines between Bay of Bengal seawater (SW), Godavari river water (RW) and the average Godavari coastal groundwater (GW, large red triangle with original data points blurred in the background), b) $^{87}Sr/^{86}Sr$ vs. 1/Sr (μM^{-1}) plot in a smaller scale focusing on the estuary during dry season and groundwater average. The Bay of Bengal endmember Sr and $^{87}Sr/^{86}Sr$ data is from seawater samples off the coast of Odisha published by Danish et al. (2020).*

The mixing proportions of three endmembers; groundwater, fresh river water and seawater were recalculated using a simmr package, a Bayesian stable isotope mixing model implemented in R (Parnell et al., 2010, Zhang et al., 2021). The proportional contribution from each of the defined sources are estimated based on measured source specific isotopic tracers such as $^{87}Sr/^{86}Sr$ and $\delta^{18}O$. The results indicate that the proportion of groundwater contribution during dry season varies from 40% to 15% between salinity of 0.4 and 20 (here onwards upper estuary) to 15 to 10% at salinity between salinity of 20 and of 30 (lower estuary), indicating a higher contribution of groundwater in the upper estuary (Fig. 3). During dry season, due to low salinity, Sr concentration and low riverine discharge in the upper estuary, the contribution from groundwater with higher Sr concentration can significantly reduce the $^{87}Sr/^{86}Sr$ ratio. In the lower region of the estuary, where salinity and Sr concentration were high due to tidal

influence, groundwater discharge acts as a source of more radiogenic $^{87}Sr/^{86}Sr$, shifting the estuary samples above the mixing line (Fig. 2). Therefore, Sr fluxes resulting from groundwater discharge with a distinct $^{87}Sr/^{86}Sr$ ratio can explain the observed non-conservative behaviour in the estuary (Damodararao and Singh, 2022).

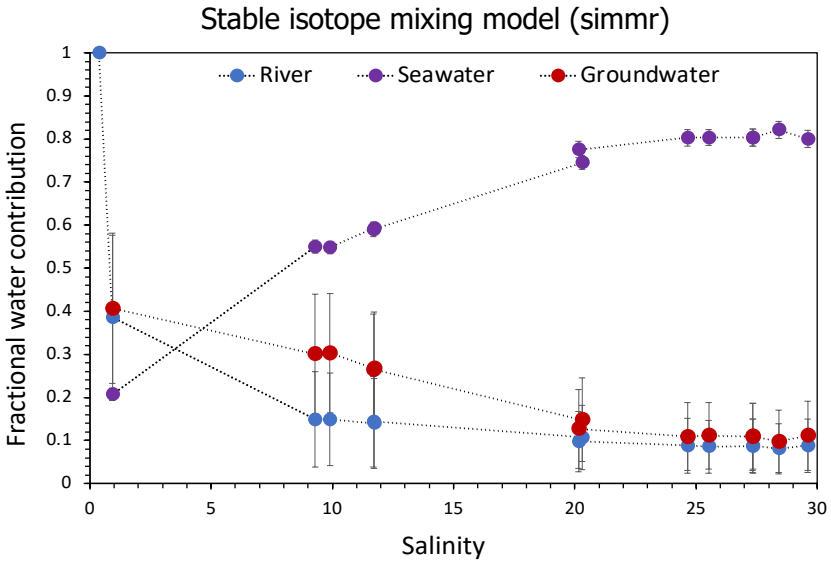

Figure 3*. Fractional water contribution of river water, groundwater, and seawater for dry season Godavari estuary samples along the salinity gradient.*

One must be cautious here to assign groundwater as the only significant Sr source to lower estuary given that the average Sr content in groundwater is much lower than the seawater dominated in the lower estuarine region. The other possible Sr sources to lower estuary which are more radiogenic than seawater should be evaluated. Firstly, carbonate dissolution from suspended matter and sediment can be an additional source of Sr to the estuary, but the average $^{87}Sr/^{86}Sr$ ratio of carbonates from peninsular India is much lower than groundwater and seawater ($^{87}Sr/^{86}Sr$ ratio of 0.707, Nagarajan et al., 2013, Govind et al., 2021). Thus, carbonate dissolution cannot explain the more radiogenic signature in the lower part of the estuary. Suspended particulate matter in the Godavari river is estimated to be highly radiogenic with an $^{87}Sr/^{86}Sr$ ratio ranging from 0.720 to 0.745 and can be a source of radiogenic Sr to the lower estuary (Ahmed et al., 2009, Jeandel and Oelkers, 2015, Damodararao and Singh, 2022). However, the dissolution of riverine suspended matter and bedload are known to release only 0.2% of Sr to the estuary. Such process can only have a minor impact on the Sr concentration and $^{87}Sr/^{86}Sr$ (Jones et al., 2012), especially in the dry season where suspended particles content of continental origin is low (Mangalaa et al., 2017). Overall, during the dry season, the distribution of Sr is controlled by two processes; i) simple mixing between more concentrated

less radiogenic (0.70926) seawater and low Sr more radiogenic (0.71477) river water, ii) additional groundwater discharge with Sr concentration from 1 to 15 µM and $^{87}Sr/^{86}Sr$ of 0.71187±0.001 (n=20).

4.2. Tracing sources of Sr and Ca in the estuary

4.2.1 Sr and $^{87}Sr/^{86}Sr$ ratio

In contrast to the dry season, Godavari estuary during the wet season exhibits a radiogenic and comparatively narrow range of $^{87}Sr/^{86}Sr$ (0.71598 to 0.71708) with a uniformly diluted Sr concentration (0.87±0.04 µM) (Fig. 2). Together with the absence of salinity gradient (salinity<0.2) in the wet season, $^{87}Sr/^{86}Sr$ signatures indicate that estuary was dominated by fresh river water from lower reaches of Godavari, resulting from the opening of dam. The $^{87}Sr/^{86}Sr$ values were slightly radiogenic compared to river water endmember during the dry season ($^{87}Sr/^{86}Sr$ ratio of 0.71477), but comparable to previously published $^{87}Sr/^{86}Sr$ of 0.71630 from Dowleiswaram dam (Fig. 2, Sharma et al 2007). As discussed earlier, the reduction in riverine endmember $^{87}Sr/^{86}Sr$ ratio during the dry season can be explained by inputs from less radiogenic groundwater and tidal mixing. In wet season, the input of groundwater into the estuary can be neglected as the $^{87}Sr/^{86}Sr$ ratio of the estuary is more radiogenic than groundwater, which are also almost an order of magnitude higher in Sr concentration (Fig. 2). Neglecting any input from seawater, the Sr source from silicate and carbonate weathering in the river basin is possible during the wet season into the estuary. Based on a two-component mixing model with silicate (0.750±0.049, Jayananda et al., 2015) and carbonate (0.707±0.003, Nagarajan et al., 2013) endmembers, the average contribution of Sr from carbonate weathering during wet season estuary was estimated to be 79±15% (simmr package in R, Fig. S2). However, such calculations are prone to high uncertainty due to variability associated with the endmember composition (Nagarajan et al., 2013, Jayananda et al., 2015, Govind et al., 2021,). Given that carbonate rock from the basin typically exhibit a less $^{87}Sr/^{86}Sr$ ratio, the radiogenic Sr isotopic signature during the wet season can be attributed to an increase in water flux from silicate weathering regimes in downstream tributaries of the Godavari, such as Sabari and Indravati rivers. Both tributaries drain Precambrian granite, gneiss, charnockites rock and Eastern khondalites belt (Jha et al., 2009). Archean-Proterozoic gneiss complexes in the Indian craton region are known to contain radiogenic rocks, such as granitic gneiss ($^{87}Sr/^{86}Sr$ ratio between 0.703 to 0.865, Jayananda et al., 2015) and khondalites ($^{87}Sr/^{86}Sr$ ratio between 0.797 to 1.049, Rickers et al., 2001). During monsoon, more $^{87}Sr/^{86}Sr$ signatures resulting from water-

rock interactions with such radiogenic phases reach downstream Godavari and then the estuarine region. Suspended particulate matter in the downstream Godavari basin during the post-monsoon also exhibited $^{87}Sr/^{86}Sr$ value ranging from 0.720 to 0.746, indicating the erosion of radiogenic mineral phases from the Archean-Proterozoic gneiss complexes (Ahmed et al., 2009, Damodararao and Singh, 2022). Spatio-temporal variability in monsoonal precipitation also accounted for the variability in $^{87}Sr/^{86}Sr$ ratio of offshore sediments, where the higher contribution from Archean-Proterozoic gneiss complexes during monsoon led to more radiogenic sediments (Peketi et al., 2020). Overall, fresh river water influx into the estuary during heavy monsoonal precipitation from lower tributaries draining old silicate rocks with radiogenic Sr composition can explain the homogenous, radiogenic $^{87}Sr/^{86}Sr$ values in the estuary during the wet season.

4.2.2. Ca and $\delta^{44/40}Ca$

At the global scale, almost two-thirds of the riverine Ca is derived from weathering of carbonate rocks in the river basin and the rest from silicate weathering, meteoric input and evaporites (Berner and Bern 1997, Gaillardet et al., 1999). We can neglect the input from atmospheric deposition as rainwater input of Ca is minor in the Godavari basin and no significant evaporite deposits are reported in the region (Biksham and Subramanian, 1988, Jha et al., 2009). Seasonal variability in carbonate and silicate weathering fluxes in river basins occurs due to the differential sensitivity of carbonate and silicate minerals to monsoonal runoff (Tipper et al., 2006, Jha et al., 2009). The $\delta^{44/40}Ca$ values at the most upstream Godavari river water end member was 1.29‰ and 0.90‰ during the dry and wet seasons, respectively, more on the heavier range of previously reported $\delta^{44/40}Ca$ at the mouth of the large rivers (from 0.67 to 1.25‰, an average of 0.86±0.29‰) (Zhu and MacDougall, 1998, Schmitt et al., 2003, Tipper et al., 2010).

The seasonal disparity between river water endmember can result from, i) interactions with groundwater and seawater, particularly during the dry season, ii) less precipitation and/or more contribution from carbonate weathering during the wet season as a result of undersaturation of calcite and low pH in the river water (Fig. S3). Resuspension of carbonates in riverine bedload due to high discharge and dissolution of Vindhyan carbonate present in the middle and lower reaches of the Godavari river can be a potential source of easily weatherable carbonates in the basin, especially during the monsoon (Jha et al., 2009, Mishra et al., 2011). To explain the variability of the estuary and groundwater, the sources of Ca may be restricted to three

endmembers, i) silicate rocks drained by the river and aquifer, ii) carbonate rocks present in the sediments and also pedogenic carbonates formed in soil and saprolite, iii) Bay of Bengal seawater in the estuary (during the dry season). As observed in Fig. 4, most of the estuary samples and groundwaters show a linear correlation with Sr/Ca, but cannot be explained by simple mixing between the three proposed endmembers (Nelson et al., 2022). Assuming no fractionation associated with the dissolution of silicates and carbonates (Alkhatib et al., 2022), the pattern indicates that the $\delta^{44/40}$Ca of water samples are driven by processes rather than mixing (Fig. 4), and it is discussed in the next section. Additionally, the estuary shows a characteristically lower Sr/Ca ratio with a lighter $\delta^{44/40}$Ca, closer to a carbonate end member, during wet season confirming an increased contribution from carbonate weathering during monsoon. There is, however, more than one potential mixing line possible among the end members given a large number of mineral phases and preferential weathering in the basin (Banerjee and Chakrabarti 2018), heterogenous chemical composition (Jayananda et al., 2015) and associated large variability in $\delta^{44/40}$Ca (Fantle and Tipper 2014).

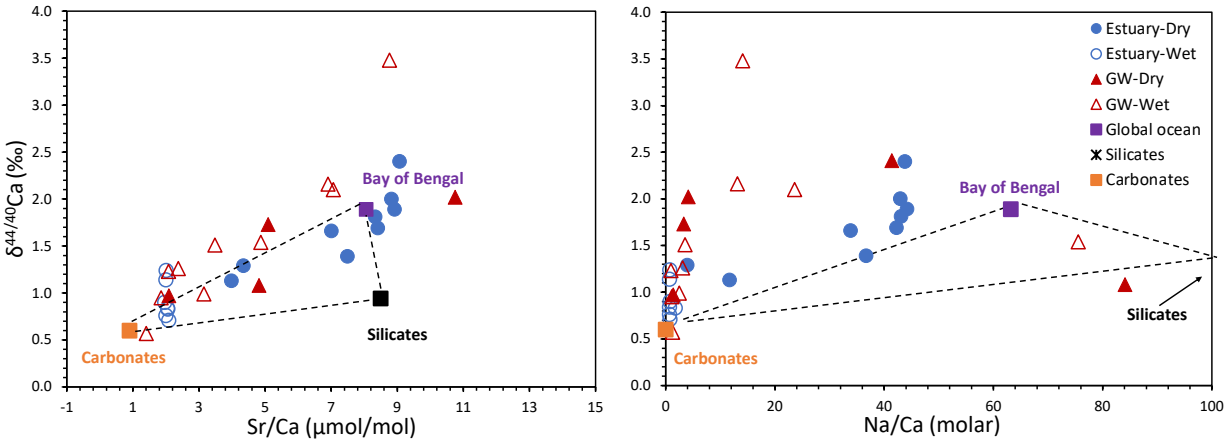

Figure 4. *Plot between a) Sr/Ca ratio (µmol/mol) vs. $\delta^{44/40}$Ca and b) a) Na/Ca molar ratio vs. $\delta^{44/40}$Ca of the estuary and groundwater samples from Godavari. The end members identified in the plot are based on Gaillardet et al (1997) for elemental ratios and Fantle and Tipper, (2014), Jayananda et al (2015), Chakrabarti et al., (2018) for isotopic ratios.*

4.3. Effect of mixing vs. fractionation on $\delta^{44/40}$Ca during dry season

4.3.1 Three end-member mixing

The Ca concentration in the estuary increases linearly with salinity during the dry season, indicating mixing between fresh river water and seawater but remains homogenous during the wet season (Fig. S1). The Ca concentration shows an excess compared to the theoretical mixing line in the upper estuary, indicating a source of Ca likely resulting from groundwater input as

evidenced by Sr isotopes (Fig. S1). The mixing plots of $\delta^{44/40}Ca$ *vs.* salinity shows a non-conservative behaviour, with a lighter than expected $\delta^{44/40}Ca$ in the upper estuary (ES2, ES3, ES4) and a heavier $\delta^{44/40}Ca$ at the middle estuary (ES6, ES7) (Fig. 5a). The value at the most downstream sampling location, including surface and bottom estuary, is identical to global seawater average $\delta^{44/40}Ca$ of 1.89±0.16‰ (Fantle and Tipper 2014). In the upper estuary, the lighter than expected $\delta^{44/40}Ca$ can occur due to two plausible reasons, i) discharge of groundwater with lighter $\delta^{44/40}Ca$, ii) dissolution of carbonates due to undersaturation in calcite and aragonite. Firstly, based on the mixing hypothesis, the depletion in $\delta^{44/40}Ca$ should be explained by the discharge of groundwater adjacent to the upper estuary (GW3), which exhibits a Ca concentration of 1378 µM and $\delta^{44/40}Ca$ of 0.97‰ (Fig. 5b). Assuming the proportions of groundwater discharge (f_{GW}) estimated from mixing model based on $^{87}Sr/^{86}Sr$ (Section 4.1), expected Ca isotopic composition from simple binary mixing between seawater and fresh river water ($\delta^{44/40}Ca_{mix}$) and Ca isotopic composition of adjacent groundwater $\delta^{44/40}Ca_{GW}$, we can recalculate the expected estuary Ca isotopic composition using equation Eq. (1):

$$\delta^{44/40}Ca_{exp} = f_{GW} * \delta^{44/40}Ca_{GW} + (1- f_{GW}) * \delta^{44/40}Ca_{mix} \qquad \text{Eq. (1)}$$

Here $\delta^{44/40}Ca_{exp}$ is the expected Ca isotopic composition from three endmember mixing and f_{GW} is the proportion of groundwater. The calculation indicates that the groundwater discharge can explain three of the observed deviations, except ES3 where the groundwater discharge can drive the $\delta^{44/40}Ca_{exp}$ to a lighter $\delta^{44/40}Ca$ (Table 2). This can be indicative of variable discharge patterns, associated errors in calculating the proportion of discharge using $^{87}Sr/^{86}Sr$ and dominance of processes driving the $\delta^{44/40}Ca$.

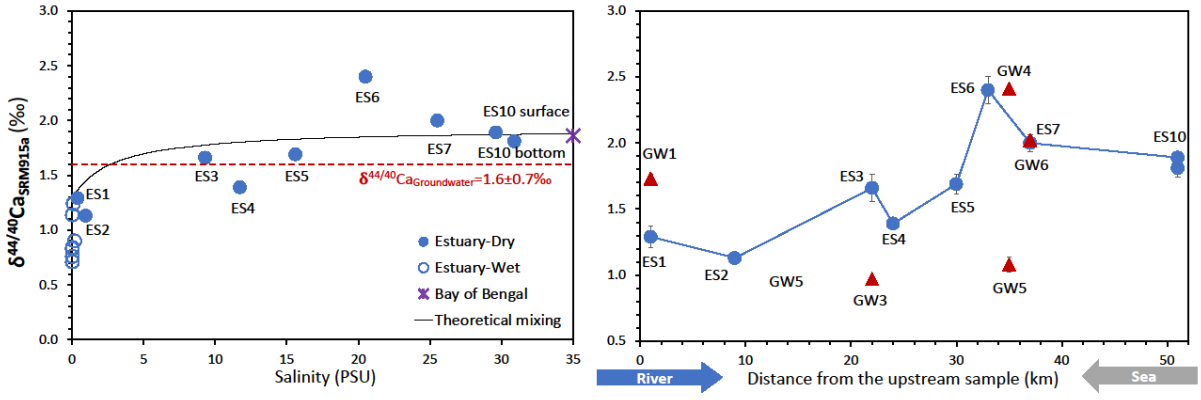

Figure. 5 *a) $\delta^{44/40}Ca$ vs. salinity, b) $\delta^{44/40}Ca$ vs. distance from the most upstream sample (km) for estuary and groundwater samples from Godavari. Note that the salinity in groundwater is assumed to be 0.1 and the theoretical mixing line is between global ocean average of $\delta^{44/40}Ca$ and fresh Godavari river water endmember (Fantle and Tipper, 2014, Chakrabarti et al., 2018). The external reproducibility for $\delta^{44/40}Ca$ measurements were better than 0.1‰.*

Table 2. *The calculation for impact of groundwater discharge to estuary on δ44/40Ca of the estuary. The groundwater δ44/40Ca value are from the adjacent aquifers: GW1 for ES1, GW3 for ES2, ES3, ES4, and ES5, GW6 for ES6 and GW 4 for ES7, ES10 (See text section 4.4 and Fig. 6 for details)*

Estuary	Salinity	$\delta^{44/40}Ca_{mea}$	$\delta^{44/40}Ca_{GW}$	$\delta^{44/40}Ca_{mix}$	$\Delta^{44/40}Ca$	f_{GW}	$\delta^{44/40}Ca_{exp}$	$\delta^{44/40}Ca_{exp}$- $\delta^{44/40}Ca_{mea}$
		‰	‰	‰	‰		‰	‰
ES1	0.4	1.29	1.7	1.37	-0.08	-	-	-
ES2	0.9	1.13	1.0	1.45	-0.32	0.73	-0.02	-0.03
ES3	9.3	1.66	1.0	1.788	-0.13	0.57	-0.19	-0.34
ES4	11.7	1.39	1.0	1.815	-0.43	0.50	0.00	0.01
ES5	20.3	1.69	1.0	1.864	-0.17	0.25	-0.01	-0.05
ES6	24.7	2.4	2.4	1.877	0.52	0.12	-0.05	-0.46
ES7	25.5	2	2.0	1.879	0.12	0.12	-0.01	-0.10
ES10	29.6	1.89	2.0	1.888	0.00	0.05	0.00	0.00
ES10	29.6	1.81	2.0	1.888	-0.08	0.05	0.00	0.08

4.3.2 Tracing the origin of heavy $\delta^{44/40}Ca$ in estuary

The heavier than expected $\delta^{44/40}Ca$ in lower estuary cannot be explained neither simple mixing nor groundwater input, given groundwaters are typically lower in $\delta^{44/40}Ca$ and lower in Ca concentration. In river systems, three major processes enrich the solution with heavy Ca isotopes; 1) biotic uptake (Cobert et al., 2011, Schmitt et al., 2013), 2) precipitation of $CaCO_3$ polymorphs such as calcite, aragonite, vaterite, ikaite (Tang et al., 2012), and 3) adsorption onto phyllosilicates (Brazier et al., 2019). Given that this non-conservative behaviour occurs within an estuarine system, we can neglect the influence of plant uptake. In addition, no calcifying organisms were reported in the estuary (Bharati et al., 2022). The Godavari estuary during the dry season was undersaturated in montmorillonites, thus fractionation associated with clay formation is unlikely in the estuary. The near saturation or oversaturation of calcite exists in the lower estuary, which can favour carbonate precipitation (Fig. S3). The previous works from Himalayan rivers have shown that precipitation of secondary calcite can remove up to 70% of the dissolved Ca (Jacobson et al., 2002, Bickle et al., 2005).

Godavari estuary is highly productive during the low discharge period due to low suspended load and water column stability, supporting intense phytoplankton blooms (Acharyya et al., 2012, Chapter IIIa of thesis). Photosynthetic activity by cyanobacteria and diatoms can promote calcite precipitation by increasing the pH and degree of supersaturation of $CaCO_3$ in the microenvironment (Merz, 1992, Riding, 2006). Additionally, diatoms and associated extracellular polymeric substances (EPS) can act as potential nucleating surfaces for

amorphous calcium carbonates (Stanton et al., 2022). Interestingly, the excess $\delta^{44/40}Ca$ compared to binary mixing ($\Delta^{44}Ca = \delta^{44/40}Ca_{measured}-\delta^{44/40}Ca_{mix}$, Table 2) in the estuary during dry season shows a positive correlation with the fucoxanthin (a diatom pigment) and chlorophyll, indicative of diatom induced carbonate precipitation in the lower estuary (Fig. 6a, Fig. S4). The interpretation is also consistent with a positive correlation between $\delta^{44/40}Ca$ and $\delta^{30}Si$, the latter driven by diatom uptake during the dry season (Fig. 6b, Chapter IIIa). The estuary also exhibits a positive correlation between $\Delta^{44}Ca$ and $\Delta^{13}C_{DIC}$, indicating that the excess carbon isotopic composition of the inorganic carbon pool driven by biotic uptake of lighter ^{12}C is also associated with an excess $\delta^{44/40}Ca$, associated with excess carbonate precipitation (Fig. S4, Sarma et al unpublished, personal communication). Recent works have demonstrated that one mechanism driving isotopic disequilibrium of calcite with co-existing fluids is photosynthetic activity and organic matter dissolution (Grim et al., 2021).

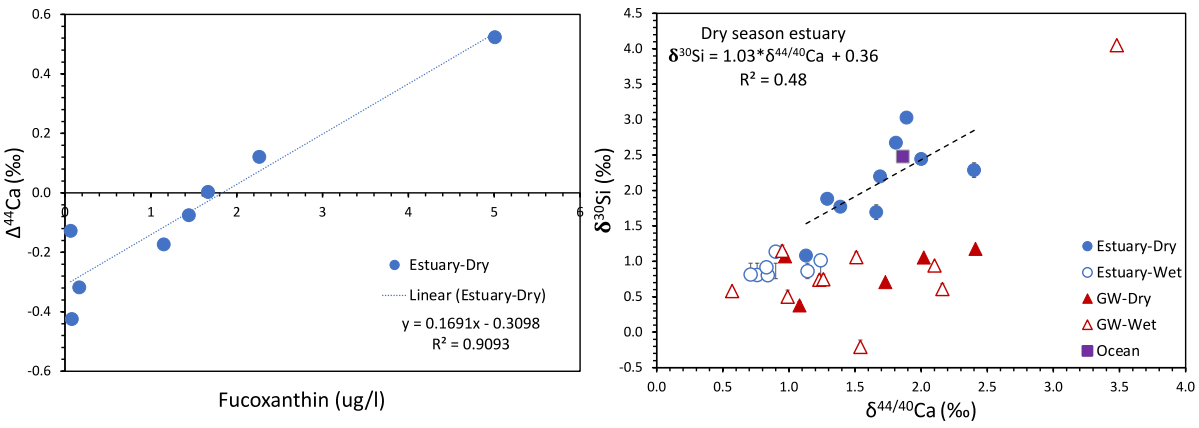

Figure 6. *a) The plot between fucoxanthin concentration in the estuary samples during dry season and $\Delta^{44}Ca$ ($\delta^{44/40}Ca_{measured}-\delta^{44/40}Ca_{mix}$) showing a strong positive correlation ($R^2=0.9$, $p<0.05$), b) plot between $\delta^{44/40}Ca$ and $\delta^{30}Si$ showing a positive weak correlation. Note here the $\delta^{30}Si$ value for the ocean is from Bay of Bengal data by Singh et al, (2015) and $\delta^{44/40}Ca$ data is from Fantle and Tipper, (2014) which matches deep BoB water from Chakrabarti et al., 2018.*

However, the interpretation also poses two questions, i) can the dissolution of carbonates driven by low photosynthetic activity and undersaturation of calcites explain the depletion we observe in the upper estuary? ii) does resuspension and dissolution of precipitated carbonates occur during the wet season leading to a lower $\delta^{44/40}Ca$ and high suspended load and dissolved organic carbon (Table 1, Kumar et al., 2022). We cannot exclude the possibility of dissolution driven by low fucoxanthin in the upper estuary, however, the fast sinking of precipitated carbonate phases makes it unlikely (Stanton et al 2022). To summarize, spatially heterogenous non-conservative behaviour of $\delta^{44/40}Ca$ in the estuary can be explained by two different

mechanisms: groundwater discharge from the adjacent aquifer in the upper estuary can explain lighter $\delta^{44/40}Ca$ than expected from simple mixing, and excess Ca, while in calcite saturated lower estuary the excess $\delta^{44/40}Ca$ is driven by precipitation of carbonates induced by diatom and cyanobacterial photosynthesis.

4.4. Groundwater Ca cycling and $\delta^{44/40}Ca$ variability

Godavari groundwater exhibits large variability in $\delta^{44/40}Ca$, ranging from 0.57 to 3.48‰, with an average of 1.6‰, heavier than the global groundwater average of 0.86‰, and exhibits no significant seasonal variability (Table 1, Tipper, 2016). Additionally, most groundwater $\delta^{44/40}Ca$ are heavier than the dominant Ca sources such as silicate rocks and carbonates, with few groundwater samples exhibiting $\delta^{44/40}Ca$ heavier than seawater clearly indicating dominance of processes that can fractionate Ca isotopes (Fig. 4). Along with secondary carbonate $CaCO_3$ precipitation, plant uptake (Schmitt et al., 2013, 2018) and adsorption onto phyllosilicates (Brazier et al., 2019) occurring in soil and saprolite can lead to enrichment of ^{44}Ca in shallow groundwaters of Godavari. To evaluate various fractionation pathways and the associated evolution of Ca isotopes in aquifer we can apply Rayleigh (Eq. (2)) and batch (Eq. (3)) fractionation models as follows:

$$\text{Rayleigh model: } \delta^{44/40}Ca_{meas.} = \delta^{44/40}Ca_o + 1000*(\alpha\text{-}1) * \ln(f_{Ca}) \quad \text{Eq. (2)}$$

$$\text{Batch/equilibrium model: } \delta^{44/40}Ca_{meas.} = \delta^{44/40}Ca_o - 1000*(\alpha\text{ -}1) * (1\text{- } f_{Ca}) \quad \text{Eq. (3)}$$

$\delta^{44/40}Ca_{meas}$ is the measured Ca isotopic composition of the dissolved phase and α is the fractionation factor between carbonates and dissolved phase. The $\delta^{44/40}Ca_o$ is the initial Ca isotopic composition of the reservoir, which is assumed to be the lowest $\delta^{44/40}Ca$ reported for groundwater in the present study (GW7, $\delta^{44/40}Ca$=0.57‰). The $\delta^{44/40}Ca$ composition of the selected aquifer is also close to the global average carbonate rock endmember, indicating a system dominated by carbonate weathering with minor precipitation and or uptake (Fantle and Tipper, 2014). Given $\delta^{44/40}Ca$ of all groundwater, the sample follows a linear trend and assuming that Ca is selectively incorporated into secondary carbonate phases relative to Sr, we can use the Ca/Sr ratio of the initial reservoir (GW7) to estimate the fraction of Ca remaining in the solution (f_{Ca})

$$f_{Ca} = (Ca/Sr)_{mea} / (Ca/Sr)_{GW7} \quad \text{Eq. (4)}$$

Here $(Ca/Sr)_{mea}$ is the measured Ca/Sr ratio in water samples. Estimated values of f_{Ca} indicate that Ca removed from the solution ranges from 23 to 98% (Fig. 7). The evolution of $\delta^{44/40}Ca$ in

the majority of the water samples broadly fits with a Rayleigh-type model, with a fractionation factor (α) between 0.9993 and 0.9980 (Fig. 7, Gussone et al., 2005). Firstly, the fractionation factors associated with adsorption onto montmorillonites are low (fractionation factor between 0.9998 and 0.9999) and cannot explain the observed variability in Godavari groundwater (Fig. 7, Brazier et al., 2019). The magnitude of isotopic fractionation during carbonate precipitation depends on the structure of the solid and physicochemical conditions during precipitation, $\alpha_{\text{calcite-sol}}$ ranging from 0.9985 to 1 (Lemarchand et al 2004, Gussone et al 2005, Tang et al 2012). Here we adopted the higher value of the fractionation factor reported by Druhan et al., (2013) during calcite precipitation in groundwater. Calcium is an essential nutrient for plants and uptake of Ca through the roots is known to fractionate against heavier ^{44}Ca, enriching the soil solution in $\delta^{44/40}$Ca with a reported fractionation factor of 0.9988 (Wiegand et al., 2005; Schmitt et al 2013). Interestingly, majority of the groundwater and estuary water samples fit within the range of reported α values of calcite precipitation and plant uptake, making it difficult to distinguish both processes (Fig. 7).

In order to check in situ precipitation of calcite, we performed a scanning electron microscopy (SEM) of suspended particulate matter in open well GW4 during the dry season with a heavy $\delta^{44/40}$Ca of 2.4‰. The suspended phase exhibits an abundance of Ca-rich precipitates with Mn oxide coatings, consistent with carbonate precipitation, which preferentially takes up the lighter Ca isotopes, exerts dominant control on $\delta^{44/40}$Ca (Fig. 8). The fact that wet season estuary waters plots at a high f_{Ca} and low $\delta^{44/40}$Ca confirms our earlier interpretation of higher carbonate weathering during monsoon (Fig. 7). However, two major concerns still remain to be sorted, i) the similarity in high $\delta^{44/40}$Ca of groundwater GW4 and GW6 and adjacent lower estuary (Fig. 5b), raising a possibility of surface water-groundwater interaction, ii) a piezometer (PZ3) during wet season exhibiting an exceptionally high $\delta^{44/40}$Ca and δ^{30}Si (Fig. 5, Chapter IIIa) for which no SEM sample is available. Given that Ca concentration in GW4 and GW6 during the dry season is more than 20-fold lower than that of the adjacent estuarine water, it is unlikely that heavy $\delta^{44/40}$Ca value results from mixing with Ca-enriched estuary water. Secondly, the piezometer (PZ3) with the highest $\delta^{44/40}$Ca value also exhibits an unusually high δ^{30}Si (Chapter IIIa) and radiogenic ^{87}Sr/^{86}Sr (section 4.2) similar to the upper estuary. Evidences point to a groundwater receiving high input of agricultural return flow originating from canals fed by Dowleiswaram dam, which acquired considerable signatures of plant uptake, where lighter ^{28}Si and ^{40}Ca are actively taken up by crops lead to high δ^{30}Si and $\delta^{44/40}$Ca signatures in

groundwater. To support this, PZ3 also shows very low DSi and Ca concentration, indicating significant loss of Ca and Si. Overall, Ca cycling and $\delta^{44/40}$Ca signatures in Godavari groundwaters are controlled by precipitation of secondary calcites, with minor impact from plant uptake and adsorption onto phyllosilicates.

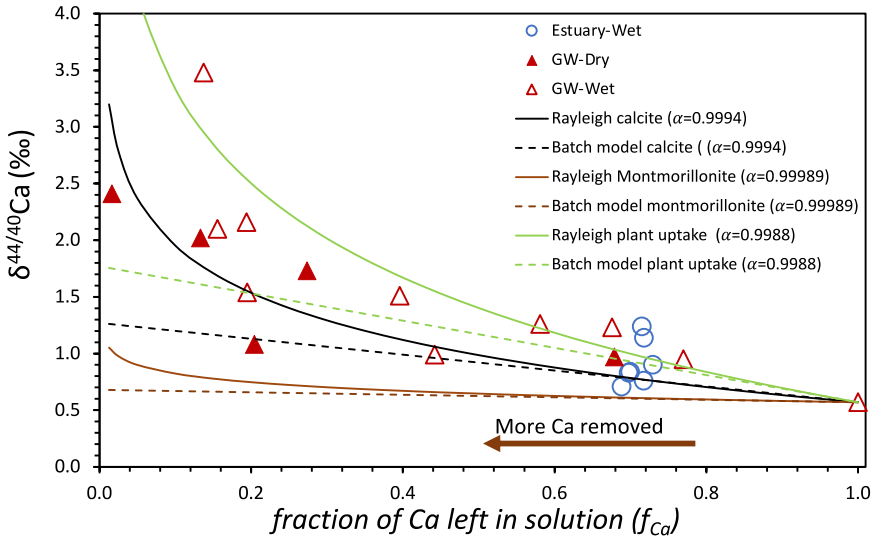

Figure 7. *The plot between $\delta^{44/40}$Ca and the fraction of Ca remaining in the solution (f_{Ca}), estimated by normalizing with Sr/Ca of lowest $\delta^{44/40}$Ca groundwater (see section 4.4 for details). The Rayleigh and batch model for three different fractionation factors (α) of: i) adsorption onto phyllosilicates (Brazier et al., 2019), calcite precipitation (Druhan et al., 2012), and iii) plant uptake (Schmitt et al., 2013).*

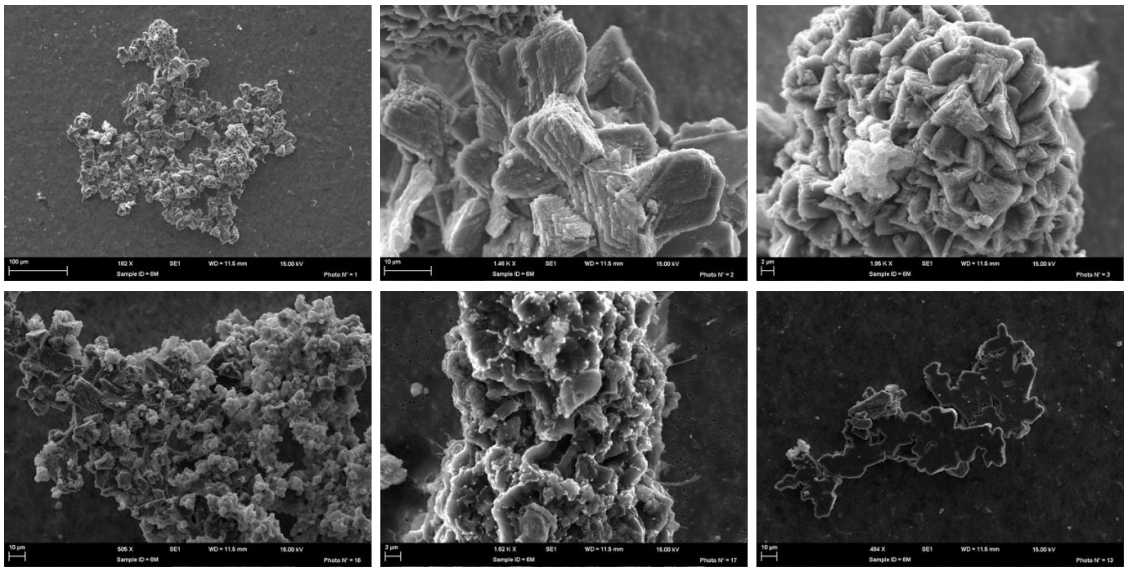

Figure 8. *The scanning electron microscopy (SEM) images of the Ca-rich aggregates and phases in groundwater sample GW4.*

5. Conclusion

The Ca and Sr isotopes were analysed in the present study to understand the sources, mixing and processes occurring in the Godavari estuary system. The primary objective was to trace various sources of Sr and Ca and estimate mixing using the $^{87}Sr/^{86}Sr$ ratio and to employ $\delta^{44/40}Ca$ to understand various processes that can impact Ca cycling in estuary and groundwater. During the dry season, both $^{87}Sr/^{86}Sr$ and $\delta^{44/40}Ca$ exhibit signatures of non-conservative mixing along the salinity gradient of the Godavari estuary. For the $^{87}Sr/^{86}Sr$ ratio, we assign the deviation from simple river water-sea water mixing to input from adjacent groundwater, which exhibits a homogenous $^{87}Sr/^{86}Sr$ ratio of 0.71187 with Sr concentration ranging from 1 to 22 µM. The fractional contribution of water masses was estimated using the Bayesian mixing model and groundwater contribution decreases along the estuarine transect, ranging from 75% at the upstream river water to 6% at the salinity of 30. The higher proportion of groundwater discharge in the upper estuary, with a Ca concentration of ~1300 µM and a lighter $\delta^{44/40}Ca$ value of 1‰, can explain the shift towards lighter $\delta^{44/40}Ca$ from the conservation mixing line between river water and seawater. Conversely, downstream locations exhibit an excess $\delta^{44/40}Ca$ compared to the mixing line, indicative of calcium carbonates precipitation . We hypothesize that the precipitation of calcium carbonate is driven by diatom activity, where photosynthesis can provide a microenvironment favouring precipitation. Extracellular polymeric substances (EPS) can also act as a nucleation site for precipitation. The hypothesis is strengthened by the linear correlation observed between diatom marker pigment (fucoxanthin), chlorophyll and $\delta^{30}Si$.

During the wet season, the entire estuary is dominated by fresh river water flow due to the opening of the dam upstream. The radiogenic $^{87}Sr/^{86}Sr$ signatures in the estuary indicate that the water influx is dominated by the Godavari river and tributaries draining the peninsular gneiss complex and khondalites, in the middle and lower reaches of Godavari. The more radiogenic signature in estuary water compared to groundwater indicates minor groundwater contribution to estuary during monsoon. Using a simple isotopic mass balance, we estimated that the carbonates contribute to almost 75% of the Sr fraction in the river water during monsoon, a proportion similar to other major rivers. The $\delta^{44/40}Ca$ signatures in the estuary during the wet season is lower than the Godavari river water endmember during the dry season with a higher Ca/Sr ratio, consistent with a higher contribution from carbonate weathering during monsoon.

Unlike estuary, groundwater samples exhibit no seasonal variability in terms of $\delta^{44/40}Ca$ and $^{87}Sr/^{86}Sr$ ratios and large spatial variability in terms of $\delta^{44/40}Ca$. The $^{87}Sr/^{86}Sr$ ratio in groundwater varies between 0.710 and 0.712, except one outlier, exhibiting a radiogenic value of 0.715 during the wet season. We assign the radiogenic values in the isolated piezometer to the local recharge of canal water sourced from the dam, used for irrigation extensively in the plains. The variability of almost 3‰ in $\delta^{44/40}Ca$ values of groundwater is primarily controlled by the precipitation of calcium carbonate phases in the aquifer, with a minor impact of plant uptake and adsorption onto clays.

Acknowledgements

The work is funded by CEFIPRA-IFCPAR support (NUNDERGROUND, project #5907). We acknowledge the National Institute of Oceanography (NIO) for providing the necessary support for the field campaign and sampling. The authors thank Dr. Satyaji Rao from the National Institute of Hydrology, Kakinada to make it available for sampling of piezometers at the Godavari region. The authors thank B.S.K Kumar for the help with field sampling and pigment analysis, Irina Djouraev and Valens Hishamunda for the help with ICPMS analysis and the ALYSES facility (IRD-SU). SPK and DC thank Sandrine Caquineau for the support and insights for SEM investigations at ALYSES facility (IRD-SU). SPK thanks IRD-Campus France for providing PhD scholarship and constant support to carry out the work. SPK sincerely thank Sourav Ganguly and Valens Hishamunda for help with the TIMS measurements at CEaS, IISc. SPK thanks Sourav Ganguly for inputs in Bayesian modelling and discussions. The authors would like to thank M. Benrahmoune (LOCEAN-IPSL) for their help in sample processing and clean lab management.

Supplementary Figures

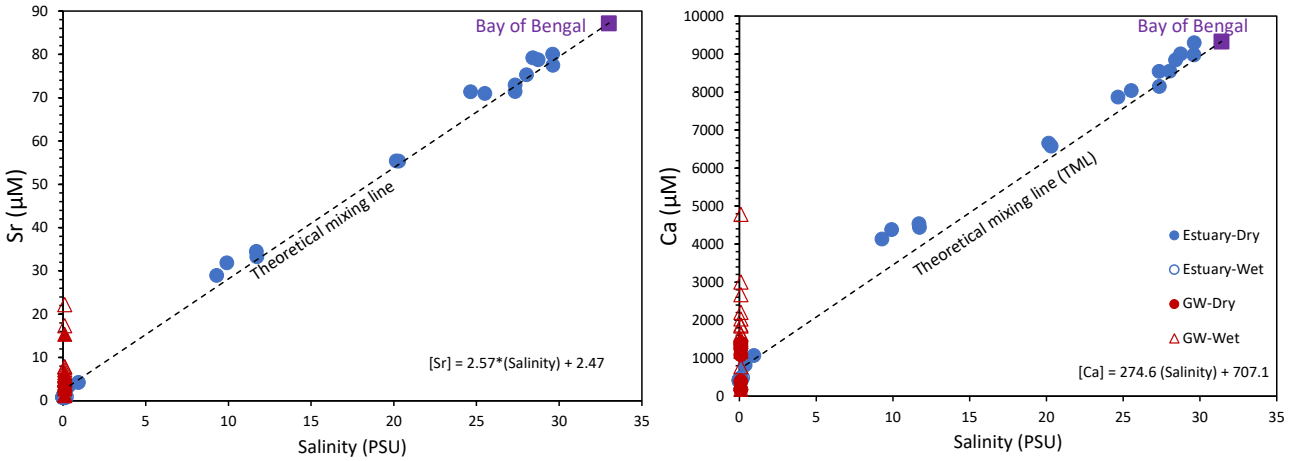

Figure S1. *The plot between salinity and Sr and Ca concentration for estuary and groundwater from Godavari. The Bay of Bengal data is from Chakrabarti et al, (2018).*

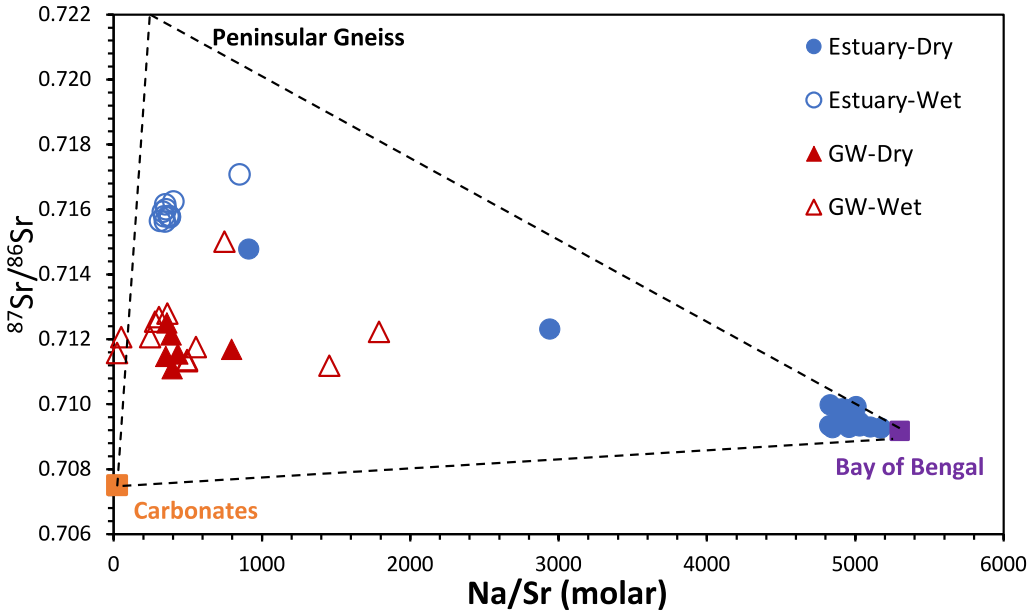

Figure S2*. Na/Sr vs.* $^{87}Sr/^{86}Sr$ *ratio for estuary and groundwater samples with various endmembers marked. The Bay of Bengal endmember is from Danish et al, (2020), Carbonate endmember from Nagarajan et al, (2013) and Govind et al, (2021) and Peninsular gneiss data from Jayananda et al, (2015).*

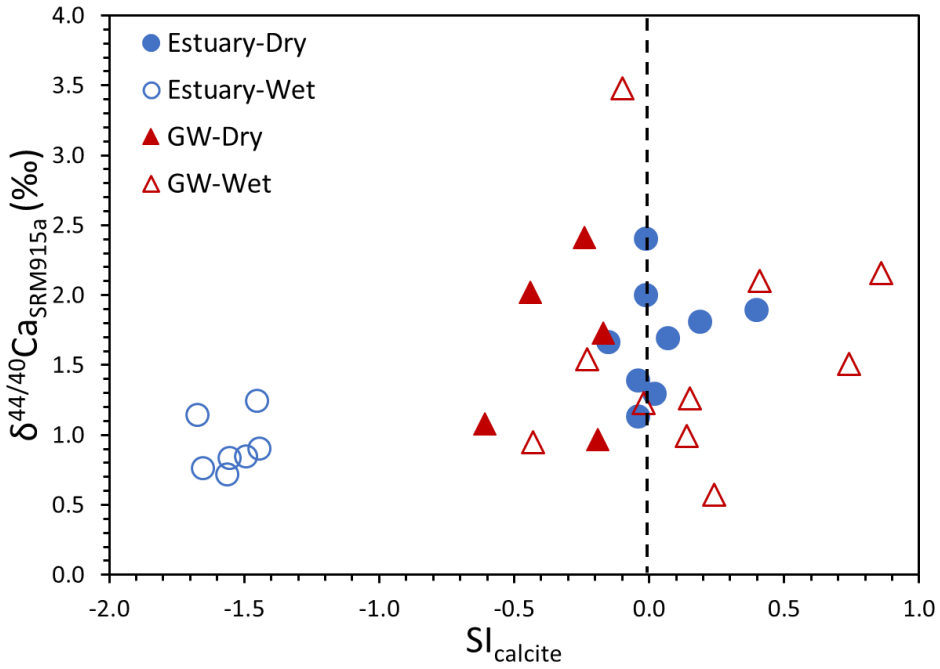

Figure S3. *The saturation index of calcite plotted against $\delta^{44/40}Ca$ for Godavari estuary and groundwater samples.*

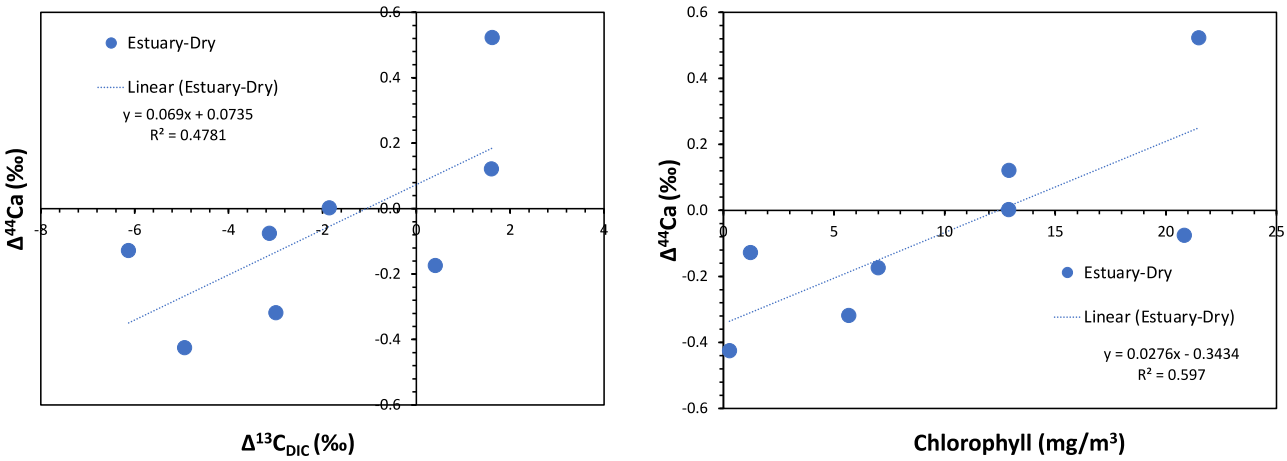

Figure S4. *The plot between $\Delta^{44}Ca$ ($\delta^{44/40}Ca_{measured}$-$\delta^{44/40}Ca_{mix}$) and a) chlorophyll ($mg/m^3$) and b) $\Delta^{13}C_{DIC}$ ($\delta^{13}C_{measured}$-$\delta^{13}C_{mix}$) measured from Godavari estuary during dry season. The $\delta^{13}C$ values of DIC are from Sarma et al. unpublished.*

IV. Minor impact of fresh submarine groundwater discharge on Si budget along Indian coastline: inferences from silicon isotopes and Ge/Si ratio

Sarath Pullyottum Kavil, Jean Riotte, Ramananda Chakrabarti, V.V.S.S Sarma, K.R. Mangalaa, J. Prunier, Arnaud Dapoigny, Damien Cardinal, *et al.*

Article in preparation for Global biogeochemical cycles

Abstract

The stable silicon isotope ratio ($\delta^{30}Si$) and Ge/Si ratio of over 80 groundwater samples were measured along the Indian coast during the dry period, spanning a wide range of climates (semi-arid to tropical wet) and aquifer lithologies (granite, basalt, laterite and alluvium). Coastal groundwater exhibits an average $\delta^{30}Si$ of 0.85±1.1‰ and Ge/Si ratio of 1.3±1.0 µmol/mol, indicating significant spatial variability. We observed no relationship with regional rainfall or lithology. The $\delta^{30}Si$ generally followed a mix between Rayleigh and steady-state behaviour with a fractionation factor between -0.5 and -2‰, predominantly controlled by the formation of secondary clay minerals in the soil and saprolite. The exceptionally high $\delta^{30}Si$, greater than 2‰ in groundwaters was indicative of unidirectional kinetic uptake, typically following a Rayleigh system, which could have resulted from irrigation return flows incorporating signatures of plant uptake through multiple cycles of pumping and recharge. The groundwaters also exhibited $\delta^{30}Si$ lighter than the upper continental crust (UCC) composition, indicative of the dissolution of secondary lighter Si sources such as clay minerals. The $\delta^{30}Si$ signatures of groundwaters were significantly lighter than the monsoonal rivers in India (1.47±0.7‰, n=16). The lower $\delta^{30}Si$ compared to the surface waters and a steady state behaviour suggests a dynamic equilibrium between Si supply and formation of secondary phases, aided by the long residence time of water aquifer systems. The fresh submarine groundwater discharge (SGD) along the Indian coast was estimated to be 2.9 GmolSi/yr, which is <1% of the riverine Si flux to the North Indian ocean. The fresh SGD Si flux along the Indian coast accounts for 0.4% of the global fresh groundwater Si flux to the ocean. The isotopic effect of Si flux to the Indian coast is less than 0.05‰ and imparts no effect on the Si isotope budget to the North Indian ocean. Extrapolated Ge flux through fresh SGD to the global ocean can be significant in oceanic Ge cycling and can contribute up to 5 to 10% of the riverine Ge input to the ocean.

Keywords: SGD, groundwater Si flux, Ge/Si ratio, riverine Si flux, land-to-ocean continuum

1. Introduction

Silicon (Si) is the second most abundant element in the Earth's crust and continental silicate weathering is a key process controlling the long-term carbon sequestration, hence regulating climate over geological time scales (Berner et al., 1983, Wollast and Mackenzie, 1989). The Si cycle begins as weathering solubilizes Si from the primary minerals, following which a fraction of the solubilized Si is incorporated into secondary phases and the rest is mobilized as dissolved silicon (DSi). The dissolved silicon can further undergo biotic uptake, by vascular plants from soil water and siliceous organisms in lakes and rivers. Both the abiotic and biotic processes of Si uptake are associated with significant isotopic fractionations, favouring preferential incorporation of light isotope ^{28}Si into the solid phase, making the residual solution heavier in $\delta^{30}Si$ (Opfergelt and Delmelle, 2012, Frings et al., 2016). Ge/Si ratio is routinely coupled with $\delta^{30}Si$ to distinguish between secondary clay formation where Ge is preferentially incorporated relative to Si and plant uptake, which discriminates against Ge (Mortlock and Froelich, 1987, Kurtz et al., 2002, Derry et al., 2005, Blecker et al., 2007, Delvigne et al., 2009). The biogenic silica (BSi) formed by plants can further undergo recycling through litterfall, which also adds a human dimension to Si cycling through landscape cultivation and Si export along with food crops (Struyf et al., 2010, Carey and Fulweiler, 2012). Finally, the Si supplied to the ocean is a key nutrient for photosynthetic marine diatoms, which are responsible for almost 20% and 40% of the global primary and marine productivity, respectively (Field et al., 1998; Tréguer et al. 2018). Total submarine groundwater discharge (SGD) is considered to be the second largest source of DSi supply to the ocean after rivers, but its global Si flux bears considerable uncertainty (4 to 25% of total Si flux to ocean, Tréguer et al., 2021). Groundwater forms an intermediate system between soil and river water but dwarfs all other hydrological systems in terms of the total volume of freshwater storage (Gleeson et al., 2015). Silicon entering groundwater inherits the signature from surface and subsurface processes which can further undergo weathering and transformation in aquifers before discharging into rivers and/or oceans (Worthington et al., 2016). Groundwater thus forms a complex system spanning $\delta^{30}Si_{DSi}$ range from -1.5 to +2.6‰, incorporating signatures from incongruent weathering of primary silicate minerals in one end to dissolution of primary and/or secondary sources such as feldspars, clays and silcretes on the other (Georg et al., 2009a, Georg et al., 2009b, Opfergelt et al., 2011; Strandmann et al., 2014, Martin et al., 2021, Chapter II, IIIa). Despite such high variability, complexity in controlling processes and direct impact on the riverine and oceanic elemental and isotopic budget, groundwater Si cycling remains overlooked.

Globally, submarine groundwater discharge (SGD) of Si to ocean, which includes both fresh terrestrial groundwater and saline groundwaters, ranges from 0.7 to 3.8 Tmol Si/yr, i.e. 8 to 46% of the riverine flux (Cho et al., 2018, Rahman et al., 2019, Tréguer et al., 2021). Recent estimate covering all major lithologies suggests that fresh terrestrial groundwater accounts for only 0.7±0.1 Tmol Si/yr, deriving primarily from, extrusive igneous and complex lithologies (Rahman et al., 2019). This contrasts with Si fluxes through groundwater discharge from the Bengal basin that was estimated to be almost 40% of the combined Ganga-Brahmaputra Si fluxes, and that can alter the silicon isotopic signature of the rivers up to 0.4‰ (Georg et al., 2009b). However, such high Si fluxes were an overestimate due to poor containment of the fresh groundwater fluxes and it was recently estimated to account ~0.6% of the total coastal groundwater discharge (Luijendijk et al., 2020). Moreover, groundwater seepage is patchy, diffuse, temporally variable, and involves multiple coastal aquifer systems (Taniguchi et al., 2002, Moore et al., 2010). Thus, the measurement of its magnitude and associated chemical fluxes is a challenging enterprise and requires extensive sampling. Even though the process is essentially ubiquitous in coastal areas, the assessment of its magnitude at any one location is subject to enough variability that measurements should be made by a variety of techniques and over large enough spatial and temporal scales to capture the heterogeneity (Burnett et al., 2006). Recently, Rahman et al, (2019) gave a comprehensive global estimate of fresh and saline SGD DSi fluxes considering variability associated with complex lithologies and the non-conservative nature of the saline SGD end member. Previous work from the Godavari estuary region on the East coast of India estimates that SGD accounts for almost 54 and 62% of the total riverine dissolved inorganic carbon and alkalinity delivery to the coast, and exhibits significant temporal variability (Rengarajan and Sarma, 2015). Additionally, the discharge of groundwaters highly enriched in nutrients such as N and P can also lead to changes in the structure and functioning of the coastal ecosystems, including harmful algal blooms related to coastal eutrophication (Welti et al., 2015, Babu et al., 2021, Kumar et al., 2021). Recent observations also indicate that groundwater interactions in subterranean mixing zones can also lead to the release of dissolved iron and toxic metalloids such as arsenic to the Bay of Bengal (Misra et al., 2020, 2022).

Si isotope analysis could help in quantifying Si SGD since groundwater has been reported to generally bear lighter Si isotopic composition compared to surface waters (e.g. Georg et al., 2009b; Sarath et al., submitted). However the number of groundwater $\delta^{30}Si$ signatures

published so far is relatively limited compared to surface waters and associated variability is1.5very large (groundwater δ^{30}Si from -2 to + 2.5 ‰ (n=66) *vs.* river data from 0 to + 4 ‰ (n=557), Frings et al., 2016). Indeed, we recently reported in the Godavari estuary that groundwater are not significantly different from surface waters during high discharge season (Chapter IIIa). Our objective is to capture the regional heterogeneity in DSi fluxes, Ge/Si ratios and δ^{30}Si composition of coastal groundwater and provide a regional estimate of fresh SGD discharge in the Indian subcontinent. In the present work, we sampled more than 80 groundwater samples from the Indian coast during the dry season, which encompasses complex aquifer lithologies including alluvium, laterite, basalt and banded gneiss complex (CGWB, 2012). Here we try to address a few pressing questions related to groundwater Si cycling, *i)* variability in δ^{30}Si and Ge/Si composition of the groundwater, *ii)* processes that exert first-order control over the δ^{30}Si variability, *iii)* impact fresh groundwater discharge of Si and Ge in oceanic budget.

2. Material and Methods

2.1. Lithology, climate and land use of Indian coast

The Indian subcontinent is bounded by the Arabian Sea in the west and the Bay of Bengal in the east. Indian peninsular coastline covers almost 5400 km, encompassing nine states from Gujarat in the west to West Bengal in the east. Coastal aquifers in India can be sedimentary as well as weathered/fractured igneous and metamorphic (Manivannan and Elango, 2019). Aquifer systems in the Indian subcontinent are dominated by alluvium in West Bengal and Odisha, Cretaceous Deccan basalts in Maharashtra and some regions of Gujarat and Karnataka, banded gneiss complex in Karnataka and Andra Pradesh, gneiss and laterite in Goa, Kerala and Tamil Nadu (CGWB, 2012). Alluvium aquifers are dominant in India, occupying almost 29.8% of the aquifers and primarily consist of quartz, plagioclase feldspars and clays (Shamsudduha et al., 2008, CGWB, 2012). Deccan tholeiite basalts form low permeability hard rock aquifers (16.15%) and the major mineral phases include olivine, plagioclase, clinopyroxenes and orthopyroxenes (Beane et al., 1986). The gneiss complex lithology (15.09%) primarily consists of quartz, biotite and plagioclase with the minor occurrence of amphiboles and pyroxenes (Braun et al., 2009). Precambrian crystalline basement rocks are overlain by Tertiary sediments and alluvium (Laluraj et al., 2005). On the Indian coast, 57% of groundwater levels are between 0 to 10 m above sea level, and only 7% of the coastal aquifers are affected by seawater intrusion. (Manivannan and Elango, 2019). Major rivers discharging to the Indian coast include

the Ganges, Brahmaputra, Godavari, Krishna, Mahanadi and Cauvery to the Bay of Bengal, and Narmada to the Arabian Sea, and form alluvium deposits near the mouth. The Bay of Bengal receives almost 1600 km^3 of fresh river water influx annually while Arabian Sea receives 300 km^3 of riverine input (Krishna et al., 2016). Rainfall in the Indian subcontinent is dominated by the summer monsoon (75-80% of total rainfall), occurring during the months from June to September followed by North East monsoon (11% of total rainfall) from October to December (Lakshmi and Satyanarayana, 2020). The west coast of India constitutes the windward side of the Western Ghats mountains and receives maximal precipitation during the summer monsoon, while the northeast monsoon rainfall is dominating rainfall on the east coast (Kumar et al., 1992, Rajeevan et al., 2012). Annual average rainfall on the east coast ranges from 300 to 2500 mm and on the west coast ranges from 1000 to 3500 mm (CGWB, 2012). More than 50% of the land area in India is under cultivation and an irrigated land area of 77 million/ha (Gopalakrishnan and Kulkarni, 2007, FAO 2015). Indian follows two main cropping seasons: Kharif season from April to September where crops are dominated by rice, sorghum, millet, maize, cotton, sugar cane, soybean, and groundnut and rabi from October to March where wheat, barley, gram, linseed, rapeseed, and mustard are grown. Coastal states are known to be major producers of rice and sugarcane with 40-80% of the agricultural land is cultivated using groundwater irrigation (Kumar et al., 2021). The coastal groundwaters are significantly impacted by fertilizer use in India, with high concentrations of nitrate reported in Odisha, Andra Pradesh, Tamil Nadu, Karnataka, Goa and Gujarat (Kumar et al., 2021).

2.2. Sampling and field measurements

Groundwater samples was collected along the entire peninsular India coastline from nine states during the dry season in April 2017. We sampled 86 groundwater from handpumps, electric pumps and open wells <300 m away from the coast. The details of the sampling locations and type are described in Table 1. Groundwater samples from open wells were collected using a 5 L Niskin bottles and the pumps were purged before sampling for analysis. The collected samples were immediately filtered using 0.22 µm cellulose acetate filters and stored in pre-cleaned containers. The conductivity was measured using with a conductivity meter (HI2003, accuracy ± 1%) and pH using a glass electrode (WTW, MultiLine P4).

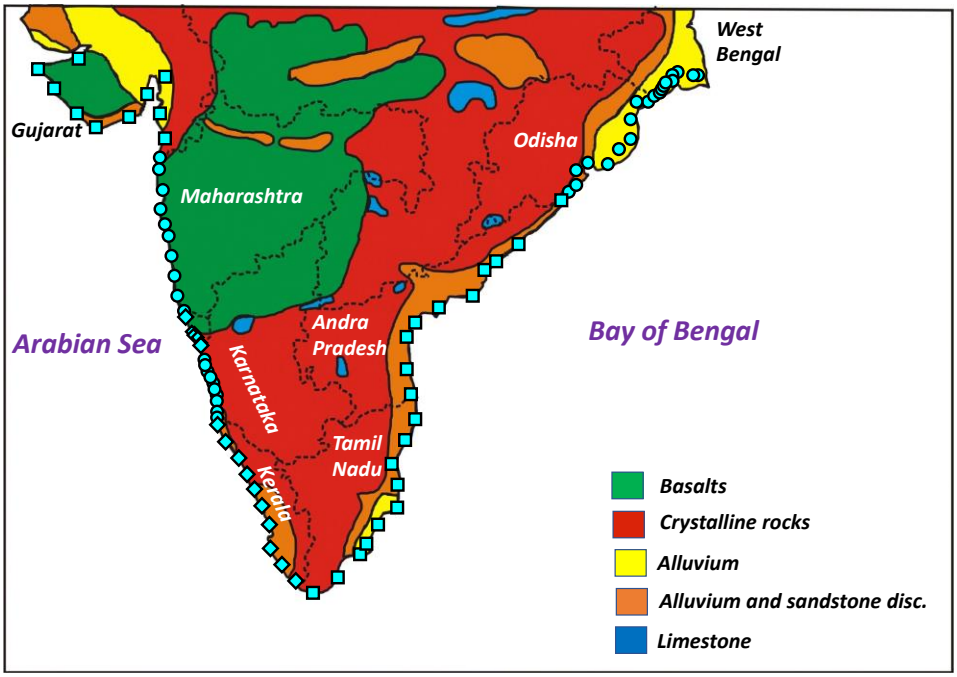

Figure 1. *Groundwater sampling locations along the Indian coast. Diamonds represent the region with annual rainfall >2000 mm, circles symbol for rainfall between 1000-2000 mm/yr and the square symbols for <1000 mm/yr. Details of the sampling are given in Table 1. The figure modified from Manivannan and Elango, (2019).*

2.3. Elemental concentration

Major cation concentrations (Na^+, K^+, Ca^{2+}, Mg^{2+}) were measured using ICP-OES iCap (Thermo Fischer Scientific) at GESE (Génie Environnemental Sols et Eaux, Sorbonne Université, Ivry Paris). Major anion concentrations were measured with an Ion Chromatograph (Metrohm COMPACT 861) in IFCWS (Indo-French Cell for Water Sciences, Indian Institute of Science, Bengaluru, India). The accuracy of measurements was monitored using multiple certified reference materials (AnionWS, ION-96.4, ION 915, SUPER-05 and BIG MOOSE 02). The average precision was monitored using standard references and was better than 10%.

2.4. Dissolved silicon and Si isotope analysis

Silicon concentration (DSi) was measured by spectrophotometer following the Grasshoff et al. (1999) protocol. Analytical quality was assessed using certified reference material, PERADE 09 (supplied by Environment Canada, lot no:0314, with DSi = 110.0±6.8 µM), during each measurement and mean reproducibility was 109.9±3 µM (n=25). We followed a slightly modified two-step pre-concentration method adapted from MAGIC- MAGnesium Co-precipitation technique (Karl and Tien, 1992; Reynolds, 2006; Hughes et al., 2011). To an initial volume of 10 ml of groundwater and surface water samples, we added 0.5 ml of $MgCl_2$

solution to match the seawater Mg concentration and were treated with 2% (v/v) of 1 M NaOH and was shaken and kept undisturbed overnight. The brucite ($Mg(OH)_2$) formed at high pH scavenges Si which gets adsorbed onto precipitated brucite. The supernatant from the first step was again subjected to second addition of 1% NaOH following, and the precipitate was recovered by centrifugation after 1-2 hrs. Both brucite precipitates were also re-dissolved with 1M HCl and merged. The DSi concentration of the supernatant was analyzed by spectrophotometer (Grasshoff et al., 1999) and found negligible (on average <2%), confirming that all the Si was adsorbed onto the brucite precipitate.

Separation of Si from other cations was carried out using cation exchange resin (BioRad DOWEX 50W-X12, 200 to 400 mesh, in H+ form) following the procedure of Georg et al. (2006). After the purification process, an aliquot was analyzed for major elements analysis (Na, Mg, Ca, K) by ICP-MS (Agilent 7500a) to ensure that the Si/X (Where X= Na, K, Ca or Mg) weight ratio is always >50 to minimize the matrix effects in the plasma. A small aliquot of purified sample was also measured for DSi concentration to check the full Si recovery (>90%) after column. The organic matrix is removed by treatment with 50 µL of 30% H_2O_2 since it has been shown to potentially induce a matrix bias during MC-ICP-MS analyses (Hughes et al., 2011). Analyses performed on a series of 35 groundwater and surface water samples, shows that the preconcentration and H_2O_2 treatment increased the DSi/DOC ratio from 18 to 7000 times, with DSi/DOC ratio >10 in the final aliquot (Annexe 1). This indicates <0.2‰ shift in Si isotope ratio from isotopic mass bias due to DOC matrix (Hughes et al., 2011). The possible remaining potential matrix effect resulting mainly from Cl^-, NO^-_3 and SO_4^{2-} was corrected by the artificial doping of anions (Merck, Suprapur grade H_2SO_4, HNO_3 and HCl) in all the samples and standards (Hughes et al., 2011). The measurements were performed on MC-ICP-MS (Thermo Neptune+, LSCE-IPSL, Gif-sur-Yvette) in dry plasma mode with Mg doping as described by Closset et al. (2016). Samples were injected into the plasma with an ApexΩ HF desolvating nebulization system connected with a PFA nebulizer (100 µL/min uptake rate) and without additional gas. The $\delta^{30}Si$ values were expressed as the permil deviation of the $^{30}Si/^{28}Si$ ratio from the quartz standard NBS28 (RM8546), expressed as

$$\delta^{30}Si_{sample} = [(^{30}Si/^{28}Si)_{sample}/(^{30}Si/^{28}Si)_{NBS28} - 1] * 1000 \qquad E(1)$$

Blank levels were below 1% of the main signal and were subtracted from each sample and standard analysis. All measurements were carried out in a matrix composed of 0.5 M HNO_3, 0.5 M HCl, 1 mM H_2SO_4 and in medium-resolution mode ($m/\Delta m > 6000$) to optimize the

separation of ^{30}Si peak and $^{14}N^{16}O$ interference and were performed on the interference-free left side of the peak (Abraham et al., 2008, Annexe 1). The $\delta^{29}Si$ and $\delta^{30}Si$ values were compared to the mass-dependent fractionation line and samples falling outside of its analytical error were excluded from the final dataset. Typical analytical conditions are provided in Table S1 of Chapter II. Laboratory protocol has been intercalibrated for seawater as part as the GEOTRACES intercalibration exercise generated over the entire procedure (Grasse et al., 2017). The analytical precision and accuracy were monitored by the long-term measurements of secondary reference material diatomite ($\delta^{30}Si$ = 1.26‰, Reynolds et al., 2007) indicated an average precision and a long-term analytical reproducibility on $\delta^{30}Si$ values of 1.19±0.18‰ (2SD, n=100, Annexe 1). Diatomite solutions processed with MAGIC give average $\delta^{30}Si$ values of 1.07±0.11‰ (2SD, n=12, Annexe 1) which is slightly lighter than unprocessed diatomite, but the difference remains within our analytical reproducibility. All the samples measured in the present study are chemically replicated at least once (average variability of 0.11±0.12‰), and 10 samples were triplicated with and average 2SD of ±0.15 ‰.

2.5. Germanium analysis

Ge concentrations in estuarine and groundwater samples were measured by isotope dilution using a ^{73}Ge spike (Neonest AB®) added to approximately 10 ml of samples before a two-step pre-concentration procedure adapted according to the MAGIC co-precipitation technique (Karl and Tien, 1992; Reynolds 2006). The Ge separation and purification were achieved using the BioRad cation exchange resin DOWEX 50W-X12 (200-400 mesh). The analyses were performed on a high-resolution inductively coupled double-focusing plasma mass spectrometer (Element XR, Thermo Fischer Scientific®) at Géosciences Environnement Toulouse (Toulouse, France). To improve the sensitivity of the analyses and to reduce the matrix interferences, a CETAC Aridus II desolvating nebulizer has been coupled to the HR-ICP-MS. An internal standard was run for every five samples as a bracketing method to correct the mass bias during the analysis. All procedure blanks analysed ranged between 1.5 to 43 pg (n=10; average=17 pg) which represented 0.3% to 21% of the sample concentrations. Ge concentrations were tested via repeated analyses of the reference material SLRS-6 (NRC Canada) and were in accordance with published values (Yeghicheyan et al. 2019).

3. Results

3.1. Sampling and elemental composition

Sampling details, DSi concentrations and $\delta^{30}Si$ signatures are given in Table 1. The conductivity of groundwater samples ranged from 92 to 8770 µS/cm, with an average of 1400 µS/cm and the average pH was 6.7±0.7. The brackish nature of groundwater can be indicative of seawater intrusion and/or excess contribution from fertilizers. The fraction of seawater was estimated using Cl as a conservative tracer (Appelo and Postma, 2005), and initial freshwater was assumed to be similar to Netravathi river (Sarath et al., 2022). The fraction of seawater ranged from 0 to 13%, with just 8 groundwaters exhibiting greater than 5% seawater contribution. Na was the dominant cation in groundwater for most samples followed by Mg, K and Ca. On a molar basis the concentration of anion from the groundwater decreased in the order $[Cl^{-}] > [SO_4^{2-}] > [NO_3^{-}] >]F^{-}] > [PO_4^{3-}]$ (Table 1).

3.2. Dissolved silicon (DSi) and silicon isotopes

The DSi concentration in groundwater ranged from 77 to 1350 µM, with an average of 484 µM (Table 1, Fig. 2). The highest DSi concentrations were observed in Maharashtra, Gujarat and alluvium aquifers in Odisha and West Bengal and the lowest in southern states of Kerala, Tamil Nadu and Andra Pradesh. The average DSi concentrations in groundwater from the Indian coast were in between the global coastal fresh groundwater average from extrusive igneous (604±192 µM) and complex lithologies (288±245 µM) (Rahman et al., 2019). The $\delta^{30}Si$ values of coastal groundwater ranged from -1.07 to 4.5‰, with an average composition of 0.91±1.21‰ (1SD, n=86). The highest $\delta^{30}Si$ was observed in intensely cultivated coastal states of Andra Pradesh and Tamil Nadu while the lowest $\delta^{30}Si$ was found in West Bengal and Odisha. Such $\delta^{30}Si$ average is at the higher end of the groundwater $\delta^{30}Si$ globally compiled up to now, 0.49±0.94‰ (n=66), with an upper limit of $\delta^{30}Si$ increased to 4.5‰ (Frings et al 2016 and references therein, Ehlert et al., 2016a, Martin et al 2021). We did not find any statistically significant variability between the groundwater collected from open wells and pumps in terms of DSi and $\delta^{30}Si$. We also observed high variability within aquifer systems with comparable lithologies for DSi and $\delta^{30}Si$ (Fig. S1). Overall, there was no statistically significant relationship between DSi and $\delta^{30}Si$.

***Table 1**. The sample details and elemental concentration of coastal groundwater. The standard deviation (1SD) for $\delta^{30}Si$ is represent true standard deviation of triplicates (marked *) or variability in chemical replicates.*

ID	Well type	pH	Cond.	DSi	Na	K	Mg	Ca	Cl	NO_3	SO_4	$\delta^{30}Si$	SD	Ge/Si
			µS/cm	mM	mM	mM	mM	mM	mM	mM	mM	‰	‰	µmol/mo
Gujarat														
GJ1	Pump	7.12	1120	0.42	5.66	0.03	2.07	0.10	5.53	0.09	0.60	4.08	0.2*	0.36
GJ2	Pump	7.49	1360	0.47	11.8	0.04	0.31	0.05	1.72	0.36	0.46	1.09	0.1	0.21
GJ3	Pump	7.13	2110	0.74	5.89	0.05	6.21	0.12	11.4	0.20	0.98	3.99	0.0	n.a.
GJ4	Pump	7.41	2900	0.83	5.79	0.44	3.50	0.20	12.8	0.69	1.80	1.72	0.0	0.37
GJ5	Pump	6.86	1960	0.60	6.98	0.07	1.86	0.04	7.15	1.16	1.07	2.52	0.1	0.30
GJ6	Pump	7.23	8770	0.71	50.8	1.55	18.8	0.46	60.0	0.09	17.5	1.72	0.0*	1.28
GJ7	Borewell	7.10	2210	0.64	7.79	1.42	1.97	2.10	14.7	0.57	0.88	0.35	0.0	4.00
GJ8	Borewell	7.04	1430	0.29	6.02	1.57	0.87	0.25	5.04	0.02	0.51	0.88	0.1	3.45
GJ9	Pump	7.32	4750	1.09	30.7	3.08	3.52	0.18	32.9	1.63	2.31	0.62	0.2	0.31
GJ10	Pump	7.29	1040	0.37	4.83	0.42	0.80	0.24	2.60	1.22	0.41	0.50	0.2	1.36
Maharashtra														
MH1	Pump	6.32	200	0.98	0.38	0.07	0.08	0.11	0.52	0.01	0.05	0.68	0.0	2.03
MH2	Pump	5.60	1457	0.75	0.26	0.04	0.58	1.15	0.31	0.02	9.71	0.18	0.0	2.16
MH3	Pump	4.87	200	0.57	0.31	0.02	0.10	0.16	0.41	0.04	0.03	0.63	0.2	0.99
MH4	Pump	6.22	280	0.41	0.71	0.09	0.16	0.63	0.75	0.20	0.26	0.52	0.1	4.10
MH5	Pump	5.96	160	0.69	0.37	0.00	0.14	0.22	0.37	0.00	0.04	1.00	0.1	0.76
MH6	Borewell	6.27	230	0.46	0.73	0.17	0.31	0.40	0.55	0.23	0.05	0.66	0.0	0.45
MH7	Pump	7.33	2270	0.96	21.1	0.25	1.76	0.10	17.6	0.01	1.83	0.99	0.0	0.28
MH8	Pump	7.14	1250	1.35	7.36	0.21	1.28	0.07	4.44	0.07	0.58	0.86	0.0	0.17
MH9	Borewell	6.82	410	0.35	0.69	0.04	0.85	1.02	0.39	0.01	0.10	1.26	0.1	0.58
MH10	Pump	6.79	560	0.68	1.05	0.00	0.77	0.44	0.89	0.03	0.19	1.05	0.1*	0.79
Goa														
GA1	Pump	6.65	460	0.69	0.81	0.07	0.75	0.46	1.03	0.05	0.11	1.10	0.0	0.55
GA2	Pump	6.66	4480	0.27	29.9	0.22	3.04	2.60	43.3	0.06	1.18	1.20	0.0*	0.52
GA3	Borewell	5.75	130	0.15	0.63	0.04	0.08	0.09	0.64	0.09	0.02	0.63	0.2*	0.57
GA4	Pump	5.37	150	0.38	0.65	0.08	0.13	0.16	0.75	0.16	0.06	1.14	0.1*	0.62
GA5	Borewell	5.98	182	0.58	0.30	0.09	0.17	0.41	0.32	0.01	0.01	0.63	0.1	n.a.
GA6	Pump	6.41	430	0.84	1.25	0.11	0.26	0.66	0.73	0.15	0.31	0.46	0.1	1.62
GA7	Borewell	6.37	1541	0.63	7.32	0.13	1.86	0.75	14.6	0.02	0.58	0.66	0.2	0.87
Karnataka														
KA-1	Pump	5.05	520	0.77	2.67	0.32	0.34	0.22	2.96	1.43	0.04	0.27	0.1	1.25
KA-2	Pump	5.98	260	0.29	0.84	0.47	0.14	0.41	0.59	0.31	0.29	1.01	0.1	0.50
KA-3	Pump	5.60	310	0.67	0.66	0.11	0.24	0.61	0.46	0.94	0.23	-0.22	0.0*	4.06
KA-4	Pump	5.33	150	0.38	0.56	0.03	0.06	0.08	0.59	0.13	0.01	1.33	0.1	0.94
KA-5	Borewell	6.71	510	0.51	1.54	0.48	0.24	1.22	1.66	0.73	0.24	0.17	0.0	n.a.
KA-6	Pump	5.62	190	0.59	0.62	0.01	0.11	0.32	0.90	0.24	0.10	-0.17	0.1	1.17
KA-7	Borewell	4.79	170	0.84	0.82	0.17	0.07	0.09	1.21	0.14	0.03	0.76	0.2	2.08
KA-8	Pump	6.10	190	1.07	0.36	0.08	0.52	0.20	0.26	0.00	0.02	0.91	0.1	1.72
KA-9	Pump	5.83	99	1.14	0.38	0.05	0.09	0.12	0.34	0.01	0.04	1.39	0.1	0.88
KA-10	Pump	6.65	970	0.52	3.39	0.14	1.16	1.41	6.33	0.42	0.56	1.36	0.1	1.11
Kerala														
KL-1	Pump	6.02	334	0.31	1.45	0.28	0.15	0.28	1.70	0.38	0.24	-0.01	0.1*	1.65
KL-2	Pump	5.63	150	0.12	0.69	0.07	0.07	0.23	0.69	0.15	0.06	0.11	0.1	2.40
KL-3	Pump	5.67	478	0.34	2.10	0.21	0.54	0.31	2.28	0.02	0.58	1.25	0.1	0.64
KL-4	Pump	5.96	92	0.08	0.29	0.09	0.07	0.12	0.36	0.01	0.04	0.74	0.4	1.26
KL-5	Borewell	7.05	480	0.14	0.73	0.37	0.19	0.68	0.68	0.26	0.31	-0.40	0.0	2.90
KL-6	Pump	6.15	150	0.17	0.48	0.07	0.06	0.28	0.40	0.03	0.25	0.52	0.1	1.75
KL-7	Borewell	5.88	140	0.18	0.24	0.09	0.05	0.38	0.41	0.03	0.08	-0.10	0.1	3.82
KL-8	Pump	6.33	180	0.20	0.67	0.15	0.15	0.43	0.80	0.42	0.16	1.29	0.1	1.15
KL-9	Pump	6.42	260	0.44	0.91	0.14	0.18	0.59	0.83	0.10	0.29	0.38	0.2	1.09
KL-10	Pump	5.63	140	0.32	0.61	0.05	0.07	0.12	0.65	0.00	0.04	0.49	0.7	0.80

ID	Well typ.	pH	Cond. µS/cm	DSi mM	Na mM	K mM	Mg mM	Ca mM	Cl mM	NO_3 mM	SO_4 mM	$\delta^{30}Si$ ‰	1SD ‰	Ge/Si µmol/mol
TN-1	Pump	7.16	5420	0.16	34.9	0.89	5.19	1.04	40.8	0.06	4.93	0.74	0.2	1.12
TN-2	Pump	6.31	280	0.23	0.79	0.06	0.40	0.31	1.08	0.24	0.16	1.32	0.1*	0.73
TN-3	Pump	6.85	2090	0.15	9.89	0.83	2.14	0.39	9.69	0.01	1.94	1.88	0.1	0.13
TN-4	Borewell	7.25	2280	0.13	14.8	1.07	1.74	0.33	14.1	0.03	1.93	1.50	0.2	0.88
TN-5	Pump	7.15	2750	0.09	10.8	2.76	2.50	1.12	11.7	5.20	2.05	1.19	0.0	0.54
TN-6	Pump	7.09	810	0.78	3.63	0.19	0.62	1.61	3.69	0.77	0.42	0.65	0.0	1.26
TN-7	Pump	7.20	1370	0.17	7.16	0.21	0.86	0.34	6.41	0.58	0.52	0.70	0.1	0.57
TN-8	Pump	7.36	5820	0.19	40.1	4.71	3.51	0.80	42.0	3.60	4.00	4.21	0.0*	0.08
TN-9	Borewell	7.10	1100	0.14	2.90	1.93	2.00	0.16	2.50	0.00	1.08	3.26	0.0	n.a.
TN-10	Pump	7.08	1760	0.20	8.68	0.80	1.09	1.58	11.9	2.63	0.88	0.94	0.0	0.40
Andra Pradesh														
AP-1	Pump	7.26	983	0.52	2.84	1.15	0.75	1.00	2.88	0.87	0.39	0.59	0.0	2.33
AP-3	Pump	6.47	730	0.25	2.31	0.14	0.51	1.32	3.50	0.01	0.53	1.93	0.2	1.01
AP-4	Pump	7.02	1140	0.22	4.19	0.15	1.03	0.99	4.64	0.04	0.34	0.48	0.1	1.05
AP-5	Borewell	6.90	260	0.27	0.84	0.06	0.40	0.57	0.57	0.03	0.13	1.68	0.1	1.13
AP-6	Pump	7.33	5310	0.09	32.8	1.51	9.56	0.06	30.2	0.02	4.95	n.a.	n.a.	n.a.
AP-7	Borewell	7.79	6920	0.09	64.2	1.08	1.55	0.33	54.0	0.19	1.50	0.38	0.1	1.21
AP-8	Pump	7.28	6010	0.21	29.5	7.37	4.78	4.33	43.0	6.88	3.27	0.94	0.1	0.70
AP-9	Pump	7.55	2100	0.17	29.4	0.26	0.08	0.03	7.56	1.41	1.92	3.14	0.6	0.24
AP-10	Pump	7.07	1500	0.29	9.22	0.32	1.24	1.45	6.96	1.17	2.18	0.69	0.0	0.58
Odisha														
OD-1	Borewell	7.26	840	0.09	3.39	0.10	0.76	0.36	0.26	0.03	0.13	-0.15	0.1	1.02
OD-2	Borewell	7.03	570	0.53	1.66	0.03	0.87	0.61	0.74	0.06	0.06	-0.04	0.2	2.68
OD-3	Pump	7.25	1030	0.44	5.73	0.15	0.91	0.43	3.95	0.06	0.32	-1.07	0.1	3.25
OD-4	Pump	7.16	715	0.10	4.19	0.24	0.57	1.19	2.83	0.00	0.08	-0.55	0.1	0.82
OD-5	Pump	6.17	650	0.24	2.97	0.27	0.57	0.43	2.35	0.01	0.22	0.47	0.1	1.46
OD-6	Borewell	6.85	830	0.81	2.75	0.20	0.90	0.42	2.50	0.01	0.13	0.40	0.2	2.07
OD-7	Pump	6.29	240	0.52	0.77	0.14	0.17	0.44	0.36	0.06	0.04	0.12	0.0	2.31
OD-8	Pump	6.37	665	0.88	1.43	0.65	0.61	1.29	2.94	0.45	0.21	0.54	0.1	0.83
OD-9	Borewell	7.07	876	1.25	4.40	0.04	1.31	0.40	3.78	0.00	1.06	0.82	0.1	0.76
OD-10	Pump	6.89	5830	1.07	20.4	12.8	7.86	0.50	37.2	2.56	4.96	0.72	0.3	1.19
West Bengal														
WB-1	Pump	7.30	1042	0.51	8.75	0.15	0.50	0.17	2.09	0.12	0.31	-0.66	0.2	16.30
WB-2	Pump	7.31	1100	0.68	6.60	0.17	1.26	0.76	2.83	0.04	0.78	-0.51	0.1	2.36
WB-3	Pump	7.21	1250	0.41	5.94	0.10	0.85	0.76	3.89	0.02	0.54	-0.49	0.1	0.66
WB-4	Pump	7.03	1350	0.69	9.00	0.16	0.68	0.19	5.63	0.01	0.24	-0.37	0.0	1.28
WB-5	Borewell	7.49	1600	0.41	9.32	0.08	1.05	0.43	9.84	0.01	0.35	-0.35	0.0	1.72
WB-6	Pump	7.12	1500	0.43	6.26	0.13	1.63	0.41	7.57	0.04	0.48	-0.21	0.2	1.68
WB-7	Pump	7.03	1647	0.71	6.78	0.16	2.81	1.01	12.5	0.02	0.42	-0.31	0.1	2.81
WB-8	Pump	7.35	3680	0.33	26.6	1.20	3.09	0.44	20.2	0.13	3.99	4.48	0.0	0.18
WB-9	Pump	6.91	610	0.44	3.01	0.11	1.08	0.41	2.25	0.01	0.10	-0.84	0.0	0.31
WB-10	Borewell	7.26	923	0.74	4.36	0.34	2.04	0.43	2.93	0.16	1.18	1.59	0.0	0.61

3.3. Germanium concentration and Ge/Si ratio

The Ge concentration in groundwater ranged from 0.04 to 8.3 nM, with an average of 0.67 nM (±1.04, n=81). The value is in the higher range of reported Ge concentration of groundwater, ranging from 0.03 to 0.5 nM (Aguirre et al., 2017, Baronas et al, 2020). The Ge/Si ratio in groundwater ranged from 0.08 to 16.3 µmol/mol, with an average of 1.46 µmol/mol. We considered one groundwater sample from West Bengal (WB1) with an anomalously high Ge concentration of 8.3 nM (more than 10 times the average) as an outlier and henceforth excluded from calculations and plots. Overall, Ge/Si ratio exhibits a weak – but significant, negative correlation with $\delta^{30}Si$ in coastal groundwater ($R^2 = 0.24$, p value<0.001).

4. Discussion

The present study highlights the large variability in $\delta^{30}Si$ composition of groundwater compared to river water, indicating complex dynamics of Si cycling in the coastal critical zone. The discussion section reviews several processes influencing the Si cycling in coastal groundwater and assesses the impact of fresh submarine groundwater discharge (fSGD) on the Indian coast.

4.1. Sources of Si in coastal groundwater

The dissolved silicon (DSi) concentration in coastal groundwater samples varied strongly with an average of 484±304 µM and almost 5.5‰ variability in $\delta^{30}Si$, from -1.07 to 4.5‰ (Table 1, Fig. 2). The average of coastal groundwater from the present study was 0.91±1.21‰, heavier than the global groundwater average reported at 0.49±0.94‰ but highly heterogenous (Frings et al 2016 and references therein, Ehlert et al., 2016a, Martin et al 2021). Silicon in coastal groundwaters can originate primarily from two sources, water-rock interactions as meteoric water percolates through unsaturated zones and seawater intrusion and circulation within the aquifer. In the present study, only a few samples exhibit higher conductivity and Cl concentration indicative of seawater intrusion (Table 1). Thus, given the low DSi in seawater compared to groundwater, we will mostly discuss our results on the Si dynamics of fresh groundwater having a minor impact from seawater mixing. Additionally, neglecting minor input from atmospheric deposition (<5 µM DSi, Riotte et al., 2014), the primary source of DSi in groundwater is weathering of silicate minerals which can be immobilized by shallow soil and saprolite processes before reaching the saturated zone (Georg et al., 2009a, Strandmann et al., 2014, Chapter II). On average, coastal groundwater exhibited a $\delta^{30}Si$ of 0.85±1.1‰, heavier than the upper continental crust value (UCC) of -0.25±0.16‰ (Ziegler et al., 2005, Savage et al., 2013) and granitic gneiss value of Peninsular gneiss of -0.34±0.08‰ (Riotte et al., 2018a), indicating incongruent nature of silicate weathering. Our interpretation relies on two underlying assumptions: i) whole rock $\delta^{30}Si$ signature is considered as a reasonable approximation for Si released during weathering, ii) isotopic fractionation during dissolution is also considered transient and will be negligible as weathering progresses over time (Ziegler et al., 2005, Geilert et al., 2014, Frings et al., 2021a). A first look at the global compilation of the groundwater $\delta^{30}Si$ *vs.* DSi shows no general pattern, and exhibited no relationship with regional rainfall and aquifer lithology (Fig. 2, Fig. S1). Unlike river systems, which can integrate weathering signatures from the entire basin as well as in situ processes, aquifers are

spatially limited and reflect local weathering and biogeochemical processes. Absence of any such global relationship is not surprising given the differences in the aquifer lithology and diversity of processes that can fractionate Si isotopes in the system. However, three main aspects of the $\delta^{30}Si$ variation with DSi is of interest here, marked as A, B, and C in Fig. 2.

Domain A: $\delta^{30}Si>2‰$

The domain contains exclusively groundwater from alluvium aquifers with $\delta^{30}Si>2‰$ (Fig. S1), indicative of fast kinetic processes that can significantly fractionate Si isotopes without re-equilibration or isotopic exchange (Zheng et al., 2019, Fernandez et al., 2019). Weathering solubilizes Si from primary minerals and the fraction of Si transferred into the groundwater system depends on the extent of incorporation into clay minerals, adsorption onto secondary Fe and Al oxy-hydroxide minerals and, plant uptake (Opfergelt and Delmelle, 2012). All mentioned processes take up lighter Si isotopes, leaving the residual groundwater/soil solution heavier. In shallow aquifer systems with regular irrigation and contribution from agricultural return flows, multiple cycles of return flow can enrich the $\delta^{30}Si$ through plant uptake (Ding et al., 2008, Jafari et al., 2019).

Domain B: high DSi and homogenous $\delta^{30}Si$

Groundwater samples with DSi>1000 µM were associated with limited variability in $\delta^{30}Si$ with an average of 0.83±0.2‰, similar to the global groundwater average (Fig. 2). Higher DSi in groundwater can result from various processes such as, i) high weathering rates and abundance of highly weatherable primary minerals such as basalts (Das et al., 2005), ii) lower fraction of Si lost from solution as a result of secondary processes, iii) dissolution of precipitated secondary phases such as phytolith and clays and, iv) high evapotranspiration due or not to irrigation. Interestingly, even though local lithology can be a determining factor for the DSi behaviour in groundwater, samples in region B cover diverse lithologies such as alluvium in Odisha (this study), banded gneiss complex in Karnataka (inland Berambadi watershed, Chapter II), and basaltic terrains in both Maharashtra (present study) and hot springs from Iceland (Opfergelt et al., 2011) (Fig. 2). Moreover, if we assume that congruent weathering of primary minerals with limited secondary precipitation results in high DSi, the $\delta^{30}Si$ should approach UCC values, which is not the case here. Indeed, the dissolution of secondary sources of Si, such as phytoliths and clay minerals, can increase the DSi but at the same time lead to a lighter $\delta^{30}Si$ in groundwater (Georg et al., 2009a, 2009b, Fraysse et al., 2009, Dellinger et al., 2014). Also, biogenic Si phases, such as phytoliths, are unlikely to contribute to deep groundwaters (Farmer et al., 2005). Excessive evapotranspiration can be associated with both arid conditions and irrigation practices, which is observed in the Berambadi watershed (Chapter

II). Multiple cycles of return flows related to irrigation can significantly enrich DSi in soil solution and groundwater and promote the secondary mineral formation and preservation in the soil and saprolite layers (Frings et al 2016, Park et al., 2018). However, why such processes lead to homogenization in $\delta^{30}Si$ from varying lithological and climatic conditions remains unclear and requires further investigation. The question is also pertinent to the fact that globally groundwater (0.77±0.9‰) and soil water (0.75‰, Sutton et al., 2018) exhibit a higher DSi and a lower $\delta^{30}Si$ compared to surface waters (1.28±0.68‰, Frings et al., 2016; see also Chapter II). One possibility is that groundwater reflects a mix between systems influenced by kinetic unidirectional processes and a metastable equilibrium condition, where the neoformation of new secondary phases follows isotopic re-equilibration with coevolving surrounding fluids. The bulk isotopic signatures of the secondary phases are inherited from initial kinetic fractionation associated with the formation of precursor amorphous phases and are preserved (Oelze et al., 2015, Roerdink et al., 2015, Fernandez et al., 2019). On the other hand, fluid residence time sets the hydrological limit in river systems to attain chemical equilibrium and determines the solute fluxes as well as the isotopic composition (Maher et al., 2011). Such explanation remains speculative at this point without a further sampling of precipitating phases to establish a mass balance. The ab initio calculation indicate that under isotopic equilibrium lighter ^{28}Si is not preferentially taken up by the precipitating phases and the fact that the majority of clay minerals are lighter relative to bedrock suggests that true equilibrium is rarely attained (Méheut et al., 2009, Cornelis et al., 2014, , Frings et al., 2021a). Secondary mineral formation generally follows the transformation of Al hydroxides to high surface area amorphous precursors through Si adsorption, and over time are converted to crystalline clays (Oelze et al., 2014). Longer fluid residence time in aquifers provide ideal environments where slow re-equilibration with the fluids can lead to diminishing of kinetic signatures preserved in the amorphous precursors and secondary clays, depending on the surface area and depth of isotopic exchange (Maher et al., 2011, Fernandez et al., 2019). Fluid residence time imparts significant control over the DSi fluxes and isotopic composition, resulting in lower groundwater $\delta^{30}Si$ compared to surface river waters, which are dominated by kinetic isotopic fractionation resulting from weathering and biotic uptake.

Domain C: $\delta^{30}Si$ lighter than UCC

The domain C (Fig 2) is characterized by the $\delta^{30}Si$ signatures of the groundwaters close to, or even lower than the upper continental crust composition. These groundwater originate from alluvial aquifers in West Bengal and Odisha, sandstone aquifers from the Navajo aquifer system (Georg et al., 2009b) and the Great Artesian basin (Strandmann et al., 2014). Even

though the re-equilibration and/or congruent weathering can lead to close to UCC δ^{30}Si composition, groundwater with lighter δ^{30}Si (-0.83±0.36‰) can only be explained by selective dissolution of light secondary phases in the aquifers (Georg et al 2009b, Strandmann et al 2014). Interestingly, the samples marked in region C exhibits a Ge/Si ratio ranging from 0.3 to 3.3 μmol/mol, and the primary Si source was attributed to the dissolution of secondary Si sources, such as clays (Fig. 3b). The clay dissolution should release the Ge and lighter ^{28}Si incorporated into clays, potentially increasing the Ge/Si ratio and decreasing the δ^{30}Si (Georg et al., 2009b). However, we also observe lower Ge/Si, which can be due to excess contribution from low Ge/Si sources such as quartz (dominant in the alluvial aquifers) or due to preferential loss of re-solubilized Ge due to adsorption and coprecipitation with Fe-oxyhydroxides (Pokrovsky et al., 2006). We can also neglect the preferential weathering of lighter primary minerals such as biotite (-1.01±0.4‰, Frings et al., 2021b) here, since the aquifer lithology is dominated by quartz followed by feldspars and clays (Zhu et al., 2006, Georg et al., 2009a, 2009b, Strandmann et al., 2014). In summary, the groundwater Si can be sourced from both primary and secondary phases, and subsequently undergo significant fractionation depending on the secondary processes and dynamics of fluid-mineral interaction.

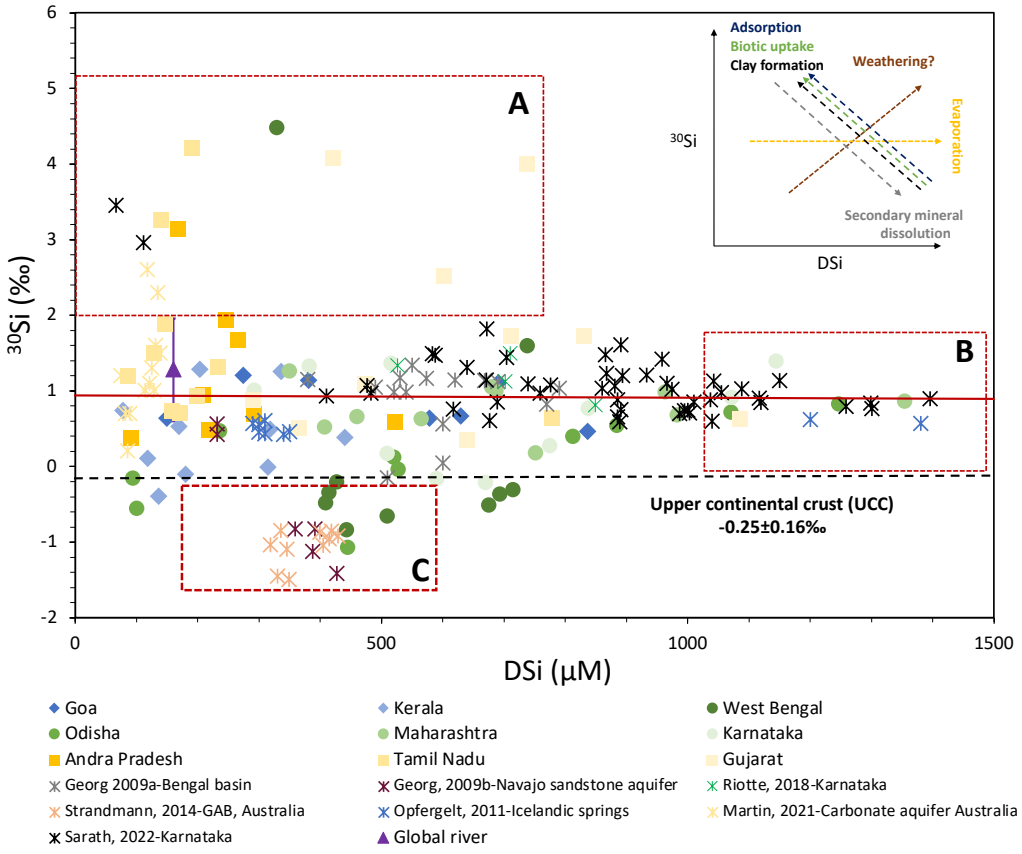

Figure 2. *δ^{30}Si vs. DSi relationship in groundwater from the present study and also compiled from selected previous works (Georg et al 2009a, Georg et al 2009b, Riotte et al 2018, Strandmann et al 2014, Opfergelt et al 201, Martin et al 2021, Sarath 2023 Chapter II). Three regions are marked with dotted boxes as A, B and C see section 4.1 for details. The groundwater samples are classified based on regional rainfall data from IMD, 2015 (Diamonds represent the region with annual rainfall >2000 mm, circles symbol for rainfall between 1000-2000 mm/yr and the square symbols for <1000 mm/yr). The dashed horizontal line represents upper continental crust and the red line indicates groundwater average. The global river water δ^{30}Si and DSi data from Frings et al., 2016.*

4.2. Evolution of δ^{30}Si and Ge/Si in groundwater

With exception of groundwaters marked as A, B and C in Fig. 2, the majority of the groundwater remain unremarkable with δ^{30}Si between UCC composition of -0.25‰ and 2‰, within a wide DSi range of 100 to 1000 µM. To understand the controls of weathering and formation of secondary phases and/or uptake over Si isotopic composition in groundwater, we estimated the fraction of Si remaining in the dissolved phase by normalizing it with a conservative element in solution and bedrock as;

$$f_{Si} = (DSi/Na^*)_{groundwater}/(Si/Na)_{bedrock} \qquad E(2)$$

Here we assume the stoichiometric release of Si and Na from the bedrock as a result of silicate weathering and preferential loss of Si from solution by incorporation into secondary phases (Georg et al 2006, Hughes et al 2013). The f_{Si} values indicate the relative extent of incorporation of Si into the secondary phases and also biotic uptake, with a value of 0 implying complete removal whereas the f_{Si} value of 1 indicates all mobilized Si remains in the solution. The '*' denotes the atmospheric/seawater correction to discard any contribution from atmospheric deposits and seawater mixing. We must be cautious in using a single Si/Na ratio for the parent bedrock, given the diversity of lithologies along the coast: the ratio varies from 3.73 (quartz-corrected granitic gneiss, Braun et al., 2009) to 10.6 (typical basalts, Peng et al., 1998) depending on the sampling location. In the present study, in order to compare all over India, we employed the granitic gneiss value which is closer to the UCC composition, with full knowledge that f_{Si} changes significantly in the case of basaltic regimes (almost 2-3 times lower f_{Si}, Wedepohl, 1995, Peng et al., 1998). Another caveat of using the ratio lies in the assumption of conservative behaviour of Na and neglecting additional secondary sources of Si. Despite the limitations, we can gain a broad understanding of the evolution of Si isotopes in groundwater by looking at the relationship between f_{Si} and δ^{30}Si.

According to this normalization procedure, the fraction of silicon incorporated into secondary phases would range from 18 to >99%, indicating a significant loss of solubilized Si. Most of the samples lie within the Rayleigh and steady-state fractionation models with fractionation

factors ($^{30}\varepsilon$) varying from -0.5 to -2‰ (Fig. 3a). The variability associated with the fractionation factor reflects the different processes that can fractionate the Si isotopes in surface and subsurface environments. The δ^{30}Si of the remaining groundwater depends on the $^{30}\varepsilon$ associated with the processes, ranging from -0.4 to -3.3‰ for secondary mineral precipitation, +0.3 to -1.9‰ for plant uptake, and -1.1 to -1.5‰ for Fe-Al oxyhydroxides (Delstanche et al., 2009, Frings et al., 2021a). Furthermore, successive dissolution/precipitation and adsorption/desorption cycles can significantly enrich the residual solution in heavier Si isotopes (Basile-Doelsch et al., 2005). The magnitude of fractionation factors during secondary phase precipitation is also shown to vary depending on the fluid-mineral interaction dynamics, where fast unidirectional kinetic fractionation can lead to enrichment in lighter Si isotopes of solids, while the enrichment is diminished or even absent under equilibration between precipitating solids and solution (Oelze et al., 2014, Oelze et al., 2015, Roedink et al., 2015). To complement the δ^{30}Si we used Ge/Si ratio, which can also be controlled by both abiotic processes such as secondary clay formation and adsorption onto Fe-oxyhydroxides, and plant uptake from shallow soil layers and saprolite (Kurtz et al., 2002, Derry et al., 2005, Opfergelt et al., 2010). Starting from a silicate endmember Ge/Si ratio, assumed to be 2 μmol/mol (Lugolobi et al., 2010), groundwater samples range Ge/Si range from 0.08 to 4.1 μmol/mol, the lower range is typical of the stream and river water while the higher end was observed in soil porewater (Fig. 3b, Lugolobi et al., 2010, Baronas et al., 2018, 2020). To simplify the interpretation, we can first consider the weathering controls on Ge/Si ratio and δ^{30}Si, where secondary clays are usually enriched in Ge (>4 μmol/mol) leaving the residual soil solution and groundwater with low Ge/Si (<1 μmol/mol). Thus, the decreasing Ge/Si and increasing δ^{30}Si trend indicates weathering and formation of secondary clays and the extent of incorporation and type of clay formed can dictate the Ge/Si ratio in groundwater (Fig. 3b, Opfergelt et al., 2010, Frings et al., 2021b). It is interesting to note that all the heavy δ^{30}Si signatures (> 3‰) were associated with a low f_{Si} (<0.1) and plots in a Rayleigh model between $^{30}\varepsilon$ of -0.5 and -2‰, indicating that Si is constantly removed from the system with little to no backward reaction or unidirectional kinetic processes and exhibits a low Ge/Si ratio. We propose two explanations for such behaviour:

i) groundwaters with heavy δ^{30}Si can be indicative of plant uptake from the soil solution and/or shallow groundwaters following a unidirectional kinetic isotopic fractionation with $^{30}\varepsilon$ associated with the crop type (see also Chapter II and IIIa where this has been suggested for some groundwaters). The fraction of Si taken up

and initial silicon isotopic composition can be altered through successive return-flow cycles (Riotte et al., 2018b, Frick et al., 2020, Frings et al., 2021a). A low Ge/Si ratio, may indicate plant uptake either by discriminating against Ge and ^{30}Si or uptake without any discrimination against Ge from a low Ge/Si soil solution. Plant discrimination against Ge was recently disputed given that a significant pool of Ge can be complexed with organic matter in non-phytolith compartments, especially roots (Delvigne et al., 2009; Kaiser et al., 2020, Frings et al., 2021b),

ii) in deeper groundwaters such signatures can be indicative of an isolated aquifer system with precipitation of amorphous silica following a with significant DSi loss and kinetic enrichment (Oelze et al., 2014). At high f_{Si} values, it is difficult to distinguish both the steady state and Rayleigh models, but as the f_{Si} decreases, we see two behaviours segregating with groundwater following either one depending on the uptake process and related fractionation factor. The groundwater forms a part of weathering zone where fluids can attain signatures from both unidirectional kinetic fractionation and a more steady state behaviour where the loss of Si through biotic and abiotic processes are balanced by fresh input through silicate weathering as discussed in Chapter II.

Even with such a broad trend between Ge/Si and $\delta^{30}Si$, we observed large variability, which can be due to our assumption of a single silicate endmember composition (Fig. 3b). Ge/Si ratio of primary minerals ranges from 0.5 μmol/mol in quartz to 6.1 μmol/mol in biotite and 7 μmol/mol in hornblende, while the $\delta^{30}Si$ of the primary mineral is also shown to vary from -0.07‰ in quartz to -1.01‰ in biotite (Kurtz et al 2002, Lugolobi et al 2010, Frings et al 2021a). Contribution from different primary minerals to total weathering and associated inter-mineral variability in both Ge/Si and $\delta^{30}Si$ can be significant to spatially distinct aquifer systems. Similar variability in Ge/Si also exists for the clay fractions precipitated in soils, reported from close to granitic values in smectite-dominated clays to almost 6.5 μmol/mol in kaolinite-dominated clay fractions (Kurtz et al., 2002, Lugolobi et al., 2010, Opfergelt et al., 2010, Frings et al., 2021b). Recently, using a thermodynamic modelling approach, Perez-Fodich and Derry (2020) concluded that the Ge/Si ratios of the fluid phase are controlled by precipitation kinetics and re-equilibration of precipitating solids. Longer residence time can favour re-equilibration, resulting from the continuous exchange of Ge and Si between groundwater and precipitated

secondary minerals can lead to an increase in the Ge/Si ratio of groundwater (Perez-Fodich and Derry, 2020).

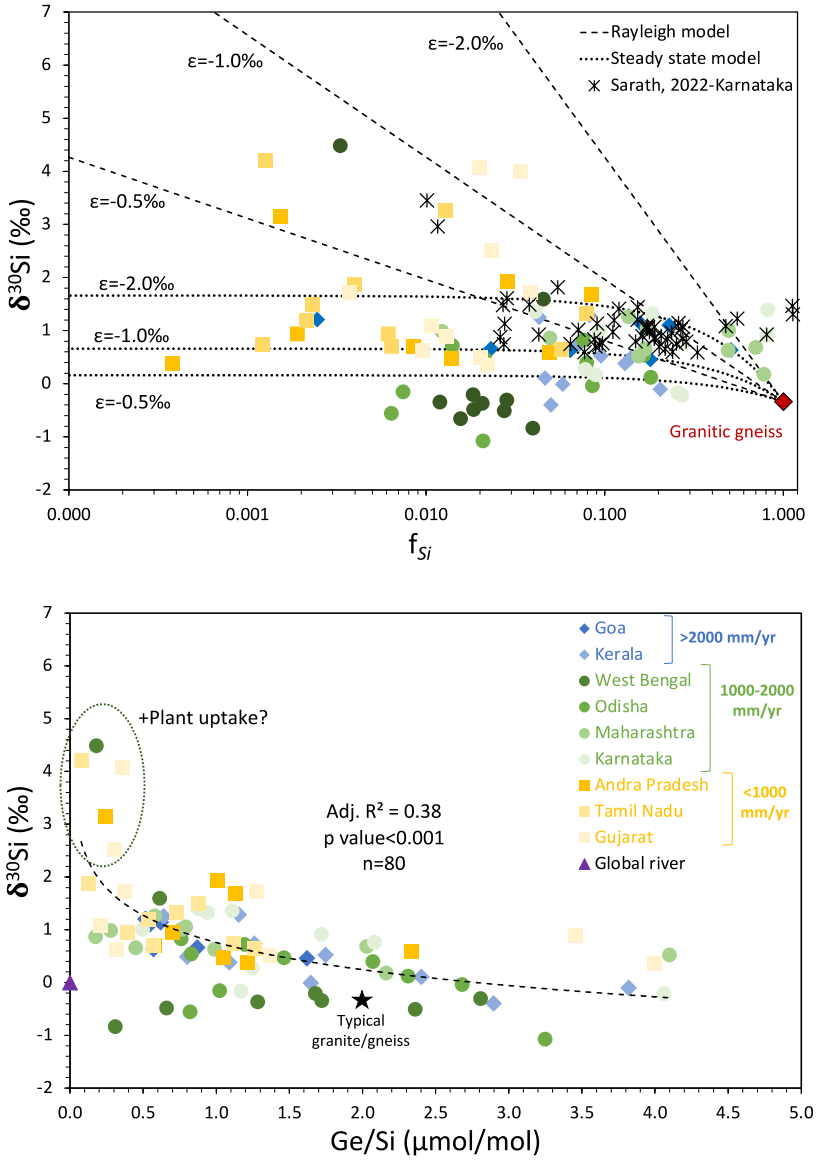

Figure 3. *a) The $\delta^{30}Si$ plotted against the fraction of Si remaining in the solution (f_{Si}) for all the coastal groundwater samples and groundwater samples from Chapter II for Karnataka. The dotted lines and dashed lines represent the steady state fractionation model and Rayleigh model respectively with different fractionation factors (ε), b) the plot between $\delta^{30}Si$ and Ge/Si ratio for coastal groundwater samples. The black star indicates the silicate bedrock end member (Lugolobi et al 2010, Savage et al 2013). The global river average is from Baronas et al, (2018). An outlier sample with a Ge/Si ratio of 16.3 µmol/mol and $\delta^{30}Si$ of -0.66‰ (from West Bengal (WB1)) is omitted from the figure. The color code represents mean annual rainfall for the coastal states.*

We also observed a more than 10-fold increase in Ge concentration compared to average groundwater (8.3 nM and Ge/Si ratio of 16.3) in groundwater in West Bengal (WB1), which clearly indicates contamination of Ge in groundwater. We suspect contamination of this

particular aquifer with coal fly ashes or coal-bearing phases which can have a Ge/Si ratio of up to 2500 μmol/mol (Froelich et al., 1985, Hu et al, 2009). Overall, the Ge/Si ratio and evolution of δ^{30}Si in groundwater is broadly consistent with a primary weathering control, with heterogenous lithology and surface water use. The impact of plant uptake and dissolution of biogenic silica (BSi) are restricted to shallow aquifers where they can significantly alter δ^{30}Si and Ge/Si.

4.3. Fresh submarine groundwater fluxes to coastal ocean and isotope budget

Dissolved silicon (DSi) in submarine groundwater discharge (SGD) is a mixture of two components: DSi from fresh terrestrial groundwater (fresh SGD) resulting from weathering reactions in the aquifers, and a recycled saline groundwater (here onwards saline SGD) originating from seawater but attaining unique signature from water-rock interaction in subsurface region (Burnett et al., 2003, Moore et al., 2010, Rahman et al., 2019). Fresh SGD can be considered as a source of new DSi to the coastal ocean, while saline SGD can be a mixture of new Si source resulting from dissolution of coastal terrigenous sediments and recycled DSi from regeneration of biogenic silica (Anschutz et al., 2009, Ehlert et al., 2016b, Rahman et al., 2019). Overall, Tréguer et al, (2021) estimated that SGD driven Si fluxes to the ocean ranges between 0.7 to 3.8 TmolSi/yr, 0.7 TmolSi/yr being the lower estimate based only on fresh groundwater, while 3.8 TmolSi/yr is the upper estimate for total SGD (Cho et al., 2018, Rahman et al., 2019). The terrestrial SGD estimates vary considerably depending on the study region and typically contribute less than 10% of the riverine DSi flux (Rahman et al., 2019, Luijendijk et al., 2020).

In order to calculate the Si flux from fresh SGD, we extracted the fresh SGD water fluxes (km^3/yr) from each Indian coastal state from the published global coastline by Zhou et al (2019). The water flux for each state includes integration of multiple catchments, and for each catchments the flux is an average of three recharge models (MOSAIC, NOAH, VIC models, see Zhou et al. (2019) for details). The SGD water flux is converted to Si flux along the coast using the average DSi of groundwater for each state (Table 2). Please note here that the fresh SGD flux for each state represent the total fresh groundwater discharged to the respective coast without considering saline/recycled SGD. The δ^{30}Si, DSi and discharge values of the monsoonal rivers in India from Mangalaa. (2016) and Mangalaa et al. (2017) were used to compare surface water from peninsular rivers with the groundwater Si fluxes to the Indian coast (Table 3).

***Table 2**. The details of fresh groundwater discharge, Si and Ge flux, and Si isotopic composition for coastal groundwaters. The fresh SGD is based on Zhou et al, (2019).*

State	Fresh SGD flux	DSi	Si flux	$\delta^{30}Si_{avg}$	SD	Ge	Ge flux
	km^3/y	µM	Gmol/yr	‰	‰	nM	kmol/yr
Gujarat	0.35	615.5	0.22	1.75	1.4	0.71	0.25
Maharashtra	0.76	719.9	0.55	0.78	0.3	0.46	0.35
Goa	0.07	505.7	0.03	0.73	0.4	0.17	0.01
Karnataka	0.45	678.8	0.31	0.64	0.6	0.36	0.16
Kerala	0.78	229.5	0.18	0.52	0.6	0.32	0.25
Tamil Nadu	0.19	223.1	0.04	1.56	1.1	0.3	0.06
Andra Pradesh	0.25	233.2	0.06	1.17	0.9	0.71	0.18
Odisha	0.48	593.4	0.29	0.29	0.7	1.16	0.56
West Bengal	2.29	535	1.23	0.24	1.5	1.56	3.57
			2.9 GmolSi/yr	**0.56‰**			**5.4 kmolGe/yr**

***Table 3.** The details of discharge, Si flux and $\delta^{30}Si$ composition of monsoonal rivers in India (data from Mangalaa, (2016), Mangalaa et al., 2017). Sampling was carried out during wet period in 2014. The river water endmember sample is from upper estuary and consequently each DSi and $\delta^{30}Si$ represents a single sample and thus no standard deviation is reported.*

State	River	Discharge	DSi	Si flux	$\delta^{30}Si$
		km^3/yr	µM	Gmol/yr	‰
Gujarat	Narmada	45.63	176	8.03	1.8
	Tapi	14.88	178	2.65	1.8
Goa	Zuari	3.25	114	0.37	0.5
	Mandovi	3.31	124	0.41	0.4
Karnataka	Kali	4.79	114	0.55	0.8
	Netravathi	11.06	130	1.44	0.6
Kerala	KBW	12.33	105	1.3	0.6
Tamil Nadu	Ponnaiyar	1.6	326	0.52	2.8
	Cauvery	21.35	349	7.45	2
	Vellar	0.9	519	0.47	2.1
Andra Pradesh	Godavari	121	250	21.5	0.9
	Krishna	69.79	327	22.84	1.9
Odisha	Mahanadi	66.89	149	9.95	1.5
	Rushikulya	1.93	242	0.47	1.9
West Bengal	Haldia	50.46	101	5.09	1.6
	Subernereka	12.36	202	2.49	1.7
				85.5 GmolSi/yr	**1.65‰**

The estimated total terrestrial SGD-driven DSi flux from the Indian coastline is 2.9 GmolSi/yr, which represents 3.4% of the total monsoonal riverine DSi flux to the Indian coast, which reduces to <1% of the estimated Si supply by rivers to the North Indian ocean after correcting for contribution from rivers which were not sampled (e.g. Ganges, Mangalaa et al., 2017, Table 3). The estimated fresh SGD Si flux from Indian coast is 0.4% of the global terrestrial fresh SGD Si delivery to the ocean (Rahman et al., 2019, Luijendijk et al., 2020). However, the fresh SGD water flux by Zhou et al, (2019) is estimated using a surface water budget approach, is likely an overestimate given the model provides little consideration of subsurface controls on groundwater discharge (Luijendijk et al., 2020). Thus, our estimates of the terrestrial SGD will be on the higher end compared to the recent estimate by Luijendijik et al, (2020) considering hydrogeological parameters on groundwater flow. Considering the total terrestrial SGD flux by Zhou et al (2019) and Luijendijk et al (2020), and an average Ge concentration in groundwater of 0.67 nM from the present study, we can calculate a total terrestrial SGD-driven Ge flux of 0.15-0.3*10^6 mol Ge/yr, which is almost 5-10% of the total estimated riverine Ge input (Mortlock et al., 1993; Elderfield and Schultz, 1996; King et al., 2000). Thus, the coastal groundwater supply of Ge to the oceanic Ge budget is significant and with an average Ge/Si ratio of 1.3 µmol/mol, distinct from Ge/Si ratio of riverine (0.7 µmol/mol) and hydrothermal input (8-14 µmol/mol) (Rouxel et al., 2017). The next step would be estimating the impact of groundwater Si fluxes on the isotopic composition of the total Si flux to the Bay of Bengal and Arabian Sea. The weighted δ^{30}Si for coastal fresh groundwater discharge was 0.56‰, while the riverine Si flux was significantly higher with a δ^{30}Si of 1.65‰ (Table 2, 3). However, the isotopic effect of fresh groundwater Si fluxes on the Arabian Sea and Bay of Bengal is <0.05‰ compared to riverine discharge which is within our analytical uncertainty, due to low Si discharge through fresh SGD. Overall, the impact of terrestrial fresh groundwater discharge to silicon isotopic composition and Si flux to the Indian coast is negligible compared to the rivers.

5. Conclusion

The analysis of groundwater from 86 sites in Indian coast demonstrate no general trend in δ^{30}Si with DSi, lithology or regional rainfall, with considerable variability in δ^{30}Si (-1.1 to 4.5) and DSi (100-1400 µM). The average δ^{30}Si of Indian coastal groundwater (0.85±1.1‰, 1SD, n=85) was higher than the published groundwater δ^{30}Si average so far (0.49±0.9‰, 1SD, n=66) and significantly lower than the surface water from Indian monsoonal estuaries (1.47±0.7‰, n=16). Overall, based on the δ^{30}Si *vs.* DSi plot we can characterize three peculiar regions; i)

groundwaters with $\delta^{30}Si>2‰$ are indicative of aquifers which incorporates signatures of unidirectional kinetic fractionation, possibly from plant uptake and/or amorphous Si precipitation, ii) groundwaters from various lithology exhibiting a DSi>1000 µM and a homogenous $\delta^{30}Si$ close to overall groundwater average, indicating processes that can solubilize Si without significant fractionation, iii) groundwaters with $\delta^{30}Si$ lower than UCC composition, which indicates dissolution of secondary Si sources (e.g. clays and silcretes). In general, groundwaters follow a mix of steady state and Rayleigh fractionation system, with fractionation factors between -0.5 to 2‰, within the previously published fractionation factors for secondary mineral formation and biotic uptake. Overall, groundwater represents a highly heterogenous reservoir of Si, incorporating signatures from various abiotic and biotic processes that can fractionate Si, with a 5.5‰ variability of $\delta^{30}Si$. Our results highlight the importance of systematic sampling of groundwaters inorder to decipher the variability associated with $\delta^{30}Si$ of Si sources to the rivers and other fluvial systems. Additionally, we used the surface water and groundwater DSi and $\delta^{30}Si$ to estimate the total Si flux to Bay of Bengal and Arabian sea through riverine input and fresh submarine groundwater discharge. Our results indicate that fresh SGD only account for <1% of the total Si input to Arabian sea and Bay of Bengal, and imparts no significant isotopic impact to the coastal $\delta^{30}Si$. However, based on the published global fresh SGD fluxes, Ge delivery through fresh SGD can account for almost 5-10% of the riverine supply and can be a missing source to Ge cycling in global ocean. This study offers a large dataset for groundwater $\delta^{30}Si$, which displays significant spatial variability and emphasise the importance of groundwaters as a highly heterogenous terrestrial Si reservoir.

Acknowledgements

The work is funded by CEFIPRA-IFCPAR support (NUNDERGROUND, project #5907). We acknowledge NIO for providing necessary support for field campaign and sampling. We thank B.S.K Kumar and his team in NIO for sampling and field work. The authors thank Aurélie Marquet and Frédéric Candaudap for their support to HR-ICPMS analyses, Benjamin Baud for the water sampling during field work, Pierre Burckel and Irina Djouraev for the help with ICPMS to check for Si chemistry ALYSES facility (IRD-SU). SPK thank IRD-Campus France for providing Ph.D. scholarship and constant support to carry out the work. The authors would like to thank M. Benrahmoune (LOCEAN-IPSL) for help in sample processing and clean lab management.

Supplementary figures

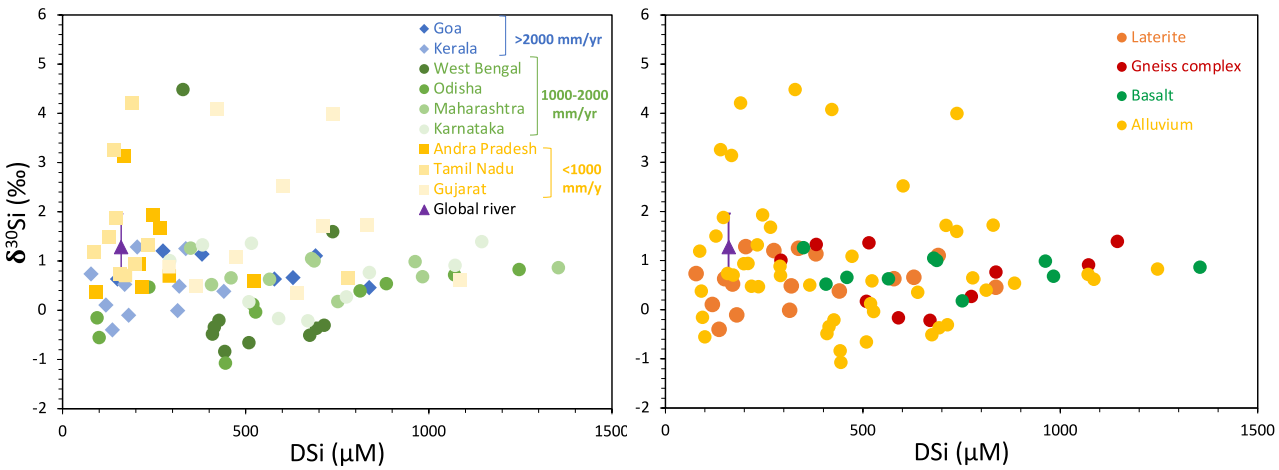

Figure S1. *The relationship between $\delta^{30}Si$ vs. DSi for coastal groundwaters categorized based on, a) regional rainfall (IMD, 2015) and b) aquifer lithology. The color code for left panel represents the mean annual rainfall for each state and right represent the lithology.*

V. Conclusion and perspectives

1. General conclusion

The present research was undertaken as a part of the Indo-French CEFIPRA project NUNDERGROUND (Nutrients transfers through groundwater in India), aiming to understand the pathways and impact of groundwater discharge into surface waters and coastal ocean. Broadly, the thesis focusses on understanding the controls on biogeochemical cycling of Si in groundwater, under varying spatial and temporal scales. The rationale was to first report and explain the variability in δ^{30}Si we observe based on differences in land use and seasonality compared to surface water and to apply the understanding to a coastal setting where surface water-groundwater interactions are known to occur. Interestingly, groundwater exhibits one of the largest variations in silicon isotopic composition on Earth, ranging from -1.5 to 4.5‰ (see Chapter II, IIIa, IV and Frings et al., 2016). Almost 5.5‰ range of groundwaters is larger than river water and seawater, but lower than plants and other sedimentary siliceous precipitates (Frings et al., 2016, Poitrasson et al., 2017). Previous groundwater δ^{30}Si measurements ranged from -1.5 to 2.6 ‰, with an average of 0.49±0.9‰ (1SD, n=66). With addition of groundwater samples from the thesis multiplying by more than three times the number of groundwater δ^{30}Si data published so far, the average is now raised to 0.81±0.9‰ (1SD, n=224) and gets closer to the river average (1.28±0.7‰, Frings et al., 2016). We have very limited understanding on groundwater Si cycling, and earlier works restricts the discussion to higher weathering fluxes related to longer residence time and dissolution of secondary phases leading to a lower δ^{30}Si (Georg et al., 2009a, Georg et al., 2009b, Strandmann et al., 2014). Evident from the previous groundwater compilation and the present research is the heterogeneity in groundwater δ^{30}Si at small spatial scale, where we observed values ranging from -0.2 to 4‰ in the span of few kilometre's. A primary conclusion from the present work is that, rather than climate, lithology, and land use, groundwater δ^{30}Si is largely dependent on the local biotic and abiotic fractionation within the weathering zone. We will now discuss some of the primary objectives mentioned earlier in Chapter 1 as separate questions and provide relevant conclusion we gathered from the current research.

Q1. What is the anthropogenic impact (land use) on groundwater δ^{30}Si and silicon cycle?

Soil and ecosystems act a "filter" for Si solubilized during weathering through uptake and precipitation of biogenic silica (BSi) by plants and/or other pedogenic forms of Si. Land use changes can significantly alter the Si cycle as the accumulated Si in agricultural crops are

harvested and are not recycled, which can deplete the soil BSi pools and reducing the baseflow delivery of Si (Struyf et al., 2010, Carey and Fulweiler, 2012). As discussed in Chapter II, our first objective was to understand the impact of land-use changes in groundwater Si cycling in watersheds with similar lithology and comparable climate. Our study was motivated by Vandevenne et al, (2015), where the authors have observed an increase in δ^{30}Si of signatures in soil water samples across a temperate land use gradient, from 0.62±0.3‰ in forest soil water to 1.61±0.1‰ in old croplands, that seems to be indeed transferred to surface waters up to upper estuary (Delvaux et al., 2010). Surprisingly, our research suggests no such significant differences in the δ^{30}Si of groundwater from forested Mule Hole watershed and agricultural Berambadi watershed, despite Berambadi displaying higher DSi due to repeated cycles of irrigation and pumping (Fig. 1).

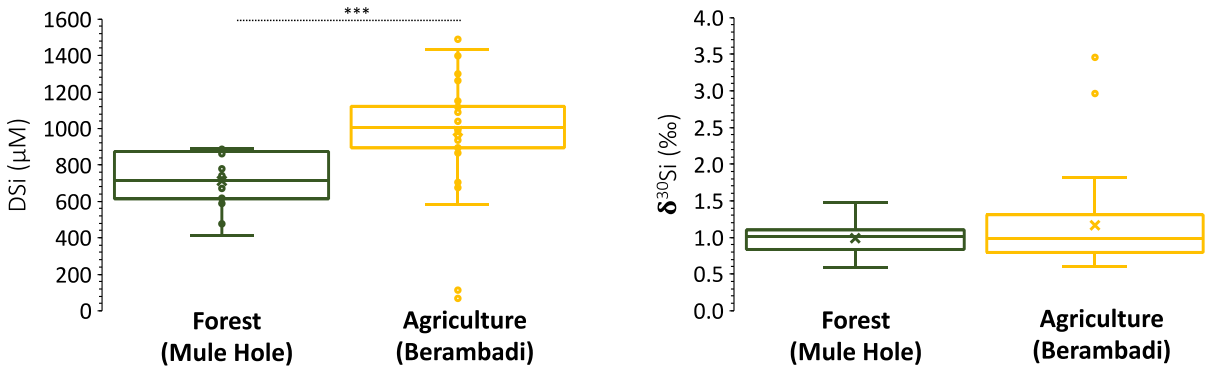

Figure 1. *The box plot showing variability in DSi and δ^{30}Si between forested Mule Hole watershed and agricultural Berambadi watershed. The '***' denote significant difference with p-value <0.001.*

However, measured soil solutions from Mule Hole and Berambadi were similar in δ^{30}Si (1.6±0.2‰) and significantly higher than groundwater with a lower DSi (515±120 µM). This observation poses two additional questions; i) a higher DSi and lighter δ^{30}Si indicates an additional lighter source of Si to groundwater as soil water percolates through unsaturated zone, ii) similarity in soil solutions from forested and agricultural watersheds indicates minor effect of land use and/or Si isotopic fractionation by plants. Through a simple isotopic mass balance, we estimated that almost 43% and 32% of the Si in Mule Hole and Berambadi groundwater is deriving from weathering in deeper regolith layers, effectively homogenizing the δ^{30}Si of groundwater (Fig. 2). Silicon isotopic fractionation by plants depends on the plant species, with

fractionation factors ranging from +0.3‰ in cucumber to -1.7‰ in rice (Ding et al., 2008, Sun et al., 2016). The lack of highly fractionating crops might explain the similarity in δ^{30}Si of soil solution between Mule Hole and Berambadi.

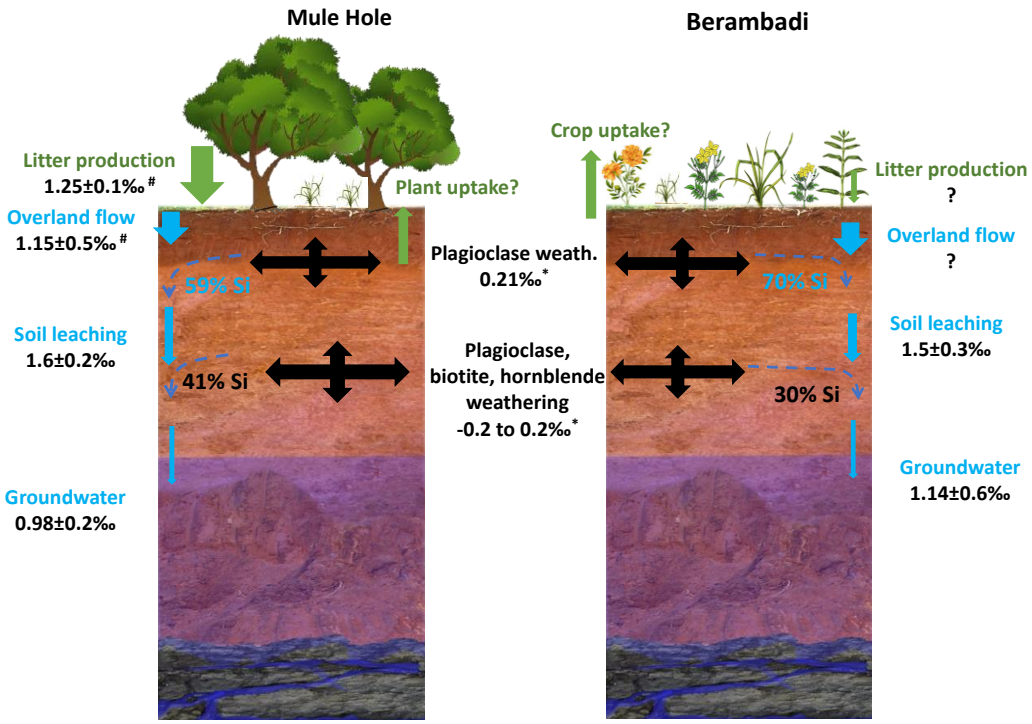

Figure 2. *The schematic showing the evolution of δ^{30}Si signatures from different hydrological compartments in Mule Hole and Berambadi. The percolating meteoric water incorporates δ^{30}Si signatures from shallow and deep weathering Si fluxes before reaching groundwater. The '#' represent values from Riotte et al. (2018) and '*' are theoretically calculated (see Chapter II for details).*

Q2. Does the seasonal monsoonal climatic regime in India have an impact on groundwater δ^{30}Si?

We observe no seasonal variability in groundwater δ^{30}Si composition, watershed scale and pair wise for individual groundwater samples, indicating significant buffer to seasonal monsoon precipitation (Fig. 3). Longer residence time of groundwater in unsaturated zones can lead to extended water rock interactions, effectively equilibrating the groundwater. This can be contrasted with significant temporal variability in δ^{30}Si of two major rivers from South India, Netravathi and Kaveri (Fig. 4, Sarath et al., 2022). Seasonal changes in δ^{30}Si of river water is primarily driven by varying contribution from surface and subsurface water to the river basin, which is supported by similar pattern of low δ^{30}Si during wet season. As presented in Fig. 2, soil water forms the heaviest δ^{30}Si pool in Mule Hole, while the overland/surface flow is lighter due to ASi dissolution, and groundwater is lighter resulting from deep weathering Si fluxes

(Riotte et al 2018, Chapter II). Additionally, Kaveri river is also influenced contribution from agricultural return flow in downstream basin, increasing the $\delta^{30}Si$ (Sarath et al., 2022). We must be cautious in assigning groundwater a single low $\delta^{30}Si$, since we observe significant variability groundwater $\delta^{30}Si$ spatially. Future works on groundwater $\delta^{30}Si$ should focus more on understanding the spatial heterogeneity rather than temporal sampling.

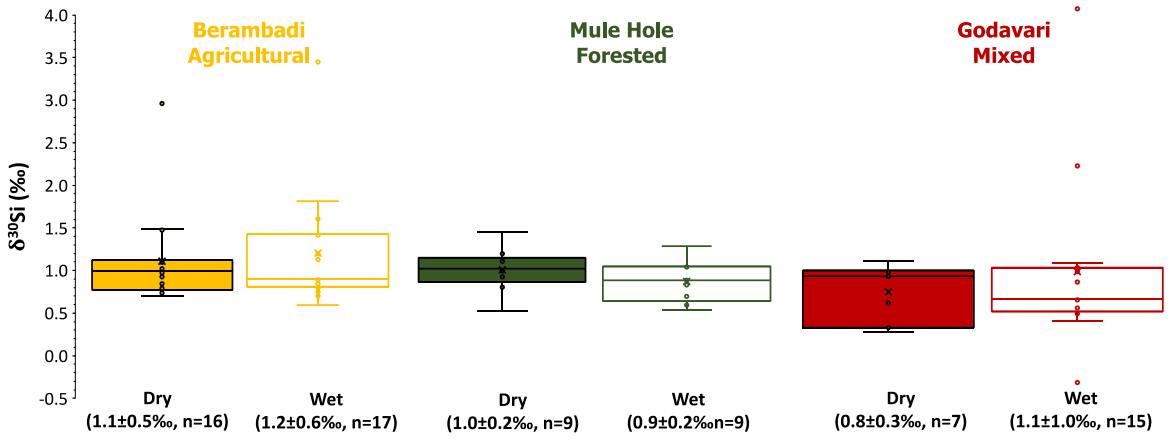

Figure 3. *Box plot showing seasonal variability in $\delta^{30}Si$ of groundwater from three watersheds studied in the thesis. None of the watersheds exhibit any significant variability in $\delta^{30}Si$.*

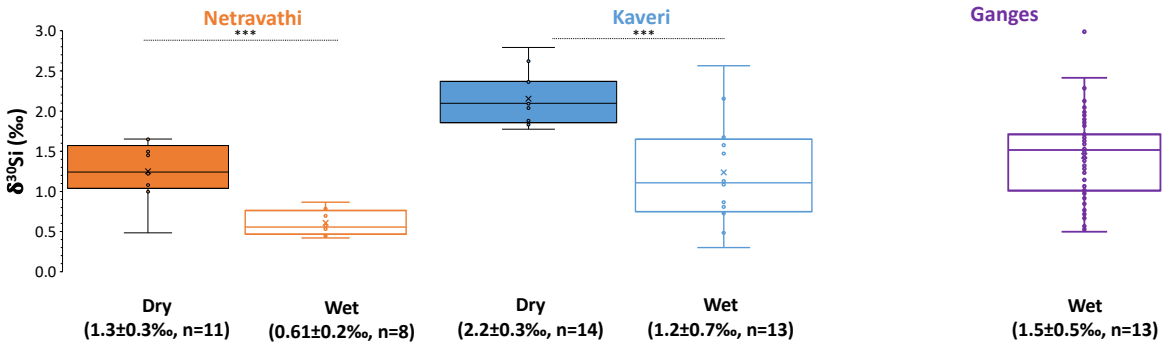

Figure 4. *Box plot showing seasonal variability in $\delta^{30}Si$ of Netravathi and Kaveri river water from South India, published Sarath et al, (2022). The data for Ganges is during August and September and considered as wet season (Fontorbe et al., 2013, Frings et al., 2015). The '***' denote significant difference in t-test with p-value <0.001.*

Q3. Are groundwater $\delta^{30}Si$ signatures significantly different than surface waters?

Overall, $\delta^{30}Si$ signatures of groundwater from present study is significantly lower than the riverine $\delta^{30}Si$ published so far from India (Fontorbe et al., 2013, Frings et al., 2015-Ganges, Sarath et al., 2022-Kaveri, Netravathi; Figures 4 and 5). Previous works have attributed low

δ^{30}Si in groundwater resulting from dissolution of secondary clays minerals and silcretes (Georg et al 2009a, 2009b, Strandmann et al 2014). However, dissolution of secondary minerals only account for a small subset of samples and we show that in majority of the groundwater, δ^{30}Si is driven by primary silicate weathering and secondary clay formation. The comparatively low δ^{30}Si of groundwater primarily results from high residence time and extended water rock interactions, where a dynamic equilibrium is established between the Si supply from weathering and secondary mineral formation. Recent works on laboratory amorphous silica precipitation experiments and modelling suggests that an isotopic re-equilibration is possible and depends on the surface area and depth into mineral surface that a coevolving fluid can access (Fernandez et al., 2019). Groundwater systems which can re-equilibrate with amorphous precursors of clay minerals can acquire lower δ^{30}Si signatures, which is not the case for river water.

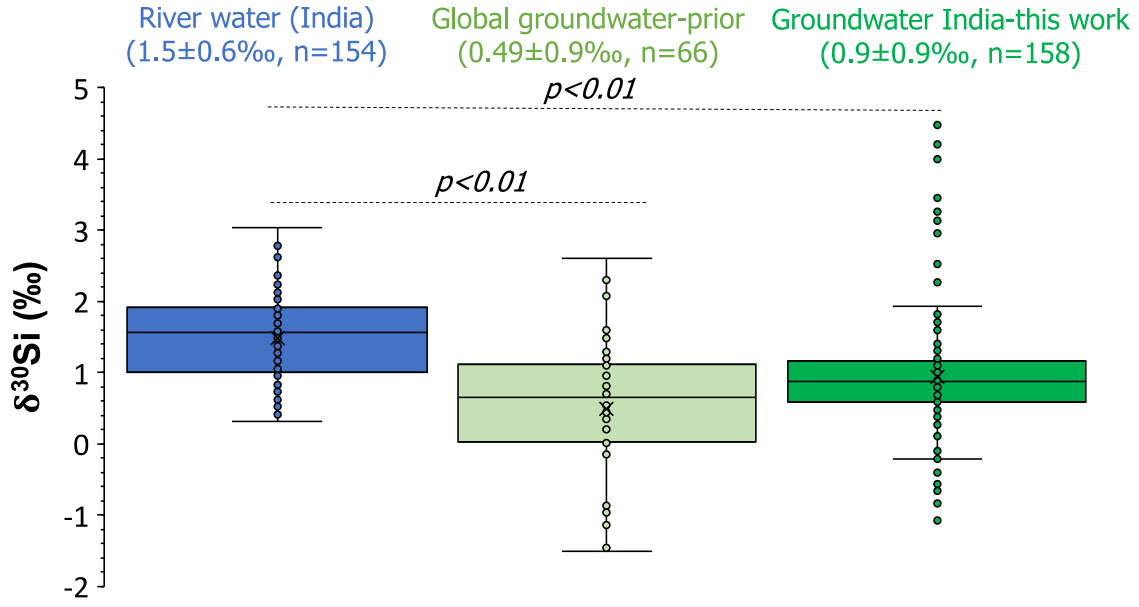

Figure 5. *The δ^{30}Si variability in surface water and groundwater from Indian subcontinent (Fontorbe et al., 2013, Frings et al., 2015, 2016, Mangalaa, 2016, Martin et al., 2021, Sarath et al., 2022).*

Q4. How much is the fresh SGD driven Si and Ge flux to the Indian coast? Is there any Si isotopic effect related to the Si flux?

Our estimation of fresh submarine groundwater derived Si flux along Indian coast suggest that the groundwater derived Si flux accounts for only 3.2% of the riverine flux from peninsular rivers of India (Chap. 4). Adding the Si flux from Himalaya rivers reduces the fresh SGD contribution to <1% of total riverine Si flux to North Indian Ocean (Chap. 4 and Mangalaa et al., 2017). Even though the groundwater exhibits a distinct δ^{30}Si signatures compared to rivers,

the low Si contribution lead to minor impact on coastal Si isotope budget. However, fresh SGD Si fluxes can be substantial and important for mountainous regions, active coastlines, tropical islands, karstic carbonate or volcanic systems and areas with low surface runoff (Zhou et al., 2019, Santos et al., 2021). Globally, the fresh groundwater discharge can deliver almost 0.15-0.3*10^6 mol Ge/yr, which is almost 5-10% of the global riverine Ge delivery to the ocean. Our estimate suggests that Ge delivery by SGD can be a significant input to the coastal ocean and must be considered for future works on oceanic Ge budget.

		DSi	Si flux	$\delta^{30}Si_{avg}$	Ge	Ge flux
		µM	Gmol/yr	‰	nM	kmol/yr
Bay of Bengal	River	264	70.7	1.69	-	-
	Groundwater	400	1.6	0.31	0.93	4.37
Arabian sea	River	135	14.7	1.47	-	-
	Groundwater	550	1.3	0.83	0.41	1.03
Indian ocean	Total	-	**88.3**	**1.61**	-	**5.4**

Table 1. *The riverine and groundwater derived Si and Ge flux, and weighted δ^{30}Si composition to Bay of Bengal and Arabian sea. The river water data from Mangalaa (2016) and the fresh SGD flux from Zhou et al (2019) and Luijendijk et al., 2020.*

The overall results of the present research hold important implications for continental Si cycling and Si delivery to coastal ocean:

1. The δ^{30}Si of groundwater is highly variable, and assigning groundwater contribution to observed riverine or estuarine δ^{30}Si composition requires extensive sampling of the watershed in question. Groundwater can acquire signatures of surface and subsurface processes depending on the depth to water table and soil water flow paths.
2. Estuaries are highly dynamic systems where river water signatures can be significantly modulated depending on the extend of mixing and biotic as well as abiotic processes. In case of Si, estuaries can act as a filter for DSi supply to ocean, where almost 15% of the riverine Si is converted to biogenic silica (BSi) by diatoms.
3. Fresh groundwater discharge only accounts minor Si fluxes into coastal ocean and have negligible impact on coastal ocean δ^{30}Si signature.

All of these aspects should be taken into consideration for future works on continental and oceanic biogeochemical cycles.

2. Perspectives

The main findings form the thesis also raise several questions inviting follow up research, which includes:

- A major drawback of the Chapter II was the low impact of above ground crops on the $\delta^{30}Si$ of soil solution in Berambadi. We observe similar $\delta^{30}Si$ between soil solution from Berambadi and Mule Hole, which can arise from low fractionation factor of the deciduous trees in Mule Hole and crops like turmeric, tomato and cabbage in Berambadi. A future work could focus exclusively on paddy fields or banana fields, where extensive groundwaters and soil solutions sampling for $\delta^{30}Si$ can verify the impact of land use alterations on groundwater Si cycling.
- The volume of fresh SGD only represents <1% of the total SGD water fluxes (Kwon et al., 2014), and estimate provided in the present work only represent a small portion of total SGD Si flux to Indian coast. Further sampling of saline groundwater is required to understand the impact of SGD fluxes in coastal oceans. We suggest strategic sampling and $\delta^{30}Si$ analysis of fresh and saline groundwater from coastal areas known to be SGD hotspots based on proxies such as radium isotopes.
- In India, most of the discharge is largely dominated by monsoon that prevent diatoms growth, estuaries can be a major sink for biogenic silica (BSi) through diatom productivity and very little is known about the estuarine filter capacity of other large rivers. The available data is consistent with at Si filter capacity of 15% we observe in Godavari (Chapter IIIa, Frings et al., 2016). Further evaluation of estuarine systems to understand BSi burial, preservation and redissolution is essential to constrain DSi fluxes to global ocean and oceanic Si cycle.
- The fractionation factors for clays are highly variable, and literature value range from -0.1 to -0.7‰ for smectites ($\Delta^{30}Si_{clay\text{-}parent\ silicate\ material}$ values from Georg et al., 2009a, Opfergelt et al., 2012, and Frings et al., 2021a) and kaolinite type clays which are more fractionated with $\Delta^{30}Si_{clay\text{-}parent\ silicate\ material}$ values from -1‰ to -2‰ (Riotte et al., 2018a and Frings et al., 2021a). It remains unclear what drives such variability within the clay types and we must cautious for weathering reactions where solid transformation of parent mineral to clays can occur (e.g. biotite to smectite, Frings et al., 2021a). Additionally when the weathering reaction and clay neoformation occurs through dissolution-reprecipitation pathway, it remains to be seen if fractionation factor should be considered as a difference in isotopic composition of clay and parent bedrock or

fluids from which clays precipitates (such as soil solutions, groundwater). Further investigations is necessary to explain exact pathways and fractionation mechanism for precipitation of clay types.

- Germanium is routinely coupled with $\delta^{30}Si$ to trace Si cycling, especially in terrestrial environments. Our preliminary analysis suggests that Ge/Si and $\delta^{30}Si$ are decoupled during plant uptake, with groundwaters influenced by plant uptake showing low Ge/Si ratio and a high $\delta^{30}Si$ (Fig. 6). This observation can result from no discrimination or preferential uptake of Ge relative to Si during plant uptake, which can support the existence of a significant Ge pool complexed with organic matter in the roots of plants (Frings et al., 2021). We also observe a decrease in Ge concentration along the estuarine transect in Godavari during both dry and wet season, indicating a significant sink for Ge in estuaries (Fig. 6). We hypothesize that such a behaviour can result from active diatom uptake of Ge during dry season and scavenging of Ge by particulate organic phases and Fe oxyhydroxides during wet season. However, the data is yet to be validate. Future research can benefit from complementing $\delta^{30}Si$ with Ge/Si to evaluate biotic uptake and adsorption processes.

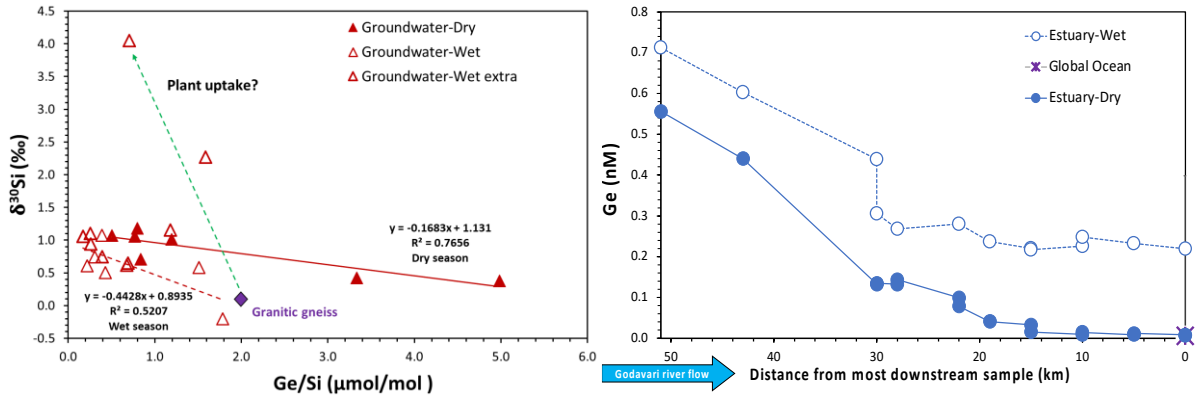

Figure 6. a) $\delta^{30}Si$ vs. Ge/Si analyzed in groundwaters from Godavari region. The two trendlines are for dry and wet seaosn respectively. The granitic gneiss value from Lugolobi et al, (2010) and Riotte et al, (2018), b) The Ge concentration along the estuarine transect, which is given as distance from the most downstream sample. Oceanic Ge concentration from Froelich et al, (1992).

ANNEXE

Annexe 1. Analytical details of silicon isotope measurements using MC-ICPMS

Annexe 2. Supplementary paper published on dissolved Si isotope composition of two contrasting river basins in South India.

Annexe 1. Analytical details for Si isotopes

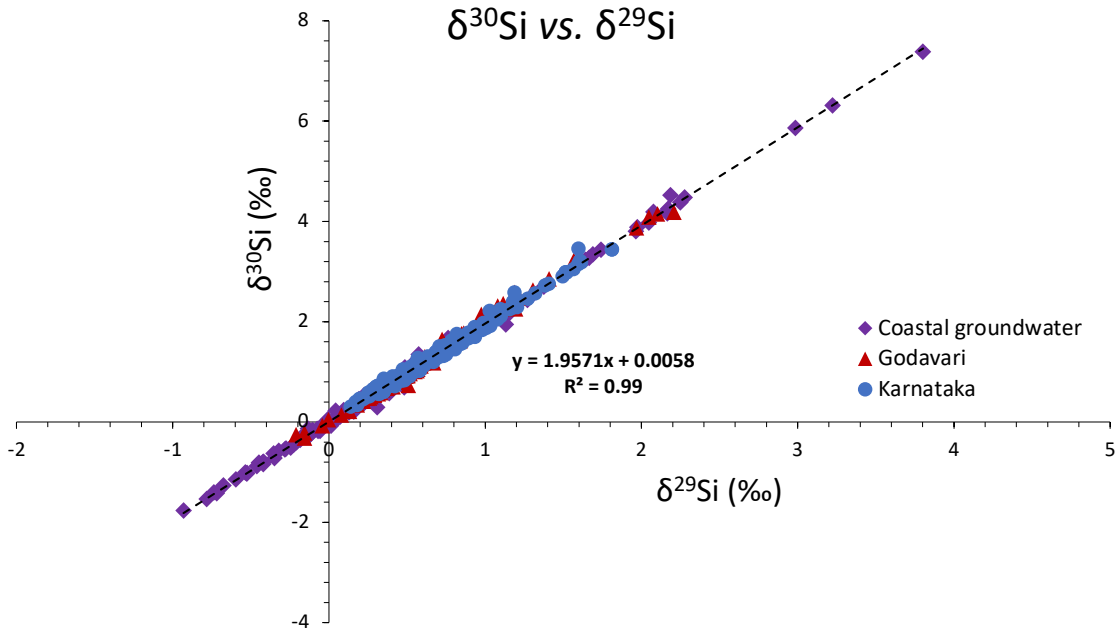

Figure A1. *The plot between $\delta^{30}Si$ and $\delta^{29}Si$ for all the samples analysed for the thesis. The three major regions are given with a different symbol. The heavy isotopic composition for a groundwater (>6‰) was removed from the thesis due to suspicion of precipitation post sampling. The internal error for the analysis is within the symbol size.*

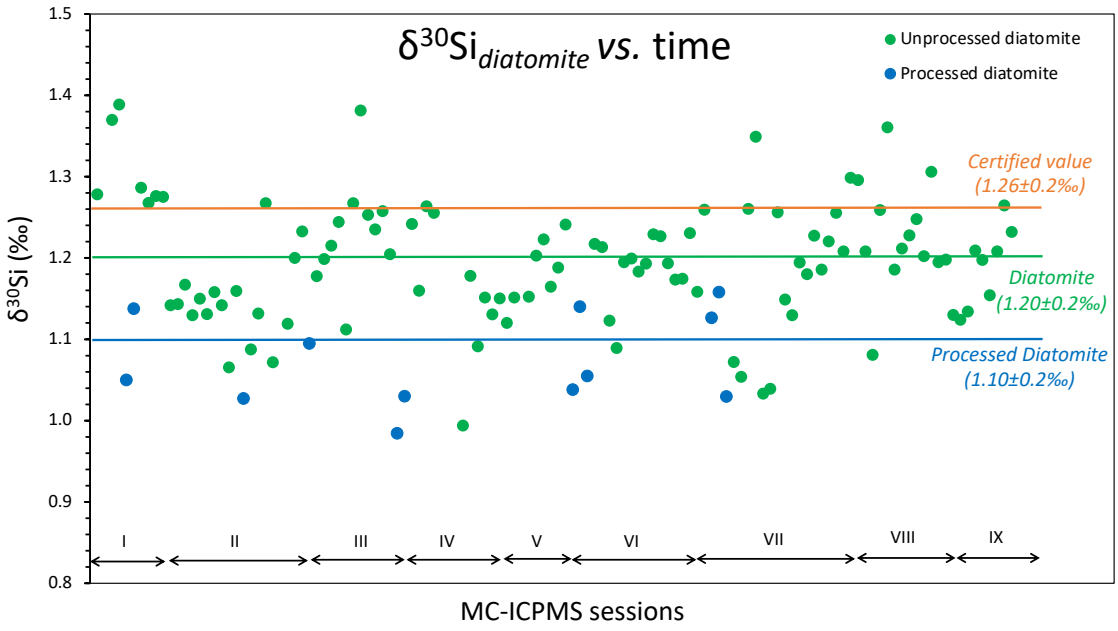

Figure A2. *The variability of reference standard diatomite with time. The bulk diatomite (without MAGIC pre-concentration and chromatographic purification) are given in green with the 2SD marked as shaded green region, the processed diatomite average is given in blue and the certified value and 2SD in orange. The sessions are, I and II-January 2020, III-June 2020, IV, V-December 2021, VI-January 2022, VII-February 2022, VIII-March 2022, IX- October 2022.*

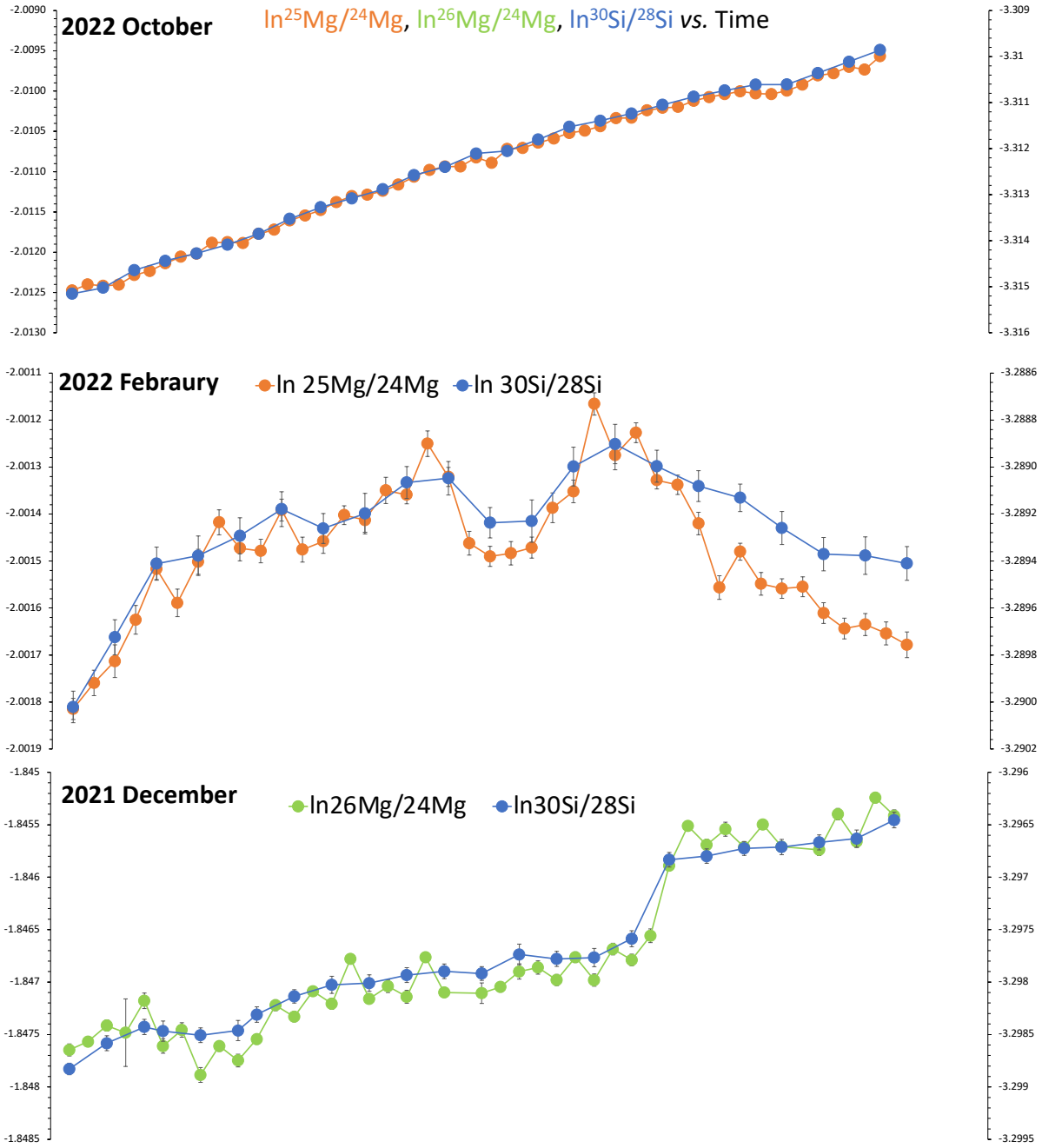

Figure A3. *Typical mass bias plot to check the validity of Mg external standard correction during MC-ICPMS sessions. The Mg doping technique and external normalization is described in Cardinal et al. (2003). The ln(^{25}Mg/^{24}Mg) and ln(^{26}Mg/^{24}Mg) for both samples and NBS28 bracketing standards are given in orange and green with internal error. The ln(^{30}Si/^{28}Si) for NBS28 bracketing standards are given in blue with internal errors. The X axis represent time during analytical session and the plots represent a single analytical session from three different MC session during the PhD.*

Table A1. *The details of verification for dissolved organic matter removal tests conducted on selected groundwater and surface water samples (see Hughes et al. (2011) for details. The dissolved organic carbon (DOC) and dissolved silicon (DSi) were analysed before and after MAGIC, chromatographic purification and H_2O_2 addition.*

ID	DSi ini. ppm	DOC ini. ppm	Si/DOC initial	H_2O_2	DSi aft. ppm	DOC aft. ppm	Si/DOC After MAGIC
7M	17.47	3.2	5.4	Yes	21.2	0.94	22
7A	19.11	1.2	15.9	Yes	21.2	0.02	965
2A	6.54	1.5	4.3	Yes	8.6	0.05	172
1M	9.80	2.0	4.9	Yes	12.6	0.10	124
4M	9.30	1.5	6.3	Yes	12.3	0.06	220
10M	2.32	2.8	0.8	Yes	17.2	0.92	18
16A	6.65	4.0	1.7	Yes	9.2	0.13	68
18A	6.64	2.9	2.3	Yes	9.3	0.08	122
26M	46.56	16.6	2.8	Yes	71.4	0.01	7144
29M	26.57	10.8	2.5	Yes	36.5	0.04	1014
31M	31.35	11.1	2.8	Yes	43.7	0.05	873
33M	29.34	7.7	3.8	Yes	33.4	0.05	619
34M	14.54	10.7	1.4	Yes	18.5	0.16	117
41M	15.37	11.1	1.4	Yes	18.7	0.07	274
43M	24.52	10.7	2.3	Yes	29.4	0.08	386
47M	17.46	6.5	2.7	Yes	26.0	0.04	721
35A	6.42	9.8	0.7	Yes	7.3	0.24	30
40A	30.31	1.6	19.3	Yes	37.8	0.00	-
42A	8.53	2.1	4.0	Yes	11.8	0.21	56
43A	13.86	2.5	5.6	Yes	17.5	0.19	93
61A	35.54	6.1	5.8	Yes	46	0.05	958
WB10	13.0	8.9	1.5	Yes	23.2	0.04	610
OD1	35.0	11.3	3.1	Yes	39.0	0.02	2439
KA9	6.1	19.3	0.3	Yes	8.4	0.01	840
GJ5	14.7	26.5	0.6	Yes	16.9	0.22	75
GJ6	15.2	22.2	0.7	Yes	18.5	0.06	330
GJ8	11.7	35.5	0.3	Yes	14.4	0.08	190
MH1	3.7	10.7	0.4	Yes	4.3	0.09	46
MH2	26.4	20.0	1.3	Yes	29.5	0.20	149
MH4	3.8	26.7	0.1	Yes	5.5	0.02	236
GA1	15.8	26.3	0.6	Yes	26.1	0.11	247
GA5	3.0	19.7	0.2	Yes	4.7	0.08	61
KA5	5.2	20.6	0.3	Yes	7.5	0.03	226
KA6	4.6	20.6	0.2	Yes	7.0	0.12	57
GJ1	18.1	15.2	1.2	No	21.0	1.73	12
GJ2	24.0	19.5	1.2	No	27.6	1.52	18
GJ9	15.8	32.0	0.5	No	19.5	1.81	11
MH3	15.8	33.8	0.5	No	19.3	1.15	17
MH5	8.4	8.8	1.0	No	12.1	1.12	11
MH10	37.6	32.1	1.2	No	48.3	1.14	42
GA2	8.8	15.0	0.6	No	11.6	1.58	7
GA6	3.2	8.9	0.4	No	4.2	1.09	4
KA1	6.0	25.3	0.2	No	8.7	0.90	10
KA2	10.4	34.6	0.3	No	14.7	1.13	13

Annexe 2. Supplementary article

Chemical Geology 604 (2022) 120883

Contents lists available at ScienceDirect

Chemical Geology

journal homepage: www.elsevier.com/locate/chemgeo

Seasonal, weathering and water use controls of silicon cycling along the river flow in two contrasting basins of South India

P.K. Sarath [a,*], K.R. Mangalaa [a,1], D. Cardinal [a], G.P. Gurumurthy [d], A. Dapoigny [e], V.V.S.S. Sarma [f], J. Riotte [b,c]

[a] LOCEAN-IPSL, Sorbonne Université (SU, CNRS, IRD MNHN), Paris 75005, France
[b] Géosciences Environnement Toulouse - GET (IRD, CNRS, CNES, Université Toulouse III), 31400 Toulouse, France
[c] Indo-French Cell for Water Sciences, IRD, Indian Institute of Science, Bangalore, 560012, India
[d] Birbal Sahni Institute of Palaeosciences (BSIP), Lucknow 226007, Uttar Pradesh, India
[e] LSCE-IPSL, CEA-CNRS-UVSQ, Universite Paris Saclay, 91198 Gif-sur-Yvette, France
[f] National Institute of Oceanography–CSIR (NIO), Regional Centre of Visakhapatnam, 530017, India

ARTICLE INFO

Editor: Dr Oleg Pokrovsky

Keywords:
Silicon isotopes
Tropical rivers
Dissolved silicon
Kaveri
Netravathi

ABSTRACT

We present the first study of river water silicon isotopic composition from two contrasting basins in South India, the east flowing Kaveri river and the west flowing Netravathi river. Both rivers originate from the Western Ghats. River water samples were collected from mainstream, tributaries and reservoirs at different locations along the river flow during dry and wet (monsoon) seasons, with an additional post-monsoon sampling in Netravathi. High rainfall in Netravathi basin and upper reaches of Kaveri induce intense weathering in the region, with superposing contribution from anthropogenic controls in downstream Kaveri. The $\delta^{30}Si_{DSi}$ values range from +0.42 to +1.65‰ for Netravathi river basin and + 0.32 to +2.85‰ for Kaveri river basin. Silicate weathering index (R_e) shows intense weathering associated with monosiallitization (kaolinite-gibbsite formation) in Netravathi basin and relatively moderate weathering with bisiallitization (smectite-kaolinite formation) in Kaveri basin. The seasonal changes in $\delta^{30}Si_{DSi}$ and R_e in each basin shows similar patterns, with a likely higher and heavier contribution of soil water from deeper soil profiles closer to weathering front and bedrock, associated with significant secondary mineral formation during dry season and leaching of superficial soil profiles during the high discharge periods of monsoon. We provide a theoretical framework to estimate relative contribution of silicate weathering vs. anthropogenic processes on riverine $\delta^{30}Si_{DSi.}$ R_e is broadly correlated with $\delta^{30}Si_{DSi}$ and an isotopic mass balance involving the whole rock composition (excluding the stable quartz and sericite) shows that the $\delta^{30}Si$ in river water are well explained by silicate weathering and gibbsite-kaolinite formation in the Netravathi and upper upper reaches of Kaveri. However, silicate weathering explains only partially the heavier $\delta^{30}Si_{DSi}$ signatures in the middle and lower reaches of the Kaveri, and the additional enrichment of about +1.06‰ can be attributed to uptake of silicon and Si-depleted return flow through irrigated agriculture in the basin. This study confirms the major control of pedoclimatic conditions on the $\delta^{30}Si$ of rivers and provides for the first time an estimation of the impact of human activities on the silicon isotopic signature of rivers.

1. Introduction

Silicon (Si) is the second most abundant element in the Earth's crust and is present in particulate and dissolved forms in rivers, estuaries and oceans. Chemical weathering is the major source of Si supply to the terrestrial and aquatic systems. During chemical weathering of primary silicate minerals, silicon is partly released as a solute (dissolved silicon, DSi hereafter), with an intermediate behaviour in between the one of typical soluble elements with low ionic radius to charge ratio (r/z) that form oxyanions (similar to elements such as S, P, N, C), while the other Si fraction is immobilized into secondary clay minerals (similar to poorly soluble element with medium r/z e.g. Al). Silicon has three stable isotopes, ^{28}Si (92.2%), ^{29}Si (4.7%) and ^{30}Si (3.1%) with their respective percentage of terrestrial abundance (Poitrasson, 2017). The formation of

* Corresponding author.
E-mail address: sarath.pullyottum-kavil@locean.ipsl.fr (P.K. Sarath).
[1] Now at: Ministry of Earth Sciences, Prithvi Bhawan, Lodhi road, New Delhi, 110003, India.

https://doi.org/10.1016/j.chemgeo.2022.120883
Received 20 October 2021; Received in revised form 11 April 2022; Accepted 22 April 2022
Available online 27 April 2022

secondary minerals during silicate weathering can lead to preferential incorporation of lighter Si isotope which leads to enrichment of isotopically heavy DSi with a higher δ^{30}Si value (up to +4.7‰) compared to unweathered silicate rocks (−0.3‰; Savage et al., 2013, Savage et al., 2012; Poitrasson, 2017). DSi is largely dominated by orthosilicic acid, H_4SiO_4 (>98% at pH <8) and serves as an important nutrient for aquatic silicifying organisms and, terrestrial plants defense against biotic and abiotic stress. Indeed, vegetation plays an important role in Si biogeochemical cycle via precipitation of phytoliths (amorphous or biogenic silica, BSi) that are recycled into the soil or exported to rivers through erosion (Alexandre et al., 1997; Derry et al., 2005). In aquatic systems, diatom uptake also alters the Si biogeochemical cycle via conversion of DSi to biogenic silica (BSi) (Conley, 1997). Si uptake and biomineralization by biological process also leads to preferential incorporation of ^{28}Si enriching the DSi pool in heavy isotopes. Consequently, these continental processes control the Si supply to the estuaries and coastal waters which represents 70% of external DSi supply to the ocean (Tréguer et al., 2021). Urbanization and anthropogenic activities like agriculture and construction of reservoirs can reduce the supply of Si to estuarine and coastal ecosystems. Such effects are well documented in several aquatic environments (Conley et al., 2000; Humborg et al., 2002; Hughes et al., 2012; Meunier et al., 2015). Deforestation can enhance the soil erosion leading to increase in DSi supply into aquatic ecosystems (Struyf et al., 2010; Vandevenne et al., 2012; Mangalaa et al., 2017). Increasing anthropogenic activities have drawn much attention to understand their impact on the global biogeochemical Si cycle. Tropical rivers are known for their high DSi flux because of warm and wet climatic conditions, which favour intense chemical and physical weathering and runoff (Hughes et al., 2012; Dürr et al., 2011). Hence, the understanding of the Si cycle in tropical regions is of particularly high relevance in this context. In recent years, Si isotopes have been proved to be a valuable tool for tracing several processes affecting the Si biogeochemical cycle such as secondary mineral formation (Georg et al., 2007), mixing of the different DSi sources (Georg et al., 2006a, 2006b), biological uptake (Ding et al., 2004; Engström et al., 2010), anthropogenic effects such as damming (Hughes et al., 2012) and land use (Delvaux et al., 2013).

Despite being the major contributor of DSi to the ocean, many tropical rivers remain understudied. This results in large uncertainties in estimating net DSi fluxes to the ocean (±25%, Tréguer et al., 2021). In the present work, we study the Si cycle in two contrasting tropical rivers of Southern India, Kaveri (also known as Cauvery) and Netravathi. Both river headwaters originate from the Western Ghats, but the Kaveri basin is draining eastward to the Bay of Bengal while the Netravathi flows westward to the Arabian Sea. Because of the very humid climate along the western coast, the Netravathi basin experiences intense weathering and higher Si supply to the coast compared to Kaveri (Gurumurthy et al., 2012). The upper Kaveri basin is characterized by a sharp rainfall gradient, from 3000 mm/yr to about 500 mm/yr within a span of 100 km. Most of the Kaveri basin experiences semi-arid to sub-humid conditions (Meunier et al., 2015). Such contrasting land use and climate in these two tropical rivers make the comparison of both systems particularly interesting for understanding how Si cycle gets affected by natural (weathering) and anthropogenic (agricultural land use) pressures.

Therefore, we aim 1) to determine the seasonal variability of silicon isotopic signature in the Kaveri and Netravathi river basins and to identify the factors driving the Si isotopic compositions in these two river systems, and 2) to understand the effects of weathering, climate, and anthropogenic activities on the Si cycle along the river course before entering the estuaries.

2. Study area and methods

2.1. River Settings, climate and hydrology

Kaveri basin is located between 10° 07 'N to 13°28' N and 75° 28′E to 79° 52′E. The river runs about 765 km towards the southeast and drains an area of 85,626 km^2 from the Western Ghats to the Bay of Bengal (Fig. 1a) and drains three states of India with 41% in Karnataka (source of Kaveri, Thala Kaveri), 55% in Tamil Nadu and the remaining 3% in Kerala. Kaveri river basin covers a major part of the South Indian peninsula and is constituted by three sub-basins namely upper (Western Ghats), middle (Mysore plateau) and lower (delta) basins. The important tributaries joining the Kaveri are Hemavathi (H), Kabini (K), Shimsha (S) and Arkavathi (A), Bhavani (Fig. 1a). The Kaveri river basin experiences tropical monsoon climate with influence of southwest (SW) monsoon (June to September) in upper basin and northeast (NE) monsoon in lower basin (October–November). The Western Ghats create a rain shadow that affects the SW monsoonal winds in the East inducing on the Deccan Plateau a sharp rainfall gradient from West (humid) to East (semi-arid). Therefore, Kaveri basin receives maximum rainfall during SW monsoon mainly in the upper reaches and partly in middle reaches which are responsible for 80% of the annual water flow and sediment load (Pattanaik et al., 2013). Hence, the spatial rainfall distribution ranges from 6000 mm/yr in the Western Ghats, to 300 mm/yr in the eastern parts during NE monsoon (Meunier et al., 2015). The catchments of Arkavathi and Shimsha tributaries, which receive only 700–800 mm/yr rainfall, i.e., semi-arid conditions, are exposed to diverse urban and agriculture pollutions. The Arkavathi river especially drains Bangalore and is considerably polluted (35 to 45% pollution index, based on anions potentially brought by human activities (SO_4^{2-}, NO_3^- and Cl^-) compared to alkalinity, Pacheco and van der Weijden, 1996). Both Arkavathi and Shimsha discharges are controlled by numerous dams, which are limiting the flow towards the Kaveri to a mixture of domestic and industrial effluents (Lele et al., 2013), return flow from irrigated agriculture (paddy fields) and local groundwater contribution. The historical runoff of the Kaveri used to be 21.3 km^3 yr^{-1} i.e., 262mm/yr (Integrated Hydrological Data Book, 2012, cited by Meunier et al., 2015) but diversion of water to meet domestic and irrigation demands accounts for 80% of total runoff, resulting in a low discharge of just 4.5 km^3 yr^{-1} to the sea (Meunier et al., 2015). Agriculture is the major land use in the Kaveri basin covering 66% of the total area, followed by forest cover (20%, WRIS. Kaveri Basin Report: Govt. of India, 2014).

The Netravathi basin – lies between 12°29′11″N to 13°11'11″N and 74° 49′08″E to 75°47′53″E and is surrounded by Tunga-Bhadra basin in the North, Kaveri basin in the East and by the Arabian Sea in the West. It originates from densely forested Western Ghats (Chikmagalore) and runs about 147 km southwest to the Arabian Sea forming a common estuary with Gurupur river at Mangalore (Fig. 1b). The total drainage area of the basin is 3657 km^2. The major tributaries of Netravathi basin are Shanthimageru (Sha), Gundiya hole (Gun), Shishilahole (Shi) and Neriya hole (Ner) (Fig. 1b). The basin is characterized by high humidity and heavy rainfall (3600–4200 mmyr^{-1}, data from http://www.imd.gov.in cited by Gurumurthy et al., 2012). Similar to upper Kaveri basin, the river flow is controlled by the SW monsoon with 94% of total discharge occurring during June to October (Gurumurthy et al., 2012, Gurumurthy et al., 2014). The annual discharge from the river Netravathi is 12 km^3 yr^{-1} (Karnataka Irrigation Department 1986 cited by Gurumurthy et al., 2012). Upper basin situated in the western ghats is densely forested, limiting erosion in the basin (Ganasri and Ramesh, 2016). The major contrasting features of both river basins are summarised in Table 1.

2.2. Geology of Kaveri and Netravathi Basin

2.2.1. Kaveri

The upper and middle reaches of the basin are composed of a silicate Precambrian basement comprising peninsular gneiss, charnockites and granitic rocks associated with metasedimentary and mafic rocks (Naqvi and Rogers, 1987; Shadakshara Swamy et al., 1995). The lower reaches of Shimsha drain mafic granulite, foliated charnockites and granitoid

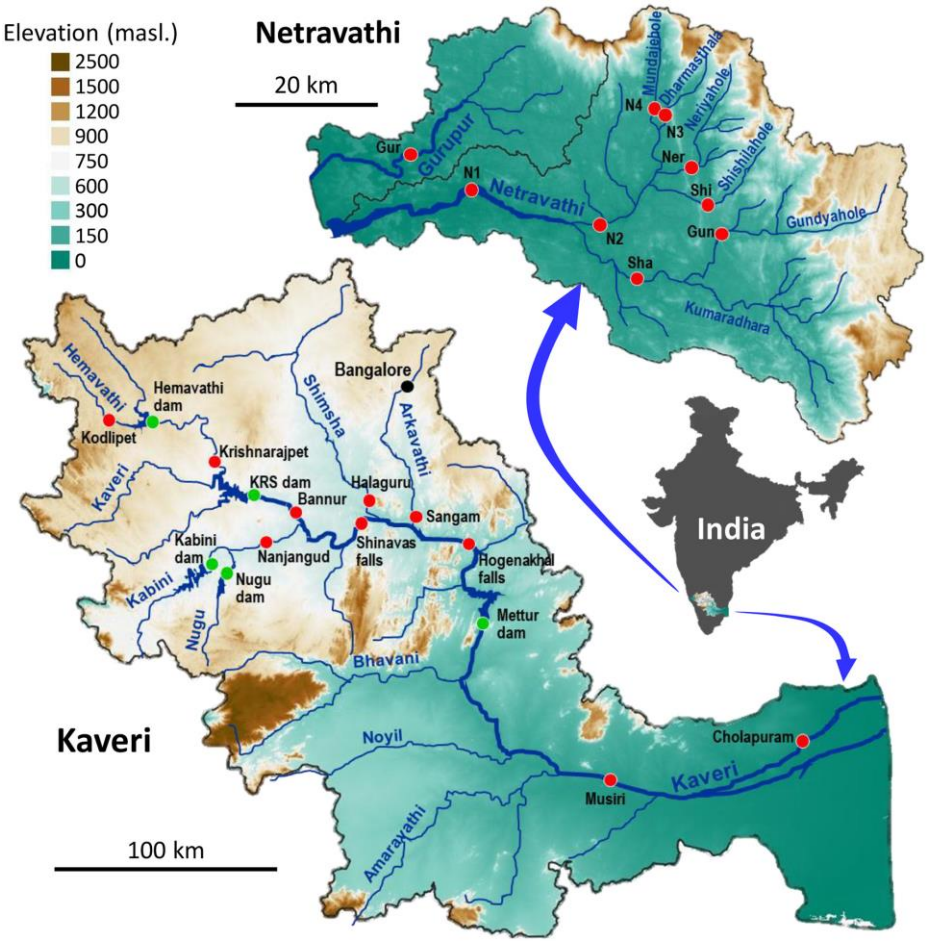

Fig. 1. Location maps of Kaveri/Cauvery (a) and Netravathi (b) basins showing the sampling stations (samples from dam/reservoir is indicated in green filled circles and river water in red circles), (b) Netravathi mainstream sampling stations are indicated by the letter "N" and the numbers are the station number. Tributaries of Netravathi basin are indicated by their first three letters (for example, Sha = Shanthimugeru, Gun = Gundyahole etc.). "Gur" represents Gurupur river, flowing adjacent to the Netravathi basin (modified from Meunier et al., 2015 and Gurumurthy et al., 2012).

gneisses (Pattanaik et al., 2013). The lower reaches of Kaveri flow through the Cretaceous deposits composed of conglomeratic sandstone, limestone, shale and finally the alluvium plains (Pattanaik et al., 2007). The δ^{30}Si of the gneiss bedrock from Mule Hole in Kaveri basin reported by Riotte et al. (2018) is at -0.34 ± 0.08‰. The Precambrian gneiss is a part of TTG (Tonalite–trondhjemite–granodiorite) felsic source rocks but it is a metasediment, which is probably why it is quite light compared to some other Archean rocks (André et al., 2019). The weathered layer (regolith) consists of thick laterite in the humid zone, ferralsol/vertisol developed on saprolite in semi-arid zone of upper and middle reaches, and alluvium in the lower reaches.

2.2.2. Netravathi

The basin primarily drains the metamorphic changeover zone of west dharwar craton comprising trondhjemite – tonalite - granodiorite suite (Naqvi and Rogers, 1987). Overall, the basin is composed of 83% migmatites and granodiorites, 6% metasediments, 5% charnockites and 2% amphibolites (Gurumurthy et al., 2012, 2015a, 2015b) (Fig. 1b). The regolith thickness ranges from 20 to 30 m and is primarily composed of thick laterites (Gurumurthy et al., 2012).

2.3. Materials and methods

2.3.1. Sampling and determination of major elements concentrations

In Kaveri basin, the water samples were collected in 10 riverine and 5 dam stations during dry season (May 2007) and southwest monsoon/wet season (July 2007). In Netravathi basin, the samples were collected at 9 riverine stations (no reservoirs) during dry season (April 2010), summer monsoon (July 2010) and post monsoon (December 2010). Dissolved cations were measured by Atomic Absorption Spectroscopy at Geosciences Environment Toulouse and DSi was determined by spectrophotometry (Molybdate blue method) at the Indo-French Cell for Water Sciences (IRD-IISc, Bangalore). The sample collection procedures and details about chemical analyses (dissolved load concentration) are described in Meunier et al. (2015) for Kaveri basin and in Gurumurthy et al. (2012) for Netravathi basin. Typical precision for cation

Table 1
Main characteristics of the two river basins (from Gurumurthy et al., 2012 for Netravathi and Meunier et al., 2015 for Kaveri).

	Netravathi	Kaveri
River length (km)	147	765
Location of spring	Western Ghats	Western Ghats
Watershed area (km^2)	3657	85,626
Flow direction	South-west into Arabian Sea	South-east into Bay of Bengal
Net annual discharge ($km^3\ yr^{-1}$)	12 (94% from SW monsoon)	4.5 (mainly SW monsoon and partially from NE monsoon)
Climate	Tropical humid	Tropical humid to semi-arid
Annual rainfall ($mm.yr^{-1}$)	3600-4200	6000 in the Western Ghats to 300 in the East part of Karnataka Plateau
Theoretical runoff ($mm.yr^{-1}$)	3300	260
Land use	51% agricultural land, 35% forest	66% agricultural land, 20% forest
Number of dams	9	96
Population density	397 km^{-2}	1500 km^{-2}
Lithology	Gneiss, metasediments, charnockites	Gneiss, charnockites and granitic rocks + Cretaceous deposits and Quaternary alluvium in lower reaches

concentration were better than 10%. We analysed certified reference material (PERADE-09, Environment Canada) for DSi measurements along with samples which showed a reproducibility of 97.4%. Finally, we verified before the isotopic analysis that the DSi concentration remained stable over time by further DSi measurements at LOCEAN-IPSL.

2.3.2. Si isotopes measurement

The Si fraction was separated from sample matrix with a 2-steps procedure carried out by adapting the protocol MAGIC- MAGnesium Co-precipitation technique (Karl and Tien, 1992; Reynolds et al., 2006; Hughes et al., 2011). After adding $MgCl_2$ to the river water samples to match the seawater Mg concentration, samples were treated with 2% (*v*/v) of 1M NaOH. The brucite $Mg(OH)_2$ formed at high pH scavenges Si which gets adsorbed onto precipitated brucite. The brucite was separated from the supernatant by centrifugation and redissolved in 1 M HCl. The supernatant from the first step was then subjected to second addition of 1% NaOH following the same step. The second brucite precipitate was also redissolved with 1 M HCl and merged with the previous one. The DSi concentration of the dissolved brucite and supernatant was analysed by spectrophotometer (Grasshoff et al., 1999). We verified that the yield of the MAGIC precipitation was 100% by testing the absence of DSi in the second supernatant.

Si purification was carried out using cation exchange resin (BioRad cation exchange resin DOWEX 50 W-X12, 200 to 400 mesh, in H^+ form) following the procedure of Georg et al. (2006a, 2006b). The procedure blank values are monitored continuously and were below 1% of the main signal, i.e. they were considered as negligible. After the purification process, an aliquot was analysed for major elements analysis (Na, Mg, Ca, Al) by ICP-MS (Agilent 7500a) to ensure that the Si/X cations weight ratio is always >50 and then minimize the matrix effects in the plasma. The potential matrix effect resulting mainly from Cl^- and SO_4^{2-} was corrected by the artificial doping of anions (Suprapur H_2SO_4 and HCl) in all the samples and standards (Hughes et al., 2011). The isotopic measurements, 60 cycles of 4 s each, were performed on MC-ICP-MS Neptune+ (LSCE-IPSL, Gif-sur-Yvette) in dry plasma mode with Mg doping as described by Closset et al. (2016) (Table S1 for details). During the isotopic measurements, rinsing solution blanks were measured between each sample standard, and then subtracted. Our method has been intercalibrated for sea water in GEOTRACES measurements (Grasse et al., 2017). $\delta^{30}Si$ is expressed relative to the standard (NBS28) as;

$$\delta^{30}Si\ (‰) = \left(\left({}^{30}Si/{}^{28}Si\right)_{sample} \Big/ \left({}^{30}Si/{}^{28}Si\right)_{standard} - 1 \right) * 1000$$

The analytical precision and accuracy were monitored by the long-term measurements of secondary reference material Diatomite every ten samples. The reproducibility of the measurements was calculated using the standard deviation of 40 standard analyses over one-year measurements ($\delta^{30}Si = +1.28 \pm 0.1‰$, $\delta^{29}Si = +0.65 \pm 0.08‰$, 2SD). They are well in agreement with the consensus isotopic composition of diatomite ($\delta^{30}Si = +1.26 \pm 0.2‰$, $\delta^{29}Si = +0.64 \pm 0.14‰$, 2SD; Reynolds et al., 2007). Due to insufficient volume of samples, the Si isotopic data of the river waters could not be replicated. However, we checked the reproducibility of Si isotopic analyses during the same period on 43 Indian estuarine water samples that have been fully replicated. The average reproducibility on $\delta^{30}Si$ is ±0.2‰ (±2 SD).

Table 2
Si isotopes, DSi and dissolved cations (*atmospheric contribution corrected) and R_e index measured in the Kaveri River basin during dry and wet periods, respectively. Dissolved cations and R_e are from Meunier et al. (2015).

Kaveri	$\delta^{30}Si_{DSi}$	Std. Err.	DSi	Na*	Ca*	K*	Mg*	R_e
	‰		μM					
Dry season reservoirs								
Hemavathi dam	2.1	0.05	208	90	211	28	114	2.0
KRS dam	n.m.	n.m.	309	432	596	30	518	2.4
Nugu dam	2.8	0.04	231	107	234	55	147	2.1
Kabini Dam	1.9	0.05	234	76	165	26	107	1.8
Mettur dam	2.4	0.06	296	621	460	44	527	2.8
River + tributaries								
Kodlipet	1.9	0.04	352	116	139	40	118	1.8
Krishnarajpet	2.2	0.05	232	109	292	33	165	2.0
Nanjangad	1.9	0.05	320	269	481	29	404	2.2
Bannur	2.1	0.04	362	360	890	43	603	2.2
Shinavas falls	1.8	0.07	393	475	600	29	557	2.4
Shimsha river/ Halaguru	2.1	0.05	697	2266	423	79	801	3.7
Arkavathi river/ Sangam	2.4	0.04	602	791	839	86	689	2.5
Hogenekhal falls	1.9	0.05	427	557	594	30	612	2.4
Musiri	2.4	0.17	397	486	416	57	481	2.5
Cholapuram	2.7	0.05	393	415	656	86	553	2.4
Wet season reservoirs								
Hemavathi dam	1.6	0.04	159	142	149	35	81	2.6
KRS dam	1.2	0.04	160	56	185	27	92	1.9
Nugu dam	2.2	0.04	227	69	182	60	109	2.0
Kabini Dam	n.m.	n.m.	131	14	85	26	41	1.5
Mettur dam	1.5	0.04	198	264	353	38	280	2.5
River + tributaries								
Kodlipet	0.3	0.05	145	21	55	12	34	1.1
Krishnarajpet	1.1	0.05	153	32	119	30	62	1.8
Nanjangad	0.8	0.04	158	21	89	25	46	1.5
Bannur	0.5	0.04	172	49	190	24	91	1.8
Shinavas falls	0.8	0.04	176	49	281	25	86	1.9
Shimsha river/ Halaguru	2.6	0.01	540	2270	531	87	850	3.7
Arkavathi river/ Sangam	0.8	0.04	191	92	244	30	128	2.1
Hogenekhal falls	0.9	0.03	260	106	261	34	136	2.0
Musiri	n.m.	n.m.	n. m.	352	507	52	328	2.8
Cholapuram	1.7	0.01	246	298	473	48	300	2.4

n.m.: not measured.

3. Results

3.1. Dissolved silicon and cations

The DSi concentrations for Kaveri and Netravathi water samples are provided in Tables 2 and 3, respectively. Though the origin of both rivers is Western Ghats, the DSi concentrations of the Kaveri river basins was significantly higher than Netravathi irrespective of the seasons (p = 0.002). DSi values in the Netravathi and in the upstream Kaveri with its tributaries in the Western Ghats are similar but fluctuate with the seasons. DSi concentration within main stream (Fig. 2a) samples in Kaveri are homogenous with 365 ± 63 μM and 192 ± 48 μM during dry and wet seasons respectively and exhibits significantly higher DSi during dry season ($p < 0.001$). The DSi concentration of tributaries Hemavathi and Kabini are comparable to the mainstream for both seasons. DSi of tributaries Shimsha and Arkavathi are almost two times higher than the mainstream during dry period but only Shimsha showed similar high DSi during wet season (Fig. 2a). Kaveri reservoirs also showed significant seasonal variation during dry and wet periods (256 ± 44 and 175 ± 38 μM, respectively, $p = 0.01$) with lower DSi concentration than the main stream during dry period and similar concentration as mainstream during wet period.

In Netravathi – similar to Kaveri, the DSi concentrations within main stream (Fig. 2b) samples are homogenous with 250 ± 39 μM, 169 ± 22 μM and 151 ± 23 μM during dry, wet, and post-monsoon periods, respectively. The concentrations are significantly different between dry and wet periods of the main stream ($p = 0.02$). The Gurupur river exhibits contrasting DSi concentration compared to Netravathi during all seasons likely because it is only draining the lowland area (Table 3, Fig. 2b). In contrast, the other tributaries exhibit similar concentrations to the mainstream during dry, wet and post monsoon seasons (230 ± 46, 158 ± 16 and 161 ± 10 μM, respectively). Except for the seasonal difference, DSi appears to be relatively homogenous over the entire basin.

In order to assess the contribution of bedrock weathering to the flux exported by the river, cations concentrations were corrected from atmospheric deposits. This approach assumes a negligible contribution of KCl fertilizer and evaporite rocks to the riverine Cl as already discussed in Gurumurthy et al. (2012) and Meunier et al. (2015). The absence of evaporite in these river basins is attested by the pure magmatic origin of their bedrocks. KCl is however applied as fertilizer in Indian agriculture, like in many other countries. Enquiries of fertilizer consumption at Indian states level indicate that the amount of Cl annually brought by fertilizers remains minor compared to the Cl brought by atmospheric inputs (particularly in high rainfall areas). This broad balance in favour of atmospheric sources at large scale does not prevent from observing locally a significant influence of fertilizers on the composition of water, as for example in the groundwater of Kaveri middle reaches (Buvaneshwari et al., 2020). Locally and particularly when a stream is fed by groundwater in an intensive agricultural area, the proportion of anthropogenic Cl may dominate. In absence of specific geochemical signature of anthropogenic Cl, it is not possible to quantify this excess and correct its influence. In this case, the Cl-atmospheric correction is overestimated but to an unknown extent. The good agreement between Na/Cl ratio of rain and seawater has been documented in Netravathi by Gurumurthy et al. (2012). The atmospheric corrected major cations (indicated by *), already published by Meunier et al. (2015) for the Kaveri, are mentioned in Table 2. Those calculated for Netravathi are given in Table 3. The average total dissolved cation concentrations (ΣC^{+}*) of the Kaveri basin are 1417 ± 876 μM and 717 ± 902 μM during dry and wet seasons respectively and for Netravathi, 299 ± 58, 143 ±

Table 3
Si isotopes, DSi and dissolved cations (*atmospheric contribution corrected) measured in the Netravathi river basin during dry, wet and post monsoon period (Data from Gurumurthy et al., 2012).

Netravathi		$\delta^{30}Si_{DSi}$	Std. Err.	DSi	Na*	Ca*	K*	Mg*	R_e
		‰		μM					
Dry season									
N2	Mugeru	1.6	0.04	220	115	109	41	63	2.3
Sha	Shanthimageru	n.m.	n.m.	240	101	98	40	89	2.1
Gun	Gundyahole	1.7	0.04	268	115	111	43	86	2.1
Shi	Shishilahole	0.5	0.03	163	58	55	21	33	1.9
Ner	Neriyahole	1.4	0.04	250	111	78	26	61	2.1
N3	Dharmasthala	n.m.	n.m.	232	112	103	31	54	2.2
N4	Mundaje Hole	1.5	0.04	307	146	98	25	58	2.1
Gur	Gurupura River	n.m.	n.m.	166	99	108	36	64	2.4
Wet Season-Monsoon									
N1	Bantwal BC Road	0.8	0.04	169	36	48	18	31	1.3
N2	Mugeru	0.6	0.05	155	46	54	16	32	1.7
Sha	Shanthimageru	0.5	0.06	141	34	48	16	35	1.5
Gun	Gundyahole	n.m.	n.m.	147	35	46	15	34	1.4
Shi	Shishilahole	0.5	0.07	170	42	52	14	36	1.4
Ner	Neriyahole	0.4	0.06	173	53	49	13	34	1.5
N3	Dharmasthala	0.7	0.09	182	55	63	15	37	1.6
N4	Mundaje Hole	0.9	0.09	198	64	60	15	37	1.6
Gur	Gurupura River	0.4	0.04	389	26	40	14	19	−2.2#
Post monsoon									
N2	Mugeru	1.0	0.03	160	94	77	17	58	2.3
Sha	Shanthimageru	1.2	0.05	176	66	65	15	64	1.8
Gun	Gundyahole	1.1	0.03	159	100	73	17	71	2.3
Shi	Shishilahole	1.2	0.03	153	82	68	14	74	2.1
Ner	Neriyahole	n.m.	n.m.	158	74	65	14	72	2.0
N3	Dharmasthala	n.m.	n.m.	144	116	88	18	56	2.6
N4	Mundaje Hole	1.5	0.03	122	107	82	16	57	2.6
Gur	Gurupura River	1.2	0.03	249	63	69	18	46	1.3

n.m.: not measured.
#: Please note that the Re calculation in Gurupura river during monsoon is negative due to overestimation of the atmospheric input and was removed from subsequent figures.

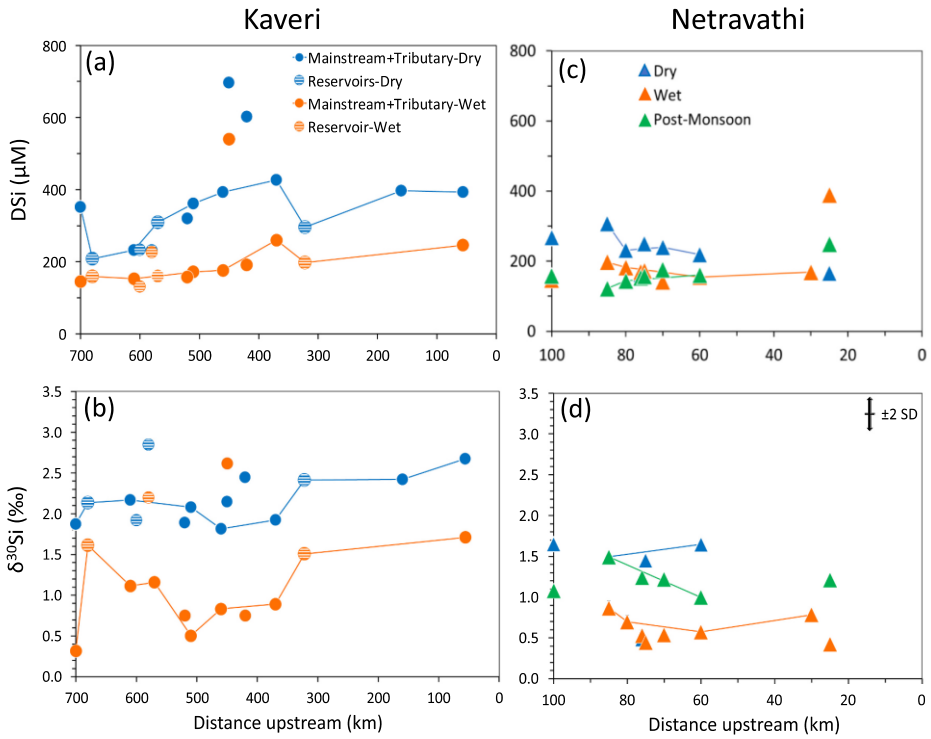

Fig. 2. Spatial and seasonal variability of dissolved Si (DSi) and silicon isotopes of DSi ($\delta^{30}Si_{DSi}$) in the Kaveri (2a, 2b) and Netravathi (2c, 2d) river basins during dry (blue) and wet (orange) periods. Post-monsoon data is available also for Netravathi (green). Water flow is from left to right. The filled circles in Kaveri represent the mainstream and tributaries, and the circle with patterns represent the dams/reservoir (Table 1 for more details). The samples along the mainstream are connected with lines. (For interpretation of the references to colour in this figure legend, the reader is referred to the web version of this article.)

23 µM and 239 ± 28 µM during dry, wet and post monsoon seasons, respectively. ΣC^{+} * was higher in Kaveri compared to Netravathi during both seasons, with the solutes of both basins being less concentrated during wet period. It is also notable that the ΣC^{+} * of the mainstream and tributaries of Kaveri basin tend to increase towards the lower reaches during both seasons (more intensely during dry season) and exceptionally very high concentrations in Shimsa for both seasons and Arkavathi for dry season. In contrast, the ΣC^{+}* in Netravathi tend to be similar in the entire basin during all seasons except Shishilahole of dry period.

3.2. Weathering index

The proxy of silicate weathering degree based on river water geochemistry, molar ratio R_e, originally proposed by Tardy (1971) and modified by Boeglin and Probst (1998), has been calculated by Gurumurthy et al. (2012) for the Netravathi and by Meunier et al. (2015) for the Kaveri. This ratio is based on the concentrations of cations and silicon resulting from silicate weathering in river water.

$$R_e = \frac{(3Na^+ + 3\,K^+ + 1.25Mg^{2+} + 2Ca^{2+} - DSi)}{(0.5\,Na^+ + 0.5\,K^+ + 0.75\,Mg^{2+} + Ca^{2+})} \quad (1)$$

The coefficients used in the above formula correspond to an average granite containing feldspar, mica, and Mg-silicate minerals such as amphiboles. If the $R_e = 0$, the weathering is intense and forms gibbsite (allitization), if $R_e = 2$, kaolinite is essentially formed (monosiallitization), if $R_e = 4$, the weathering products are mainly smectites (bisiallitization). R_e indeed reflects the molar ratio (SiO_2/Al_2O_3) of the secondary minerals formed in the weathering profile (Tardy, 1971).

The R_e calculated for Kaveri basin ranges from 1.77 to 3.73 (2.35 ± 0.47) and 1.09 to 3.76 (2.10 ± 0.62) during dry and wet periods, respectively (Meunier et al., 2015). The most downstream values measured at Kollidam, which can be considered as integrative of the whole river basin, were 2.36 and 2.43 respectively. Shimsha showed the relatively high R_e value of 3.73 and 3.69 respectively. In Netravathi, R_e ranges from 1.9 to 2.4, 1.3 to 1.7 and 1.3 to 2.6 during dry, wet and post monsoon respectively (Gurumurthy et al., 2012 and Table. 2). There is a significant seasonal difference of R_e between dry and wet periods with significantly lower R_e during wet period compared to dry period ($p < 0.001$).

3.3. Silicon isotopes

The Si isotope compositions of Kaveri and Netravathi river basins are given in Tables 2 and 3. All the samples of Kaveri and Netravathi basins carry a positive value of $\delta^{30}Si_{DSi}$ within the range of recent global river water compilation (Frings et al., 2016 and the references within). The average $\delta^{30}Si_{DSi}$ of the river Kaveri (+1.73 ± 0.71‰) is ~0.7‰ heavier than the Netravathi basin (+0.99 ± 0.43‰) (Fig. 2c and d). The $\delta^{30}Si_{DSi}$ of the Kaveri and Netravathi basins are well comparable with large river basins: +0.9 ± 0.4‰ for Congo basin (Cardinal et al., 2010; Hughes et al., 2011); +1.0 ± 0.6‰ for Amazon basin (Hughes et al., 2013); +1.3 ± 0.5‰ for Yellow river (Ding et al., 2011); +1.5 ± 0.5‰ for Ganges-Brahmaputra basin (Fontorbe et al., 2013; Frings et al., 2015); +1.6 ± 0.4‰ for Tana basin, Kenya (Hughes et al., 2012); +2.1 ± 0.7‰ for Yangtze basin (Ding et al., 2004), while the world river (non-weighted)

average has been estimated to be +1.28 ± 0.7‰ (Frings et al., 2016). Kaveri basin signature is heavier than most global river basins but similar to Ganges-Brahmaputra and Tana basins whereas Netravathi is closer to the humid tropical basins, notably large and mostly pristine Amazon, and Congo basins. In Kaveri basin, seasonal influence is well evidenced between dry (base flow, +2.2 ± 0.3‰) and wet (high flow, +1.2 ± 0.7‰) seasons with a + 1‰ heavier $\delta^{30}Si_{DSi}$ during dry period (Fig. 2c). Noteworthy, there is no significant variability of silicon isotopes between reservoirs, tributaries, and mainstream during dry and wet period, except Nugu dam where the heaviest isotopic composition was measured during dry period (Table 1 and Fig. 2c). Like Kaveri basin, Netravathi also shows a significant seasonal difference in $\delta^{30}Si_{DSi}$ but no significant spatial heterogeneity within the river basin, except the light composition of Shishilahole tributary during dry period (Table 2 and Fig. 2d).

Discharge weighed Si isotopic composition delivered to the estuary by both rivers are calculated using the silicon isotopic signatures and DSi for both dry and wet seasons from the most downstream stations of Kaveri and Netravathi. The data for sampling discharge and DSi flux calculation of Netravathi (1.5 and 9.5 km^3 for dry and wet period discharge) and Kaveri (4.3 and 17 km^3 for dry and wet period discharge) was obtained from Mangalaa et al. (2017) and Meunier et al. (2015) respectively. The weighted $\delta^{30}Si$ signature of DSi exported to the Kaveri estuary is estimated at +1.98‰ which is heavier than the world average (around +0.74‰, Frings et al., 2016) while the $\delta^{30}Si$ signature of DSi exported to the Netravathi estuary is estimated to be +0.93‰, highlighting the contrasted weathering conditions and other factors prevailing in the two watersheds.

4. Discussion

Riverine DSi shows enrichment in heavier isotope of Si relative to the mean continental crust and lies within the range of world rivers reported so far (−0.1‰ up to +3.4‰; Frings et al., 2016; Sutton et al., 2018). Enriched $\delta^{30}Si_{DSi}$ signatures in river water generally result from two main processes: silicate weathering in the regolith resulting in secondary clay mineral formation and, biological uptake. Biological uptake can be of plant uptake from soil porewater, diatom uptake in rivers and streams, also human induced through irrigated agriculture (diversion of surface or ground water, with further release of Si-depleted water by return flow from the paddy fields) and diatom growth in dams/reservoirs. All processes preferentially incorporate lighter Si isotope resulting in heavy Si isotopic composition of the residual dissolved phase. In the next sections we discuss the respective influences of weathering intensity in silicon isotopic composition of river water according to the contrasted pedoclimatic conditions prevailing in Kaveri and Netravathi basins and the influence of anthropogenic factors.

4.1. Weathering processes

4.1.1. Weathering regimes and seasonality of Si and cations in rivers

Silicate weathering rate (SWR) of Netravathi watershed is among the highest reported for granitic gneiss terrain (42 tons/km^2/yr, Gurumurthy et al., 2012), while the estimated SWR in Kaveri basin is almost 4-fold lower (9.4 tons/km^2/yr at Musiri, Pattanaik et al., 2013), reflecting the contrasting weathering regimes. The Western Ghats receive maximum rainfall from SW monsoon, which accounts for 94% of the flow in Netravathi and almost 80% of the total annual flow in the upper reaches of the Kaveri River (Gurumurthy et al., 2012; Pattanaik et al., 2013). In both Kaveri and Netravathi, we observe broad positive and significant correlations between $\delta^{30}Si_{DSi}$, DSi and ΣC^{+*} concentrations (Fig. 3a, b, Fig. S1) indicating that $\delta^{30}Si_{DSi}$ compositions are significantly controlled by weathering intensity and clay mineral formation in both river basins. However, the overall positive correlation

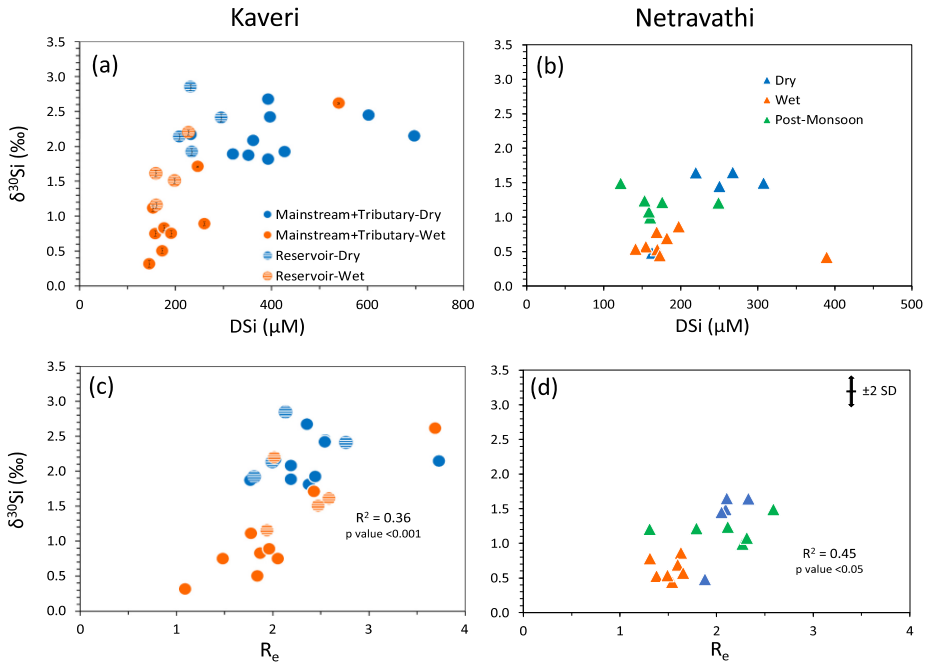

Fig. 3. Evolution of the isotopic signature ($\delta^{30}Si_{DSi}$) in the river Kaveri and Netravathi during different seasons, with dissolved Si concentration (3a, 3b) and R_e (3c, 3d).

between Si isotopic signature and DSi concentration is also driven by seasonal contrasts with higher DSi and heavier $\delta^{30}Si_{DSi}$ during dry season and lower DSi and lighter $\delta^{30}Si_{DSi}$ during wet season (Fig. 3a and b), while $\delta^{30}Si_{DSi}$ vs. DSi concentration or vs. $\Sigma C^{+}*$ do not exhibit clear relationship among samples collected from a single season. To look further into weathering processes, we compared $\delta^{30}Si_{DSi}$ with R_e as a proxy for silicate weathering, calculated using cation concentration corrected for atmospheric inputs. Since lithologies of basins encompass gneissic and schist belts in the Netravathi and peninsular gneiss, granitic rocks along with amphibolites in Kaveri, R_e is a more suitable proxy to describe weathering intensity and to compare with other tropical rivers rather than DSi/Na* or DSi/(Na* + K*) (Tables 1 and 2, Fig. S1). Coefficients used in the R_e (Eq. (2)) correspond to an average granitic composition with feldspars, micas, and amphiboles, and do not take into account spatial heterogeneities in bedrock composition within each basin. However, it is considered that tributaries and mainstream at least partly average this heterogeneity, which is consistent with good relationship between R_e and DSi/Na* ratio (Fig. S1, Tables 1 and 2).

Seasonal changes in river water geochemistry in Netravathi and Kaveri is affected by monsoon intensity and differences in water-rock interactions within the regolith (weathered rock also named saprolite, and topsoil) and at the weathering front with the fresh bedrock. Given that clay mineral form over months to millennia from metastable amorphous phases (Thiry, 2000), the seasonal changes in the R_e can be attributed to differences in soil-water interaction depths from different levels of the weathering profile leached, i.e., topsoil, saprolite or weathering front (Schaller et al., 2021). The upper range of the relationship between $\delta^{30}Si_{DSi}$ and R_e, heavy Si isotopic signature and high R_e corresponding to the dry period, shows that weathering leachates measured in the river results from smectite formation environment (bisiallitization). By contrast, the lower range of the relationship with lighter Si isotopic signature and low R_e, corresponding to monsoon period, tends to release dissolved elements leached out from a weathering environment where kaolinite-gibbsite formation dominates (monosiallitization and allitization; Fig. 3b, d). However, the stability of minerals can change seasonally depending on the chemical composition of the soil solution and temperature (Zabowski and Ugolini, 1992). In our case, during dry season in both basins, the river base flow is sustained by groundwater, i.e., water that interacted for a long duration while percolating through the thick weathering profile (Mukherjee et al., 2015) down to fresh bedrock minerals at the weathering front, allowing efficient cation and DSi leaching. During monsoon, the rainwater percolates predominantly in surface and subsurface depths with only cation-depleted primary minerals (such as quartz) or secondary minerals (such as kaolinite) in the saprolite and soil, recording a more intense weathering signature (Fig. 3). Seasonal changes of Si isotopic compositions and weathering intensity in these two basins could be defined by the type and duration of water-soil-rock interactions i.e., contributions in various proportions of surface and subsurface flows from different depths as schematically summarised in Fig. 4. Overall, R_e values are lower for Netravathi compared to Kaveri, in line with the more intense weathering fluxes exported by the west flowing river and with the thick lateritic profiles developed in Western Ghats. Intense runoff (3300 mm/yr in Netravathi basin, Gurumurthy et al., 2012) enhances weathering intensity, resulting over long timescales to weathering profiles dominated by kaolinite type clays and iron aluminium oxyhydroxides mineral assemblages (Deepthy and Balakrishnan, 2005). In contrast, Kaveri on the eastern side has shallower and immature weathering profiles characterized by much more complex clay mineral assemblages with both 2:1 clay such as smectites and 1:1 clay such as kaolinites together with residual primary minerals (Deepthy and Balakrishnan, 2005).

4.1.2. *Theoretical framework to understand weathering controls of $\delta^{30}Si_{DSi}$*

Determining how much of the silicon isotopic signature of rivers comes from weathering or biological processes is not trivial because in a watershed both processes are involved to varying degrees depending on the environment. It is often considered that plant Si removal at steady state, has no impact on dissolved fluxes (Cornelis et al., 2011). However, in anthropized hydrosystems, the effects of irrigated agriculture and dams on these fluxes and their isotopic signatures remain difficult to estimate. At the soil-plant scale the contribution of specific silicate

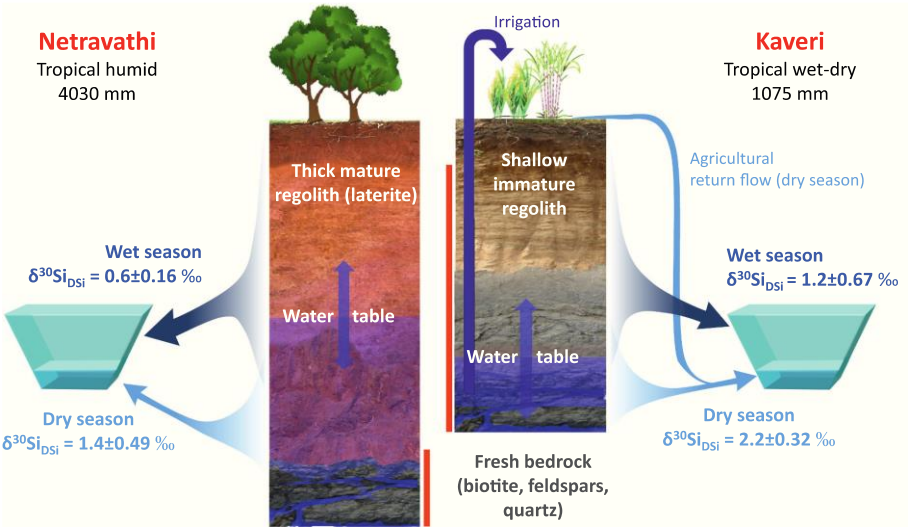

Fig. 4. A schematic of the results from the current study comparing the silicon cycling from two contrasting watersheds in South India. Red bars refer to the section of weathering profile where cation bearing (Na^+, K^+, etc.) primary minerals are still present and are leached. Please note that the weathering profile given is just a representative for middle/lower reaches of Kaveri, the humid high elevation profile in Western Ghats is similar to Netravathi (Deepthy and Balakrishnan, 2005; Braun et al., 2009; Gurumurthy et al., 2012; Meunier et al., 2015).

minerals on $\delta^{30}Si_{DSi}$ can be estimated by combining chemical fluxes and a theoretical isotopic balance, e.g., plagioclase weathering and kaolinite formation from sodium flux and $\delta^{30}Si$ signatures of source rock and clays (Riotte et al. 2018). Such isotope budgets have recently also been proposed for other ubiquitous silicates (Frings et al., 2021). At the scale of a tropical watershed, however, the intense weathering conditions and large spatial scale allow an alternative approach to estimate $\delta^{30}Si_{DSi}$ resulting from weathering of silicate rocks as a function of weathering conditions. This approach is not based on individual minerals that would each be transformed into different clays according to their Si, Al, and cation content, but rather makes the more realistic assumption that all the primary weatherable minerals are weathered and contribute to the formation of secondary phases by releasing silicon and cations within the weathering profile. The isotopic balance is thus carried out by considering; (1) the bulk elemental composition of the gneiss bedrock but removing the fraction of Si and Al in minerals resistant to weathering (quartz, zircon, muscovite/sericite), (2) that the production of secondary minerals is constrained by the Al content of all the weatherable minerals, (3) that the fraction of silicon released in solution and eventually to the river is a function of the type of secondary minerals formed, i.e. of the number of Si atoms allocated in each clay mineral thereafter referred to R_{theo}. This R_{theo} indeed corresponds to the theoretical meaning of R_e: gibbsite (0: no Si incorporated, i.e., allitization), kaolinite (2: two Si incorporated per mole of kaolinite, i.e., monosiallitization) or smectite (4: four Si incorporated per mole of smectite, i.e., bisiallitization) formations (see Eqs. (4) and (6) and details given in Table 4). This conceptual model allows to compare the evolution of the theoretical R_{theo} and the $\delta^{30}Si_{DSi}$ deduced from the isotopic balance. We used the equations below to calculate the fraction of silicon immobilized as clays ($f_{Si\text{-}clay}$), the fraction of silicon released as dissolved silicon ($f_{Si\text{-}DSi}$) and the resulting silicon isotopic composition of dissolved silicon ($\delta^{30}Si_{DSi}$).

$$f_{Si-DSi} + f_{Si-clay} = 1 \quad (2)$$

$$\delta^{30}Si_{DSi} = \frac{\left(\delta^{30}Si_{bedrock} - f_{Si-clay} * \delta^{30}Si_{clay}\right)}{f_{Si-DSi}} \quad (3)$$

For R_{theo} between 0 and 2 secondary minerals formed in soil are only gibbsite and kaolinite and $f_{gibbsite} + f_{kaolinite} = 1$ and;

$$R_{theo} = 2 * f_{kaolinite} \quad (4)$$

$$f_{Si-clay} = Al_{normalized} * f_{gibbsite} * (Si/Al)_{gibbsite} + Al_{normalized} * f_{kaolinite} * (Si/Al)_{kaolinite} \quad (5)$$

For R_{theo} between 2 and 3 secondary minerals formed in soil are only kaolinite and smectite $f_{smectite} + f_{kaolinite} = 1$ and;

$$R_{theo} = 2 * f_{kaolinite} + 4 * f_{smectite} \quad (6)$$

$$f_{Si-clay} = Al_{normalized} * f_{kaolinite} * (Si/Al)_{kaolinite} + Al_{normalized} * f_{smectite} * (Si/Al)_{smectite} \quad (7)$$

Here $f_{gibbsite}$, $f_{kaolinite}$ and $f_{smectite}$ are the proportion of gibbsite, kaolinite and smectite formed during weathering. In Eqs. (5) and (7), Al is normalized to silicon from the chemical and mineralogical composition of the gneiss as source rock, proposed by Braun et al. (2009) for Mule Hole (in the Western Ghats, part of the upper Kaveri basin) and Si/Al ratio of clay types are based on stoichiometry (Table 4). $\delta^{30}Si$ composition of the bedrock (−0.34‰) and clay fraction (−1.3‰) reported in Riotte et al. (2018a, 2018b) from the Kaveri basin are used for $\delta^{30}Si_{bedrock}$ and $\delta^{30}Si_{clay}$ (details of the bedrock composition, secondary product and $\delta^{30}Si$ value ranges are given in Table 4, Table 5).

Since the isotopic balance is strongly dependent on the $\delta^{30}Si$ of the secondary phase, in Eq. (3) we considered both the extreme values published in the literature for $\delta^{30}Si_{clays}$ (−2.1‰ in humid tropics of Sri Lanka comparable to Netravathi and $\delta^{30}Si$ of −0.5‰ for smectite type clays which is lighter than the bedrock; Frings et al., 2021; Georg et al., 2009), along with value measured in kaolinite dominated clay fraction from Mule Hole soils of Kaveri basin (−1.3‰; Riotte et al., 2018a, 2018b) (Fig. 5). The evolution of $\delta^{30}Si$ as a function of R_{theo} is considered robust between 0 and 2 because the conditions for intense weathering are met (Table 5). On the other hand, R_{theo} beyond 2 corresponds to progressive formation of smectite type clays with lower intensity of weathering, which is consistent with the observation that a part of the weatherable primary minerals is still present in weathering profiles (see e.g., Violette et al., 2010 for Mule Hole). Therefore, the evolution of $\delta^{30}Si$ for R_{theo} between 2 and 3 (still dominant kaolinite formation) is only indicative. For R_{theo} of 0, the $\delta^{30}Si$ corresponds to the signature of the parent rock which is expected as Si is not incorporated into any secondary mineral. $\delta^{30}Si_{DSi}$ then increases with R_{theo} as the silicon immobilized in the clays are lighter in silicon isotopic composition. Thus, at R_{theo} of 2 (kaolinite formation) the maximum $\delta^{30}Si$ of the solute phase is 1.2‰. Beyond 2 the $\delta^{30}Si$ increases up to 5.7‰ which could explain in part certain high $\delta^{30}Si_{DSi}$ signatures of world rivers. Current framework also allows to check the whole rock weathering including the stable minerals such as quartz and sericite, which shows relatively low fractionation in $\delta^{30}Si_{DSi}$ with increasing R_{theo}. Gneiss composition corrected for stable minerals such as quartz and muscovite better represents the measured values in natural river water samples compared to whole rock weathering scenario, indicating negligible Si leaching from the resistant mineral phases (Fig. 5).

In the Netravathi, the spatio-temporal variations of R_e and $\delta^{30}Si$ observed match the theoretical curve defined by the lightest $\delta^{30}Si$ kaolinite formation (−2.1‰ found in humid tropics similar to Netravathi climate) and few samples within $\delta^{30}Si_{clay}$ of −1.3‰. This means that the local or seasonal weathering conditions taking place in this river basin are sufficient to explain the $\delta^{30}Si$ variability in the river system. In

Table 4
The stoichiometric composition and $\delta^{30}Si$ of the bedrock and possible secondary product compositions used to derive the theoretical relationships between $\delta^{30}Si_{DSi}$ and weathering intensity in the river basins ($^{\nabla}$ Braun et al., 2009; $^{\#}$ Opfergelt and Delmelle, 2012; * Frings et al., 2021; $^{\Phi}$ Riotte et al., 2018a, 2018b).

$Bedrock_{initial}$	Secondary product	$\delta^{30}Si_{clay}$	R_{theo}
Whole Gneiss$^{\nabla}$	Gibbsite, $Al(OH)_3$	-	0
$Si_{1.14}Al_{0.27}Ca_{0.04}Mg_{0.06}$ $Na_{0.14}$ $K_{0.04}$	Kaolinite, $Si_2Al_2O_5(OH)_4$	−1 to −2 ‰*	2
$\delta^{30}Si = -0.34‰^{\Phi}$	Smectite $Si_4O_{10}(OH)_2Mg_{0.33}Al_{1.67}Ca_{0.16}$	−0.2 to −1 ‰$^{\#}$	4
Gneiss without quartz and sericite$^{\nabla}$	Gibbsite, $Al(OH)_3$	-	0
$Si_{0.57}Al_{0.26}$ $Ca_{0.04}Mg_{0.06}$ $Na_{0.14}$ $K_{0.02}$	Kaolinite, $Si_2Al_2O_5(OH)_4$	−1 to −2 ‰*	2
$\delta^{30}Si = -0.34‰^{\Phi}$	Smectite $Si_4O_{10}(OH)_2Mg_{0.33}Al_{1.67}Ca_{0.16}$	−0.2 to −1 ‰$^{\#}$	4

Table 5
Calculated values of $\delta^{30}Si_{DSi}$ and theoretical weathering index (R_{theo}) using the equations given in the text. Two scenarios involving either weathering of gneiss with and without quartz and sericite mineral fraction is considered for calculating the evolution of the Rtheo and $\delta^{30}Si_{DSi}$.

$f_{gibbsite}$	$f_{kaolinite}$	$f_{smectite}$	$f_{Si\text{-}clay}$	$f_{Si\text{-}DSi}$	$\delta^{30}Si_{DSi}$	R_{theo}
Weathering of gneiss without quartz and sericite						
1	0	0	0.00	1.00	−0.34	0
0.5	0.5	0	0.23	0.77	−0.06	1
0	1	0	0.45	0.55	0.46	2
0	0.5	0.5	0.77	0.23	2.90	3
Weathering of whole gneiss						
1	0	0	0.00	1.00	−0.34	0
0.5	0.5	0	0.12	0.88	−0.21	1
0	1	0	0.24	0.76	−0.04	2
0	0.5	0.5	0.40	0.60	0.30	3

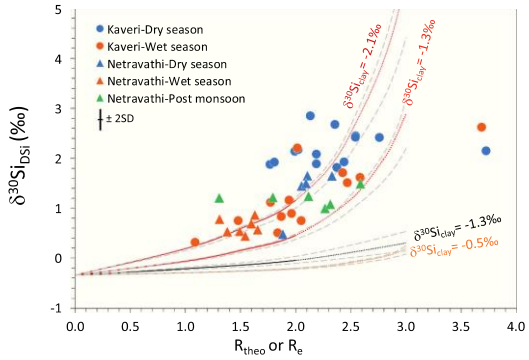

Fig. 5. The evolution of R_{theo} and $\delta^{30}Si_{DSi}$ as rock weathers and transforms into secondary products plotted along with measured R_e of river water samples from Kaveri and Netravathi. Trendline for three different silicon isotopic compositions for the clay is plotted for the gneiss weathering corrected for quartz and sericite contribution (maroon, red and orange for $\delta^{30}Si_{product}$ values of −2.1‰, −1.3‰ and −0.5‰ respectively). The scenario for whole gneiss weathering and $\delta^{30}Si_{product}$ of −1.3‰ is shown in black. The grey dashed lines represent the sensitivity depending on the deviation in the chemical composition in the intial rock composition (Braun et al., 2009). R_e calculation in Gurupura river is negative due to overestimation of the atmospheric input is not displayed. (For interpretation of the references to colour in this figure legend, the reader is referred to the web version of this article.)

contrast, only few samples from Kaveri tributaries and the mainstream show $\delta^{30}Si_{DSi}$ signatures consistent with theoretical R_{theo} for $\delta^{30}Si_{clay}$ of −1.3‰ (which is observed in Kaveri basin by Riotte et al., 2018a, 2018b). Overall $\delta^{30}Si_{DSi}$ of the Kaveri samples was on average + 0.67 ± 0.4‰ and + 1.34 ± 0.4‰ heavier during wet season and dry season respectively than the theoretical value expected by a single control of silicate weathering with $\delta^{30}Si_{clays}$ of −1.3‰. This discrepancy shows that the heavy $\delta^{30}Si$ signatures observed especially during the dry season can partly be the result of biological and/or anthropogenic processes (see section 4.2 for details).

4.1.3. Comparison with other tropical rivers

Overall, the seasonal variations of major elements as well as of $\delta^{30}Si_{DSi}$ are similar with those of the Amazon basin and tributaries (Hughes et al., 2013) as observed in the $\delta^{30}Si_{DSi}$ vs. R_e index comparison

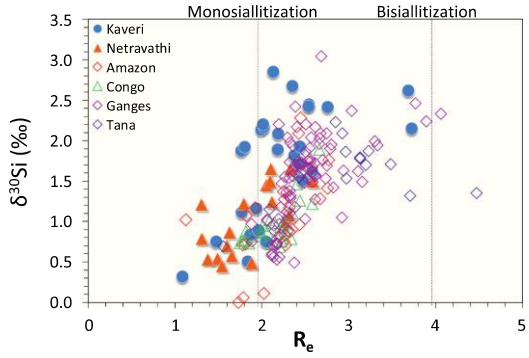

Fig. 6. $\delta^{30}Si_{DSi}$ and R_e of the present study compared with the values from other studies global river water (see text for details, Amazon from Hughes et al. (2013); Congo from Hughes et al. (2011); Tana from Hughes et al. (2012); Ganges from Fontorbe et al. (2013)).

with other tropical rivers (Fig. 6). The range of weathering index in the present study is comparable to the R_e values of other worldwide rivers (discussed in Gurumurthy et al., 2012): Ganges-Brahmaputra (2.2), Amazon (2.1) and Congo-Zaire (2.1) are similar to Kaveri basin, whereas, the Orinoco (1.6), Parana (1.4) and Mekong (1.7) are more comparable to the Netravathi basin. It is also interesting to note from the Fig. 6, that the two contrasted Indian tropical basins with many anthropogenic pressures are behaving similarly as the tributaries and mainstream of the Amazon basin (data from Hughes et al., 2013), Congo river (Hughes et al., 2011), Tana river (Hughes et al., 2012) that are very different in size and type (e.g., with much less anthropogenic impact especially for Congo and Amazon) indicating that silicate weathering remains a major process that controls the Si isotopic variability. Likewise, in Ganges combination of both above mentioned processes control the $\delta^{30}Si_{DSi}$ variability (Fontorbe et al., 2013). Compilation of the R_e and $\delta^{30}Si_{DSi}$ from tropical rivers indicates a broad decrease of $\delta^{30}Si_{DSi}$ with increasing weathering intensity which is consistent with the $\delta^{30}Si$ of soils (Opfergelt and Delmelle, 2012).

4.2. Biotic and anthropogenic impacts

4.2.1. Water use and crops

Vegetation cover and aquatic diatoms can significantly affect Si cycling in surface water by controlling riverine DSi load (Derry et al., 2005; Cornelis et al., 2011). Deforestation and conversion to agricultural field also affect Si cycling by enhancement of erosion and dissolution of amorphous silica (ASi) that increases riverine DSi. Conversely, phytoliths may decrease riverine DSi due to crops harvesting and subsequent removal from the system (Conley et al., 2008). Regarding Si isotopic signatures, more intensive agricultural activities can lead to more incorporation of lighter Si isotopes in the plants, leaving heavier Si isotopic signature in the soil solution (Vandevenne et al., 2012, Riotte et al., 2018a, 2018b) and rivers (Delvaux et al., 2013). Contrasting land use and land cover in Kaveri and Netravathi basins can significantly impact $\delta^{30}Si_{DSi}$ and river water geochemistry. Indeed, Kaveri River basin with higher agricultural land area (almost 66%) show higher $\delta^{30}Si_{DSi}$ compared to the Netravathi during dry season. However, there is also an overlapping signal from the abiotic weathering process arising from these various lithologies, climate and anthropogenic influences in the overall $\delta^{30}Si_{DSi}$ signature. The broad increase in $\delta^{30}Si_{DSi}$ along the Kaveri course could indeed result from the multiple return flows from paddy fields irrigation in command areas (almost 80% of the surface water is deviated for irrigation; Meunier et al., 2015), or from a larger fraction of Si incorporated in the clays of the semi-arid middle and lower reaches. DSi removal in cultivated regions of Kaveri basin where silicon-accumulating crops such as paddy, sugarcane and maize are grown, will be dominated by the plant uptake upon adsorption which fractionates against $^{30}Si_{DSi}$, leading to a heavy isotopic signature in soil solution (Riotte et al., 2018a, 2018b). The primary purpose of the dams and reservoirs in Kaveri is to provide water through canals for irrigating the cultures located downstream each structure (named command areas). The water in excess returns to the main river channel as return flow with a relatively heavier $\delta^{30}Si_{DSi}$ as observed in stagnant water of paddy fields (upto +4.4‰, Riotte et al., 2018b). The contribution of SW monsoon decreases towards lower reaches of Kaveri with Shimsha and Arkavathi watersheds receiving only limited rainfall (Pattanaik et al., 2013). These two tributaries are dammed and the water reaching Kaveri is a mix of sewage, return flow from irrigated agriculture and possible local groundwater contributions. Therefore, the exceptionally heavy isotopic composition at Shimsha river on the lower reach in both seasons (+2.1 and + 2.6‰) and the Arkavathi during dry season (+2.4‰) can result from dissolved Si that has encountered several cycles of isotopic enrichments due to plant uptake combined to evaporation that has increased Si concentration. This is consistent with high total cations and comparable values of major cations during dry and wet seasons of Shimsha river. Such heavy $\delta^{30}Si$ corresponds to return flow from

irrigated agriculture that leaves the residual DSi fraction of these waters, enriched in ^{30}Si (Riotte et al., 2018b). Kaveri river water samples also showed a broad range of Cl concentration with an average of 646 μM for both seasons which is almost 8-fold higher than Netravathi. Such high concentration is likely to result from the combined effect of evapotranspiration, irrigation, and recycling, along with additional inputs from fertilizers such as potash (KCl), which is well documented in an agricultural watershed in Kabini basin (Buvaneshwari et al., 2020). During the wet period, the dilution effect is generally seen in dissolved load concentration, but the contrasted Si isotopic composition cannot be only explained by a dilution process. Si isotopic signature of the mainstream is gradually getting heavier towards the lower reach, while the tributaries and reservoirs exhibit higher variability during wet period (Fig. 2b). Therefore, as discussed in section 4.1.2 and seen in Fig. 5 weathering predominantly controls Si isotope variations in the upper reaches of Kaveri receiving the maximum precipitation while increased contribution of return flow from irrigated agriculture into the mainstream and tributaries leads to an increase in $\delta^{30}Si_{DSi}$ of DSi in the lower reaches of Kaveri.

4.2.2. Amorphous silica (ASi) and dams

The relationship between amorphous silica (ASi) and $\delta^{30}Si_{DSi}$ in rivers suspended matter are not straightforward, as shown by Hughes et al. (2011) in the Congo River, because of the importance of fast diatoms settling in the sediment. According to the only three counting available, the ASi fraction in Kaveri River is constituted half by phytoliths (mainly originating from grass and sedge species) and half by diatom frustules (Meunier et al., 2015), except in reservoir where diatoms largely dominate. In the case of the Kaveri River, we did not observe any correlation between $\delta^{30}Si_{DSi}$ and ASi, indicating increase in ASi fraction, resulting from an increased diatom growth, cannot account for the heavy silicon isotopic compostion (ASi data from Meunier et al., 2015). To check for the role of diatoms in the river basin during dry season, we also used the approach detailed in Hughes et al. (2011) (Appendix A). However, the calculation suggests that the influence of diatom uptake is unlikely to explain the variability of $\delta^{30}Si_{DSi}$ in Kaveri basin during the dry season due to the unrealistic BSi required for such heavy $\delta^{30}Si_{DSi}$ and the lack of any correlation with ASi. Phytoliths are labile Si pools with dissolution rates lower than secondary clay minerals and can be an important contributor to riverine silicon cycling (Fraysse et al., 2009). Previous study from Mule Hole watershed in Kabini basin shows that δ^{30}Si of soil and suspended load ASi fraction dominated by phytolith varies in a narrow range from +1.1 to +1.4‰ (Riotte et al., 2018a), which are unlikely to explain the heavy silicon isotopic composition during dry season.

Reservoirs and dams increase the residence time of water and favour enhanced diatom growth and accumulation in sediments which cause a decline in DSi downstream the reservoir (Conley et al., 2000; Humborg et al., 2002; Hughes et al., 2012). Meunier et al. (2015) reported a dominance of diatoms in the ASi pool of the Nugu reservoir that may explain decrease of DSi content. Reservoirs in the present study do not show any significant difference in Si concentration or isotopic signature compared to the mainstream and tributaries for both seasons except Nugu reservoir during dry season (+2.8‰, Table 2, Fig. 2 a, c). Nugu reservoir also shows higher ASi (73.8 μM) and low DSi (231 μM) and was reported to have higher diatom abundance (94%) in the ASi fraction relative to the other adjacent reservoirs, clearly indicating increased diatom production leading to higher $\delta^{30}Si_{DSi}$ value of the water (Fig. 2 a, c and Meunier et al., 2015). Using this isotopic composition as the $\delta^{30}Si_0$ and applying Eqs. (a) and (b) in Appendix, gives calculated BSi of 258 μM and 693 μM for Rayleigh and steady state models, respectively. The value obtained by the Rayleigh model is larger but comparable to the highest value calculated in Malebo pool by Hughes et al. (2011) in which 215 μM of DSi has been consumed and appears realistic for diatom production within a tropical lake during summer. However, none of the other Kaveri reservoirs showed enhanced ASi values, which indicate negligible role of biotic uptake at the scale of the Kaveri Basin. During the wet season, higher discharge and turbidity limit diatom growth as clearly shown by the extreme shallowness of photic depth, 0.13 ± 0.1 m, during high discharge in Godavari estuary (Sarma et al., 2009). There are no ASi data measured from Netravathi basin to assess the biological uptake, but comparatively fewer dams in this basin and lighter Si isotopic composition than Kaveri suggest limited impact of biotic process in Si biogeochemical cycling in Netravathi. Kaveri river and its tributaries have been supporting irrigated agriculture in middle and lower reaches for centuries (two millennia in the Kaveri delta) and the dams and reservoirs were primarily built to retain monsoon flow and sustain agriculture through canal irrigation during dry season. Higher extent of cultivation and irrigation with the help of reservoirs and dams can lead to significant DSi removal over time and a heavier isotopic signature for agriculture return flow. Such impacts from biotic uptake can overlap with weathering controls of $\delta^{30}Si_{DSi}$ values in river water spatially and temporally.

5. Conclusions

In this study, we report the first dataset of riverine $\delta^{30}Si_{DSi}$ signatures in the Kaveri and Netravathi River Basins, both originating from the Western Ghats (India) but flowing east and west directions, respectively with contrasting land use and climate. Both basins are seasonally well marked, and the $\delta^{30}Si_{DSi}$ in Kaveri river is ~1‰ heavier than that of Netravathi River. This results in a weighted $\delta^{30}Si_{DSi}$ of DSi exported to estuary more fractionated in Kaveri (+1.98‰) than in Netravathi (+0.93‰). The $\delta^{30}Si_{DSi}$ is mainly controlled by weathering regime and water flow which is in turn driven by the short- and long-term hydrological conditions prevailing in each catchment. The long term explains the thickness and abundance of cation-depleted weathering profiles while the short term seasonal scale explains the different levels of water-rock interaction in the weathering profile. We compare $\delta^{30}Si_{DSi}$ signatures with R_e weathering index based on water cation geochemistry. Low R_e in Netravathi indicates intense weathering with formation of kaolinite-gibbsite in the river basin, while most of the Kaveri basin is dominated by smectite-kaolinite assemblage. Both river basins display similar $\delta^{30}Si_{DSi}$ seasonal pattern, with higher $\delta^{30}Si_{DSi}$ and R_e during dry season resulting from soil water release close to the weathering front (i.e., deep saprolite and bedrock) and lower $\delta^{30}Si_{DSi}$ and lower R_e during wet season due to intense weathering. The weathering index Re calculated for both rivers is comparable to the values of other tropical rivers, for instance the Amazon river and its tributaries. We propose a new conceptual approach based on bedrock element geochemistry and redistribution during weathering of Si into secondary mineral on the one hand and released to dissolved phase on the other hand (R_{theo} directly comparable to R_e), to calculate expected $\delta^{30}Si_{DSi}$ signatures. Comparison between calculated and measured $\delta^{30}Si_{DSi}$ allows to estimate whether river Si isotopic signatures can be fully explained only by weathering or if other processes are involved. In Netravathi basin we show that weathering processes are sufficient to explain the $\delta^{30}Si_{DSi}$ signatures and that anthropogenic pressures have a minor contribution. But in Kaveri we found that the $\delta^{30}Si_{DSi}$ are on average + 0.67 ± 0.4‰ and + 1.34 ± 0.4‰ heavier during wet season and dry season respectively than the expected theoretical curve. We ascribe this offset to canal irrigation downstream major dams during dry season that leads to return flow contribution to the river which increases $\delta^{30}Si_{DSi}$ in the river, leading to overall enriched signature in river water. We also suggest that diatoms Si uptake in the Kaveri stream is generally negligible except in the Nugu reservoir (Kaveri tributary) in dry season. Overall, the present study

emphases the control of climatic conditions the $\delta^{30}Si$ of the studied rivers, through the intensity of silicate weathering and nature of the secondary clays produced. It also quantifies, for the first time, the effect of anthropogenic activities (daming and irrigated agriculture) on the silicon isotopic composition of rivers.

Supplementary data to this article can be found online at https://doi.org/10.1016/j.chemgeo.2022.120883.

Declaration of Competing Interest

The authors declare that they have no known competing financial interests or personal relationships that could have appeared to influence the work reported in this paper.

Acknowledgements

The authors would like to thank M. Benrahmoune (LOCEAN-IPSL) for help in sample processing and clean lab management. This work has been supported by the French National programme EC2CO (BIO-HEFECT) - LEFE (CYBER) managed by INSU-CNRS (project SINDIA). K. R. Mangalaa scholarship has been mainly provided by the Erasmus Mundus Action 2 of the European Union (GATE project), with additional support from the Scientific Department of French Embassy in India and by the European Union Seventh Framework Program under grant agreement #294146 (MuSiCC Marie Skłodowska-Curie Actions CIG). We warmly thank IRD for providing Sarath P.K. Ph.D. scholarship and constant support. The work also benefited from CEFIPRA-IFCPAR support (NUNDERGROUND, project # 5907) and from analyses at ALYSES facility (IRD-SU). We thank the AE Oleg Pokrovsky, Luc André and three anonymous reviewers for their thorough comments that greatly helped to improve this manuscript.

Appendix A. Checking the role of diatoms on $\delta^{30}Si$ composition of river water

Here, we assume that the heavier isotopic composition of Kaveri basin in dry season results from the diatom uptake and the $\delta^{30}Si$ is used as a proxy to quantify the uptake mechanism. Based on our assumption, the production of BSi (biogenic silica) as the only main output of DSi for the given water, then f_{Si} = DSi/(DSi + BSi), and one can rewrite the Rayleigh and Steady state equations as:

$$\text{Rayleigh}: \text{BSi} = \text{DSi} \times \left[exp\left(\left(\delta^{30}Si_0 - \delta^{30}Si\right)/\varepsilon\right) - 1\right] \quad \text{(a)}$$

$$\text{Steady state}: \text{BSi} = \text{DSi} \times \left[\left(\varepsilon/\delta^{30}Si - \delta^{30}Si_0 + \varepsilon\right) - 1\right] \quad \text{(b)}$$

$\delta^{30}Si_0$ is considered as 1.81‰, which is the lightest in the river stream during dry period. The fractionation factor (ε) is −1.2‰ (Fripiat et al., 2011; Alleman et al., 2005; Georg et al., 2006a, 2006b).

Based on both Rayleigh and steady state models, the calculated BSi varied 174 ± 165 and 294 ± 350 μM in the mainstream and tributaries of Kaveri respectively whereas the measured ASi values varied 5.6 ± 8.9 μM (Meunier et al., 2015). Moreover, no relation was observed between measured ASi and calculated BSi. It is not realistic to have such high BSi production by diatoms to explain the isotopic composition in the basin because the residence time of the water in the stream is too short to allow such dense growth of diatoms. Moreover, this mechanism is even true for the reservoirs due to the quick usage of water for irrigation. On contrary, in river Congo, higher stability of water flow made favorable for diatom growth was noticed by Hughes et al. (2011) and that could explain the relationship between Si isotopes and ASi.

References

Alexandre, A., Meunier, J.D., Colin, F., Koud, J.M., 1997. Plant impact on the biogeochemical cycle of silicon and related weathering processes. Geochim. Cosmochim. Acta 61, 677–682.
Alleman, L.Y., Cardinal, D., Cocquyt, C., Plisnier, P.D., Descy, J.P., Kimirei, I., Sinyinza, D., André, L., 2005. Silicon isotopic fractionation in Lake Tanganyika and its main tributaries. J. Great Lakes Res. 31, 509–519.
André, L., Abraham, K., Hofmann, A., Monin, L., Kleinhanns, I.C., Foley, S., 2019. Early continental crust generated by reworking of basalts variably silicified by seawater. Nat. Geosci. 2019 12 (9 12), 769–773. https://doi.org/10.1038/s41561-019-0408-5.
Boeglin, J.L., Probst, J.L., 1998. Physical and chemical weathering rates and CO2 consumption in a tropical lateritic environment: the upper Niger Basin. USDA for. Serv. - Gen. Tech. Rep. RMRS-GTR 148, 137–156.
Braun, J.J., Descloitres, M., Riotte, J., Fleury, S., Barbiéro, L., Boeglin, J.L., Violette, A., Lacarce, E., Ruiz, L., Sekhar, M., Mohan Kumar, M.S., Subramanian, S., Dupré, B., 2009. Regolith mass balance inferred from combined mineralogical, geochemical and geophysical studies: Mule Hole gneissic watershed, South India. Geochim. Cosmochim. Acta 73, 935–961.
Buvaneshwari, S., Riotte, J., Sekhar, M., Sharma, A.K., Helliwell, R., Kumar, M.S.M., Braun, J.J., Ruiz, L., 2020. Potash fertilizer promotes incipient salinization in groundwater irrigated semi-arid agriculture. Sci. Rep. 10, 1–14. Available at: https://doi.org/10.1038/s41598-020-60365-z.
Cardinal, D., Gaillardet, J., Hughes, H.J., Opfergelt, S., André, L., 2010. Contrasting silicon isotope signatures in rivers from the Congo Basin and the specific behaviour of organic-rich waters. Geophys. Res. Lett. 37 (12).
Closset, I., Cardinal, D., Rembauville, M., Thil, F., Blain, S., 2016. Unveiling the Si cycle using isotopes in an iron-fertilized zone of the Southern Ocean: from mixed-layer supply to export. Biogeosciences 13, 6049–6066.
Conley, D.J., 1997. Riverine contribution of biogenic silica to the oceanic silica budget. Limnol. Oceanogr. 42, 774–777.
Conley, D.J., Stålnacke, P., Pitkänen, H., Wilander, A., 2000. The transport and retention of dissolved silicate by rivers in Sweden and Finland. Limnol. Oceanogr. 45, 1850–1853. Available at: http://doi.wiley.com/10.4319/lo.2000.45.8.1850.
Conley, D.J., Humborg, C., Smedberg, E., Rahm, L., Papush, L., Danielsson, Å., Clarke, A., Pastuszak, M., Aigars, J., Ciuffa, D., Mörth, C.M., 2008. Past, present and future state of the biogeochemical Si cycle in the Baltic Sea. J. Mar. Syst. 73, 338–346.
Cornelis, J.T., Delvaux, B., Georg, R.B., Lucas, Y., Ranger, J., Opfergelt, S., 2011. Tracing the origin of dissolved silicon transferred from various soil-plant systems towards rivers: a review. Biogeosciences 8, 89–112.
Deepthy, R., Balakrishnan, S., 2005. Climatic control on clay mineral formation: evidence from weathering profiles developed on either side of the Western Ghats. J. Earth Syst. Sci. 114, 545–556.
Delvaux, C., Cardinal, D., Carbonnel, V., Chou, L., Hughes, H.J., André, L., 2013. Controls on riverine δ30Si signatures in a temperate watershed under high anthropogenic pressure (Scheldt - Belgium). J. Mar. Syst. 128, 40–51.
Derry, L.A., Kurtz, A.C., Ziegler, K., Chadwick, O.A., 2005. Biological control of terrestrial silica cycling and export fluxes to watersheds. Nature 433, 728–731. Available at: www.nature.com/nature.
Ding, T., Wan, D., Wang, C., Zhang, F., 2004. Silicon isotope compositions of dissolved silicon and suspended matter in the Yangtze River, China. Geochim. Cosmochim. Acta 68, 205–216.
Ding, T.P., Gao, J.F., Tian, S.H., Wang, H.B., Li, M., 2011. Silicon isotopic composition of dissolved silicon and suspended particulate matter in the Yellow River, China, with implications for the global silicon cycle. Geochim. Cosmochim. Acta 75, 6672–6689.
Dürr, H.H., Meybeck, M., Hartmann, J., Laruelle, G.G., Roubeix, V., 2011. Global spatial distribution of natural riverine silica inputs to the coastal zone. Biogeosciences 8, 597–620. https://doi.org/10.5194/bg-8-597-2011.
Engström, E., Rodushkin, I., Ingri, J., Baxter, D.C., Ecke, F., Österlund, H., Öhlander, B., 2010. Temporal isotopic variations of dissolved silicon in a pristine boreal river. Chem. Geol. 271, 142–152.
Fontorbe, G., De La Rocha, C.L., Chapman, H.J., Bickle, M.J., 2013. The silicon isotopic composition of the Ganges and its tributaries. Earth Planet. Sci. Lett. 381, 21–30.
Fraysse, F., Pokrovsky, O.S., Schott, J., Meunier, J.D., 2009. Surface chemistry and reactivity of plant phytoliths in aqueous solutions. Chem. Geol. 258, 197–206. https://doi.org/10.1016/J.CHEMGEO.2008.10.003.
Frings, P.J., Clymans, W., Fontorbe, G., Gray, W., Chakrapani, G., Conley, D.J., De La Rocha, C., 2015. Silicate weathering in the Ganges alluvial plain. Earth Planet. Sci. Lett. 427, 136–148.

Frings, P.J., Clymans, W., Fontorbe, G., De La Rocha, C.L., Conley, D.J., 2016. The continental Si cycle and its impact on the ocean Si isotope budget. Chem. Geol. 425, 12–36.
Frings, P.J., Oelze, M., Schubring, F., Frick, D.A., von Blanckenburg, F., 2021. Interpreting silicon isotopes in the Critical Zone. Am. J. Sci. 321, 1164–1203. https://doi.org/10.2475/08.2021.02.
Fripiat, F., Cavagna, A.J., Dehairs, F., Speich, S., André, L., Cardinal, D., 2011. Silicon pool dynamics and biogenic silica export in the Southern Ocean inferred from Si-isotopes. Ocean Sci. 7, 533–547.
Ganasri, B.P., Ramesh, H., 2016. Assessment of soil erosion by RUSLE model using remote sensing and GIS - a case study of Nethravathi Basin. Geosci. Front. 7, 953–961.
Georg, R.B., Reynolds, B.C., Frank, M., Halliday, A.N., 2006a. Mechanisms controlling the silicon isotopic compositions of river waters. Earth Planet. Sci. Lett. 249, 290–306.
Georg, R.B., Reynolds, B.C., Frank, M., Halliday, A.N., 2006b. New sample preparation techniques for the determination of Si isotopic compositions using MC-ICPMS. Chem. Geol. 235, 95–104.
Georg, R.B., Reynolds, B.C., West, A.J., Burton, K.W., Halliday, A.N., 2007. Silicon isotope variations accompanying basalt weathering in Iceland. Earth Planet. Sci. Lett. 261, 476–490.
Georg, R.B., Zhu, C., Reynolds, B.C., Halliday, A.N., 2009. Stable silicon isotopes of groundwater, feldspars, and clay coatings in the Navajo Sandstone aquifer, Black Mesa, Arizona, USA. Geochim. Cosmochim. Acta 73, 2229–2241. https://doi.org/10.1016/J.GCA.2009.02.005.
Grasse, P., Brzezinski, M.A., Cardinal, D., De Souza, G.F., Andersson, P., Closset, I., Cao, Z., Dai, M., Ehlert, C., Estrade, N., François, R., Frank, M., Jiang, G., Jones, J.L., Kooijman, E., Liu, Q., Lu, D., Pahnke, K., Ponzevera, E., Schmitt, M., Sun, X., Sutton, J.N., Thil, F., Weis, D., Wetzel, F., Zhang, A., Zhang, J., Zhang, Z., 2017. GEOTRACES inter-calibration of the stable silicon isotope composition of dissolved silicic acid in seawater. J. Anal. At. Spectrom. 32, 562–578. Available at: https://pubs.rsc.org/en/content/articlehtml/2017/ja/c6ja00302h.
Grasshoff, K., Kremling, K., Ehrhardt, M., 1999. Methods of Seawater Analysis 3rd Edison Completely Revised and, Extended edition. Wiley- VCH. ISBN 3-527-29589-5.
Gurumurthy, G.P., Balakrishna, K., Riotte, J., Braun, J.J., Audry, S., Shankar, U.H.N., Manjunatha, B.R., 2012. Controls on intense silicate weathering in a tropical river, southwestern India. Chem. Geol. 300–301, 61–69.
Gurumurthy, G.P., Balakrishna, K., Tripti, M., Audry, S., Riotte, J., Braun, J.J., Udaya Shankar, H.N., 2014. Geochemical behaviour of dissolved trace elements in a monsoon-dominated tropical river basin, Southwestern India. Environ. Sci. Pollut. Res. 21, 5098–5120. https://doi.org/10.1007/s11356-013-2462-7.
Gurumurthy, G.P., Balakrishna, K., Tripti, M., Riotte, J., Audry, S., Braun, J.J., Lambs, L., Udaya Shankar, H.N., 2015a. Sources of major ions and processes affecting the geochemical and isotopic signatures of subsurface waters along a tropical river, Southwestern India. Environ. Earth Sci. 73, 333–346.
Gurumurthy, G.P., Balakrishna, K., Tripti, M., Riotte, J., Audry, S., Braun, J.J., Udaya Shankar, H.N., 2015b. Use of Sr isotopes as a tool to decipher the soil weathering processes in a tropical river catchment, southwestern India. Appl. Geochem. 63, 498–506.
Hughes, H.J., Sondag, F., Cocquyt, C., Laraque, A., Pandi, A., André, L., Cardinal, D., 2011. Effect of seasonal biogenic silica variations on dissolved silicon fluxes and isotopic signatures in the Congo River. Wiley Online Libr. 56, 551–561.
Hughes, H.J., Bouillon, S., André, L., Cardinal, D., 2012. The effects of weathering variability and anthropogenic pressures upon silicon cycling in an intertropical watershed (Tana River, Kenya). Chem. Geol. 308–309, 18–25.
Hughes, H.J., Sondag, F., Santos, R.V., André, L., Cardinal, D., 2013. The riverine silicon isotope composition of the Amazon Basin. Geochim. Cosmochim. Acta 121, 637–651.
Humborg, C., Blomqvist, S., Avsan, E., Bergensund, Y., Smedberg, E., Brink, J., Mörth, C.-M., 2002. Hydrological alterations with river damming in northern Sweden: Implications for weathering and river biogeochemistry. Glob. Biogeochem. Cycles 16, 12-1-12–13.
Integrated Hydrological Data Book, 2012. Central Water Commission. Delhi, New.
Karl, D.M., Tien, G., 1992. MAGIC: a sensitive and precise method for measuring dissolved phosphorus in aquatic environments. Limnol. Oceanogr. 37, 105–116. Available at: http://doi.wiley.com/10.4319/lo.1992.37.1.0105.
Lele, S., Srinivasan, V., Jamwal, P., Thomas, B.K., Eswar, M., Md. Zuhail, T., 2013. Water Management in Arkavathy Basin: A situational analysis. In: Environment and Development Discussion Paper.
Mangalaa, K.R., Cardinal, D., Brajard, J., Rao, D.B., Sarma, N.S., Djouraev, I., Chiranjeevulu, G., Murty, K.N., Sarma, V.V.S.S., 2017. Silicon cycle in Indian estuaries and its control by biogeochemical and anthropogenic processes. Cont. Shelf Res. 148, 64–88.
Meunier, J.D., Riotte, J., Braun, J.J., Sekhar, M., Chalié, F., Barboni, D., Saccone, L., 2015. Controls of DSi in streams and reservoirs along the Kaveri River, South India. Sci. Total Environ. 502, 103–113.
Mukherjee, A., Saha, D., Harvey, C.F., Taylor, R.G., Ahmed, K.M., Bhanja, S.N., 2015. Groundwater systems of the Indian Sub-Continent. J. Hydrol. 4, 1–14. https://doi.org/10.1016/J.EJRH.2015.03.005.
Naqvi, S.M., Rogers, J.W., 1987. Precambrian Geology of India. Clarendon Press, Oxford University Press, New York.
Opfergelt, S., Delmelle, P., 2012. Silicon isotopes and continental weathering processes: Assessing controls on Si transfer to the ocean. Compt. Rendus Geosci. 344, 723–738.
Pacheco, F., van der Weijden, C.H., 1996. Contributions of Water-Rock Interactions to the Composition of Groundwater in Areas with a Sizeable Anthropogenic Input: a Case Study of the Waters of the Fundão Area, Central Portugal. Water Resour. Res. 32, 3553–3570. https://doi.org/10.1029/96WR01683.
Pattanaik, J.K., Balakrishnan, S., Bhutani, R., Singh, P., 2007. Chemical and strontium isotopic composition of Kaveri, Palar and Ponnaiyar rivers: Significance to weathering of granulites and granitic gneisses of southern Peninsular India. Curr. Sci. 93 (4), 523–531.
Pattanaik, J.K., Balakrishnan, S., Bhutani, R., Singh, P., 2013. Estimation of weathering rates and CO2 drawdown based on solute load: significance of granulites and gneisses dominated weathering in the Kaveri River basin, Southern India. Geochim. Cosmochim. Acta 121, 611–636.
Poitrasson, F., 2017. Silicon isotope geochemistry. Rev. Mineral. Geochem. 82, 289–344.
Reynolds, B.C., Aggarwal, J., André, L., Baxter, D., Beucher, C., Brzezinski, M.A., Engström, E., Georg, R.B., Land, M., Leng, M.J., Opfergelt, S., Rodushkin, I., Sloane, H.J., van den Boorn, S.H.J.M., Vroon, P.Z., Cardinal, D., 2007. An inter-laboratory comparison of Si isotope reference materials. J. Anal. At. Spectrom. 22, 561–568. Available at: https://pubs.rsc.org/en/content/articlehtml/2007/ja/b616755a.
Reynolds, B.C., Georg, R.B., Oberli, F., Wiechert, U., Halliday, A.N., 2006. Re-assessment of silicon isotope reference materials using high-resolution multi-collector ICP-MS. J. Anal. At. Spectrom. 21, 266–269. https://doi.org/10.1039/B515908C.
Riotte, J., Meunier, J.D., Zambardi, T., Audry, S., Barboni, D., Anupama, K., Prasad, S., Chmeleff, J., Poitrasson, F., Sekhar, M., Braun, J.J., 2018a. Processes controlling silicon isotopic fractionation in a forested tropical watershed: Mule Hole critical Zone Observatory (Southern India). Geochim. Cosmochim. Acta 228, 301–319.
Riotte, J., Sandhya, K., Prakash, N.B., Audry, S., Zambardi, T., Chmeleff, J., Buvaneshwari, S., Meunier, J.D., 2018b. Origin of silica in rice plants and contribution of diatom Earth fertilization: insights from isotopic Si mass balance in a paddy field. Plant Soil 423, 481–501.
Sarma, V.V.S.S., Gupta, S.N.M., Babu, P.V.R., Acharya, T., Harikrishnachari, N., Vishnuvardhan, K., Rao, N.S., Reddy, N.P.C., Sarma, V.V., Sadhuram, Y., Murty, T.V. R., Kumar, M.D., 2009. Influence of river discharge on plankton metabolic rates in the tropical monsoon driven Godavari estuary, India. Estuar. Coast. Shelf Sci. 85, 515–524.
Savage, P.S., Georg, R.B., Williams, H.M., Turner, S., Halliday, A.N., Chappell, B.W., 2012. The silicon isotope composition of granites. Geochim. Cosmochim. Acta 92, 184–202.
Savage, P.S., Georg, R.B., Williams, H.M., Halliday, A.N., 2013. The silicon isotope composition of the upper continental crust. Geochim. Cosmochim. Acta 109, 384–399.
Schaller, J., Puppe, D., Kaczorek, D., Ellerbrock, R., Sommer, M., 2021. Silicon cycling in soils revisited. Plants 10, 295. Available at: https://www.mdpi.com/2223-7747/10/2/295.
Shadakshara Swamy, N., Jayananda, M., Janardhan, A.S., 1995. Geochemistry of Gundlupet gneisses, Southern Karnataka: A 2.5 Ga old reworked sialic crust. In: India as a Fragment of East Gondwana. Gondwana Research Group.
Struyf, E., Smis, A., Van Damme, S., Garnier, J., Govers, G., Van Wesemael, B., Conley, D. J., Batelaan, O., Frot, E., Clymans, W., Vandevenne, F., Lancelot, C., Goos, P., Meire, P., 2010. Historical land use change has lowered terrestrial silica mobilization. Nat. Commun. 1, 1–7.
Sutton, J.N., André, L., Cardinal, D., Conley, D.J., De Souza, G.F., Dean, J., Dodd, J., Ehlert, C., Ellwood, M.J., Frings, P.J., Grasse, P., Hendry, K., Leng, M.J., Michalopoulos, P., Panizzo, V.N., Swann, G.E.A., 2018. A review of the stable isotope bio-geochemistry of the global silicon cycle and its associated trace elements. Front. Earth Sci. 5, 112.
Tardy, Y., 1971. Characterization of the principal weathering types by the geochemistry of waters from some European and African crystalline massifs. Chem. Geol. 7, 253–271.
Thiry, M., 2000. Palaeoclimatic interpretation of clay minerals in marine deposits: an outlook from the continental origin. Earth Sci. Rev. 49, 201–221. https://doi.org/10.1016/S0012-8252(99)00054-9.
Tréguer, P.J., Sutton, J.N., Brzezinski, M., Charette, M.A., Devries, T., Dutkiewicz, S., Ehlert, C., Hawkings, J., Leynaert, A., Liu, S.M., Monferrer, N.L., López-Acosta, M., Maldonado, M., Rahman, S., Ran, L., Rouxel, O., 2021. Reviews and syntheses: the biogeochemical cycle of silicon in the modern ocean. Biogeosciences 18, 1269–1289. https://doi.org/10.5194/BG-18-1269-2021.
Vandevenne, F., Struyf, E., Clymans, W., Meire, P., 2012. Agricultural silica harvest: have humans created a new loop in the global silica cycle? Front. Ecol. Environ. 10, 243–248. Available at: http://doi.wiley.com/10.1890/110046.
Violette, A., Goddéris, Y., Maréchal, J.C., Riotte, J., Oliva, P., Kumar, M.S.M., Sekhar, M., Braun, J.J., 2010. Modelling the chemical weathering fluxes at the watershed scale in the Tropics (Mule Hole, South India): Relative contribution of the smectite/kaolinite assemblage versus primary minerals. Chem. Geol. 277, 42–60. https://doi.org/10.1016/J.CHEMGEO.2010.07.009.
WRIS, 2014. Kaveri Basin Report: Gov. of India - MoWR, 141.
Zabowski, D., Ugolini, F.C., 1992. Seasonality in the mineral stability of a subalpine Spodosol. Soil Sci. 154 (6), 497–507.

Bibliography

Abraham K., Opfergelt S., Fripiat F., Cavagna A. J., de Jong J. T. M., Foley S. F., André L. and Cardinal D. (2008) δ^{30}Si and δ^{29}Si Determinations on USGS BHVO-1 and BHVO-2 Reference Materials with a New Configuration on a Nu Plasma Multi-Collector ICP-MS. *Geostand. Geoanalytical Res.* 32, 193–202.

Acharya S. S., Hishamunda V. and Chakrabarti R. (2022) Natural Sources and anthropogenic Influences on the River Water and Groundwater Chemistry of the Lower Mahanadi Basin: Insights From Radiogenic Sr Isotopes and Major Ion Chemistry. *Front. Water* 4, 38.

Acharyya T., Sarma V. V. S. S., Sridevi B., Venkataramana V., Bharathi M. D., Naidu S. A., Kumar B. S. K., Prasad V. R., Bandyopadhyay D., Reddy N. P. C. and Kumar M. D. (2012) Reduced river discharge intensifies phytoplankton bloom in Godavari estuary, India. *Mar. Chem*. 132–133, 15–22.

Alkhatib M., Alkhatib S., Qurie M. and Qutob M. (2022) Calcium isotope fractionation during the partial dissolution of artificial calcite. *J. Sea Res.* 190, 102301.

Alleman L. Y., Cardinal D., Cocquyt C., Plisnier P. D., Descy J. P., Kimirei I., Sinyinza D. and André L. (2005) Silicon isotopic fractionation in Lake Tanganyika and its main tributaries. *J. Great Lakes Res*. 31, 509–519.

Amanambu A. C., Obarein O. A., Mossa J., Li L., Ayeni S. S., Balogun O., Oyebamiji A. and Ochege F. U. (2020) Groundwater system and climate change: Present status and future considerations. *J. Hydrol*. 589, 125163.

Ameijeiras-Mariño Y., Opfergelt S., Schoonejans J., Vanacker V., Sonnet P., de Jong J. and Delmelle P. (2017) Impact of low denudation rates on soil chemical weathering intensity: A multiproxy approach. *Chem. Geol*. 456, 72–84.

Amos S., Gross J. L. and Thoennessen M. (2011) Discovery of the calcium, indium, tin, and platinum isotopes. *At. Data Nucl.* Data Tables 97, 383–402.

Anderson S. P., von Blanckenburg F. and White A. F. (2007) Physical and chemical controls on the critical zone. *Elements* 3, 315–319.

Andersson P. S., Wasserburg G. J., Ingri J. and Stordal M. C. (1994) Strontium dissolved and particulate loads in fresh and brackish waters: The Baltic Sea and Mississippi Delta. *Earth Planet. Sci. Lett.* 124, 195–210.

Anschutz P., Smith T., Mouret A., Deborde J., Bujan S., Poirier D. and Lecroart P. (2009) Tidal sands as biogeochemical reactors. *Estuar. Coast. Shelf Sci.* 84, 84–90.

Appelo C. A. J. and Postma D. (2004) Geochemistry, groundwater and pollution, second edition. Geochemistry, Groundw. Pollution, Second Ed., 1–649.

Babu D. S. S., Khandekar A., Bhagat C., Singh A., Jain V., Verma M., Bansal B. K. and Kumar M. (2021) Evaluation, effect and utilization of submarine groundwater discharge for coastal population and ecosystem: A special emphasis on Indian coastline. *J. Environ. Manage.* 277, 111362.

Bain D. C. and Bacon J. R. (1994) Strontium isotopes as indicators of mineral weathering in catchments. *CATENA* 22, 201–214.

Banerjee A. and Chakrabarti R. (2018) Large Ca stable isotopic (δ44/40Ca) variation in a hand-specimen sized spheroidally weathered diabase due to selective weathering of clinopyroxene and plagioclase. *Chem. Geol.* 483, 295–303.

Banerjee A., Chakrabarti R. and Mandal S. (2016) Geochemical anatomy of a spheroidally weathered diabase. *Chem. Geol*. 440, 124–138.

Banner R J. L. (1995) Application of the trace element and isotope geochemistry of strontium to studies of carbonate diagenesis. *Sedimentology* 42, 805–824.

Barnes C. J. and Allison G. B. (1983) The distribution of deuterium and ^{18}O in dry soils: 1. Theory. *J. Hydrol*. 60, 141–156.

Baronas J. J., Hammond D. E., Berelson W. M., McManus J. and Severmann S. (2016) Germanium–silicon fractionation in a river-influenced continental margin: The Northern Gulf of Mexico. *Geochim. Cosmochim. Acta* 178, 124–142.

Baronas J. J., Hammond D. E., McManus J., Wheat C. G. and Siebert C. (2017) A global Ge isotope budget. *Geochim. Cosmochim. Acta* 203, 265–283.

Baronas J. J., Torres M. A., West A. J., Rouxel O., Georg B., Bouchez J., Gaillardet J. and Hammond D. E. (2018) Ge and Si isotope signatures in rivers: A quantitative multi-proxy approach. *Earth Planet. Sci. Lett.* 503, 194–215.

Baronas J. J., West A. J., Burton K. W., Hammond D. E., Opfergelt S., Pogge von Strandmann P. A. E., James R. H. and Rouxel O. J. (2020) Ge and Si Isotope Behavior During Intense Tropical Weathering and Ecosystem Cycling. *Global Biogeochem. Cycles* 34, e2019GB006522.

Basu A. R., Jacobsen S. B., Poreda R. J., Dowling C. B. and Aggarwal P. K. (2001) Large groundwater strontium flux to the oceans from the bengal basin and the marine strontium isotope record. *Science* (80-.). 293, 1470–1473.

Beane J. E., Turner C. A., Hooper P. R., Subbarao K. V. and Walsh J. N. (1986) Stratigraphy, composition and form of the Deccan Basalts, Western Ghats, India. *Bull. Volcanol.* 1986 481 48, 61–83.

Beck A. J., Charette M. A., Cochran J. K., Gonneea M. E. and Peucker-Ehrenbrink B. (2013) Dissolved strontium in the subterranean estuary – Implications for the marine strontium isotope budget. *Geochim. Cosmochim. Acta* 117, 33–52.

Berner R. A. and Berner E. K. (1997) Silicate Weathering and Climate. *Tecton. Uplift Clim. Chang.*, 353–365.

Berner R. A., Lasaga A. C. and Garrels R. M. (1983) Carbonate-silicate geochemical cycle and its effect on atmospheric carbon dioxide over the past 100 million years. Am. J. Sci.; (United States) 283:7, 641–683.

Bernstein L. R. (1985) Germanium geochemistry and mineralogy. *Geochim. Cosmochim. Acta* 49, 2409–2422.

Bhaduri A., Amarasinghe U. and Shah T. (2012) An analysis of groundwater irrigation expansion in India. *Int. J. Environ. Waste Manag.* 9, 372–387.

Bharathi M. D., Sarma V. V. S. S. and Ramaneswari K. (2018) Intra-annual variations in phytoplankton biomass and its composition in the tropical estuary: Influence of river discharge. *Mar Pollut Bull* 129, 14–25.

Bharathi M. D., Venkataramana V. and Sarma V. V. S. S. (2022) Phytoplankton community structure is governed by salinity gradient and nutrient composition in the tropical estuarine system. *Cont. Shelf Res.* 234, 104643.

Bhattacharya S., Chaudhary A. K. and Basei M. (2012) Original nature and source of khondalites in the Eastern Ghats Province, India. *Geol. Soc. Spec. Publ.* 365, 147–159.

Bickle M. J., Chapman H. J., Bunbury J., Harris N. B. W., Fairchild I. J., Ahmad T. and Pomiès C. (2005) Relative contributions of silicate and carbonate rocks to riverine Sr fluxes in the headwaters of the Ganges. *Geochim. Cosmochim. Acta* 69, 2221–2240.

Biksham G. and Subramanian V. (1988) Nature of solute transport in the Godavari Basin, India. *J. Hydrol.* 103, 375–392.

Biswas H., Cros A., Yadav K., Ramana V. V., Prasad V. R., Acharyya T. and Babu P. V. R. (2011) The response of a natural phytoplankton community from the Godavari River Estuary to increasing CO2 concentration during the pre-monsoon period. *J. Exp. Mar. Bio. Ecol.* 407, 284–293.

Blecker S. W., King S. L., Derry L. A., Chadwick O. A., Ippolito J. A. and Kelly E. F. (2007) The ratio of germanium to silicon in plant phytoliths: Quantification of biological discrimination under controlled experimental conditions. *Biogeochemistry* 86, 189–199.

Blum J. D., Erel Y. and Brown K. (1993) $^{87}Sr/^{86}Sr$ ratios of sierra nevada stream waters: Implications for relative mineral weathering rates. *Geochim. Cosmochim. Acta* 57, 5019–5025.

Bouchez J., Von Blanckenburg F. and Schuessler J. A. (2013) Modeling novel stable isotope ratios in the weathering zone. *Am. J. Sci.* 313, 267–308.

Boulton G. S., Caban P. E. and Van Gijssel K. (1995) Groundwater flow beneath ice sheets: Part I — Large scale patterns. *Quat. Sci. Rev.* 14, 545–562.

Brantley S. L., Chesley J. T. and Stillings L. L. (1998) Isotopic ratios and release rates of strontium measured from weathering feldspars. *Geochim. Cosmochim. Acta* 62, 1493–1500.

Brantley S. L., Goldhaber M. B. and Vala Ragnarsdottir K. (2007) Crossing Disciplines and Scales to Understand the Critical Zone. *Elements* 3, 307–314.

Brantley S. L., McDowell W. H., Dietrich W. E., White T. S., Kumar P., Anderson S. P., Chorover J., Ann Lohse K., Bales R. C., Richter D. D., Grant G. and Gaillardet J. (2017) Designing a network of critical zone observatories to explore the living skin of the terrestrial *Earth. Earth Surf. Dyn.* 5, 841–860.

Brantley S. L., Megonigal J. P., Scatena F. N., Balogh-Brunstad Z., Barnes R. T., Bruns M. A., Van Cappellen P., Dontsova K., Hartnett H. E., Hartshorn A. S., Heimsath A., Herndon E., Jin L., Keller C. K., Leake J. R., Mcdowell W. H., Meinzer F. C., Mozdzer T. J., Petsch S., Pett-Ridge J., Pregitzer K. S., Raymond P. A., Riebe C. S., Shumaker K., Sutton-Grier A., Walter R. and Yoo K. (2011) Twelve testable hypotheses on the geobiology of weathering. *Geobiolog*y 9, 140–165.

Bratton J. F. (2010) The three scales of submarine groundwater flow and discharge across passive continental margins. *J. Geol.* 118, 565–575.

Braun J. J., Descloitres M., Riotte J., Fleury S., Barbiéro L., Boeglin J. L., Violette A., Lacarce E., Ruiz L., Sekhar M., Mohan Kumar M. S., Subramanian S. and Dupré B. (2009) Regolith mass balance inferred from combined mineralogical, geochemical and geophysical studies: Mule Hole gneissic watershed, South India. *Geochim. Cosmochim. Acta* 73, 935–961.

Brazier J. M., Schmitt A. D., Gangloff S., Pelt E., Chabaux F. and Tertre E. (2019) Calcium isotopic fractionation during adsorption onto and desorption from soil phyllosilicates (kaolinite, montmorillonite and muscovite). *Geochim. Cosmochim. Acta* 250, 324–347.

Broecker W. S. (1971) A kinetic model for the chemical composition of sea water. *Quat. Res. 1, 188–207.*

Broecker W. S. (1997) Thermohaline circulation, the achilles heel of our climate system: Will man-made CO2 upset the current balance? *Science* (80-.). 278, 1582–1588.

Broecker W. S. and Peng T. (1982) Tracers in the Sea., Eldigio Press, New York. 700pp

Burnett W. C., Aggarwal P. K., Aureli A., Bokuniewicz H., Cable J. E., Charette M. A., Kontar E., Krupa S., Kulkarni K. M., Loveless A., Moore W. S., Oberdorfer J. A., Oliveira J., Ozyurt N., Povinec P., Privitera A. M. G., Rajar R., Ramessur R. T., Scholten J., Stieglitz T., Taniguchi M. and Turner J. V. (2006) Quantifying submarine groundwater discharge in the coastal zone via multiple methods. *Sci. Total Environ.* 367, 498–543.

Burnett W. C., Bokuniewicz H., Huettel M., Moore W. S. and Taniguchi M. (2003) Groundwater and pore water inputs to the coastal zone. *Biogeochem.* 2003 661 66, 3–33.

Burton J. H. (2017) Strontium isotopes. Encycl. Earth Sci. Ser., 916–919.

Buvaneshwari S., Riotte J., Sekhar M., Sharma A. K., Helliwell R., Kumar M. S. M., Braun J. J. and Ruiz L. (2020) Potash fertilizer promotes incipient salinization in groundwater irrigated semi-arid agriculture. *Sci. Rep.* 10, 1–14.

Buvaneshwari S., Sekhar M., Mohan Kumar M. S., Giriraja P. R., Buvaneshwari S., Riotte J., Sekhar M., Mohan Kumar M. S., Sharma A. K., Duprey J. L., Praveenkumarreddy Y., Moger H., Braun J. J., Ruiz L., Riotte J., Audry S., Braun J. J., Durand P., Ruiz L. and Sharma A. K. (2017) Groundwater resource vulnerability and spatial variability of nitrate contamination: Insights from high density tubewell monitoring in a hard rock aquifer. Sci. Total Environ. 579, 838–847.

C. Unnikrishnan Warrier, M. Praveen Babu, P. Manjula, K. T. Velayudhan, A. Shahul Hameed and K. Vasu (2010) Isotopic characterization of dual monsoon precipitation – evidence from Kerala, India on JSTOR. *Curr. Sci.* 98, 1487–1495.

Calmels D., Galy A., Hovius N., Bickle M., West A. J., Chen M. C. and Chapman H. (2011) Contribution of deep groundwater to the weathering budget in a rapidly eroding mountain belt, Taiwan. *Earth Planet. Sci. Lett.* 303, 48–58.

Cardinal D., Gaillardet J., Hughes H. J., Opfergelt S. and André L. (2010) Contrasting silicon isotope signatures in rivers from the Congo Basin and the specific behaviour of organic-rich waters. Geophys. Res. Lett. 37.

Cardinal D., Savoye N., Trull T. W., Dehairs F., Kopczynska E. E., Fripiat F., Tison J. L. and André L. (2007) Silicon isotopes in spring Southern Ocean diatoms: Large zonal changes despite homogeneity among size fractions. Mar Chem 106, 46–62.

D. Cardinal, L.Y. Alleman, J. De Jong, K. Ziegler, L. André. (2003) Isotopic composition of silicon measured by multicollector plasma source mass spectrometry in dry plasma mode J. Anal. Atom. Spectrom., 18, 213-218

Carey J. C. and Fulweiler R. W. (2012) The Terrestrial Silica Pump. PLoS One 7, e52932.

Carey J. C. and Fulweiler R. W. (2014) Salt marsh tidal exchange increases residence time of silica in estuaries. Limnol. Oceanogr. 59, 1203–1212.

Carey J. C. and Fulweiler R. W. (2016) Human appropriation of biogenic silicon – the increasing role of agriculture. *Funct. Ecol.* 30, 1331–1339.

Cartwright I., Weaver T. and Petrides B. (2007) Controls on 87Sr/86Sr ratios of groundwater in silicate-dominated aquifers: SE Murray Basin, Australia. Chem. Geol. 246, 107–123.

Cenki-Tok B., Chabaux F., Lemarchand D., Schmitt A. D., Pierret M. C., Viville D., Bagard M. L. and Stille P. (2009) The impact of water-rock interaction and vegetation on calcium isotope fractionation in soil- and stream waters of a small, forested catchment (the Strengbach case). Geochim. Cosmochim. Acta 73, 2215–2228.

CGWB (2012) Aquifer systems of India. Ministry of Water Resources. Govt. of India

Chakrabarti R., Mondal S., Acharya S. S., Lekha J. S. and Sengupta D. (2018) Submarine groundwater discharge derived strontium from the Bengal Basin traced in Bay of Bengal water samples. Sci. Reports 2018 81 8, 1–10.

Chakrabarti R., Mondal S., Jacobson A. D., Mills M., Romaniello S. J. and Vollstaedt H. (2021) Review of techniques, challenges, and new developments for calcium isotope ratio measurements. Chem. Geol. 581, 120398.

Chester R. (1990) The transport of material to the oceans: the river pathway. Mar. Geochemistry, 14–82.

Chester R. and Jickells T. (2012) Marine Geochemistry. Springer Dordrecht. 702pp.

Chitra-Tarak R., Ruiz L., Dattaraja H. S., Mohan Kumar M. S., Riotte J., Suresh H. S., McMahon S. M. and Sukumar R. (2018) The roots of the drought: Hydrology and water uptake strategies mediate forest-wide demographic response to precipitation. *J. Ecol.* 106, 1495–1507.

Cho H. M., Kim G., Kwon E. Y., Moosdorf N., Garcia-Orellana J. and Santos I. R. (2018) Radium tracing nutrient inputs through submarine groundwater discharge in the global ocean. Sci. Reports 2018 81 8, 1–7.

Chorover J., Kretzschmar R., Garica-Pichel F. and Sparks D. L. (2007) Soil biogeochemicial processes within the critical zone. Elements 3, 321–326.

Clark, I.D., 2015 Groundwater geochemistry and isotopes, first ed. CRC Press, Boca Raton.

Closset I., Cardinal D., Rembauville M., Thil F. and Blain S. (2016) Unveiling the Si cycle using isotopes in an iron-fertilized zone of the Southern Ocean: From mixed-layer supply to export. Biogeosciences 13, 6049–6066.

Cobert F., Schmitt A. D., Bourgeade P., Labolle F., Badot P. M., Chabaux F. and Stille P. (2011) Experimental identification of Ca isotopic fractionations in higher plants. Geochim. Cosmochim. Acta 75, 5467–5482.

Conley D. J., Humborg C., Smedberg E., Rahm L., Papush L., Danielsson Å., Clarke A., Pastuszak M., Aigars J., Ciuffa D. and Mörth C. M. (2008) Past, present and future state of the biogeochemical Si cycle in the Baltic Sea. *J. Mar. Syst.* 73, 338–346.

Coplen T. B. (2011) Guidelines and recommended terms for expression of stable-isotope-ratio and gas-ratio measurement results. Rapid Commun. Mass Spectrom. 25, 2538–2560.

Coplen T. B., Böhlke J. K., De Bièvre P., Ding T., Holden N. E., Hopple J. A., Krouse H. R., Lamberty A., Peiser H. S., Révész K., Rieder S. E., Rosman K. J. R., Roth E., Taylor P. D. P., Vocke R. D. and Xiao Y. K. (2002) Isotope-abundance variations of selected elements (IUPAC technical report). Pure Appl. Chem. 74, 1987–2017.

Cornelis J. T., Delvaux B., Cardinal D., André L., Ranger J. and Opfergelt S. (2010) Tracing mechanisms controlling the release of dissolved silicon in forest soil solutions using Si isotopes and Ge/Si ratios. Geochim. Cosmochim. Acta 74, 3913–3924.

Cornelis J. T., Delvaux B., Georg R. B., Lucas Y., Ranger J. and Opfergelt S. (2011) Tracing the origin of dissolved silicon transferred from various soil-plant systems towards rivers: A review. *Biogeosciences* 8, 89–112.

Cornelis J. T., Weis D., Lavkulich L., Vermeire M. L., Delvaux B. and Barling J. (2014) Silicon isotopes record dissolution and re-precipitation of pedogenic clay minerals in a podzolic soil chronosequence. Geoderma 235–236, 19–29.

Crossland C. J., Baird D., Ducrotoy J.-P., Lindeboom H., Buddemeier R. W., Dennison W. C., Maxwell B. A., Smith S. V. and Swaney D. P. (2005) The Coastal Zone — a Domain of Global Interactions., 1–37.

Cuthbert M. O., Gleeson T., Moosdorf N., Befus K. M., Schneider A., Hartmann J. and Lehner B. (2019) Global patterns and dynamics of climate–groundwater interactions. Nat. Clim. Chang. 2019 92 9, 137–141.

Dai, A., & Trenberth, K. E. (2002). Estimates of freshwater discharge from continents: Latitudinal and seasonal variations. Journal of Hydrometeorology, 3(6), 660–687.

Dalin C., Wada Y., Kastner T. and Puma M. J. (2017) Groundwater depletion embedded in international food trade. Nat. 2017 5437647 543, 700–704.

Damodararao K. and Singh S. K. (2022) Substantial submarine groundwater discharge in the estuaries of the east coast of India and its impact on marine strontium budget. Geochim. Cosmochim. Acta 324, 66–85.

Danish M., Tripathy G. R. and Rahaman W. (2020) Submarine groundwater discharge to a tropical coastal lagoon (Chilika lagoon, India): An estimation using Sr isotopes. Mar. Chem. 224, 103816.

Das A., Krishnaswami S., Sarin M. M. and Pande K. (2005) Chemical weathering in the Krishna Basin and Western Ghats of the Deccan Traps, India: Rates of basalt weathering and their controls. Geochim. Cosmochim. Acta 69, 2067–2084.

Dauphas N. and Schauble E. A. (2016) Mass Fractionation Laws, Mass-Independent Effects, and Isotopic Anomalies. Annual Reviews of Earth and Planetary Sciences, 44, 709–783.

Davis A. C., Bickle M. J. and Teagle D. A. H. (2003) Imbalance in the oceanic strontium budget. Earth Planet. Sci. Lett. 211, 173–187.

De La Rocha C. L., Brzezinski M. A., DeNiro M. J. and Shemesh A. (1998) Silicon-isotope composition of diatoms as an indicator of past oceanic change. Nat. 1998 3956703 395, 680–683.

De Souza G. F., Reynolds B. C., Rickli J., Frank M., Saito M. A., Gerringa L. J. A. and Bourdon B. (2012) Southern Ocean control of silicon stable isotope distribution in the deep Atlantic Ocean. Global Biogeochem. Cycles 26.

Dellinger M., Gaillardet J. Ô., Bouchez J., Calmels D., Galy V., Hilton R. G., Louvat P. and France-Lanord C. (2014) Lithium isotopes in large rivers reveal the cannibalistic nature of modern continental weathering and erosion. *Earth Planet. Sci. Lett*. 401, 359–372.

Delstanche S., Opfergelt S., Cardinal D., Elsass F., André L. and Delvaux B. (2009) Silicon isotopic fractionation during adsorption of aqueous monosilicic acid onto iron oxide. *Geochim. Cosmochim. Acta* 73, 923–934.

Delvaux C., Cardinal D., Carbonnel V., Chou L., Hughes H. J. and André L. (2013) Controls on riverine δ^{30}Si signatures in a temperate watershed under high anthropogenic pressure (Scheldt — Belgium). *J. Mar. Syst*. 128, 40–51.

Delvigne C., Opfergelt S., Cardinal D., Delvaux B. and André L. (2009) Distinct silicon and germanium pathways in the soil-plant system: Evidence from banana and horsetail. J. Geophys. Res. *Biogeosciences* 114.

Demarest M. S., Brzezinski M. A. and Beucher C. P. (2009) Fractionation of silicon isotopes during biogenic silica dissolution. *Geochim. Cosmochim. Acta* 73, 5572–5583.

DeMaster D. J. (2002) The accumulation and cycling of biogenic silica in the Southern Ocean: revisiting the marine silica budget. *Deep Sea Res.* Part II Top. Stud. Oceanogr. 49, 3155–3167.

Derry L. A., Kurtz A. C., Ziegler K. and Chadwick O. A. (2005) Biological control of terrestrial silica cycling and export fluxes to watersheds. *Nature* 433, 728–731.

Dewandel B., Gandolfi J. M., de Condappa D. and Ahmed S. (2008) An efficient methodology for estimating irrigation return flow coefficients of irrigated crops at watershed and seasonal scale. *Hydrol. Process*. 22, 1700–1712.

Dewandel B., Lachassagne P., Wyns R., Maréchal J. C. and Krishnamurthy N. S. (2006) A generalized 3-D geological and hydrogeological conceptual model of granite aquifers controlled by single or multiphase weathering. *J. Hydrol.* 330, 260–284.

Dhana Laskhmi D. and Satyanarayana A. N. V. (2020) Climatology of landfalling atmospheric Rivers and associated heavy precipitation over the Indian coastal regions. *Int. J. Climatol.* 40, 5616–5633.

Ding T. P., Tian S. H., Sun L., Wu L. H., Zhou J. X. and Chen Z. Y. (2008) Silicon isotope fractionation between rice plants and nutrient solution and its significance to the study of the silicon cycle. *Geochim. Cosmochim. Acta* 72, 5600–5615.

Ding T. P., Zhou J. X., Wan D. F., Chen Z. Y., Wang C. Y. and Zhang F. (2008) Silicon isotope fractionation in bamboo and its significance to the biogeochemical cycle of silicon. *Geochim. Cosmochim. Acta* 72, 1381–1395.

Ding T.P. (1996) Silicon isotope geochemistry. Geological Publishing House (Beijing), 125pp.

Ding, T., Wan, D., & Zhang, F. (2004). Silicon isotope compositions of dissolved silicon and suspended matter in the Yangtze River, China. *Geochim. Cosmochim. Acta*, 68(2), 205–216

Döll P. and Fiedler K. (2008) Global-scale modeling of groundwater recharge. *Hydrol. Earth Syst. Sci.* 12, 863–885.

Druhan J. L., Steefel C. I., Williams K. H. and DePaolo D. J. (2013) Calcium isotope fractionation in groundwater: Molecular scale processes influencing field scale behavior. *Geochim. Cosmochim. Acta* 119, 93–116.

Duque C., Michael H. A. and Wilson A. M. (2020) The Subterranean Estuary: Technical Term, Simple Analogy, or Source of Confusion? *Water Resour. Res.* 56, e2019WR026554.

Edmond J. M. (1992) Himalayan tectonics, weathering processes, and the strontium isotope record in marine limestones. *Science* (80-.). 258, 1594–1597.

Ehlert C., Doering K., Wallmann K., Scholz F., Sommer S., Grasse P., Geilert S. and Frank M. (2016b) Stable silicon isotope signatures of marine pore waters – Biogenic opal dissolution versus authigenic clay mineral formation. *Geochim. Cosmochim. Acta* 191, 102–117.

Ehlert C., Reckhardt A., Greskowiak J., Liguori B. T. P., Böning P., Paffrath R., Brumsack H. J. and Pahnke K. (2016a) Transformation of silicon in a sandy beach ecosystem: Insights from stable silicon isotopes from fresh and saline groundwaters. *Chem. Geol.* 440, 207–218.

Elderfield H. and Schultz A. (2003) Mid-Ocean Ridge Hydrothermal Fluxes and the Chemical Composition of the Ocean. *Annu. Rev. Earth Planet. Sci.* 24, 191–224.

Ellwood M. J. and Maher W. A. (2003) Germanium cycling in the waters across a frontal zone: the Chatham Rise, New Zealand. *Mar. Chem.* 80, 145–159.

Epstein E. (2009) Silicon: Its manifold roles in plants. *Ann. Appl. Biol*. 155, 155–160.

Epstein E. and Epstein C. E. (2009) Silicon: its manifold roles in plants. *Ann. Appl. Biol*. 155, 155–160.

Famiglietti J. S. (2014) The global groundwater crisis. *Nat. Clim. Chang*. 2014 411 4, 945–948.

Fan Y. (2015) Groundwater in the Earth's critical zone: Relevance to large-scale patterns and processes. *Water Resour. Res.* 51, 3052–3069.

Fan Y., Li H. and Miguez-Macho G. (2013) Global patterns of groundwater table depth. *Science* (80-.). 339, 940–943.

Fantle M. S. and Tipper E. T. (2014) Calcium isotopes in the global biogeochemical Ca cycle: Implications for development of a Ca isotope proxy. *Earth-Science Rev*. 129, 148–177.

FAO Statistical Yearbook 2013: World Food and Agriculture, (2013) 289 pp.

FAO. (2015). Food and Agriculture Organization of the United Nations. http://faostat.fao.org/

Farmer V. C., Delbos E. and Miller J. D. (2005) The role of phytolith formation and dissolution in controlling concentrations of silica in soil solutions and streams. *Geoderma* 127, 71–79.

Faure G. and Powell J. L. (1972) Strontium Isotope Geology. Springer Berlin, Heidelberg. 189pp.

Faure, G., Principles of isotope geology (1986), John Wiley & Sons: New York, 1986, 141.

Faure, G., (2001) Origin of Igneous Rocks: The Isotopic Evidence., Springer-Verlag, Heidelberg. 496pp

Ferguson G. and Gleeson T. (2012) Vulnerability of coastal aquifers to groundwater use and climate change. *Nat. Clim. Chang.* 2012 25 2, 342–345.

Fernandez N. M., Zhang X. and Druhan J. L. (2019) Silicon isotopic re-equilibration during amorphous silica precipitation and implications for isotopic signatures in geochemical proxies. *Geochim. Cosmochim. Acta* 262, 104–127.

Field C. B., Behrenfeld M. J., Randerson J. T. and Falkowski P. (1998) Primary production of the biosphere: Integrating terrestrial and oceanic components. *Science* (80-.). 281, 237–240.

Field J. P., Breshears D. D., Law D. J., Villegas J. C., López-Hoffman L., Brooks P. D., Chorover J., Barron-Gafford G. A., Gallery R. E., Litvak M. E., Lybrand R. A., McIntosh J. C., Meixner T., Niu G.-Y., Papuga S. A., Pelletier J. D., Rasmussen C. R. and Troch P. A. (2015) Critical Zone Services: Expanding Context, Constraints, and Currency beyond Ecosystem Services. *Vadose Zo*. J. 14, 1–7.

Fischer C., Aubron C., Trouvé A., Sekhar M. and Ruiz L. (2022) Groundwater irrigation reduces overall poverty but increases socioeconomic vulnerability in a semiarid region of southern India. *Sci. Reports 2022* 121 12, 1–16.

Fishman R. M., Siegfried T., Raj P., Modi V. and Lall U. (2011) Over-extraction from shallow bedrock versus deep alluvial aquifers: Reliability versus sustainability considerations for India's groundwater irrigation. *Water Resour.* Res. 47.

Fontorbe G., de La Rocha C. L., Chapman H. J. and Bickle M. J. (2013) The silicon isotopic composition of the Ganges and its tributaries. *Earth Planet Sci Lett* 381, 21–30.

Fraysse F., Pokrovsky O. S., Schott J. and Meunier J. D. (2009) Surface chemistry and reactivity of plant phytoliths in aqueous solutions. Chem. Geol. 258, 197–206.

Frick D. A., Remus R., Sommer M., Augustin J., Kaczorek D. and Von Blanckenburg F. (2020) Silicon uptake and isotope fractionation dynamics by crop species. *Biogeosciences* 17, 6475–6490.

Frings P. J., Clymans W., Fontorbe G., de La Rocha C. L. and Conley D. J. (2016) The continental Si cycle and its impact on the ocean Si isotope budget. *Chem Geol* 425, 12–36.

Frings P. J., Clymans W., Fontorbe G., Gray W., Chakrapani G., Conley D. J. and De La Rocha C. (2015) Silicate weathering in the Ganges alluvial plain. *Earth Planet. Sci. Lett*. 427, 136–148.

Frings P. J., De La Rocha C., Struyf E., van Pelt D., Schoelynck J., Hudson M. M., Gondwe M. J., Wolski P., Mosimane K., Gray W., Schaller J. and Conley D. J. (2014) Tracing silicon cycling in the Okavango Delta, a sub-tropical flood-pulse wetland using silicon isotopes. *Geochim. Cosmochim. Acta* 142, 132–148.

Frings P. J., Oelze M., Schubring F., Frick D. A. and Blanckenburg F. von (2021a) Interpreting silicon isotopes in the Critical Zone. *Am. J. Sci*. 321, 1164–1203.

Frings P. J., Schubring F., Oelze M. and Blanckenburg F. von (2021b) Quantifying biotic and abiotic Si fluxes in the Critical Zone with Ge/Si ratios along a gradient of erosion rates. *Am. J. Sci.* 321, 1204–1245.

Fripiat F., Cavagna A. J., Dehairs F., De Brauwere A., André L. and Cardinal D. (2012) Processes controlling the Si-isotopic composition in the Southern Ocean and application for paleoceanography. *Biogeosciences* 9, 2443–2457.

Fripiat F., Cavagna A. J., Dehairs F., Speich S., André L. and Cardinal D. (2011) Silicon pool dynamics and biogenic silica export in the Southern Ocean inferred from Si-isotopes. *Ocean Sci.* 7, 533–547.

Froelich P. N. and Andreae M. O. (1981) The Marine Geochemistry of Germanium: Ekasilicon. *Science* (80-.). 213, 205–207.

Froelich P. N., Blanc V., Mortlock R. A., Chillrud S. N., Dunstan W., Udomkit A. and Peng T. -H (1992) River Fluxes of Dissolved Silica to the Ocean Were Higher during Glacials: Ge/Si In Diatoms, Rivers, and Oceans. *Paleoceanography* 7, 739–767.

Froelich P. N., Hambrick G. A., Andreae M. O., Mortlock R. A. and Edmond J. M. (1985) The geochemistry of inorganic germanium in natural waters. *J. Geophys. Res. Ocean.* 90, 1133–1141.

Gaillardet J., Braud I., Hankard F., Anquetin S., Bour O., Dorfliger N., Dreuzy J. R. de, Galle S., Galy C., Gogo S., Gourcy L., Habets F., Laggoun F., Longuevergne L., Borgne T. Le, Naaim-Bouvet F., Nord G., Simonneaux V., Six D., Tallec T., Valentin C., Abril G., Allemand P., Arènes A., Arfib B., Arnaud L., Arnaud N., Arnaud P., Audry S., Comte V. B., Batiot C., Battais A., Bellot H., Bernard E., Bertrand C., Bessière H., Binet S., Bodin J., Bodin X., Boithias L., Bouchez J., Boudevillain B., Moussa I. B., Branger F., Braun J. J., Brunet P., Caceres B., Calmels D., Cappelaere B., Celle-Jeanton H., Chabaux F., Chalikakis K., Champollion C., Copard Y., Cotel C., Davy P., Deline P., Delrieu G.,

Demarty J., Dessert C., Dumont M., Emblanch C., Ezzahar J., Estèves M., Favier V., Faucheux M., Filizola N., Flammarion P., Floury P., Fovet O., Fournier M., Francez A. J., Gandois L., Gascuel C., Gayer E., Genthon C., Gérard M. F., Gilbert D., Gouttevin I., Grippa M., Gruau G., Jardani A., Jeanneau L., Join J. L., Jourde H., Karbou F., Labat D., Lagadeuc Y., Lajeunesse E., Lastennet R., Lavado W., Lawin E., Lebel T., Bouteiller C. Le, Legout C., Lejeune Y., Meur E. Le, Moigne N. Le, Lions J., Lucas A., Malet J. P., Marais-Sicre C., Maréchal J. C., Marlin C., Martin P., Martins J., Martinez J. M., Massei N., Mauclerc A., Mazzilli N., Molénat J., Moreira-Turcq P., Mougin E., Morin S., Ngoupayou J. N., Panthou G., Peugeot C., Picard G., Pierret M. C., Porel G., Probst A., Probst J. L., Rabatel A., Raclot D., Ravanel L., Rejiba F., René P., Ribolzi O., Riotte J., Rivière A., Robain H., Ruiz L., Sanchez-Perez J. M., Santini W., Sauvage S., Schoeneich P., Seidel J. L., Sekhar M., Sengtaheuanghoung O., Silvera N., Steinmann M., Soruco A., Tallec G., Thibert E., Lao D. V., Vincent C., Viville D., Wagnon P. and Zitouna R. (2018) OZCAR: The French Network of Critical Zone Observatories. *Vadose Zo. J.* 17, 1–24.

Gaillardet J., Dupré B., Allègre C. J. and Négrel P. (1997) Chemical and physical denudation in the Amazon River Basin. *Chem. Geol.* 142, 141–173.

Gaillardet J., Dupré B., Louvat P. and Allègre C. J. (1999) Global silicate weathering and CO2 consumption rates deduced from the chemistry of large rivers. *Chem. Geol.* 159, 3–30.

Gallinari M., Ragueneau O., Corrin L., DeMaster D. J. and Tréguer P. (2002) The importance of water column processes on the dissolution properties of biogenic silica in deep-sea sediments I. Solubility. *Geochim. Cosmochim. Acta* 66, 2701–2717.

Galloway J. N., Aber J. D., Erisman J. W., Seitzinger S. P., Howarth R. W., Cowling E. B. and Cosby B. J. (2003) The Nitrogen Cascade. *Bioscience* 53, 341–356.

Garnier J., Beusen A., Thieu V., Billen G. and Bouwman L. (2010) N:P:Si nutrient export ratios and ecological consequences in coastal seas evaluated by the ICEP approach. *Global Biogeochem. Cycles* 24.

Geilert S., Vroon P. Z., Roerdink D. L., Van Cappellen P. and van Bergen M. J. (2014) Silicon isotope fractionation during abiotic silica precipitation at low temperatures: Inferences from flow-through experiments. *Geochim. Cosmochim. Acta* 142, 95–114.

Georg R. B., Reynolds B. C., Frank M. and Halliday A. N. (2006) New sample preparation techniques for the determination of Si isotopic compositions using MC-ICPMS. *Chem. Geol.* 235, 95–104.

Georg R. B., Reynolds B. C., Frank M. and Halliday A. N. (2006a) Mechanisms controlling the silicon isotopic compositions of river waters. *Earth Planet. Sci. Lett.* 249, 290–306.

Georg R. B., West A. J., Basu A. R. and Halliday A. N. (2009a) Silicon fluxes and isotope composition of direct groundwater discharge into the Bay of Bengal and the effect on the global ocean silicon isotope budget. *Earth Planet. Sci. Lett.* 283, 67–74.

Georg R. B., Zhu C., Reynolds B. C. and Halliday A. N. (2009b) Stable silicon isotopes of groundwater, feldspars, and clay coatings in the Navajo Sandstone aquifer, Black Mesa, Arizona, USA. *Geochim. Cosmochim. Acta* 73, 2229–2241.

Gleeson T., Befus K. M., Jasechko S., Luijendijk E. and Cardenas M. B. (2015) The global volume and distribution of modern groundwater. *Nat. Geosci.* 2015 92 9, 161–167.

Gleeson T., Wada Y., Bierkens M. F. P. and Van Beek L. P. H. (2012) Water balance of global aquifers revealed by groundwater footprint. *Nat.* 2012 4887410 488, 197–200.

Goldschmidt, V. M., 1926. uber das krystallochemische und geochemische Verhalten des, Germaniums. Die Naturwissenschaften 14, 295-297.

Gopalakrishnan M. and Kulkarni S. A. (2007) Agricultural land drainage in India. Irrig. Drain. 56, S59–S67.

Govind A. V., Behera K., Dash J. K., Balakrishnan S., Bhutani R., Managave S. and Srinivasan R. (2021) Trace element and isotope Geochemistry of Neoarchean carbonate rocks from the Dharwar craton, southern India: Implications for depositional environments and mantle influence on ocean chemistry. *Precambrian Res.* 357, 106137.

Grasse P., Brzezinski M. A., Cardinal D., De Souza G. F., Andersson P., Closset I., Cao Z., Dai M., Ehlert C., Estrade N., François R., Frank M., Jiang G., Jones J. L., Kooijman E., Liu Q., Lu D., Pahnke K., Ponzevera E., Schmitt M., Sun X., Sutton J. N., Thil F., Weis D., Wetzel F., Zhang A., Zhang J. and

Zhang Z. (2017) GEOTRACES inter-calibration of the stable silicon isotope composition of dissolved silicic acid in seawater. J. *Anal. At. Spectrom.* 32,

Grasshoff K., Kremling K. and Ehrhardt M. (2007) Methods of Seawater Analysis: Third, Completely Revised and Extended Edition., Wiley 1–600.

Grasshoff, K., Kremling, K., Ehrhardt, M., 1999. Methods of seawater analysis, 3rd ed. Wiley-VCH, Weinheim, Germany.

Griffith E. M., Schmitt A. D., Andrews M. G. and Fantle M. S. (2020) Elucidating modern geochemical cycles at local, regional, and global scales using calcium isotopes. *Chem. Geol.* 534, 119445.

Grimm C., Mavromatis V., Leis A., Pokrovsky O. S. and Oelkers E. H. (2021) The temporal evolution of the carbon isotope composition of calcite in the presence of cyanobacteria. *Chem. Geol.* 584, 120556.

Gunnell Y. and Bourgeon G. (1997) Soils and climatic geomorphology on the Karnataka plateau, peninsular India. *CATENA* 29, 239–262.

Guo L. and Lin H. (2016) Critical Zone Research and Observatories: Current Status and Future Perspectives. *Vadose Zo.* J. 15, 1–14.

Gupta L. P., Subramanian V. and Ittekkot V. (1997) Biogeochemistry of particulate organic matter transported by the Godavari River, India. *Biogeochem*. 1997 382 38, 103–128.

Gussone N., Böhm F., Eisenhauer A., Dietzel M., Heuser A., Teichert B. M. A., Reitner J., Wörheide G. and Dullo W. C. (2005) Calcium isotope fractionation in calcite and aragonite. *Geochim. Cosmochim. Acta* 69, 4485–4494.

Gussone N., Nehrke G. and Teichert B. M. A. (2011) Calcium isotope fractionation in ikaite and vaterite. *Chem. Geo*l. 285, 194–202.

Gussone N., Schmitt A.-D., Heuser A., Wombacher F., Dietzel M., Tipper E. and Schiller M. (2016) Calcium Stable Isotope Geochemistry, Springer Berlin, Heidelberg.

Hammond D. E., McManus J. and Berelson W. M. (2004) Oceanic germanium/silicon ratios: Evaluation of the potential overprint of temperature on weathering signals. *Paleoceanography* 19.

Hans Wedepohl K. (1995) The composition of the continental crust. *Geochim. Cosmochim. Acta* 59, 1217–1232.

Harpold A. A., Lyon S. W. and Marshall J. A. (2014) Using Lidar to Advance Critical Zone Science. Eos, *Trans. Am. Geophys. Union* 95, 364–364.

He H. tao, Zhang S., Zhu C. and Liu Y. (2016) Equilibrium and kinetic Si isotope fractionation factors and their implications for Si isotope distributions in the Earth's surface environments. *Acta Geochim.* 35, 15–24.

Hendry K. R. and Robinson L. F. (2012) The relationship between silicon isotope fractionation in sponges and silicic acid concentration: Modern and core-top studies of biogenic opal. *Geochim Cosmochim Acta* 81, 1–12.

Hindshaw R. S., Reynolds B. C., Wiederhold J. G., Kretzschmar R. and Bourdon B. (2011) Calcium isotopes in a proglacial weathering environment: Damma glacier, Switzerland. *Geochim. Cosmochim. Acta* 75, 106–118.

Holmden C. and Bélanger N. (2010) Ca isotope cycling in a forested ecosystem. *Geochim. Cosmochim. Acta* 74, 995–1015.

Holmden C., Papanastassiou D. A., Blanchon P. and Evans S. (2012) δ44/40Ca variability in shallow water carbonates and the impact of submarine groundwater discharge on Ca-cycling in marine environments. *Geochim. Cosmochim. Acta* 83, 179–194.

Hu R. Z., Qi H. W., Zhou M. F., Su W. C., Bi X. W., Peng J. T. and Zhong H. (2009) Geological and geochemical constraints on the origin of the giant Lincang coal seam-hosted germanium deposit, Yunnan, SW China: *A review. Ore Geol. Rev*. 36, 221–234.

Huang S., Farkaš J. and Jacobsen S. B. (2010) Calcium isotopic fractionation between clinopyroxene and orthopyroxene from mantle peridotites. *Earth Planet. Sci. Lett.* 292, 337–344.

Hughes H. J., Delvigne C., Korntheuer M., De Jong J., André L. and Cardinal D. (2011) Controlling the mass bias introduced by anionic and organic matrices in silicon isotopic measurements by MC-ICP-MS. *J. Anal. At. Spectrom*. 26, 1892–1896.

Hughes H. J., Sondag F., Santos R. V., André L. and Cardinal D. (2013) The riverine silicon isotope composition of the Amazon Basin. *Geochim. Cosmochim. Acta* 121, 637–651.

Humborg C., Ittekkot V., Cociasu A. and Bodungen B. V. (1997) Effect of Danube River dam on Black Sea biogeochemistry and ecosystem structure. *Nat.* 1997 3866623 386, 385–388.

Jacobson A. D., Blum J. D., Chamberlain C. P., Poage M. A. and Sloan V. F. (2002) Ca/Sr and Sr isotope systematics of a Himalayan glacial chronosequence: carbonate versus silicate weathering rates as a function of landscape surface age. *Geochim. Cosmochim. Acta* 66, 13–27.

Jacobson A. D., Grace Andrews M., Lehn G. O. and Holmden C. (2015) Silicate versus carbonate weathering in Iceland: New insights from Ca isotopes. *Earth Planet. Sci. Lett.* 416, 132–142.

Jafari H., Sudegi A. and Bagheri R. (2019) Contribution of rainfall and agricultural returns to groundwater recharge in arid areas. J. Hydrol. 575, 1230–1238.

James I. Drever (1997) The Geochemistry of Natural Waters: Surface and Groundwater Environments - James I. Drever - Google Livres., Prentice Hall.

Janardhan A. S. and Vidal P. (1982) Rb-Sr dating of the Gundlupet geniss around Gundlupet, Southern Karnataka. *J. Geol. Soc. India* 23, 578–580.

Jayananda M., Chardon D., Peucat J. J., Tushipokla and Fanning C. M. (2015) Paleo- to Mesoarchean TTG accretion and continental growth in the western Dharwar craton, Southern India: Constraints from SHRIMP U–Pb zircon geochronology, whole-rock geochemistry and Nd–Sr isotopes. *Precambrian Res.* 268, 295–322.

Jeandel C. and Oelkers E. H. (2015) The influence of terrigenous particulate material dissolution on ocean chemistry and global element cycles. *Chem. Geol.* 395, 50–66.

Jha P. K., Tiwari J., Singh U. K., Kumar M. and Subramanian V. (2009) Chemical weathering and associated CO2 consumption in the Godavari river basin, India. *Chem. Geol.* 264, 364–374.

Jiao J. and Post V. (2019) Coastal hydrogeology. Cambridge University Press. 1–403.

Jones M. T., Pearce C. R. and Oelkers E. H. (2012) An experimental study of the interaction of basaltic riverine particulate material and seawater. *Geochim. Cosmochim. Acta* 77, 108–120.

Jones M. T., Pearce C. R., Jeandel C., Gislason S. R., Eiriksdottir E. S., Mavromatis V. and Oelkers E. H. (2012) Riverine particulate material dissolution as a significant flux of strontium to the oceans. *Earth Planet. Sci. Lett.* 355–356, 51–59.

K.L. Rao (1975) India's Water Wealth, its Assessment Uses and Projections Orient Longman New Delhi, 255

Kaiser S., Wagner S., Moschner C., Funke C. and Wiche O. (2020) Accumulation of germanium (Ge) in plant tissues of grasses is not solely driven by its incorporation in phytoliths. Biogeochemistry 148, 49–68.

Kang J. T., Ionov D. A., Liu F., Zhang C. L., Golovin A. V., Qin L. P., Zhang Z. F. and Huang F. (2017) Calcium isotopic fractionation in mantle peridotites by melting and metasomatism and Ca isotope composition of the Bulk Silicate Earth. Earth Planet. Sci. Lett. 474, 128–137.

Karl D. M. and Tien G. (1992) MAGIC: A sensitive and precise method for measuring dissolved phosphorus in aquatic environments. Limnol. Oceanogr. 37, 105–116.

Kasting J. F. and Catling D. (2003) Evolution of a Habitable Planet. Annu. Rev. Astron. Astrophys. 41, 429–463.

Keller C., Guntzer F., Barboni D., Labreuche J. and MEUNIER J. D. (2012) Impact of agriculture on the Si biogeochemical cycle: Input from phytolith studies. *Comptes Rendus Geosci.* 344, 739–746.

King S. L., Froelich P. N. and Jahnke R. A. (2000) Early diagenesis of germanium in sediments of the Antarctic South Atlantic: in search of the missing Ge sink. Geochim. Cosmochim. Acta 64, 1375–1390.

Kumar B. S. K., Sarma V. V. S. S. and Cardinal D. (2022) Tracing terrestrial versus marine sources of dissolved organic carbon in the largest monsoonal Godavari estuary in India using stable carbon isotopes. Estuar. Coast. Shelf Sci. 276, 108004.

Kumar B. S. K., Viswanadham R., Kumari V. R., Rao D. B., Prasad M. H. K., Srinivas N. and Sarma V. V. S. S. (2021) Spatial variations in dissolved inorganic nutrients in the groundwaters along the Indian coast and their export to adjacent coastal waters. Environ. Sci. Pollut. Res. 28, 9173–9191.

Kumar K. R., Pant G. B., Parthasarathy B. and Sontakke N. A. (1992) Spatial and subseasonal patterns of the long-term trends of Indian summer monsoon rainfall. Int. J. Climatol. 12, 257–268.

Kundu S., Khare D. and Mondal A. (2017) Landuse change impact on sub-watersheds prioritization by analytical hierarchy process (AHP). Ecol. Inform. 42, 100–113.

Kurtz A. C., Derry L. A. and Chadwick O. A. (2002) Germanium-silicon fractionation in the weathering environment. Geochim. Cosmochim. Acta 66, 1525–1537.

Kurylyk B. L., MacQuarrie K. T. B. and McKenzie J. M. (2014) Climate change impacts on groundwater and soil temperatures in cold and temperate regions: Implications, mathematical theory, and emerging simulation tools. Earth-Science Rev. 138, 313–334.

Kwon E. Y., Kim G., Primeau F., Moore W. S., Cho H. M., Devries T., Sarmiento J. L., Charette M. A. and Cho Y. K. (2014) Global estimate of submarine groundwater discharge based on an observationally constrained radium isotope model. Geophys Res Lett 41, 8438–8444.

Laluraj C. M., Gopinath G., Dinesh Kumar P. K. and Seralathan P. (2007) Seasonal Variations in Groundwater Chemistry of a Phreatic Coastal and Crystalline Terrain of Central Kerala, India. Environ. Forensics 7, 335–344.

Lazar T. (2003) Taiz, L. and Zeiger, E. Plant physiology. 3rd edn. Ann. Bot. 91, 750.

Lemarchand D., Wasserburg G. J. and Papanastassiou D. A. (2004) Rate-controlled calcium isotope fractionation in synthetic calcite. Geochim. Cosmochim. Acta 68, 4665–4678.

Loucaides S., Van Cappellen P. and Behrends T. (2008) Dissolution of biogenic silica from land to ocean: Role of salinity and pH. Limnol. Oceanogr. 53, 1614–1621.

Lugolobi F., Kurtz A. C. and Derry L. A. (2010) Germanium–silicon fractionation in a tropical, granitic weathering environment. Geochim. Cosmochim. Acta 74, 1294–1308.

Luijendijk E., Gleeson T. and Moosdorf N. (2020) Fresh groundwater discharge insignificant for the world's oceans but important for coastal ecosystems. Nat. Commun. 2020 111 11, 1–12.

Maavara T., Parsons C. T., Ridenour C., Stojanovic S., Dürr H. H., Powley H. R. and Van Cappellen P. (2015) Global phosphorus retention by river damming. Proc. Natl. Acad. Sci. U. S. A. 112, 15603–15608.

MacDonald A. M., Bonsor H. C., Ahmed K. M., Burgess W. G., Basharat M., Calow R. C., Dixit A., Foster S. S. D., Gopal K., Lapworth D. J., Lark R. M., Moench M., Mukherjee A., Rao M. S., Shamsudduha M., Smith L., Taylor R. G., Tucker J., Van Steenbergen F. and Yadav S. K. (2016) Groundwater quality and depletion in the Indo-Gangetic Basin mapped from in situ observations. Nat. Geosci. 2016 910 9, 762–766.

Maher K. (2011) The role of fluid residence time and topographic scales in determining chemical fluxes from landscapes. Earth Planet. Sci. Lett. 312, 48–58.

Mangalaa K. R., Cardinal D., Brajard J., Rao D. B., Sarma N. S., Djouraev I., Chiranjeevulu G., Murty K. N. and Sarma V. V. S. S. (2017) Silicon cycle in Indian estuaries and its control by biogeochemical and anthropogenic processes. Cont Shelf Res 148, 64–88.

Mangalaa Kameswari Rajasekaran. Silicon biogeochemical cycle along the land to ocean continuum: Focus on Indian monsoonal estuaries. Ph.D. thesis. Université Pierre et Marie Curie - Paris VI, 2016. English. ⟨NNT : 2016PA066713⟩. ⟨tel-01958392⟩

Manivannan V. and Elango L. (2019) Seawater intrusion and submarine groundwater discharge along the Indian coast. Environ. Sci. Pollut. Res. 26, 31592–31608.

Maréchal J. C., Varma M. R. R., Riotte J., Vouillamoz J. M., Kumar M. S. M., Ruiz L., Sekhar M. and Braun J. J. (2009) Indirect and direct recharges in a tropical forested watershed: Mule Hole, India. *J. Hydrol.* 364, 272–284.

Martin A., Meredith K., Baker A., Norman M. and Bryan E. (2020) The evolution of stable silicon isotopes in a coastal carbonate aquifer, Rottnest Island, Western Australia. Hydrol. Earth Syst. Sci. Discuss., 1–18.

Maxwell R. M. and Condon L. E. (2016) Connections between groundwater flow and transpiration partitioning. Science (80-.). 353, 377–380.

Mayfield K. K., Eisenhauer A., Santiago Ramos D. P., Higgins J. A., Horner T. J., Auro M., Magna T., Moosdorf N., Charette M. A., Gonneea M. E., Brady C. E., Komar N., Peucker-Ehrenbrink B. and Paytan A. (2021) Groundwater discharge impacts marine isotope budgets of Li, Mg, Ca, Sr, and Ba. Nat. Commun. 2021 121 12, 1–9.

McManus J., Hammond D. E., Cummins K., Klinkhammer G. P. and Berelson W. M. (2003) Diagenetic Ge-Si fractionation in continental margin environments: further evidence for a nonopal Ge sink. Geochim. Cosmochim. Acta 67, 4545–4557.

Meek K., Derry L., Sparks J. and Cathles L. (2016) 87Sr/86Sr, Ca/Sr, and Ge/Si ratios as tracers of solute sources and biogeochemical cycling at a temperate forested shale catchment, central Pennsylvania, USA. Chem. Geol. 445, 84–102.

Méheut M., Lazzeri M., Balan E. and Mauri F. (2009) Structural control over equilibrium silicon and oxygen isotopic fractionation: A first-principles density-functional theory study. Chem Geol 258, 28–37.

Meißner B., Deters P., Srikantappa C. and Köhler H. (2002) Geochronological evolution of the Moyar, Bhavani and Palghat shear zones of southern India: implications for east Gondwana correlations. *Precambrian Res.* 114, 149–175.

Merz M. U. E. (1992) The biology of carbonate precipitation by cyanobacteria. Facies 1992 261 26, 81–101.

Meunier J. D., Riotte J., Braun J. J., Sekhar M., Chalié F., Barboni D. and Saccone L. (2015) Controls of DSi in streams and reservoirs along the Kaveri River, South India. *Sci. Total Environ.* 502, 103–113.

Meybeck M. and Vörösmarty C. (2005) Fluvial filtering of land-to-ocean fluxes: from natural Holocene variations to Anthropocene. Comptes Rendus Geosci. 337, 107–123.

Michael Holly A, Post Vincent E A, Wilson Alicia M, Werner Adrian D, Michael H A, Post V E A, Wilson A M and Werner A D (2017) Science, society, and the coastal groundwater squeeze. Water Resour. Res. 53, 2610–2617.

Michalopoulos P. and Aller R. C. (1995) Rapid Clay Mineral Formation in Amazon Delta Sediments: Reverse Weathering and Oceanic Elemental Cycles. Science (80-.). 270, 614–617.

Michalopoulos P. and Aller R. C. (2004) Early diagenesis of biogenic silica in the Amazon delta: alteration, authigenic clay formation, and storage. Geochim. Cosmochim. Acta 68, 1061–1085.

Milliman J. D. (1993) Production and accumulation of calcium carbonate in the ocean: Budget of a nonsteady state. Global Biogeochem. Cycles 7, 927–957.

Milliman, J. D. (2001), River inputs, in Encyclopedia of Ocean Sciences, edited by J. H. Steele, S. A. Thorpe, and K. K. Turekian, pp. 2419–2427, Academic Press

Mishra D. C. (2011) Long hiatus in Proterozoic sedimentation in India: Vindhyan, Cuddapah and Pakhal Basins — A plate tectonic model. J. Geol. Soc. India 2011 771 77, 17–25.

Mishra V., Asoka A., Vatta K. and Lall U. (2018) Groundwater Depletion and Associated CO2 Emissions in India. Earth's Futur. 6, 1672–1681.

Misra A., Bhagat C. and Kumar M. (2022) Geochemical ratios mediated understanding of estuarine dynamics in submarine groundwater discharge prevalent basaltic aquifer. Mar. Pollut. Bull. 181, 113812.

Misra A., Singh A., Suresh Babu D. S., Jain V., Verma M., Bansal B. K. and Kumar M. (2020) Sediment and Submarine Groundwater Discharge Mediated Arsenic Flux into the Bay of Bengal, India: an Appraisal. Curr. Pollut. Reports 6, 206–216.

Mondal S. and Chakrabarti R. (2018) A novel sample loading method and protocol for monitoring sample fractionation for high precision Ca stable isotope ratio measurements using double-spike TIMS. J. Anal. At. Spectrom. 33, 141–150.

Moore T., Morris K., Blackwell G., Gibson S. and Stebbing A. (1999) An Expert System for Integrated Coastal Zone Management: A Geomorphological Case Study. Mar. Pollut. Bull. 37, 361–370.

Moore W. S. (2010) The Effect of Submarine Groundwater Discharge on the Ocean. *Annual review of marine sciences*, 2, 59–88.

Mortlock R. A. and Frohlich P. N. (1987) Continental weathering of germanium: GeSi in the global river discharge. Geochim. Cosmochim. Acta 51, 2075–2082.

Mortlock R. A., Froelich P. N., Feely R. A., Massoth G. J., Butterfield D. A. and Lupton J. E. (1993) Silica and germanium in Pacific Ocean hydrothermal vents and plumes. Earth Planet. Sci. Lett. 119, 365–378.

Mukherjee A., Saha D., Harvey C. F., Taylor R. G., Ahmed K. M. and Bhanja S. N. (2015) Groundwater systems of the Indian Sub-Continent. J. Hydrol. Reg. Stud. 4, 1–14.

Nagarajan R., Armstrong-Altrin J. S., Sial A. N., Nagendra R. and Ellam R. M. (2014) Carbon, oxygen, and strontium isotope geochemistry of the Proterozoic carbonate rocks, Bhima basin, south India: Implication for diagenesis. Carpathian J. Earth Environ. Sci. 8, 25–38.

Naqvi, S. M., Rogers J. J. W., 1987. Precambrian geology of India, Oxford Univ. Press, Oxford.

National Research Council (NRC). 2001. Basic research opportunities in the earth sciences. National Academies Press, Washington, DC.

Nedwell D. B., Jickells T. D., Trimmer M. and Sanders R. (1999) Nutrients in Estuaries. In Advances in Ecological Research (eds. N. D.B. and R. D.G.). Academic Press Inc. pp. 43–92.

Négrel P., Casanova J. and Aranyossy J. F. (2001) Strontium isotope systematics used to decipher the origin of groundwaters sampled from granitoids: the Vienne Case (France). Chem. Geol. 177, 287–308.

Négrel P., Pauwels H. and Chabaux F. (2018) Characterizing multiple water-rock interactions in the critical zone through Sr-isotope tracing of surface and groundwater. *Appl. Geochemistry* 93, 102–112.

Negrel P., Pauwels H., Dewandel B., Gandolfi J. M., Mascré C. and Ahmed S. (2011) Understanding groundwater systems and their functioning through the study of stable water isotopes in a hard-rock aquifer (Maheshwaram watershed, India). *J. Hydrol.* 397, 55–70.

Négrel P., Petelet-Giraud E. and Widory D. (2004) Strontium isotope geochemistry of alluvial groundwater: a tracer for groundwater resources characterisation. *Hydrol. Earth Syst. Sci.* 8, 959–972.

Nelson C. J., Jacobson A. D. and Weisenberger T. B. (2022) Controls on riverine calcium isotope ratios during basalt weathering in the Skagafjörður watershed, Iceland. Geochim. Cosmochim. Acta 333, 216–241.

Novak M., Holmden C., Farkaš J., Kram P., Hruska J., Curik J., Veselovsky F., Stepanova M., Kochergina Y. V., Erban V., Fottova D., Simecek M., Bohdalkova L., Prechova E., Voldrichova P. and Cernohous V. (2020) Calcium and strontium isotope dynamics in three polluted forest ecosystems of the Czech Republic, Central Europe. Chem. Geol. 536, 119472.

Ockert C., Gussone N., Kaufhold S. and Teichert B. M. A. (2013) Isotope fractionation during Ca exchange on clay minerals in a marine environment. Geochim. Cosmochim. Acta 112, 374–388.

Oelze M., von Blanckenburg F., Bouchez J., Hoellen D. and Dietzel M. (2015) The effect of Al on Si isotope fractionation investigated by silica precipitation experiments. *Chem. Geol.* 397, 94–105.

Oelze M., von Blanckenburg F., Hoellen D., Dietzel M. and Bouchez J. (2014) Si stable isotope fractionation during adsorption and the competition between kinetic and equilibrium isotope fractionation: Implications for weathering systems. Chem. Geol. 380, 161–171.

Opfergelt S. and Delmelle P. (2012) Silicon isotopes and continental weathering processes: Assessing controls on Si transfer to the ocean. Comptes Rendus Geosci. 344, 723–738.

Opfergelt S., Cardinal D., André L., Delvigne C., Bremond L. and Delvaux B. (2010) Variations of δ30Si and Ge/Si with weathering and biogenic input in tropical basaltic ash soils under monoculture. Geochim. Cosmochim. Acta 74, 225–240.

Opfergelt S., Cardinal D., Henriet C., Draye X., André L. and Delvaux B. (2006) Silicon Isotopic Fractionation by Banana (Musa spp.) Grown in a Continuous Nutrient Flow Device. Plant Soil 2006 2851 285, 333–345.

Opfergelt S., Eiriksdottir E. S., Burton K. W., Einarsson A., Siebert C., Gislason S. R. and Halliday A. N. (2011) Quantifying the impact of freshwater diatom productivity on silicon isotopes and silicon fluxes: Lake Myvatn, Iceland. Earth Planet. Sci. Lett. 305, 73–82.

Opfergelt S., Georg R. B., Delvaux B., Cabidoche Y. M., Burton K. W. and Halliday A. N. (2012) Silicon isotopes and the tracing of desilication in volcanic soil weathering sequences, Guadeloupe. Chem. Geol. 326–327, 113–122.

P S V. S., HIMANSHU K. and SUNDERRAJAN K. (2011) India's Groundwater Challenge and the Way Forward . Econ. Polit. Wkly. 46, 37–45.

Palmer M. R. and Edmond J. M. (1992) Controls over the strontium isotope composition of river water. Geochim. Cosmochim. Acta 56, 2099–2111.

Park Y., Kim Y., Park S. K., Shin W. J. and Lee K. S. (2018) Water quality impacts of irrigation return flow on stream and groundwater in an intensive agricultural watershed. Sci. Total Environ. 630, 859–868.

Parkhurst D. L. and Appelo C. A. J. (1999) User's guide to PHREEQC (Version 2): A computer program for speciation, batch-reaction, one-dimensional transport, and inverse geochemical calculations. Water-Resources Investig. Rep.

Parnell A. C., Inger R., Bearhop S. and Jackson A. L. (2010) Source Partitioning Using Stable Isotopes: Coping with Too Much Variation. PLoS One 5, e9672.

Peketi A., Mazumdar A., Pillutla S. P. K., Rai V. K., Sawant B., Chaitanya A. V. S. and krishna R. (2020) Monsoon rainfall and contrasting source rocks influenced sediment composition of peninsular basins along the east coast of India (western Bay of Bengal). Mar. Pet. Geol. 118, 104433.

Peng Z. X., Mahoney J. J., Hooper P. R., Macdougall J. D. and Krishnamurthy P. (1998) Basalts of the northeastern Deccan Traps, India: Isotopic and elemental geochemistry and relation to southwestern Deccan stratigraphy. J. Geophys. Res. Solid Earth 103, 29843–29865.

Perez-Fodich A. and Derry L. A. (2020) A model for germanium-silicon equilibrium fractionation in kaolinite. Geochim. Cosmochim. Acta 288, 199–213.

Pett-Ridge J. C., Derry L. A. and Barrows J. K. (2009) Ca/Sr and 87Sr/86Sr ratios as tracers of Ca and Sr cycling in the Rio Icacos watershed, Luquillo Mountains, Puerto Rico. Chem. Geol. 267, 32–45.

Peucker-Ehrenbrink B. and Fiske G. J. (2019) A continental perspective of the seawater 87Sr/86Sr record: A review. Chem. Geol. 510, 140–165.

Pogge von Strandmann P. A. E., Porcelli D., James R. H., van Calsteren P., Schaefer B., Cartwright I., Reynolds B. C. and Burton K. W. (2014) Chemical weathering processes in the Great Artesian Basin: Evidence from lithium and silicon isotopes. Earth Planet. Sci. Lett. 406, 24–36.

Poitrasson F. (2017) Silicon Isotope Geochemistry. Rev. Mineral. Geochemistry 82, 289–344.

Pokrovski G. S., Martin F., Hazemann J. L. and Jacques Schott (2000) An X-ray absorption fine structure spectroscopy study of germanium-organic ligand complexes in aqueous solution. Chem. Geol. 163, 151–165.

Pokrovsky O. S., Pokrovski G. S., Schott J. and Galy A. (2006) Experimental study of germanium adsorption on goethite and germanium coprecipitation with iron hydroxide: X-ray absorption fine structure and macroscopic characterization. Geochim. Cosmochim. Acta 70, 3325–3341.

Poore J. and Nemecek T. (2018) Reducing food's environmental impacts through producers and consumers. Science (80-.). 360, 987–992.

Presti M. and Michalopoulos P. (2008) Estimating the contribution of the authigenic mineral component to the long-term reactive silica accumulation on the western shelf of the Mississippi River Delta. Cont. Shelf Res. 28, 823–838.

Price J. R., Velbel M. A. and Patino L. C. (2005) Rates and time scales of clay-mineral formation by weathering in saprolitic regoliths of the southern Appalachians from geochemical mass balance. *GSA Bull.* 117, 783–794.

Quinton J. N., Govers G., Van Oost K. and Bardgett R. D. (2010) The impact of agricultural soil erosion on biogeochemical cycling. *Nat. Geosci.* 2010 35 3, 311–314.

Rad S. D., Allègre C. J. and Louvat P. (2007) Hidden erosion on volcanic islands. Earth Planet. Sci. Lett. 262, 109–124.

Rahaman W. and Singh S. K. (2012) Sr and 87Sr/86Sr in estuaries of western India: Impact of submarine groundwater discharge. Geochim. Cosmochim. Acta 85, 275–288.

Rahman S., Aller R. C. and Cochran J. K. (2016) Cosmogenic 32Si as a tracer of biogenic silica burial and diagenesis: Major deltaic sinks in the silica cycle. Geophys. Res. Lett. 43, 7124–7132.

Rahman S., Tamborski J. J., Charette M. A. and Cochran J. K. (2019) Dissolved silica in the subterranean estuary and the impact of submarine groundwater discharge on the global marine silica budget. Mar. Chem. 208, 29–42.

Rajeevan M., Unnikrishnan C. K., Bhate J., Niranjan Kumar K. and Sreekala P. P. (2012) Northeast monsoon over India: variability and prediction. Meteorol. Appl. 19, 226–236.

Raman C. V., Krishna Rao G., Reddy K. S. N. and Ramesh M. V. (1995) Clay mineral distributions in the continental shelf sediments between the Ganges mouths and Madras, east coast of India. Cont. Shelf Res. 15, 1773–1793.

Rengarajan R. and Sarma V. V. S. S. (2015) Submarine groundwater discharge and nutrient addition to the coastal zone of the Godavari estuary. Mar. Chem. 172, 57–69.

Reynolds B. C., Aggarwal J., André L., Baxter D., Beucher C., Brzezinski M. A., Engström E., Georg R. B., Land M., Leng M. J., Opfergelt S., Rodushkin I., Sloane H. J., Boorn S. H. J. M. van den, Vroon P. Z. and Cardinal D. (2007) An inter-laboratory comparison of Si isotope reference materials. J. Anal. At. Spectrom. 22, 561–568.

Reynolds B. C., Georg R. B., Oberli F., Wiechert U. and Halliday A. N. (2006) Re-assessment of silicon isotope reference materials using high-resolution multi-collector ICP-MS. J. Anal. At. Spectrom. 21, 266–269.

Reynolds J. H. and Verhoogen J. (1953) Natural variations in the isotopic constitution of silicon. Geochim. Cosmochim. Acta 3, 224–234.

Rickers K., Mezger K. and Raith M. M. (2001) Evolution of the Continental Crust in the Proterozoic Eastern Ghats Belt, India and new constraints for Rodinia reconstruction: implications from Sm–Nd, Rb–Sr and Pb–Pb isotopes. Precambrian Res. 112, 183–210.

Rickert D., Schlüter M. and Wallmann K. (2002) Dissolution kinetics of biogenic silica from the water column to the sediments. Geochim. Cosmochim. Acta 66, 439–455.

Ridgwell A., Hargreaves J. C., Edwards N. R., Annan J. D., Lenton T. M., Marsh R., Yool A. and Watson A. (2007) Marine geochemical data assimilation in an efficient Earth system model of global biogeochemical cycling. Biogeosciences 4, 87–104.

Riding R. (2006) Cyanobacterial calcification, carbon dioxide concentrating mechanisms, and Proterozoic–Cambrian changes in atmospheric composition. Geobiology 4, 299–316.

Riebe C. S., Hahm W. J. and Brantley S. L. (2017) Controls on deep critical zone architecture: a historical review and four testable hypotheses. Earth Surf. Process. Landforms 42, 128–156.

Riotte J., Maréchal J. C., Audry S., Kumar C., Bedimo Bedimo J. P., Ruiz L., Sekhar M., Cisel M., Chitra Tarak R., Varma M. R. R., Lagane C., Reddy P. and Braun J. J. (2014a) Vegetation impact on stream chemical fluxes: Mule Hole watershed (South India). *Geochim. Cosmochim. Acta* 145, 116–138.

Riotte J., Meunier J. D., Zambardi T., Audry S., Barboni D., Anupama K., Prasad S., Chmeleff J., Poitrasson F., Sekhar M. and Braun J. J. (2018a) Processes controlling silicon isotopic fractionation in a forested tropical watershed: Mule Hole Critical Zone Observatory (Southern India). Geochim. Cosmochim. Acta 228, 301–319.

Riotte J., Meunier J. D., Zambardi T., Audry S., Barboni D., Anupama K., Prasad S., Chmeleff J., Poitrasson F., Sekhar M. and Braun J. J. (2018) Processes controlling silicon isotopic fractionation in a forested tropical watershed: Mule Hole Critical Zone Observatory (Southern India). Geochim Cosmochim Acta 228, 301–319.

Riotte J., Ruiz L., Audry S., Baud B., Bedimo Bedimo J. P., Boithias L., Braun J. J., Dupré B., Duprey J. L., Faucheux M., Lagane C., Marechal J. C., Moger H., Mohan Kumar M. S., Parate H., Ribolzi O., Rochelle-Newall E., Sriramulu B., Varma M. and Sekhar M. (2021) The Multiscale TROPIcal CatchmentS critical zone observatory M-TROPICS dataset III: Hydro-geochemical monitoring of the Mule Hole catchment, south India. *Hydrol. Process.* 35, e14196.

Riotte J., Ruiz L., Audry S., Sekhar M., Mohan Kumar M. S., Siva Soumya B. and Braun J. J. (2014b) Impact of Vegetation and Decennial Rainfall Fluctuations on the Weathering Fluxes Exported from a Dry Tropical Forest (Mule Hole). *Procedia Earth Planet. Sci.* 10, 34–37.

Riotte J., Sandhya K., Prakash N. B., Audry S., Zambardi T., Chmeleff J., Buvaneshwari S. and Meunier J. D. (2018b) Origin of silica in rice plants and contribution of diatom Earth fertilization: insights from isotopic Si mass balance in a paddy field. Plant Soil 423, 481–501.

.

Robert M., Thomas A., Sekhar M., Badiger S., Ruiz L., Willaume M., Leenhardt D. and Bergez J. E. (2017) Farm Typology in the Berambadi Watershed (India): Farming Systems Are Determined by Farm Size and Access to Groundwater. *Water* 2017, Vol. 9, Page 51 9, 51.

Rodell M., Famiglietti J. S., Wiese D. N., Reager J. T., Beaudoing H. K., Landerer F. W. and Lo M. H. (2018) Emerging trends in global freshwater availability. Nat. 2018 5577707 557, 651–659.

Rodell M., Velicogna I. and Famiglietti J. S. (2009) Satellite-based estimates of groundwater depletion in India. Nat. 2009 4607258 460, 999–1002.

Roerdink D. L., van den Boorn S. H. J. M., Geilert S., Vroon P. Z. and van Bergen M. J. (2015) Experimental constraints on kinetic and equilibrium silicon isotope fractionation during the formation of non-biogenic chert deposits. Chem. Geol. 402, 40–51.

Ronchi Benedicta, Clymans Wim, Lúcia Pena Barão A., Vandevenne Floor, Struyf Eric, Batelaan Okke, Dassargues Alain, Govers Gerard, Ronchi B, Clymans W, Batelaan O, Dassargues A, Govers G, P Barão A. L., Vandevenne F and Struyf E (2013) Transport of Dissolved Si from Soil to River: A Conceptual Mechanistic Model. Silicon 2013 51 5, 115–133.

Rouxel O. J. and Luais B. (2017) Germanium Isotope Geochemistry. Rev. Mineral. Geochemistry 82, 601–656.

Roy R., Chitari R., Kulkarni V., Krishna M. S., Sarma V. V. S. S. and Anil A. C. (2015) CHEMTAX-derived phytoplankton community structure associated with temperature fronts in the northeastern Arabian Sea. Journal of Marine Systems 144, 81–91.

Rudnick R. L. and Gao S. (2003) Composition of the Continental Crust. In Treatise on Geochemistry Elsevier Inc. pp. 1–64.

Ruiz L., Varma M. R. R., Kumar M. S. M., Sekhar M., Maréchal J. C., Descloitres M., Riotte J., Kumar S., Kumar C. and Braun J. J. (2010) Water balance modelling in a tropical watershed under deciduous forest (Mule Hole, India): Regolith matric storage buffers the groundwater recharge process. *J. Hydrol*. 380, 460–472.

S. Masood A., V. M. Padmakumari and G. Anil Babu (2009) Strontium and neodymium isotopic compositions in sediments from Godavari, Krishna and Pennar rivers on JSTOR. Curr. Sci. 97, 1766–1769.

Saccone L., Conley D. J., Koning E., Sauer D., Sommer M., Kaczorek D., Blecker S. W. and Kelly E. F. (2007) Assessing the extraction and quantification of amorphous silica in soils of forest and grassland ecosystems. Eur. J. Soil Sci. 58, 1446–1459.

Saha D. and Ray R. K. (2018) Groundwater resources of India: Potential, challenges and management. Groundw. Dev. Manag. Issues Challenges South Asia, 19–42.

Santoni S., Huneau F., Garel E., Aquilina L., Vergnaud-Ayraud V., Labasque T. and Celle-Jeanton H. (2016) Strontium isotopes as tracers of water-rocks interactions, mixing processes and residence time indicator of groundwater within the granite-carbonate coastal aquifer of Bonifacio (Corsica, France). Sci. Total Environ. 573, 233–246.

Santos I. R., Chen X., Lecher A. L., Sawyer A. H., Moosdorf N., Rodellas V., Tamborski J., Cho H. M., Dimova N., Sugimoto R., Bonaglia S., Li H., Hajati M. C. and Li L. (2021) Submarine groundwater discharge impacts on coastal nutrient biogeochemistry. Nat. Rev. Earth Environ. 2021 25 2, 307–323.

Sarath P. K., Mangalaa K. R., Cardinal D., Gurumurthy G. P., Dapoigny A., Sarma V. V. S. S. and Riotte J. (2022) Seasonal, weathering and water use controls of silicon cycling along the river flow in two contrasting basins of South India. Chem Geol 604, 120883.

Sarma V. V. S. S., Gupta S. N. M., Babu P. V. R., Acharya T., Harikrishnachari N., Vishnuvardhan K., Rao N. S., Reddy N. P. C., Sarma V. V., Sadhuram Y., Murty T. V. R. and Kumar M. D. (2009) Influence of river discharge on plankton metabolic rates in the tropical monsoon driven Godavari estuary, India. Estuar. Coast. Shelf Sci. 85, 515–524.

Sarma V. V. S. S., Prasad V. R., Kumar B. S. K., Rajeev K., Devi B. M. M., Reddy N. P. C., Sarma V. V. and Kumar M. D. (2010) Intra-annual variability in nutrients in the Godavari estuary, India. Cont. Shelf Res. 30, 2005–2014.

Savage P. S., Armytage R. M. G., Georg R. B. and Halliday A. N. (2014) High temperature silicon isotope geochemistry. *Lithos* 190–191, 500–519.

Savage P. S., Georg R. B., Armytage R. M. G., Williams H. M. and Halliday A. N. (2010) Silicon isotope homogeneity in the mantle. Earth Planet. Sci. Lett. 295, 139–146.

Savage P. S., Georg R. B., Williams H. M. and Halliday A. N. (2013) The silicon isotope composition of the upper continental crust. Geochim. Cosmochim. Acta 109, 384–399.

Schmitt A. D., Borrelli N., Ertlen D., Gangloff S., Chabaux F. and Osterrieth M. (2018) Stable calcium isotope speciation and calcium oxalate production within beech tree (Fagus sylvatica L.) organs. Biogeochemistry 137, 197–217.

Schmitt A. D., Chabaux F. and Stille P. (2003) The calcium riverine and hydrothermal isotopic fluxes and the oceanic calcium mass balance. Earth Planet. Sci. Lett. 213, 503–518.

Schmitt A. D., Cobert F., Bourgeade P., Ertlen D., Labolle F., Gangloff S., Badot P. M., Chabaux F. and Stille P. (2013) Calcium isotope fractionation during plant growth under a limited nutrient supply. Geochim. Cosmochim. Acta 110, 70–83.

Sekhar M., Riotte J., Ruiz L., Jouquet P. and Braun J. J. (2016) Influences of climate and agriculture on water and biogeochemical cycles: Kabini critical zone observatory. *Proc. Indian Natl. Sci. Acad.* 82, 833–846.

Shamsudduha M., Uddin A., Saunders J. A. and Lee M. K. (2008) Quaternary stratigraphy, sediment characteristics and geochemistry of arsenic-contaminated alluvial aquifers in the Ganges–Brahmaputra floodplain in central Bangladesh. J. Contam. Hydrol. 99, 112–136.

Shand P., Darbyshire D. P. F., Gooddy D. and H. Haria A. (2007) 87Sr/86Sr as an indicator of flowpaths and weathering rates in the Plynlimon experimental catchments, Wales, U.K. Chem. Geol. 236, 247–265.

Sharma M., Balakrishna K., Hofmann A. W. and Shankar R. (2007) The transport of Osmium and Strontium isotopes through a tropical estuary. Geochim. Cosmochim. Acta 71, 4856–4867.

Shi L. and Jiao J. J. (2014) Seawater intrusion and coastal aquifer management in China: a review. Environ. Earth Sci. 72, 2811–2819.

Siebert S., Burke J., Faures J. M., Frenken K., Hoogeveen J., Döll P. and Portmann F. T. (2010) Groundwater use for irrigation - A global inventory. Hydrol. Earth Syst. Sci. 14, 1863–1880.

Singh S. P., Singh S. K., Bhushan R. and Rai V. K. (2015) Dissolved silicon and its isotopes in the water column of the Bay of Bengal: Internal cycling versus lateral transport. Geochim. Cosmochim. Acta 151, 172–191.

Singha K. and Navarre-Sitchler A. (2022) The Importance of Groundwater in Critical Zone Science. Groundwater 60, 27–34.

Smil V. (2003) Phosphorus in the environment: Natural Flows and Human Interferences. *Annual Review of Energy and the Environment.* 25, 53–88.

Soumya B. S., Sekhar M., Riotte J., Audry S., Lagane C. and Braun J. J. (2011) Inverse models to analyze the spatiotemporal variations of chemical weathering fluxes in a granito-gneissic watershed: Mule Hole, South India. *Geoderma* 165, 12–24.

Soumya B. S., Sekhar M., Riotte J., Banerjee A. and Braun J. J. (2013) Characterization of groundwater chemistry under the influence of lithologic and anthropogenic factors along a climatic gradient in Upper Cauvery basin, South India. *Environ. Earth Sci*. 69, 2311–2335.

Sridevi B., Sarma V. V. S. S., Murty T. V. R., Sadhuram Y., Reddy N. P. C., Vijayakumar K., Raju N. S. N., Jawahar Kumar C. H., Raju Y. S. N., Luis R., Kumar M. D. and Prasad K. V. S. R. (2015) Variability in stratification and flushing times of the Gautami–Godavari estuary, India. J. Earth Syst. Sci. 124, 993–1003.

Stallard R. F. and Edmond J. M. (1981) Geochemistry of the Amazon: 1. Precipitation chemistry and the marine contribution to the dissolved load at the time of peak discharge. *J. Geophys. Res. Ocean*. 86, 9844–9858.

Stanton C., Ben |, Barnes D., Lee |, Kump R. and Cosmidis J. (2022) A re-examination of the mechanism of whiting events: A new role for diatoms in Fayetteville Green Lake (New York, USA). Geobiology 00, 1–19.

Statham P. J. (2012) Nutrients in estuaries — An overview and the potential impacts of climate change. Sci. Total Environ. 434, 213–227.

Street-Perrott F. A. and Barker P. A. (2008) Biogenic silica: a neglected component of the coupled global continental biogeochemical cycles of carbon and silicon. *Earth Surf. Proc. Land.* 33, 1436–1457.

Struyf E., Smis A., Van Damme S., Garnier J., Govers G., Van Wesemael B., Conley D. J., Batelaan O., Frot E., Clymans W., Vandevenne F., Lancelot C., Goos P. and Meire P. (2010) Historical land use change has lowered terrestrial silica mobilization. Nat. Commun. 1, 1–7.

Struyf E., Van Damme S., Gribsholt B., Bal K., Beauchard O., Middelburg J. J. and Meire P. (2007) Phragmites australis and silica cycling in tidal wetlands. Aquat. Bot. 87, 134–140.

Sun X., Olofsson M., Andersson P. S., Fry B., Legrand C., Humborg C. and Mörth C. M. (2014) Effects of growth and dissolution on the fractionation of silicon isotopes by estuarine diatoms. Geochim. Cosmochim. Acta 130, 156–166.

Sun Y., Wu L. H. and Li X. Y. (2016) Experimental Determination of Silicon Isotope Fractionation in Rice. PLoS One 11, e0168970.

Sun Y., Wu L., Li X., Sun L., Gao J., Ding T. and Zhu Y. (2017) Silicon Isotope Fractionation in Maize and its Biogeochemical Significance. *Anal. Lett.* 50, 2475–2490.

Sutton J. N., André L., Cardinal D., Conley D. J., De Souza G. F., Dean J., Dodd J., Ehlert C., Ellwood M. J., Frings P. J., Grasse P., Hendry K., Leng M. J., Michalopoulos P., Panizzo V. N. and Swann G. E. A. (2018) A review of the stable isotope bio-geochemistry of the global silicon cycle and its associated trace elements. Front. Earth Sci. 5, 112.

Sutton J. N., Varela D. E., Brzezinski M. A. and Beucher C. P. (2013) Species-dependent silicon isotope fractionation by marine diatoms. Geochim. Cosmochim. Acta 104, 300–309.

Sutton J., Ellwood M. J., Maher W. A. and Croot P. L. (2010) Oceanic distribution of inorganic germanium relative to silicon: Germanium discrimination by diatoms. Global Biogeochem. Cycles 24.

Tang J., Niedermayr A., Köhler S. J., Böhm F., Kisakürek B., Eisenhauer A. and Dietzel M. (2012) Sr2+/Ca2+ and 44Ca/40Ca fractionation during inorganic calcite formation: III. Impact of salinity/ionic strength. Geochim. Cosmochim. Acta 77, 432–443.

Taniguchi M., Burnett W. C., Cable J. E. and Turner J. V. (2002) Investigation of submarine groundwater discharge. Hydrol. Process. 16, 2115–2129.

Taniguchi M., Ishitobi T. and Shimada J. (2006) Dynamics of submarine groundwater discharge and freshwater-seawater interface. J. Geophys. Res. Ocean. 111, 1008.

Tatzel M., von Blanckenburg F., Oelze M., Schuessler J. A. and Bohrmann G. (2015) The silicon isotope record of early silica diagenesis. Earth Planet. Sci. Lett. 428, 293–303.

Taylor R. G., Scanlon B., Döll P., Rodell M., Van Beek R., Wada Y., Longuevergne L., Leblanc M., Famiglietti J. S., Edmunds M., Konikow L., Green T. R., Chen J., Taniguchi M., Bierkens M. F. P., Macdonald A., Fan Y., Maxwell R. M., Yechieli Y., Gurdak J. J., Allen D. M., Shamsudduha M., Hiscock K., Yeh P. J. F., Holman I. and Treidel H. (2012) Ground water and climate change. Nat. Clim. Chang. 2012 34 3, 322–329.

Teuchies J., Vandenbruwaene W., Carpentier R., Bervoets L., Temmerman S., Wang C., Maris T., Cox T. J. S., Van Braeckel A. and Meire P. (2013) Estuaries as Filters: The Role of Tidal Marshes in Trace Metal Removal. PLoS One 8, e70381.

Thenkabail P. S., Biradar C. M., Noojipady P., Dheeravath V., Li Y., Velpuri M., Gumma M., Gangalakunta O. R. P., Turral H., Cai X., Vithanage J., Schull M. A. and Dutta R. (2009) Global irrigated area map (GIAM), derived from remote sensing, for the end of the last millennium. *Int. J. Remote Sens.* 30, 3679–3733.

Thiry M. (2000) Palaeoclimatic interpretation of clay minerals in marine deposits: an outlook from the continental origin. *Earth-Science Rev.* 49, 201–221.

Tipper E. T., Gaillardet J., Galy A., Louvat P., Bickle M. J. and Capmas F. (2010) Calcium isotope ratios in the world's largest rivers: A constraint on the maximum imbalance of oceanic calcium fluxes. Global Biogeochem. Cycles 24.

Tipper E. T., Galy A. and Bickle M. J. (2006) Riverine evidence for a fractionated reservoir of Ca and Mg on the continents: Implications for the oceanic Ca cycle. Earth Planet. Sci. Lett. 247, 267–279.

Tipper E. T., Schmitt A. D. and Gussone N. (2016) Global ca cycles: Coupling of continental and oceanic processes. Adv. Isot. Geochemistry, 173–222.

Tréguer P. J. and De La Rocha C. L. (2013) The World Ocean Silica Cycle. Ann. Rev. Mar. Sci. 5, 477–501.

Tréguer P. J., Sutton J. N., Brzezinski M., Charette M. A., Devries T., Dutkiewicz S., Ehlert C., Hawkings J., Leynaert A., Liu S. M., Monferrer N. L., López-Acosta M., Maldonado M., Rahman S., Ran L. and Rouxel O. (2021) Reviews and syntheses: The biogeochemical cycle of silicon in the modern ocean. Biogeosciences 18, 1269–1289.

Tréguer P., Bowler C., Moriceau B., Dutkiewicz S., Gehlen M., Aumont O., Bittner L., Dugdale R., Finkel Z., Iudicone D., Jahn O., Guidi L., Lasbleiz M., Leblanc K., Levy M. and Pondaven P. (2017) Influence of diatom diversity on the ocean biological carbon pump. Nat. Geosci. 2017 111 11, 27–37.

Valens H. (2021) A Geochemical and Sr, Ca, Mg, Li isotopic study of the Godavari River draining the Deccan basalts. IISc, Bangalore.

Vander Linden C. and Delvaux B. (2019) The weathering stage of tropical soils affects the soil-plant cycle of silicon, but depending on land use. *Geoderma* 351, 209–220.

Vandevenne F. I., Barão L., Ronchi B., Govers G., Meire P., Kelly E. F. and Struyf E. (2015) Silicon pools in human impacted soils of temperate zones. *Global Biogeochem. Cycles* 29, 1439–1450.

Vandevenne F. I., Delvaux C., Hughes H. J., André L., Ronchi B., Clymans W., Baraõ L., Govers G., Meire P. and Struyf E. (2015) Landscape cultivation alters δ^{30}Si signature in terrestrial ecosystems. Sci Rep 5.

Vandevenne F., Struyf E., Clymans W. and Meire P. (2012) Agricultural silica harvest: Have humans created a new loop in the global silica cycle? *Front. Ecol. Environ*. 10, 243–248.

Verma S. and Phansalkar S. J. (2003) India's Water Future 2050. Int. J. Rural Manag. 3, 149–179.

Violette A., Goddéris Y., Maréchal J. C., Riotte J., Oliva P., Kumar M. S. M., Sekhar M. and Braun J. J. (2010b) Modelling the chemical weathering fluxes at the watershed scale in the Tropics (Mule Hole, South India): Relative contribution of the smectite/kaolinite assemblage versus primary minerals. *Chem. Geol*. 277, 42–60.

Violette A., Riotte J., Braun J. J., Oliva P., Marechal J. C., Sekhar M., Jeandel C., Subramanian S., Prunier J., Barbiero L. and Dupre B. (2010a) Formation and preservation of pedogenic carbonates in South India, links with paleo-monsoon and pedological conditions: Clues from Sr isotopes, U–Th series and REEs. *Geochim. Cosmochim. Acta* 74, 7059–7085.

Vitòria L., Otero N., Soler A. and Canals A. (2004) Fertilizer characterization: Isotopic data (N, S, O, C, and Sr). Environ. Sci. Technol. 38, 3254–3262.

Wadleigh M. A., Veizer J. and Brooks C. (1985) Strontium and its isotopes in Canadian rivers: Fluxes and global implications. Geochim. Cosmochim. Acta 49, 1727–1736.

Walker J. C. G., Hays P. B. and Kasting J. F. (1981) A negative feedback mechanism for the long-term stabilization of Earth's surface temperature. J. Geophys. Res. Ocean. 86, 9776–9782.

Weider K. and Boutt D. F. (2010) Heterogeneous water table response to climate revealed by 60 years of ground water data. Geophys. Res. Lett. 37.

Weiner S. and Dove P. M. (2003) An Overview of Biomineralization Processes and the Problem of the Vital Effect. Rev. Mineral. Geochemistry 54, 1–29.

Weiss A., De La Rocha C., Amann T. and Hartmann J. (2015) Silicon isotope composition of dissolved silica in surface waters of the Elbe Estuary and its tidal marshes. Biogeochemistry 124, 61–79.

Welti N., Gale D., Hayes M., Kumar A., Gasparon M., Gibbes B. and Lockington D. (2015) Intertidal diatom communities reflect patchiness in groundwater discharge. Estuar. Coast. Shelf Sci. 163, 116–124.

Wenninger J., Beza D. T. and Uhlenbrook S. (2010) Experimental investigations of water fluxes within the soil–vegetation–atmosphere system: Stable isotope mass-balance approach to partition evaporation and transpiration. *Phys. Chem. Earth*, Parts A/B/C 35, 565–570.

Wheat C Geoffrey, Mcmanus James, Wheat C G and Mcmanus J (2008) Germanium in mid-ocean ridge flank hydrothermal fluids. Geochemistry, Geophys. Geosystems 9, 3025.

White A. F., Vivit D. V., Schulz M. S., Bullen T. D., Evett R. R. and Aagarwal J. (2012) Biogenic and pedogenic controls on Si distributions and cycling in grasslands of the Santa Cruz soil chronosequence, California. Geochim. Cosmochim. Acta 94, 72–94.

White P. J. and Broadley M. R. (2003) Calcium in plants. Ann. Bot. 92, 487–511.

Wiegand B. A., Chadwick O. A., Vitousek P. M. and Wooden J. L. (2005) Ca cycling and isotopic fluxes in forested ecosystems in Hawaii. Geophys. Res. Lett. 32, 1–4.

Will S., Paul J. C. and John R. M. (2007) The Anthropocene: Are Humans Now Overwhelming the Great Forces of Nature. AMBIO 38, 614–621.

Wollast R. and Mackenzie F. T. (1989) Global Biogeochemical Cycles and Climate. Clim. Geo-Sciences, 453–473.

World Bank Archive (WBA) (2015), http://data.worldbank.org/indicator/AG.LND.PRCP.MM

Worthington S. R. H., Davies G. J. and Alexander E. C. (2016) Enhancement of bedrock permeability by weathering. Earth-Science Rev. 160, 188–202.

Xu X. and Liu W. (2017) The global distribution of Earth's critical zone and its controlling factors. Geophys. Res. Lett. 44, 3201–3208.

Yeghicheyan D., Aubert D., Bouhnik-Le Coz M., Chmeleff J., Delpoux S., Djouraev I., Granier G., Lacan F., Piro J. L., Rousseau T., Cloquet C., Marquet A., Menniti C., Pradoux C., Freydier R., Vieira da Silva-Filho E. and Suchorski K. (2019) A New Interlaboratory Characterisation of Silicon, Rare Earth Elements and Twenty-Two Other Trace Element Concentrations in the Natural River Water Certified Reference Material SLRS-6 (NRC-CNRC). Geostand. Geoanalytical Res. 43, 475–496.

Young E. D., Galy A. and Nagahara H. (2002) Kinetic and equilibrium mass-dependent isotope fractionation laws in nature and their geochemical and cosmochemical significance. Geochim. Cosmochim. Acta 66, 1095–1104.

Zanner C. W. and Graham R. C. (2005) Deep regolith: exploring the lower reaches of soil. Geoderma 126, 1–3.

Zektser I. S. and Loaiciga H. A. (1993) Groundwater fluxes in the global hydrologic cycle: past, present and future. J. Hydrol. 144, 405–427.

Zhang A. Y., Zhang J., Hu J., Zhang R. F. and Zhang G. S. (2015) Silicon isotopic chemistry in the Changjiang Estuary and coastal regions: Impacts of physical and biogeochemical processes on the transport of riverine dissolved silica. J. Geophys. Res. Ocean. 120, 6943–6957.

Zhang J., Jin M., Cao M., Huang X., Zhang Z. and Zhang L. (2021) Sources and behaviors of dissolved sulfate in the Jinan karst spring catchment in northern China identified by using environmental stable isotopes and a Bayesian isotope-mixing model. Appl. Geochemistry 134, 105109.

Zhang Z., Cao Z., Grasse P., Dai M., Gao L., Kuhnert H., Gledhill M., Chiessi C. M., Doering K. and Frank M. (2020) Dissolved silicon isotope dynamics in large river estuaries. Geochim. Cosmochim. Acta 273, 367–382.

Zheng X. Y., Beard B. L. and Johnson C. M. (2019) Constraining silicon isotope exchange kinetics and fractionation between aqueous and amorphous Si at room temperature. Geochim. Cosmochim. Acta 253, 267–289.

Zhou Y. Q., Sawyer A. H., David C. H. and Famiglietti J. S. (2019) Fresh Submarine Groundwater Discharge to the Near-Global Coast. Geophys Res Lett 46, 5855–5863Zhu P. and Douglas Macdougall J. (1998) Calcium isotopes in the marine environment and the oceanic calcium cycle. Geochim. Cosmochim. Acta 62, 1691–1698.

Ziegler K., Chadwick O. A., White A. F. and Brzezinski M. A. (2005) δ30Si systematics in a granitic saprolite, Puerto Rico. *Geology* 33, 817–820.

Zou J., Yang Y. and Zhang H. (2018) Sr isotope fingerprinting of multiple water-source characterizations and its environmental implications in a complex lake-groundwater system, Wudalianchi, Northeast China. Chemosphere 212, 1095–1103.

List of figures and tables

Abstract

Groundwater forms a dynamic system exhibiting spatial and temporal heterogeneity, and acts as an intermediate between surface processes occurring in critical zone and the riverine systems, which ultimately delivers solutes from continents to ocean. Recent studies reveal that the submarine groundwater discharge (SGD) is a dominant pathway for nutrient delivery to the coastal ocean, often exceeding riverine nutrient fluxes, thus forming a significant component of oceanic biogeochemical cycling. However, SGD remains overlooked in coastal nutrient budgets and is difficult to quantify given large spatial and temporal variability. Among the elements delivered to the coast through SGD, silicon (Si) forms a key nutrient for diatoms, one of the dominant primary producers in freshwaters, estuary and coastal ecosystems. Tropical humid watersheds with seasonal monsoonal precipitation, commonly found in Indian subcontinent, favours intense silicate weathering resulting in high Si fluxes to surface and groundwaters. However, anthropogenic activities including agriculture and damming can significantly modulate Si cycling and requires further evaluation, particularly in groundwater. The present research investigates three major aspects of groundwater Si cycling: i) the impact of land use alterations (such as agriculture) and monsoon precipitation in groundwater dissolved silicon (DSi) and silicon isotopic signature (δ^{30}Si) by comparing an agricultural (Berambadi) and forested (Mule Hole) watersheds across two seasons, ii) elucidating groundwater-surface water interactions in the largest monsoonal estuarine system in India (Godavari) and, iii) quantify the fresh submarine groundwater derived Si fluxes to Indian Ocean using a series of coastal groundwaters along Indian coastline. We employ multiple isotopic tracers to understand biogeochemical processes in groundwater including water isotopes and $^{87}Sr/^{86}Sr$ to understand sources and mixing, δ^{30}Si and Ge/Si ratios to trace Si cycling, and $\delta^{44/40}$Ca to decipher carbonate weathering in critical zone.

The present work increased the δ^{30}Si average of global groundwater from 0.49±0.9‰ (1SD, n=66) to 0.81±0.9‰ (1SD, n=224), lower than the river water and seawater δ^{30}Si. We show that the δ^{30}Si signatures of groundwater are not impacted by land use alterations and seasonal monsoon, and are primarily driven by silicate weathering and secondary clay formation in soil and saprolite. Groundwater system generally exhibits a steady state behaviour with a dynamic equilibrium between Si supply and formation of secondary phases. We conclude that Si isotopic signatures of weathering, adsorption, and plant uptake occurring in the shallow soil and saprolite horizons are partly overprinted and homogenized by the regolith weathering in the deep critical zone. In the second part of the thesis, we study Godavari estuary and adjacent groundwater to discern sources *vs.* mixing *vs.* processes along this land-to-ocean interface. The δ^{30}Si signatures of estuary exhibit significant temporal variability, primarily driven by diatom uptake and some heterogeneous groundwater discharge during dry season while silicate weathering and secondary clay formation in the basin dominate during wet season. We note that estuaries can act as significant filters for Si supply to ocean, removing ~15% of the total DSi supplied by the Godavari river. The $\delta^{44/40}$Ca composition in Godavari estuary (1.3±0.5‰, 1SD, n=16) and groundwaters (1.6±0.7‰, 1SD, n=15) are highly heterogenous. The Ca isotopic fractionation in both estuary and groundwater are primarily driven by precipitation of secondary carbonates, a process that would require further study. Finally, the dissolved silicon and δ^{30}Si of coastal groundwater all over India indicates that fresh SGD discharge contributes to <1% of the total Si flux of the rivers and is considered to have insignificant impact on oceanic Si and isotopic budgets in North Indian Ocean.